Modelling surface climate over complex terrain for landscape ecology

Andrew Noel Joyce

Modelling Surface Climate over Complex Terrain for Landscape Ecology

by

Andrew Noel Joyce

Department of Biological Sciences
University of Durham
2000

Submitted in partial fulfilment of the requirements for the degree of
Doctor of Philosophy

"*The more that you read, the more things you will know,*
The more that you learn, the more places you'll go."

Dr. Seuss

Declaration

The material contained within this thesis has not previously been submitted for a degree at the University of Durham or at any other University. The research reported within this thesis has been conducted by the author unless indicated otherwise.

Modelling Surface Climate over Complex Terrain for Landscape Ecology

PhD Thesis Abstract

Andrew Noel Joyce, 2000

Climate exerts a fundamental control on ecosystem function, species diversity and distribution. Topographic variability may influence surface climate, through processes operating at a landscape-scale. To quantify and model such influences, the topography of a 72 km^2 area of complex terrain, (including the Moor House National Nature Reserve in northern England) was analysed at 50 m resolution. A suite of topographic variables was created, including distance relative to the Pennine ridge (*dist*), and elevation difference between each grid cell and the lowest grid cell within a specified neighbourhood (*drain*). Automatic weather stations (AWS) were deployed in a series of networks to test hypothetical relationships between landscape and climate.

Daily maximum air temperature, daily mean soil temperature and daily potential evapotranspiration can be modelled spatially using a daily lapse rate calculated from the difference between daily observations made at two base stations. On days with a south easterly wind direction, daily mean temperature is estimated as a function of lapse rate and *dist*; the spatial behaviour of temperature is consistent with a föhn mechanism. Daily minimum temperature is modelled using lapse rate and *drain* on days with a lapse rate of minimum temperature shallower than $-2.03 \times 10\ ^{o}C\ m^{-1}$, incorporating the effects of katabatic air flow. Daily solar radiation surfaces are estimated by a GIS routine that models interactions between slope and solar geometry and accounts for daily variations in cloudiness and daylight duration.

The daily climate surfaces were tested using data measured at a range of AWS locations during different times of year. The accuracy of the daily surfaces is not seasonally-dependent. The spatial climate data are particularly well suited to landscape-scale ecology because the methods account for prevailing topoclimatic constraints and because separate climate surfaces are generated for each day, capturing the high frequency variability characteristic of upland regions.

Acknowledgements

I thank my departmental supervisors Dr Bob Baxter and Professor Brian Huntley for their help and encouragement, and for having confidence that I would return from Bolivia and finish writing up. The supervision of Dr Terry Parr and John Adamson at CEH Merlewood helped with the fieldwork logistics and gave useful perspectives on the research.

I am grateful to past and present members of the Environmental Change Research Group including Dr Judy Allen, Dr Lisa Belyea, Jon Bennie, Dr Yvonne Collingham, Dr John Daniell, Andy Dean and Dr Kate Lewthwaite for their technical and practical assistance.

Thanks to my parents and Tammy for their support throughout.

Contents

Tables

Figures

Chapter 8

Chapter 1. Introduction

1.1. Defining the problem

The aim of the research is to develop methodologies to spatialise weather station data over an area of complex terrain, by testing hypotheses concerning relationships between topography and climate variables. There is a need for data spatialisation methodologies that address explicitly the topo-climatic variability influencing ecological processes. An improvement in the quality of spatially-gridded climate data will be beneficial for many ecological applications, for example as input to the ecological models used to evaluate effects of environmental change at a landscape-scale (approximately 10^2 to 10^4 m).

Station data can be interpolated numerically to a grid of any desired spatial resolution, however these methods are optimal at much larger geographical and temporal scales where station data are relatively dense and the data fields are smooth. The ecological effects of short-term events such as frosts or storms can be large, making a fine temporal resolution necessary, and landscape-scale topographic variability introduces an inherent roughness to climatic fields especially in hilly terrain. Numerical methods cannot simulate meaningful climate surfaces from the sparse and noisy station data typically available at these scales.

The work herein describes the experimental quantification of some effects of landscape-scale variability on climate within the Moor House National Nature Reserve in the northern Pennines of the United Kingdom (Figure 1.1). The fundamental hypothesis under investigation is that landscape-scale topographic effects on climate can be identified and modelled to improve daily spatial estimates of climate variables for ecological applications.

1.2. Scales of climatic variability

Climate has different meanings according to the size of the domain in question because atmospheric processes operate at characteristic scales in space and time (Linacre, 1992). As the solar energy received by the Earth is distributed by cascades of kinetic energy from large scale processes (e.g. Hadley circulation, mid-latitude depressions) to smaller scale

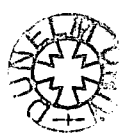

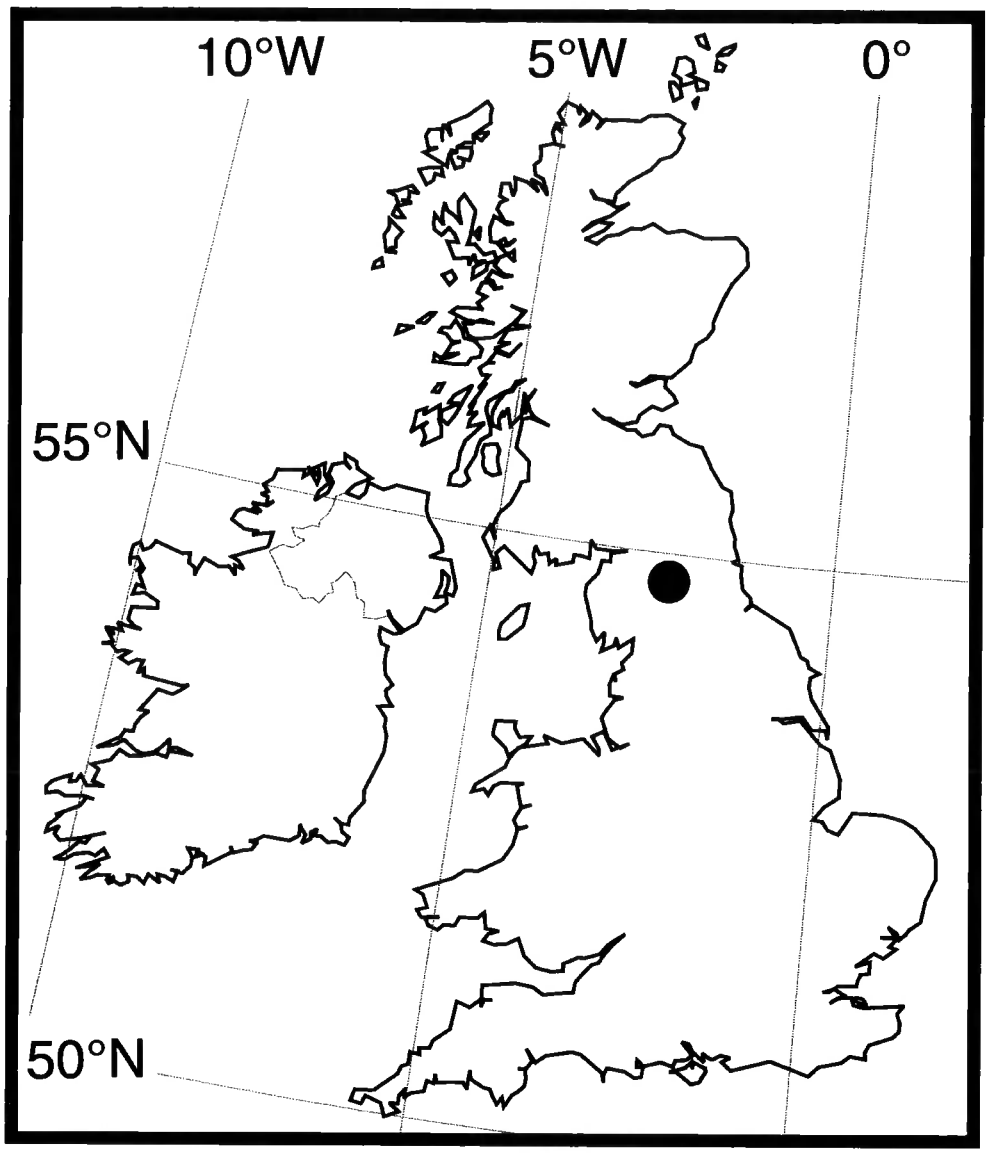

Figure 1.1. The location of the Moor House National Nature Reserve

processes (e.g. temperature inversions, sea breezes) the axes of rotation of air circulation become increasingly random. Turbulent mixing transfers heat and moisture between surface and atmosphere, and destroys gradients inherent to large-scale motion, dissipating the circulation (Salby, 1996). The definition of scales may not be entirely arbitrary. Although energy and mass cascades can be visualised as occurring over a continuum of temporal and spatial scales (Oke, 1978), peaks are identifiable in energy density spectra of atmospheric motion at frequencies of approximately 1 minute and 4 days, corresponding to micro-scale and synoptic scale atmospheric processes (Houghton, 1977). A hierarchy of characteristic spatial scales of atmospheric processes may also correspond to similar scales of organisation in other systems, for example ecosystem organisation or geomorphological process domains (Linacre, 1981).

Description and explanation of climate must recognise the relevant scale-dependant processes (Oke, 1978). At a synoptic scale the climate of the British Isles is controlled by maritime location enhanced by proximity to the warm North Atlantic Drift current (Davies, Kelly and Osborn, 1997), and by the location of the islands in the path of mid-latitude depressions (Barrow and Hulme, 1997). These geographical factors determine large scale gradients of precipitation and temperature, and provide a context in which the effects of smaller scale processes are nested. Elevation above sea level is a further fundamental control on orographic precipitation and temperature (Barrow and Hulme, 1997).

Upon the large scale patterns of climate dictated by synoptic processes is superimposed landscape-scale climatic variability arising from interactions of the surface and atmosphere and from spatial and temporal changes in the magnitude and sign of components of the surface radiation budget. The distribution of extra-terrestrial short wave radiation reaching the top of the atmosphere from the Sun is determined solely by orbital geometry (Peixoto and Oort, 1992). Similarly, for a given latitude and solar declination, incoming short wave and incoming long-wave radiation vary at a surface site primarily with solar azimuth and altitude (Oke, 1978). The fluxes of outgoing reflected short wave and emitted long wave radiation vary according to the physical properties of the surface; the outgoing short wave flux is determined by surface albedo (Equation 1.1).

$$K\uparrow = \alpha K\downarrow \qquad 1.1$$

where $K\uparrow$ = reflected short wave radiation (W m^{-2})

α = albedo

$K\downarrow$ = incident short wave radiation (W m^{-2})

Outgoing long wave flux is determined by surface emissivity and temperature, according to the Stefan-Boltzmann equation (Equation 1.2).

$$L\uparrow = \varepsilon\sigma T^4 \qquad 1.2$$

where $L\uparrow$ = emitted long wave radiation (W m^{-2})

ε = surface emissivity

σ = Stefan-Boltzmann constant (5.67×10^{-8} W m^{-2} K^{-4})

T = surface temperature (K)

The effect of topography on short wave radiation receipt over a surface can be modelled trigonometrically from slope gradient and aspect, and solar altitude and azimuth (North, 1994). The relative effect of topographical variability on radiation distribution increases with latitude. The cosine law of illumination describes the influence of slope on flux density according to Equation 1.3.

$$K\downarrow = K\downarrow_i \cos\Theta \qquad 1.3$$

where $K\downarrow_i$ = radiant flux density perpendicular to incident beam (W m^{-2})

Θ = angle between incident beam and a plane normal to the surface (degrees)

The net all-wave radiation balance at a surface can be expressed as the sum of the short wave and long wave balances (Equation 1.4).

$$Q_n = K\downarrow - K\uparrow + L\downarrow - L\uparrow \qquad 1.4$$

where Q_n = net all-wave radiation (W m^{-2})

$L\downarrow$ = incident long wave radiation (W m^{-2})

The diurnal excess of surface net radiation is distributed by fluxes of mass and energy (Oke, 1978), to the earth and atmosphere as sensible and latent heat (Equation 1.5).

$$Q_n - Q_h - Q_e = 0 \qquad 1.5$$

where Q_h = sensible heat flux (W m^{-2})

Q_e = latent heat flux (W m^{-2})

The ratio of Q_h to Q_e is the Bowen ratio B (Equation 1.6).

$$\frac{Q_h}{Q_e} = B \qquad 1.6$$

The Bowen ratio is a climatically important quantity. Low values of B occur where surface moisture is plentiful, and excess surface energy tends to be expended as latent heat during the evaporation process. High values of B indicate that surface moisture is limited and the majority of the energy flux from the surface to the atmosphere is in the form of sensible heat, raising the temperature of the lower atmosphere.

Vegetated surfaces also store heat physically and biochemically by photosynthesis (Oke, 1978). In addition to sensible heat fluxes from the surface to the ground and atmosphere, evapotranspiration is an important mechanism in the surface energy budget, allowing the transfer of energy from moist or vegetated surfaces to the atmosphere as latent heat of vaporisation. Potential evapotranspiration (*PE*) is defined as the rate at which water, if available, is removed from a short healthy vegetated surface (Burman and Pochop, 1994),

and can be estimated at a coarse resolution by empirical temperature-based methods (Thornthwaite, 1948) or by mechanistic combination methods which include radiation terms (Priestley and Taylor, 1972), and wind speed terms (Penman, 1948), accounting for physical processes. The Penman equation can be used to compare relative moisture budgets in space and time, or can be calibrated accurately for specific surfaces. *PE* can be expressed as a density of energy flux or converted to an equivalent volume of water.

The climatic control exerted by surface properties affecting absorption, reflection and re-emission of radiation and the distribution of heat can be illustrated using the example of snow. The albedo of fresh snow can reach 0.95 (Burman and Pochop, 1994), reducing short-wave radiation absorption and lowering daytime maximum temperatures (Dewey, 1977). The high emissivity of snow leads to increased long-wave radiation loss and low temperature minima. In addition, snow is an effective thermal insulator inhibiting the release of terrestrial heat. Topographic controls on radiation budget are enhanced under snow cover. Feedback processes operate to maintain low temperature and prolong cover, and can eventually affect slope development.

As well as vertical exchanges of energy, advective exchanges occur when air in horizontal motion moves across surfaces with different radiative, thermal or moisture properties, causing energy fluxes to be strongly in disequilibrium. Marked discontinuities in surface properties may cause leading-edge advection effects resulting in steep horizontal climatic gradients, for example between a stand of mature pine and an adjacent cleared area (Saunders *et al.*, 1999). An oasis effect can occur when evaporation proceeds from an isolated area at a rate higher than its surroundings and the energy required to drive evaporation exceeds the local radiative surplus (Oke, 1978). Advective processes arising from spatial differences in surface properties are further complicated by topography. Complex terrain can affect surface climate by interacting with the air flow in the free atmosphere (Guo and Palutikof, 1990) and by generating local air flows as thermal circulation systems. An orographic barrier may disrupt regional air flow and cause spatial climatic variations by numerous mechanisms. For example, a föhn effect occurs when moist air is forced to rise against windward slopes, causing cooling at the saturated adiabatic lapse rate. On the leeward side of the orographic barrier, air descends and warms

at the steeper dry adiabatic lapse rate having lost water vapour by condensation (Barry, 1992). This process can cause substantial spatial temperature anomalies either side of a mountain ridge (Sturman *et al.*, 1999). Greater prevalence of cloud in saturated air on windward slopes may also reduce insolation relative to leeward slopes. The area to the lee of the barrier may thus develop a more positive surface radiation balance and the excess energy may be converted to sensible heat, raising surface temperature.

The spatial pattern of climate over a landscape can be visualised as a mosaic resulting from interlinked topographic and micro-climatic effects. In general, topo-climates result from landscape influences on climate elements at a scale of between 100 m and 10 km (Barry, 1992), while micro-climates arise from differences in surface properties at scales smaller than 100 m (Oke, 1978). The range of scales at which atmospheric processes operate influences the selection of an appropriate sampling strategy for the observation of climatic data. Extreme care is taken in the choice of site for official climate stations, as well as in the exposure of instruments within the site (Meteorological Office, 1982). A climate station is thus regionally representative, sampling as far as possible large-scale and not landscape-scale or micro-scale effects. This sampling strategy attempts to ensure that data gathered from such a network minimise variability arising from landscape-scale roughness. Any climate surface interpolated using data from such a network will similarly lack sub-grid scale variability, a desirable feature for many applications. In order to derive a meaningful climate surface at the finer resolutions necessary for landscape-scale ecological modelling, the landscape-scale topographical variability should be intentionally sampled so the effects are captured in the station data. Topographical features identified as exerting climatic influence at a landscape-scale can then be included as predictor variables during the calculation of the climate surface.

1.3. Climatic control of species distributions

An overview of the extent to which climate controls biotic systems is presented in two sections, focusing in turn on examples from the plant and animal kingdoms. Standard nomenclature is used for flowering plants (Clapham, Tutin and Moore, 1987), grasses (Hubbard, 1954), and mosses (Smith, 1978).

1.3.1. Plant growth and distributions

The role played by climate in determining plant growth and distribution can be empirically described over broad latitudinal zones and biomes (Holdridge, 1947) and at the level of populations responding to landscape-scale and micro-climatic variation (Rorison, 1981). At a continental scale, climatic control on biotic distributions can be seen where a species meets its extreme limit with respect to one climatic element (Lamb, 1977). Observed species distributions can follow closely isotherms of long-term mean temperature, and since the European distribution of *Ilex* L., *Hedera* L. and *Viscum* L. were described in terms of climate (Iversen, 1944), many studies have expressed distributions in two-dimensional or multi-dimensional climate space. Lamb describes qualitatively the apparent climatic limits of British upland species: *Empetrum nigrum* ssp. *nigrum* L. grows in a more oceanic climate than *E. nigrum* ssp. *hermaphroditum* (Hagerup) Böcher; *Calluna vulgaris* (L.) Hull prefers a drier, colder, more continental climate than *Erica tetralix* L., while *E. erigena* R. Ross seldom occurs where winter temperature falls regularly below 3°C (Lamb, 1977).

Several groups have suggested the gross phenology of vegetation is directly influenced by climate (Lennon and Turner, 1995; Pfister, 1992), and mathematical or statistical relationships can be calculated between observed climate data and growth indices (Fritts and Shao, 1992), especially for species growing near their ecological limits. However, such techniques show that biotic responses effectively integrate climatic influences over a range of timescales. Response functions are usually improved by the inclusion of multiple independent climatic variables, but inter-correlation of climate variables often necessitates the use of orthogonal principal components to express the variance of growth in terms of climate (Bradley and Jones, 1992; Ford and Milne, 1981).

At a physiological level temperature affects many aspects of plant growth, controlling the activity of enzyme systems and reaction rates. The rates of respiration and transpiration are dependent on temperature, and except for early photochemical reactions, every step of the photosynthetic process is directly and immediately affected by temperature (Bjorkman, 1981). An optimum range of temperature can be specified over which the rate of gross

photosynthesis in a species exceeds that of respiration (Pisek *et al.*, 1973). Transplant experiments have shown large differences between species in the ability to adapt to alien temperature regimes (either warmer, cooler or more variable than native habitats), an effect arising from the response of photosynthesis to temperature (Bjorkman, 1981). The onset of emergence and physiological maturity can be controlled by accumulated thermal time, while mean temperature is an influence on flowering (McKenzie and Hill, 1989). The effects of temperature thus vary according to the phase of a plant's life-cycle as well as between species (Rorison, 1981).

A period of low temperature may be necessary to terminate dormancy in buds and seeds, and to initiate leaf expansion and shoot development (Pisek *et al.*, 1973). Exposure to temperatures below a certain threshold may also result in permanent damage. *Calluna vulgaris*, for example, is susceptible to frost damage resulting in visible injury and ion leakage from shoots (Caporn, Risager and Lee, 1994). Frost hardiness is compounded by other environmental factors such as nitrogen supply, and the presence of trace gases such as ozone (Foot *et al.*, 1996). Ecological studies identify growing season temperature as a control on vegetative and reproductive performance in *C. vulgaris*; shoot extension was less rapid, flowering was delayed and flowers persisted for longer during the cool 1982/83 season in New Zealand (Chapman and Bannister, 1995). The accumulation and duration of snow cover is a control on the distribution of vegetation at a landscape scale (Palacios and Sanchez Colomer, 1997; Schaefer and Messier, 1995), affecting the initiation of growth via radiation budget and temperature. Accumulated snow represents an important source of stored water, rapid ablation can cause a spring surge of moisture and nutrient availability to plants.

Water availability to the surface can be expressed in terms of quantity (gravimetric or volumetric water content), or in terms of energy status as soil water potential (Rundel and Jarrell, 1996). The ratio of actual to potential evapotranspiration is an index of water availability and may be a fundamental control on plant growth. Water stress prevents full stomatal opening, reducing transpiration and photosynthesis, and increasing leaf temperature (Tromp, 1980). If this happens, photosynthesis is restricted to re-assimilation of CO_2 released internally by respiration (Pisek *et al.*, 1973).

The seasonal cycle of daylight duration affects higher plants via the phytochrome system controlling many responses including shoot lengthening, changes in cell respiration and protein synthesis (Tromp, 1980). To initiate flowering, for example, a plant must receive a species-specific minimum number of photo-inductive cycles after its juvenile phase. Increasing light intensity increases the rate of photosynthesis, and can also cause the optimum rate of photosynthesis to occur at a higher temperature (Pisek *et al.*, 1973). Under given illumination the rate of photosynthesis varies with carboxylation pathway and between species (Pisek *et al.*, 1973).

High wind speeds can inhibit growth by causing chilling at the leaf and meristem, and by the direct effect of motion (Grace, 1981). Wind is also an important factor influencing the surface moisture budget, causing desiccation in extreme cases. The effect of wind on transpiration can be estimated using combination methods, e.g. the Penman-Monteith equation (Burman and Pochop, 1994). Elevation exerts considerable indirect climatic control on plant growth and distribution because air temperature, radiation intensity, wind speed and humidity are all theoretically dependent on elevation. Height, stem diameter, flower abundance, and seed set in *Calluna vulgaris* were found to decrease with elevation in a New Zealand study (Chapman and Bannister, 1994), although soil characteristics and management strategies must also be considered as important controls on plant distribution.

Process-based biogeographical models, for example BIOME (Prentice *et al.*, 1992), Century (Schimel *et al.*, 1996) and the vegetation and ecosystem modelling and analysis project (VEMAP members, 1995) incorporate physiological plant responses to climatic influences and other environmental variables such as soil, water and nutrient availability. The BIOME model employs a mechanistic approach to explaining species distribution, using as input variables the mean temperature of the coldest and warmest months, temperature sums and a moisture index (the ratio of actual to potential evapotranspiration). Vegetation distributions are estimated by classifying species into plant functional types according to shared climatic constraints (Prentice *et al.*, 1992). Human management and policy priorities may exert a primary control on geographical distributions, which will also be complicated by dynamic non-climatic processes determining succession such as

dispersal of propagules, establishment, competition, mortality and disturbance, for example by fire (Hulme, 1996; Mackey *et al.*, 1996).

The influences of climate on the development of particular species can also be modelled at a fine temporal resolution; for example, in an agricultural context models have been developed to simulate the growth and yield of crops including *Triticum* spp. (Porter, 1993), *Lupinus* spp. (Milford *et al.*, 1995) and *Lens* spp. (McKenzie and Hill, 1989). The model LENMOD (McKenzie and Hill, 1989) estimates seed yield for a lentil crop (*Lens culinaris* Medik.) using daily values of maximum and minimum air temperature, solar radiation, precipitation, potential evapotranspiration, and daylight duration. The time from sowing to crop emergence is controlled in the model by accumulated thermal time above 2°C, thereafter leaf area expansion is modelled as a linear function of temperature. The photosynthetically-active radiation intercepted by the crop is modelled as a function of solar radiation, leaf area and canopy architecture. The time from crop emergence to flowering depends on daylight duration as well as temperature. From flowering to the development of maximum leaf area, growth is proportional to solar radiation, subject to adequate soil water availability. Maximum leaf area, physiological maturity and finally seed yield are achieved in the model after a pre-determined number of degree days are accrued (McKenzie and Hill, 1989).

1.3.2. Animal growth and distributions

Diverse evidence exists for climatic influence on the ecology of animal species. Insect development rates (as for all poikilothermic organisms) can be described accurately as a function of temperature (Briere *et al.*, 1999), and the development of individual insects can be more strongly related to accumulated heat above a critical physiological threshold than to chronological age (Gullan and Cranston, 1996). Optimum mean maximum and mean minimum air temperatures (32°C and 14°C respectively) were identified for *Culicoides* mosquitoes in Spain (Ortega, Holbrook and Lloyd, 1999). Oviposition rates are also temperature dependent (Gullan and Cranston, 1996). Both the time to egg hatching and percentage of eggs hatching reach an optimum at 29°C for the nematode *Longidorus africanus* (Ploeg, 1999), while a minimum winter temperature of -35.5°C represents the

lower threshold for egg survival in the moth *Epirrita autumnata* in Finland (Virtanen, Neuvonen and Nikula, 1998).

Malaria is a vector-borne disease of global importance that causes over 300 million clinical cases annually (Patz and Lindsay, 1999). The geographical distribution of the disease has been modelled in relation to climate at regional and continental scales (Craig, Snow and le Sueur, 1999). Temperature is fundamentally important to malaria distribution, affecting the level of occurrence of mosquito vectors and the risk of epidemic. At a physiological level, development of the malaria parasite is affected by temperature thresholds, e.g. 18°C for *Plasmodium falciparum*, which is the most dominant and lethal species in Africa (Lindsay and Martens, 1998), and 15°C for *P. vivax* (Patz and Lindsay, 1999). The period required for the parasite to become infectious within the vector depends on accumulated thermal time above this threshold temperature. Experiments show that the development rate of both eggs and pupae of the mosquito *Anopheles minimus* is proportional to temperature (Muirhead-Thomson, 1951). However, development rates tend to decrease above a high-temperature threshold (e.g. 30°C for *Toxorhynchites brevipalpis*). The rate of digestion of blood meals by the mosquito is also proportional to temperature, which affects biting frequency. In addition to temperature, moisture availability is critical for successful breeding in mosquito populations (Lindsay, Parson and Thomas, 1998), with species exhibiting systematic preferences for relatively wet sites (e.g. *Anopheles gambiae*) or dry sites (e.g. *Anopheles arabiensis*). The climatic environment thus imposes physiological constraints on the development of both parasite and vector. The relative proliferation of mosquitoes within suitable climatic parameters influences both the geographical distribution of the disease vector, and the distribution of the risk of malaria transmission (Rogers and Randolph, 2000). Disease risk is also controlled by non-climatic factors such as habitat availability, land-use and management strategies.

Ninety percent of global malaria cases occur in Africa (Patz and Lindsay, 1999). Despite the lower prevalence of malaria in highland areas (due to cooler temperatures and moister conditions occurring at higher elevations) regions with high relief experience larger climatic gradients within a given area, making the geographical distribution of malaria especially sensitive within the highlands. Human populations living at high elevations are

especially susceptible to malaria due to low levels of natural immunity and paucity of health care resources (Lindsay and Martens, 1998). During a recent increase in clinical malaria cases in Rwanda, the increase was greatest in highland areas (Loevinsohn, 1994). Epidemics are more likely in regions where environmental transmission thresholds are exceeded sporadically (Lindsay and Martens, 1998), and the steep environmental gradients thus render highland areas especially susceptible. Environmental change due to agriculture and forestry development can also influence the distribution of malaria in highland areas (Lindsay and Martens, 1998) and there is a need to clarify sensitivity of transmission rates to climatic and non-climatic effects.

1.4. Observing upland climate at a fine scale

Meteorological studies in mountainous terrain are hampered by a paucity of observing stations. Data from mountain regions are usually restricted to valley locations (Barry, 1992). Practical problems (e.g. extremes of snowfall, temperature or wind) may prevent adherence to the regular protocols for meteorological observations. Mountain stations may also record conditions of purely local significance, because terrain complexity precludes a site having regionally representative exposure. The European Alps have the longest history of upland meteorological observations, e.g. the Sonnblick observatory (3106 m) in Austria has operated since 1886, and observations have been made at the Jungfraujoch (3577 m) in Switzerland since 1923. Long-running mountain top observatories in the United States include Mount Washington (1917 m) in New Hampshire and Pike's Peak (4301 m) in Colorado (Stone, 1934). In the UK, an observatory was operational at the summit of Ben Nevis (1343 m) between 1883 and 1904, when it closed due to lack of funding (Paton, 1983). The summit observations provided the basis for studies on the effects of winds on air pressure (Buchan, 1893), the distribution with elevation of temperature and humidity in depressions and anticyclones (Omond, 1900) and the occurrence of thunderstorms (Mossman, 1893). The availability of data observed simultaneously at sea level at Fort William (6.5 km distant) allowed the identification of gradients in temperature, humidity and air pressure with elevation (Omond, 1896).

Previous studies of the climate of the British uplands have identified an unusually small seasonal range of temperature and precipitation, compared to lowland sites and to uplands

in other regions (Barry, 1992), largely due to the maritime characteristics of the prevailing air masses. Lapse rates of temperature are particularly steep, resulting in dramatic changes in vegetation and land use with elevation (Manley, 1945). Regional analysis of data from paired stations shows a mean lapse rate in annual mean maximum temperature of -8.5×10^{-3} °C m^{-1} (Harding, 1978) although the lapse rates are steepest in spring and shallowest in winter (Manley, 1942) as is the case for most of Europe (Barry, 1992). Discussion of the gradient of minimum temperature at a regional scale is hindered by the effects of local topography, although the diurnal temperature range in British uplands is small relative to lowland sites (Barry, 1992). Despite the increasing availability of automatic weather station data from upland sites (e.g. Cairngorm and Aonach Mor in the Scottish Highlands) to supplement data from lowland networks (Barton, 1984), the following observation is still pertinent:

> "It behoves us to introduce more direct and comprehensive measurements of the British upland climates, which must be envisaged as more than aggregations of wet, cloud, wind, cold and snow" (Taylor, 1976).

Dynamic ecosystem models which simulate ecological processes using climate data as input usually run on a daily or monthly time-step. Such models are typically run either for a single site, or at a coarse resolution for continental or global studies. Landscape-scale applications require that climate is modelled at sufficiently fine scales to capture explicitly the spatial extent of phenomena which are topographically influenced, as well as sporadic fluctuations in the occurrence or intensity of such phenomena. Ecological scales are smaller than the resolution of most climatic data sets. The discrepancy is compounded in complex terrain, where heterogeneity in variables such as temperature, precipitation and solar radiation can be enhanced by topography. Short-term events such as frosts or heat waves, and events such as droughts that are autocorrelated in time can have profound ecological effects but are often lost from climatic data sets if the temporal resolution used for modelling is too coarse.

1.5. The need for gridded surface climate data

Climatic information can be extrapolated to individual sites using vector models, allowing ecological effects of climate to be studied at locations where climate is not measured. However, gridded climate surfaces facilitate spatial analysis, making the prediction and mapping of climate surfaces in areas between climate stations increasingly important in ecology (Lennon and Turner, 1995). A wide range of ecologically relevant climate surfaces can be calculated in addition to primary observed climate elements such as temperature and precipitation. The frequency of climatic phenomena (e.g. frosts or rain days) can be mapped, as can derived variables such as potential evapotranspiration, accumulated temperature (Hargy, 1997; Mackey *et al.*, 1996), diurnal temperature range or temperature variance over a specified timescale. For modelling purposes climatic surfaces must relate to the topographic surface. Many climate maps published in previous decades are ecologically meaningless, having been corrected to sea level, and thus fail to account for the overwhelming effect of elevation on many climatic elements (Lennon and Turner, 1995).

1.6. Available methods for gridding climate data

The simplest interpolation methods are graphical approaches such as the manual construction of isopleths (Meteorological Office, 1975) or the use of nearest neighbour values (Thiessen, 1911). Numerical interpolation methods include simple inverse-distance weighting schemes (Leemans and Cramer, 1991; Legates and Willmott, 1990), Cressman interpolation with user-specified influence radii, double-linear and polynomial interpolation (UNIRAS, 1985). Kriging and spline fitting are among the most complex examples of numerical interpolation techniques. The more complex methods are not necessarily the most powerful for a given application (Thornton, Running and White, 1997). Surfaces of mean monthly temperature were modelled for Great Britain using a range of methods (Lennon and Turner, 1995), and the best results were obtained from a mixed spline-regression model. The poorest-performing methods are those which fail to model geographical constraints at the scale in question.

The thin plate smoothing spline method (Wahba and Wendelberger, 1980) has been widely used for meteorological and climatological applications (Zheng and Basher, 1995), and is available as a set of FORTRAN routines (ANUSPLIN) (Hutchinson, 1987). Thin plate splines are defined by minimising the roughness of the interpolated surface, subject to having a specified residual from the data (Hutchinson and Gessler, 1994). The method avoids the need to estimate explicitly the spatial auto-covariance function, as with kriging (Mackey *et al.*, 1996), and allows the precise form of the response of the dependent variable to physical factors to be determined by the data points themselves rather than by *a priori* relationships (Hulme *et al.*, 1995). The thin-plate spline procedure allows multiple independent variables; additional predictor variables (or covariates) can be selected as indices of known physical causal processes. Spline surfaces can thus be part empirical and part process-based (Mackey *et al.*, 1996).

Splines can also incorporate linear sub-models, the coefficients of which are determined simultaneously with the spline fitting. Surfaces designed specifically for ecosystem modelling and impact applications have been interpolated for Europe, southern Africa, and global land areas at a spatial resolution of 0.5 degrees latitude and longitude (Hulme *et al.*, 1995; Hulme *et al.*, 1996; New, Hulme and Jones, 1999) and for Great Britain at 10 minutes latitude and longitude (Barrow, Hulme and Jiang, 1993), in all cases using a partial thin-plate spline. At these scales latitude, longitude and elevation above mean sea level are powerful statistical predictors of surface climate, capturing variability arising from synoptic processes and the effects of temperature lapse-rates and orographic rain.

Surfaces fitted using some interpolation methods may show small-scale variation near data points. Splines minimise this by assuming that observations comprise a signal component and a noise component. The spatially-coherent signal can be meaningfully interpolated whereas noise arises from sub-measurement-scale stochastic processes (Hutchinson and Gessler, 1994). Smoothing splines attempt to recover the signal and remove the noise, generally giving rise to smooth surfaces which are easy to interpret (Hutchinson and Gessler, 1994). Splines can thus serve a useful purpose in smoothing climatic data as well as for interpolation.

The spline procedure can be optimised for large data sets by using a subset of data points, or knots (Bates and Wahba, 1982). This leads to significant computational savings since the number of mathematical operations required is proportional to the cube of the number of data points used (Hutchinson and Gessler, 1994). Conversely, sparse data introduces error to the interpolation where the spatial variability of the surface is high and/or where the data points are well separated (Zheng and Basher, 1995). The value of the degrees of freedom of the residual sum of squares can therefore be a useful diagnostic tool; low values indicate data too sparse to adequately support interpolation, whereas high values imply that the model assumes neither measurement error nor micro-scale variation to exist in the data (Hutchinson and Gessler, 1994), which is unrealistic in most applications. Spline interpolation may be a suitable method for sparse data as the influence function includes a logarithmic component allowing for long range data interactions (Zheng and Basher, 1995).

The order and amount of smoothing imposed on the data can be determined objectively by minimising the generalised cross-validation (GCV) (Hutchinson and Gessler, 1994), a statistic which directly estimates prediction error without resorting to parametric model assumptions. Any interpolation method should be objective, and should allow diagnostic statistics to quantify predictive errors (Mackey *et al.*, 1996); GCV is calculated by removing each data point in turn and summing the square of the difference of each omitted value from a surface fitted to the remaining data, and is a robust estimator of overall error (Hutchinson and Gessler, 1994). GCV may be calculated implicitly because fitted values depend linearly on the data (Wahba, 1990). Splines are normally optimised automatically by choosing the order of the derivative (controlling surface roughness) and the amount of data smoothing to minimise the GCV; alternatively the user can define the degree of smoothing to obtain a subjective compromise between surface roughness and fit to the data (Zheng and Basher, 1995) based on a prior knowledge of the spatial characteristics of the signal surface and associated errors. Another statistic commonly used to quantify objectively the goodness-of-fit of a surface to the station data is the coefficient of determination (R^2). The statistic does not describe the behaviour of a surface away from the data points and requires careful interpretation; surfaces interpolated by some methods may be constrained to pass through all data points (R^2=1.0) yet may be poor predictors in data-sparse areas. The mean absolute error (MAE) and root-mean-square error (RMSE) are

alternative statistics, of the two MAE is inflated to a lesser degree by extreme outliers (Thornton *et al.*, 1997). The geographical distribution of large residuals from a surface may elucidate spatial processes overlooked by an interpolation model (Lennon and Turner, 1995).

Mechanistic modelling of landscape-scale ecological processes demands a fine temporal resolution; however, the spatial variability and roughness of interpolated surfaces increase as the time step of the input data decreases (Zheng and Basher, 1995). The climatic signal-to-noise ratio (SNR) in an interpolated surface should be maximised by using station data gathered over a common time period; if this criterion is not observed, the potential use of the surface for modelling purposes is severely reduced (Hulme *et al.*, 1995). The climatic signal can be optimised by disaggregating data by month (Mackey *et al.*, 1996), by time of day or by weather type (Palomino and Martin, 1994), a technique also used in down-scaling output from general circulation models (GCMs) of the global climate (Wilby, 1997). Classification by circulation type can be achieved subjectively (e.g. Lamb's daily weather types for the UK) or objectively using an index of pressure or wind flows.

In contrast to numerical interpolation, which relies on spatial autocorrelation in the station data to estimate a coherent climate surface, an alternative approach is the use of physical principles, empirically derived relationships, or features of statistical data distributions to extrapolate spatial variations in climate. Such methods include regression techniques establishing linear or non-linear relationships between topographic features and climate (Goodale, Aber and Ollinger, 1998; Lennon and Turner, 1995) and weather generator techniques (Wilks, 1999). Daily climate observations have been extrapolated using the MT-CLIM model (Running, Nemani and Hungerford, 1987) from one or two stations in a remote area of complex terrain where installation and maintenance of more instruments was considered unfeasible. Temperature was initially modelled taking account of elevation difference with user-specified lapse rates which were held constant in space and time. The model was subsequently developed (Thornton *et al.*, 1997) to use a truncated Gaussian filter for interpolation of data between stations onto a 500 m resolution grid, at a daily time step. Elevation, slope, aspect, latitude and albedo are used as predictors; humidity is estimated from minimum temperature and mean daytime temperature using empirical

relationships, and radiation is estimated from topographical variability and diurnal temperature range. The new version of the model estimates temperature for each cell by interpolation, weighting for distance and elevation. In the absence of solar radiation observations, insolation is modelled using latitude and solar declination to predict day length, truncated for hill slope and cloudiness using diurnal temperature range as a proxy variable. For the interpolation of daily precipitation fields, presence or absence of precipitation can be simulated prior to precipitation amount using a weather generator. A precipitation occurrence probability (POP) can be calculated for each cell by interpolating a variable for presence or absence of precipitation at data points (Thornton *et al.*, 1997). If the POP for a grid cell exceeds a critical threshold (held constant in space and time), a precipitation amount is interpolated. Alternatively, a Markov model may be used to model the presence of precipitation, or the conditional transition probability can be calculated of a wet day occurring, given that n previous days have been wet (Jones, Conway and Briffa, 1997).

The most appropriate method for spatialisation of station data is determined largely by the desired resolution of the climate surface, the density of the available station network and the smoothness of the true surface climate field. In effect, most methods (including splines and regression-based approaches) are partially empirical and partially process-based (Mackey *et al.*, 1996).

1.7. Remotely-sensed climate data

A possible alternative to gridded climate data sets spatialised from station observations is the use of remotely-sensed data, from which climatic information may be inferred. For example, the extent of cold cloud cover can be derived from the high resolution radiometer (HRR) on the European Meteorological Satellite Programme's Meteosat satellite; this variable can be used as a proxy for precipitation. The area and depth of snow cover can be sensed using visible and infra-red sensors in cloud-free conditions (Archer and Stewart, 1995), while land surface temperature and atmospheric moisture can be estimated using the NOAA Advanced Very High Resolution Radiometer (AVHRR). Evapotranspiration estimates can be obtained from LANDSAT Thematic Mapper data, which can provide a measure of variability of the partition of surface energy fluxes (Franks and Beven, 1997).

The relative benefits of station data and remotely-sensed data vary for different applications. A recent study of climatic influences on the abundance of the insect vector *Culicoides imicola* in southern Africa (Baylis, Meiswinkel and Venter, 1999) found that a bivariate model using a combination of the normalised difference vegetation index (a satellite measurement of photosynthetic activity) and remotely-sensed land surface temperature outperformed a model using observed climate variables. This result may be due in part to the relatively poor network of climate stations in the region (Hulme *et al.*, 1996). The smooth fields associated with regional scale temperature and humidity make spatialisation of station data generally more appropriate for these elements, while remotely-sensed coverages are well suited to the sampling of spatially variable climate elements such as precipitation.

Considerations specific to high-resolution upland studies include the abundance of cloud cover at high elevation sites, which may obscure the remote sensing of surface conditions. Problems of cloudiness are partially solved by the use of microwave sensors which can operate independently of cloud cover, e.g. Next Generation Weather Radar (NEXRAD), although disadvantages include the need for complex processing to interpret the radar back scatter in complex terrain. Previous studies have compared NEXRAD precipitation estimates with rain gauge data for the Appalachian Mountains; problems with the remotely sensed data included underestimation and non-detection of precipitation, as well as beam blockage in mountainous terrain which is not corrected by existing NEXRAD algorithms (Young *et al.*, 1999).

In general, the use of remotely sensed data necessitates a compromise between spatial and temporal resolution. A fine spatial resolution (30 m) is provided by polar orbiting platforms (e.g. the LANDSAT Thematic Mapper), but a given location may only be re-sampled every 16 days (Kondratyev, Johannessen and Melentyev, 1996). More frequent images are available from platforms in geostationary orbit, at a spatial resolution of approximately 1.1 km. For many ecological applications requiring data at high spatial and temporal resolutions these sampling considerations, as well as the cost of multiple coverages,

preclude the use of remotely-sensed data as a viable alternative to a network of automatic weather stations.

1.8. The study site

The northern Pennine uplands which rise between the Vale of Eden and Teesdale comprise the largest continuous area of land above 300 m elevation in England. The Moor House National Nature Reserve and the Upper Teesdale National Nature Reserve are located within the upland area and contain much of upper Teesdale and the Cross Fell range, together covering more than 8000 hectares. The area has a long history as a site for scientific research; climatic investigations at Moor House and Great Dun Fell date back to the 1930s (Manley, 1942). Annual mean temperature for Moor House (550 m) for the period 1941-70 was 5.1°C, and the mean annual precipitation total was 2010 mm (Manley, 1980) (the equivalent statistics for Durham observatory, at 102 m above sea level 50 km to the east, are 8.6°C and 649 mm). Ground frost can occur in any month, and precipitation falls on 240 days during an average year at Moor House (Pigott, 1978).

Previous work has investigated temporal variations in the relationship between elevation and temperature at isolated northern Pennine stations (Harding, 1979a) and along a transect on the escarpment west of Great Dun Fell (Pepin, Benham and Taylor, 1999). Intensive observations undertaken and analysed by Manley show the diurnal temperature range decreases systematically from the lowlands to the summits, while mean lapse rates are consistent with those measured at Ben Nevis (Manley, 1980). Lapse rates inferred from the surface observations are steep and vary diurnally and seasonally as well as with air mass and synoptic flow. Pigott (1978) estimates an annual mean wind speed of 10 m s^{-1} at Great Dun Fell summit; a dynamical modelling approach has also been applied to model wind flow and cloud development over Great Dun Fell within the context of the meso-scale atmospheric circulation (Wobrock *et al.*, 1997). Recent work has identified an increase in the variability of precipitation and runoff within the Moor House reserve, at both inter-annual and seasonal timescales (Burt, Adamson and Lane, 1998). The spatial variability of climate within the reserve, and specifically the influence of topography on climate, has not yet been addressed explicitly.

The location of the Moor House National Nature Reserve within Great Britain is shown in Figure 1.1. The Moor House and Upper Teesdale National Nature Reserves were designated as the first UK Biosphere Reserve in 1974 and together were chosen as a terrestrial site within the UK Environmental Change Network (ECN), a multi-agency research programme designed to record, analyse and predict environmental change (Burt, 1994). The Biosphere Reserve was also a flagship site for the NERC Terrestrial Initiative in Global Environmental Change (TIGER) programme, designed to investigate questions involving climatic control of ecosystem composition and diversity. Spatial data sets relevant to the study site and made available by the NERC Centre for Ecology and Hydrology (CEH, formerly the Institute of Terrestrial Ecology) include vegetation, soil and geology maps, a land cover map at 25 m resolution based on Landsat Thematic Mapper data, and a digital terrain model at a resolution of 50 m. Prior to the start of the project, automatic weather stations (AWS) were located near Moor House at grid reference NY 757328 (550 m), beside the Great Dun Fell access road at NY 699295 (465 m), NY 709302 (600 m), NY 718312 (750 m) and NY 710322 (840 m) as shown in Figure 1.2.

The vegetation at Moor House is representative of northern Pennine flora with *Calluna vulgaris*, *Eriophorum vaginatum* L., *Rubus chamaemorus* L. and *Sphagnum* L. dominating the blanket bog, while *Juncus squarrosus* L. and *Nardus stricta* L. are dominant in shallow peat (Eddy, Welch and Rawes, 1969). In the early 1980s *Eriophorum* was estimated to dominate in about 11% of the reserve (Rawes, 1983). An *Eriophorum*-dominated facies was identified above 670 m elevation and was assumed to be controlled primarily by climate, as *C. vulgaris* at high elevations on the reserve is frequently damaged by frost in winter and early spring (Eddy *et al.*, 1969). The same authors suggest that prolonged snow cover is a control on vegetation composition above 750 m, although the influence of sheep grazing on species distribution was later demonstrated experimentally, and edaphic factors also impose a spatial limitation (Rawes, 1983). Small forestry plantations of *Pinus sylvestris* L., *Picea abies* (L.) Karsten and *Larix decidua* Miller (established primarily as shelter units for grazing stock) exist at elevations up to about 570 m. Individual trees are stunted and deformed at the upper limit as the climatic environment changes with elevation (Millar, 1964). Possible responses of soil fauna to climatic change have been tested by

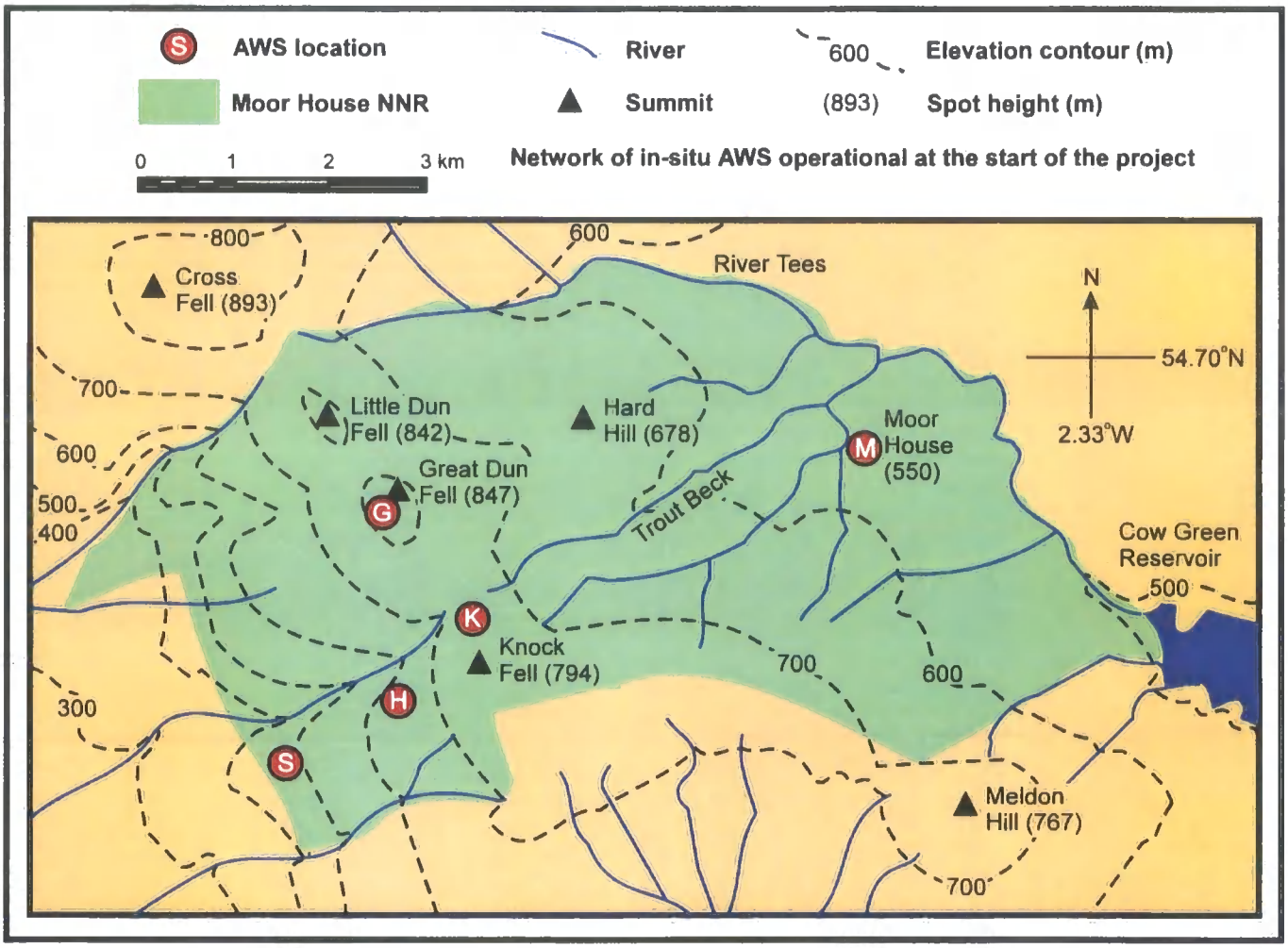

Figure 1.2. AWS locations within the study site at the start of the project. The locations are Moor House (M), Great Dun Fell summit (G), Knock Fell (K), High Carle Band (H) and Sink Beck (S).

transplanting soil cores between sites at 480 m and 845 m within the Moor House reserve (Briones, Ineson and Piearce, 1997), and by experiments designed to impose controlled environmental conditions on the soil fauna *in situ* (Millar, 1964).

Chapter 2. Topographic modelling

2.1. Hypotheses and techniques

Specific components of topographic variability must be modelled within the study site in order to quantify the influence of landscape on climate. Hypothesised relationships between landscape and climate can then be tested by installing automatic weather stations in networks designed to sample the topographic variability. Specific hypotheses regarding topography and its effect on climate include:

1. Terrain elevation above sea level within the study site can be used to predict (a) daily air temperature, (b) daily soil temperature, (c) daily potential evapotranspiration and (d) daily precipitation.

2. Daily air temperature varies systematically with slope aspect, in response to differences in the flux density of incident solar radiation.

3. The presence of terrain at higher elevation near a site affects daily air temperature at that site.

4. The presence of terrain at lower elevation near a site affects daily air temperature at that site, particularly by influencing the flow of katabatic gravity currents of cold air across the landscape.

5. Proximity to the orographic barrier of the Pennine ridge that bisects the study site exerts a systematic effect on daily air temperature, dependent on regional wind direction.

A digital terrain model (DTM) constructed at an appropriate spatial resolution is a prerequisite for all modelling procedures using elevation as a predictor variable. In addition to elevation itself, derivatives of the elevation surface can be calculated including gradient, aspect, convexities and ridges (Blaszczynski, 1997; Moore, Grayson and Ladson, 1991) as well as more abstract properties such as local surface twisting (Moore *et al.*, 1991). Gradient can show a complex relationship with elevation, depending on local relief.

Derivatives of elevation can be calculated by relating a point to its orthogonal neighbours, although a fitting scheme provides derived variables for the same locations as initial elevation data, allowing true inter-comparison (Blaszczynski, 1997). Previous work has compared the results of three algorithms for calculating slope gradient ("eight neighbours un-weighted", "steepest adjacent neighbour", and "four closest neighbours") (Moore *et al.*, 1991); correlation between the results produced by the three methods exceeds +0.99. The "eight neighbours un-weighted" method imposes least spatial bias, while the "steepest adjacent neighbour" method tends to result in systematically steeper gradients than other algorithms.

Elevation values can be smoothed, compensating for imprecise or erroneous data. Smoothing filters are commonly used in signal processing to reduce noise or variability in a data set. A data matrix may be filtered using a context operation where the output value is a function of neighbouring data points in the input matrix (Fotheringham and Rogerson, 1993), or the matrix can be smoothed to a standard value.

A consideration of relevant physical processes can aid the identification of landscape variables which may be expected to exert a climatic influence. Such variables might include the standard deviation of elevation within a specified area, the distance from the nearest coast, latitude and longitude (Lennon and Turner, 1995). These can be used arbitrarily as predictors of climate, or multiple regression model building techniques can be applied to select a model explaining the largest proportion of climatic variance for a given number of variables (Lennon and Turner, 1995).

A DTM of elevation within the study site was obtained from the NERC Centre for Ecology and Hydrology, Wallingford (formerly the Institute of Hydrology). The DTM is a raster grid, a data structure whereby the surface is divided into unit cells, each with an individual elevation value. The structure is space-filling and the uniform definition of geographical space aids analytical operations (Laurini and Thompson, 1992). The DTM has a resolution of 50 m × 50 m × 1 m and this spatial resolution was used for all subsequent modelling. The complete DTM covers the entirety of the Moor House and Upper Teesdale National Nature Reserves. For logistical reasons however, the data used for calibration and

validation of the climate surfaces could only be measured within the Moor House reserve. A sub-region of the DTM was therefore used for modelling purposes. This region is a rectangular area covering 72 km^2, measuring 11 km from east to west and 6.5 km from north to south. The south west corner of the region is located at grid reference NY 670280.

The DTM was processed using the GRID program in the ARC/INFO geographical information system, software which allows the storage, manipulation, analysis and display of information spatially referenced to the Earth's surface (Laurini and Thompson, 1992). The numerical computation software MATLAB was also used for manipulation and visualisation of the data matrices. Processing of the DTM enabled various derivatives of elevation to be calculated, each quantifying specific components of the topographic variability of the study site. The resulting topographic variables were used to test relationships between landscape and climate, as described in Chapter 5.

2.2. Elevation

The average rate of change of air temperature with altitude (the environmental lapse rate, or ELR) is approximately -6.0×10^{-3} °C m^{-1} in the free atmosphere (Barry, 1992). The ELR varies diurnally, seasonally and geographically according to the physical characteristics of the prevailing air mass. The mechanism for the systematic change of temperature with altitude is due to the fall in atmospheric pressure with altitude, such that air moving from lower to higher levels within the troposphere must expand adiabatically to compensate. In the absence of an external energy source, the work involved in expansion results in a loss of sensible heat from the system and a fall in air temperature (Peixoto and Oort, 1992). The theoretical limit to the rate of change of temperature with altitude is -9.8×10^{-3} °C m^{-1} (the dry adiabatic lapse rate, or DALR); this is the rate at which unsaturated air cools when displaced upwards (Barry, 1992).

Energy fluxes to and from the ground surface hinder direct comparisons between temperature at a given elevation at the surface and temperature at the same altitude in the free atmosphere. Nevertheless, the mechanism explains the systematic decrease in mean surface temperature with increasing elevation, and explains why topographic relief can

exert a much sharper control on surface temperature than latitude or longitude, especially in complex terrain (Taylor, 1976).

Elevation within the modelling region is depicted in Figure 2.1. This surface, and all topographic and climatic surfaces modelled subsequently, is portrayed from a virtual viewpoint south-east of the study region and 60° above the plane of the x and y axes. Elevation values range from 200 m in the south western corner of the region, to 893 m at the summit of Cross Fell. The Pennine ridge runs from the north west to the south east of the study area. To the west of the ridge lies the steep scarp slope which falls to the Eden Valley, while Moor House, the headwaters of the River Tees and the Trout Beck Valley are located in the shallower dip slope to the east.

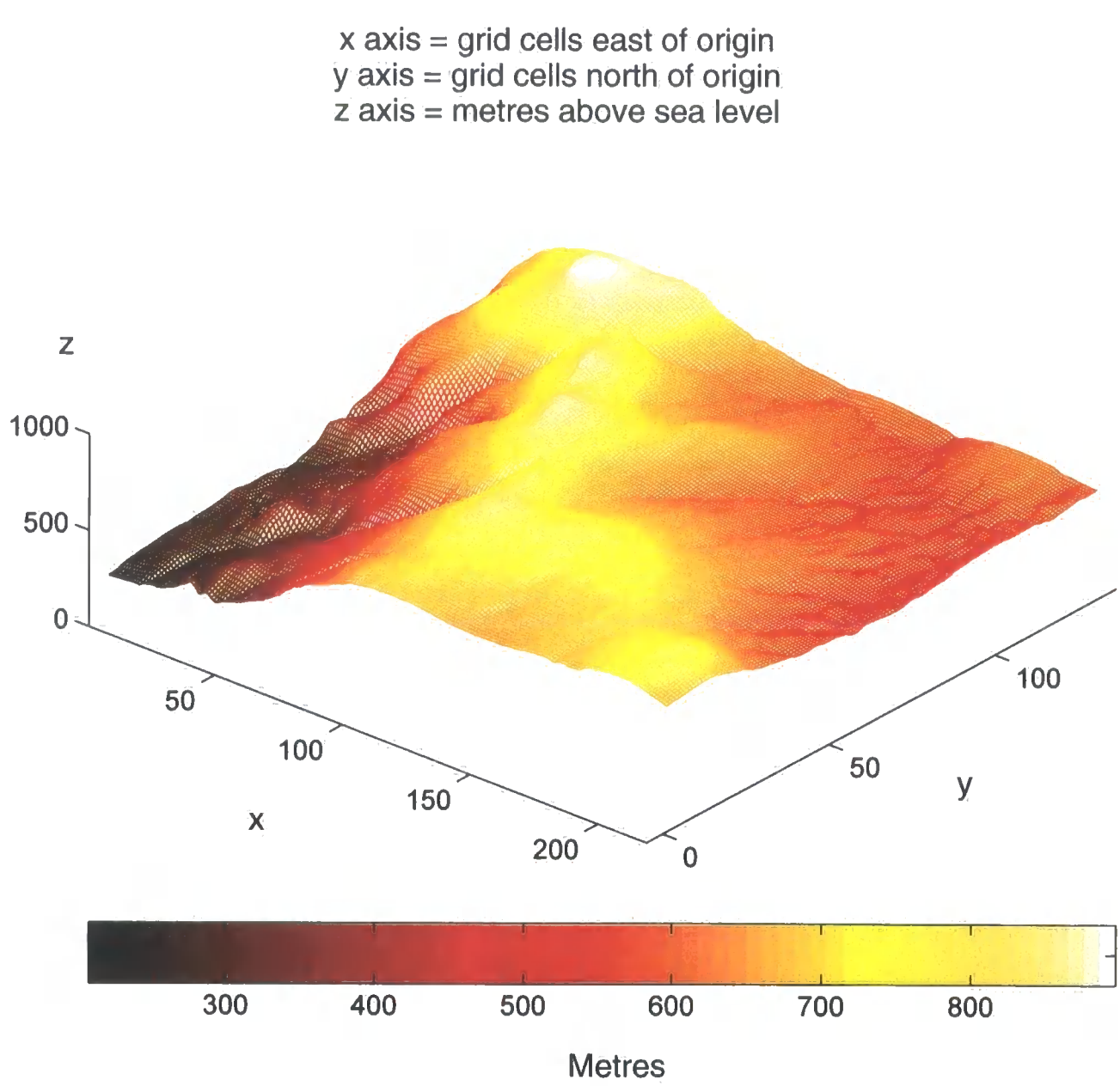

Figure 2.1. Elevation within the study site

2.3. Slope gradient

Slope gradient affects the flux density of direct-beam solar radiation to the ground as described in Equation 1.3. Gradient can therefore be an important control on solar radiation receipt at a given site, along with slope aspect, solar declination, solar azimuth and solar altitude (Geiger, Aron and Todhunter, 1995). The influence of slope variables on the radiation budget can also affect surface air temperature, as excess surface energy cascades to affect sensible heat flux as described in Equation 1.5.

Slope gradient was calculated for the study area using the *slope* function in ARC/INFO. The function returns the rate of maximum change in elevation from each grid cell to its eight nearest neighbours, in degrees. Output values can range from 0.0^{o} (horizontal slope) to 90.0^{o} (vertical slope). The resulting *slope* surface for the study area is shown in Figure 2.2. The *slope* surface clearly shows that the steepest gradients (exceeding 30^{o}) occur on the scarp slope to the west of the Pennine ridge. The shallowest gradients occur on the eastern slopes, whereas the upper reaches of the Tees Valley and the plateau between Knock Fell and Meldon Hill (see Figure 1.2) are virtually flat at a grid cell scale.

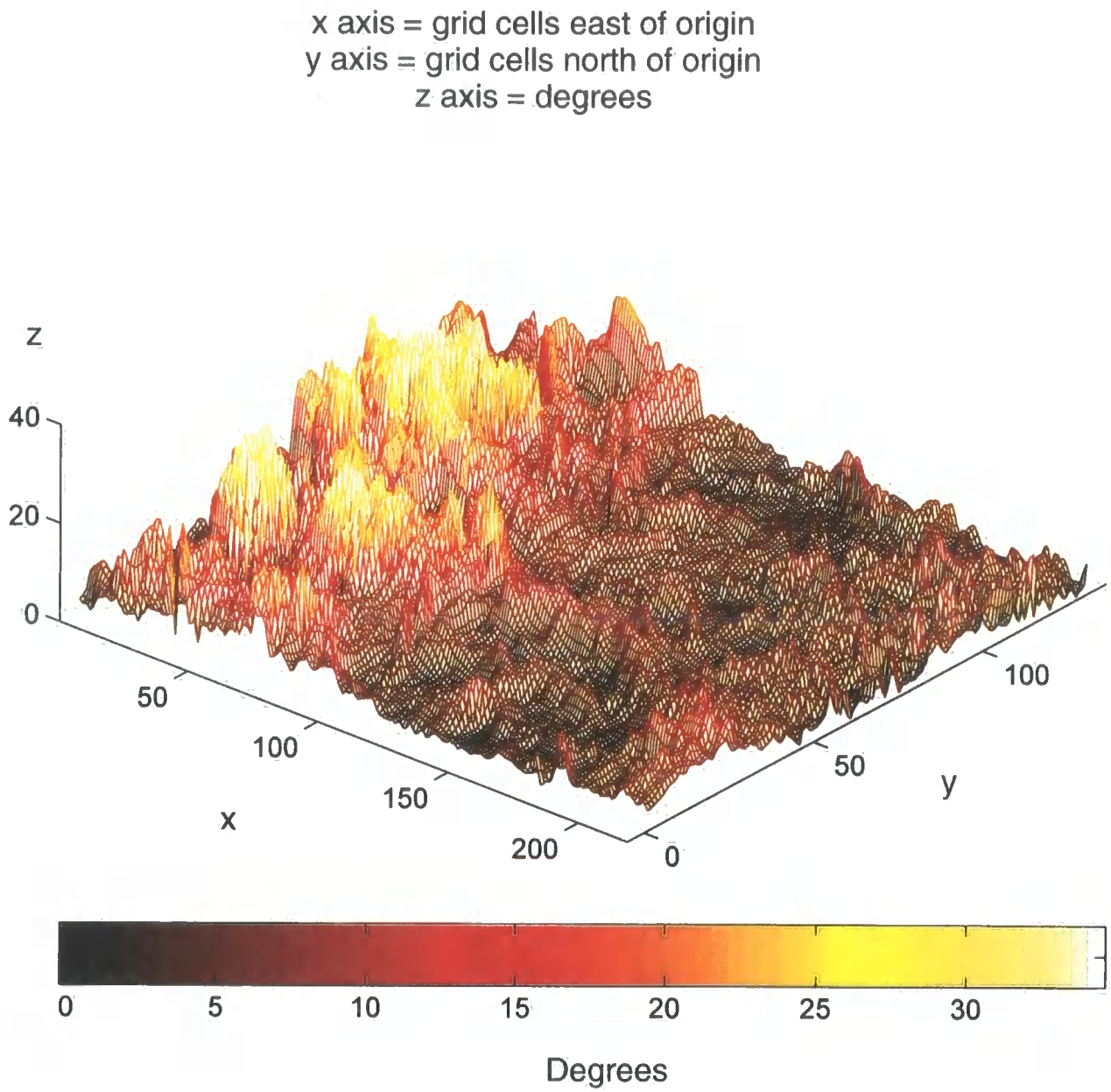

Figure 2.2. Slope gradient

2.4. Slope aspect

Slope aspect (the orientation or azimuth of the local slope) is another component of surface geometry that affects the receipt of direct-beam solar radiation according to Equation 1.3 in conjunction with slope gradient. Together, these topographical variables may influence the radiation budget at the surface and hence air temperature.

Slope aspect was calculated using the *aspect* function in ARC/INFO), which identifies the direction of maximum down slope gradient for each grid cell (expressed in positive degrees from 0.0^{o} to 360.0^{o} measured clockwise from north). The resulting *aspect* surface is shown in Figure 2.3. This variable is portrayed using a different colour scale than the other variables, in order to illustrate the continuum of data values for northerly aspects (very low and very high values of *aspect*). In the south western half of the study site, values of *aspect* predominantly range from about 200^{o} to 350^{o}, indicating a general west facing slope aspect for the grid cells in this area. In the north eastern half of the study site, values of *aspect* are mostly either above about 300^{o} or below about 100^{o}, indicating a general north east facing slope aspect. The Pennine ridge represents the boundary between these two regions.

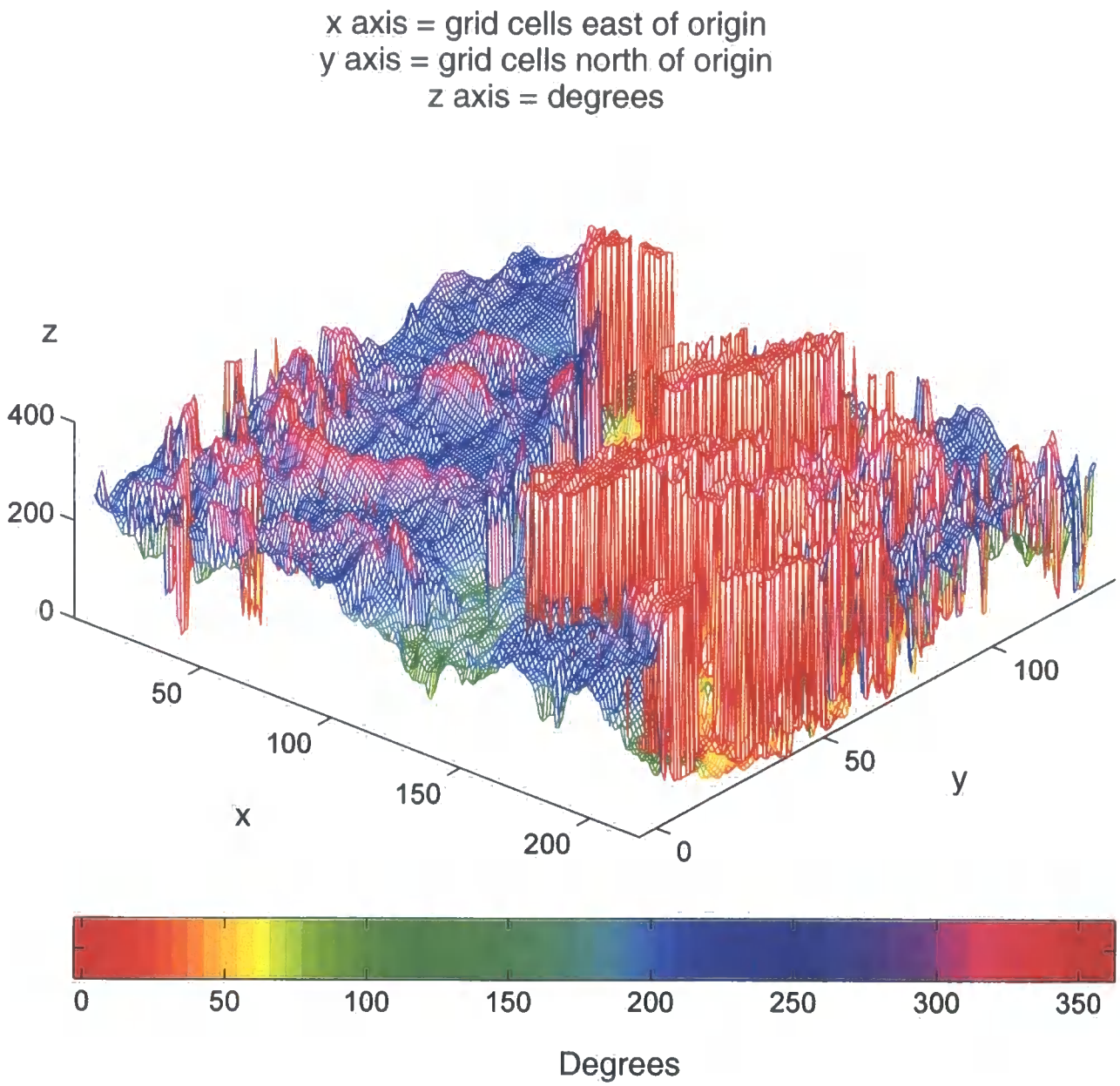

Figure 2.3. Slope aspect

2.5. Topographic shelter

Previous work has suggested that topographic shelter (the extent to which a site is surrounded by higher terrain) can affect surface climate. Shelter may influence the surface radiation balance. Sites with an elevated horizon may be shaded from direct-beam solar radiation, effectively leading to reduced local daylight duration. Shelter may also exert climatic effects independent of solar geometry; infra-red radiation emitted from surrounding slopes may be absorbed at a sheltered site, slowing the rate of nocturnal heat loss (Tabony, 1985). The topographic protection provided at a sheltered site may also reduce local exposure to advection and turbulence (Naess *et al.*, 2000) leading to lower surface wind speeds. The derivation of topographic shelter can be achieved in the field (Harrison and Kelly, 1996) using inclination of the horizon at various compass points. Alternative methodologies make use of cartographic data, calculating for example elevation changes away from a site at pre-defined distances (Tabony, 1985).

A topographic *shelter* variable was calculated for the study area, designed to quantify the elevation difference between each grid cell and higher land in the immediate vicinity. The first stage of the calculation used the DTM and the ARC/INFO command *focalmax*, which generates a new surface in which each grid cell is assigned the elevation value of the highest cell within a specified neighbourhood. The DTM was then subtracted from this new surface to model local topographic shelter. *Shelter* variables were calculated using neighbourhoods of 200 m, 300 m, 400 m, 500 m, 600 m, 700 m, 800 m, 900 m and 1 km. Figure 2.4 shows the shelter variable calculated at a 200 m neighbourhood. The largest values (around 160 m) occur at the foot of steep sections of scarp slope to the west of the Pennine crest, while values approach zero on the flat plateau areas to the east.

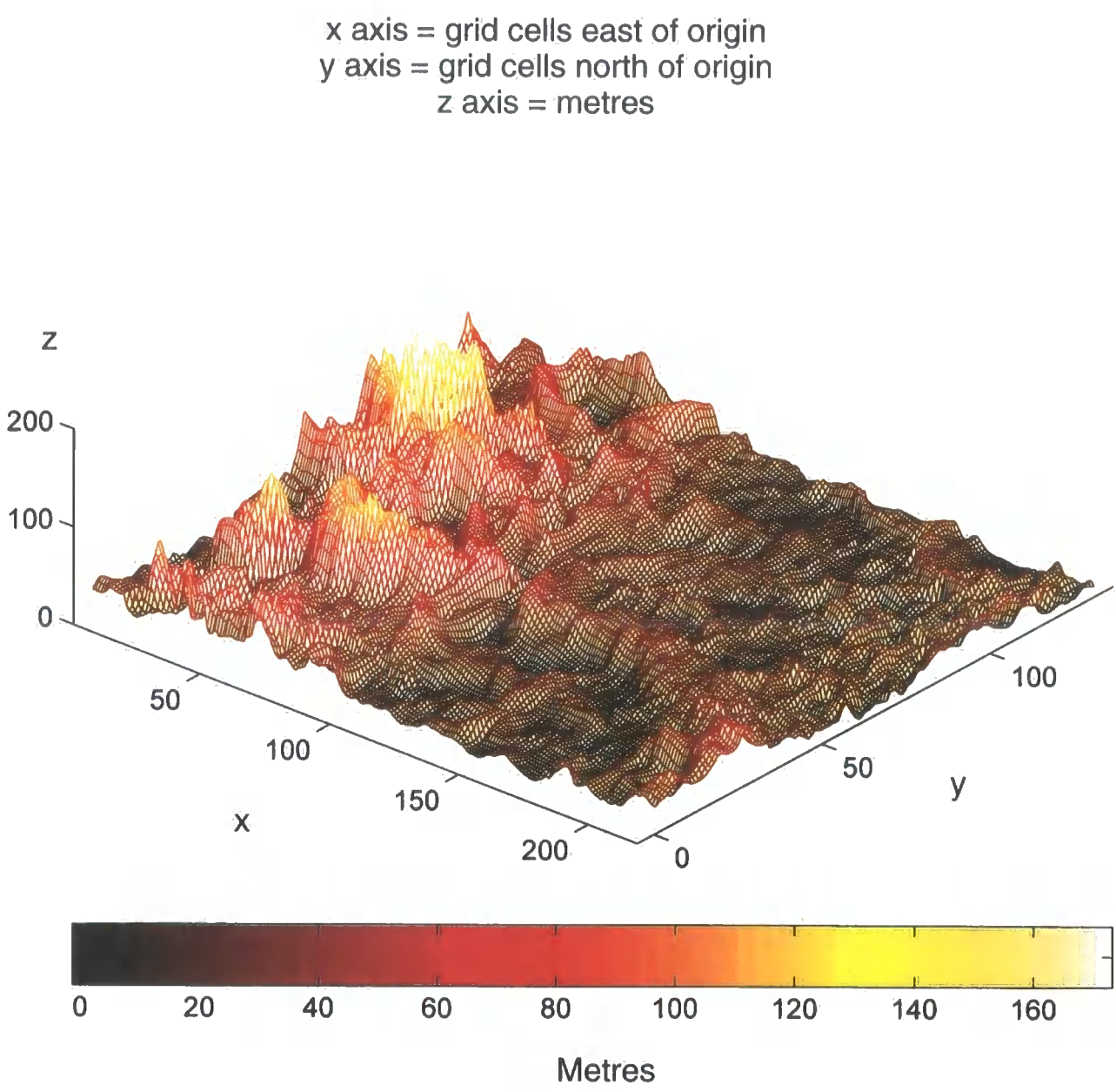

Figure 2.4. Topographic shelter (200 m)

2.6. Topographic drainage potential

During periods of negative net radiation flux in calm atmospheric conditions, air in contact with the ground may be cooled and the resulting increase in specific gravity can cause air to flow down hill in a density current (Simpson, 1999). Subsidence of a high pressure air mass during anticyclonic conditions can also cause air to sink towards the ground surface and warm adiabatically. Clear skies associated with anticyclonic conditions allow strong insolation at higher elevations and can lead to a temperature inversion especially if colder air becomes trapped in a stratified layer beneath. Katabatic flow is driven by the difference in buoyancy between separate layers of air, and its course is determined by surface topography. The resulting circulation is weak, and can easily be destroyed by advection and mixing of air in the boundary layer. Nevertheless, katabatic drainage of cold air down slope is one process whereby minimum temperatures may be affected by topography. A long history of research exists into the geographical occurrence (Geiger *et al.*, 1995) and ecological impacts (Winter, 1958) of the phenomenon. Topographic influences on the development of katabatic winds (Flocas *et al.*, 1998) and resulting spatial effects on temperature anomalies (Gustavsson *et al.*, 1998; Lindkvist and Lindkvist, 1997) have been identified for other regions of complex terrain.

In order to test the hypothesis that katabatic flow of cold air down slope under stable atmospheric conditions affects temperature within the Moor House study site, the potential for down slope drainage must be quantified for each AWS location. A variable *drain* was calculated to measure the elevation difference between each grid cell and lower land in the immediate vicinity. The DTM and the ARC/INFO command *focalmin* were used to generate a new surface in which each cell is assigned the elevation value of the lowest cell within a specified neighbourhood. This new surface was then subtracted from the DTM to model local topographic drainage potential (Appendix 2). The *drain* variable was calculated using the same neighbourhoods as described above for the shelter variables. Figure 2.5 shows *drain* calculated at a 500 m neighbourhood. The largest *drain* values occur at the top of the long steep slopes falling from Cross Fell towards the Eden Valley. Topographic drainage potential approaches 250 m in these locations. The smallest values of *drain* within the study site are less than 20 m, and occur in the Trout Beck and Tees

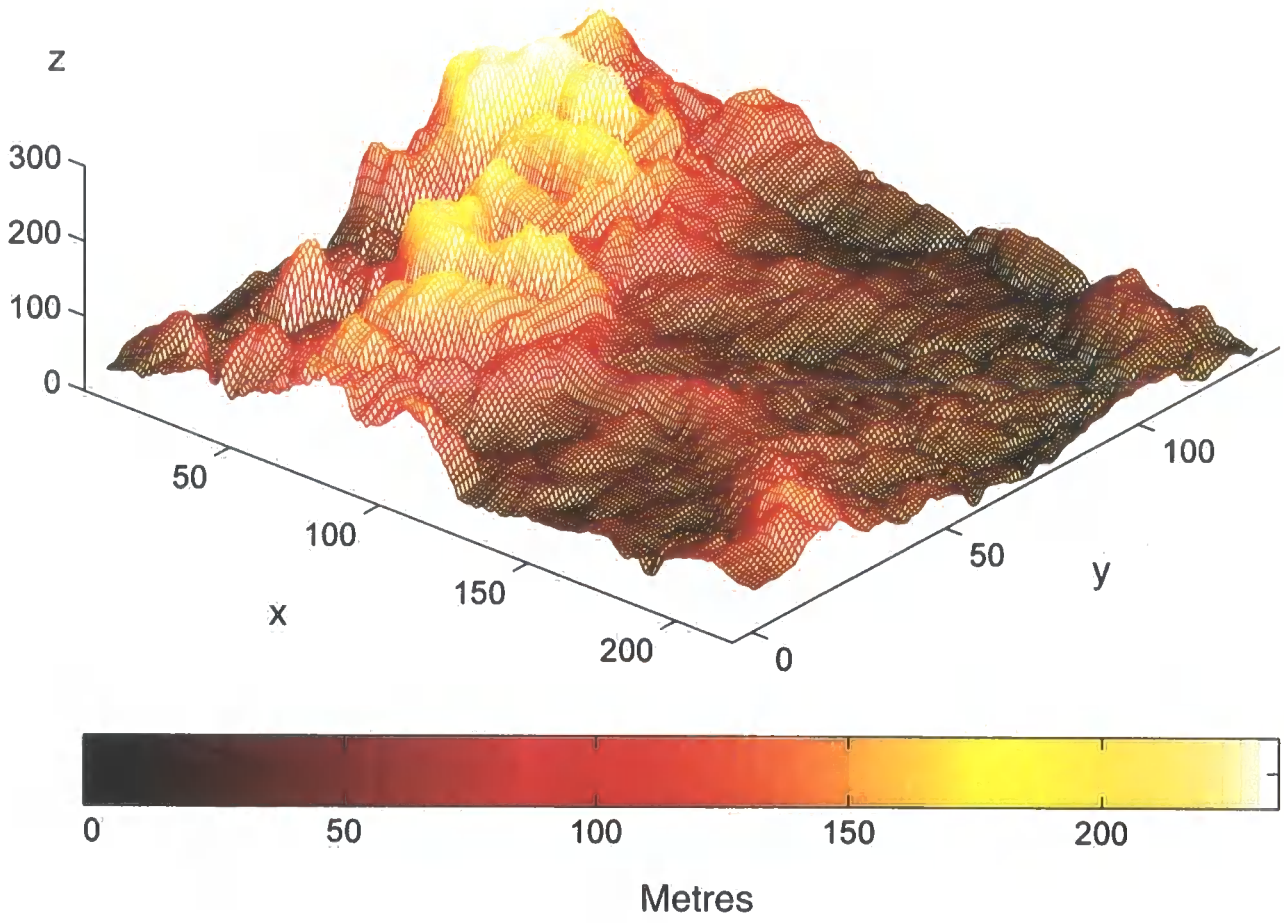

Figure 2.5. Topographic drainage potential (500 m)

Valleys. The variable quantifies the potential for katabatic flow of air down valley, and allows the identification of potential frost hollows or other areas where cold air may accumulate.

2.7. Distance relative to the Pennine ridge

The Pennine ridge forms an orographic barrier bisecting the study site from north-west to south-east. Within the Moor House reserve the elevation of the ridge falls no lower than 746 m (at the col between Great Dun Fell and Knock Fell) and rises to 845 m at Great Dun Fell. The ridge may be large enough to interact with regional air flow, giving rise to a föhn effect and causing discrepancies in temperature, solar radiation and precipitation either side of the Pennines.

Distance relative to the Pennine ridge was modelled in a two-stage process. The area of the DTM lower than 280 m elevation was masked (this criterion is only met in a single region in the south west of the study site at the foot of the scarp slope). The 280 m elevation contour lies approximately parallel to the Pennine ridge, therefore the *eucdistance* function in ARC/INFO was used to calculate the Euclidean distance from the masked area to each grid cell (Appendix 2). The resulting *dist* variable is shown in Figure 2.6; values decrease to the south west of the ridge location, and increase to the north east.

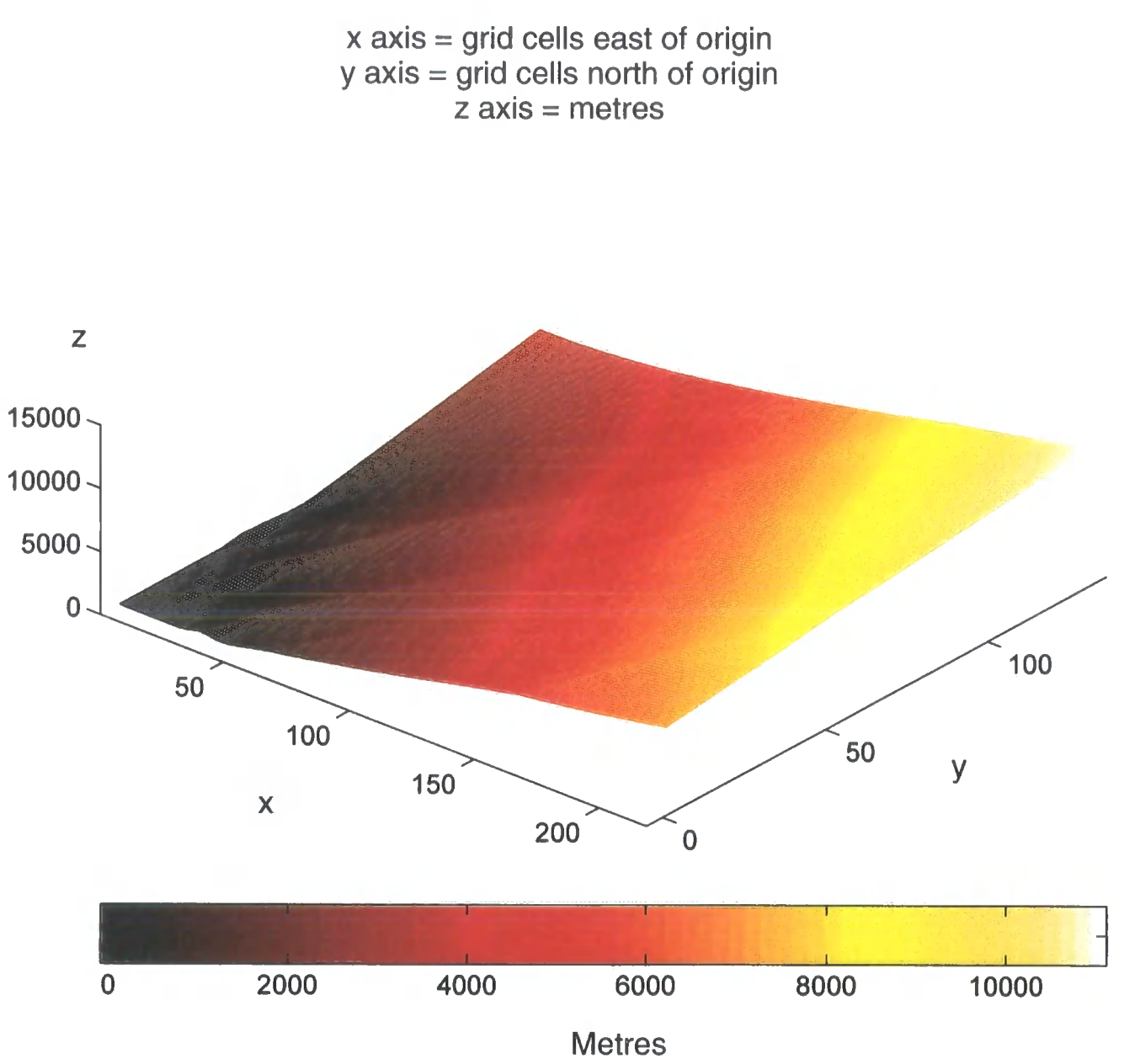

Figure 2.6. Distance relative to the Pennine ridge

2.8. Ridge topography

The occurrence of ridge or valley topography may affect surface wind speed, as the roughness of the local land surface interacts with the wind speed profile in the free atmosphere (Guo and Palutikof, 1990; Hewer, 1998). To allow investigation of the effects of ridge exposure, the variable *ridge* was calculated using the *flowaccumulation* function in ARC/INFO. *Flowaccumulation* is one of the hydrological modelling tools in ARC/INFO, and calculates for each grid cell the accumulated number of up-slope source cells. The function has been used previously for topo-climatic modelling (Virtanen *et al.*, 1998). To estimate the *ridge* variable, the *flowaccumulation* function was run on the inverse of the DTM. The procedure thus assigns high values (in excess of 5000 grid cells) to summit sites such as Cross Fell. Long continuous ridges such as the spur between Hard Hill and Great Dun Fell have *ridge* values above 1000 grid cells, whereas very low values of *ridge* occur in areas with few consecutive down-slope grid cells. The *ridge* variable is shown in Figure 2.7. The influence of *ridge* on wind speed is examined in Chapter 7.2.

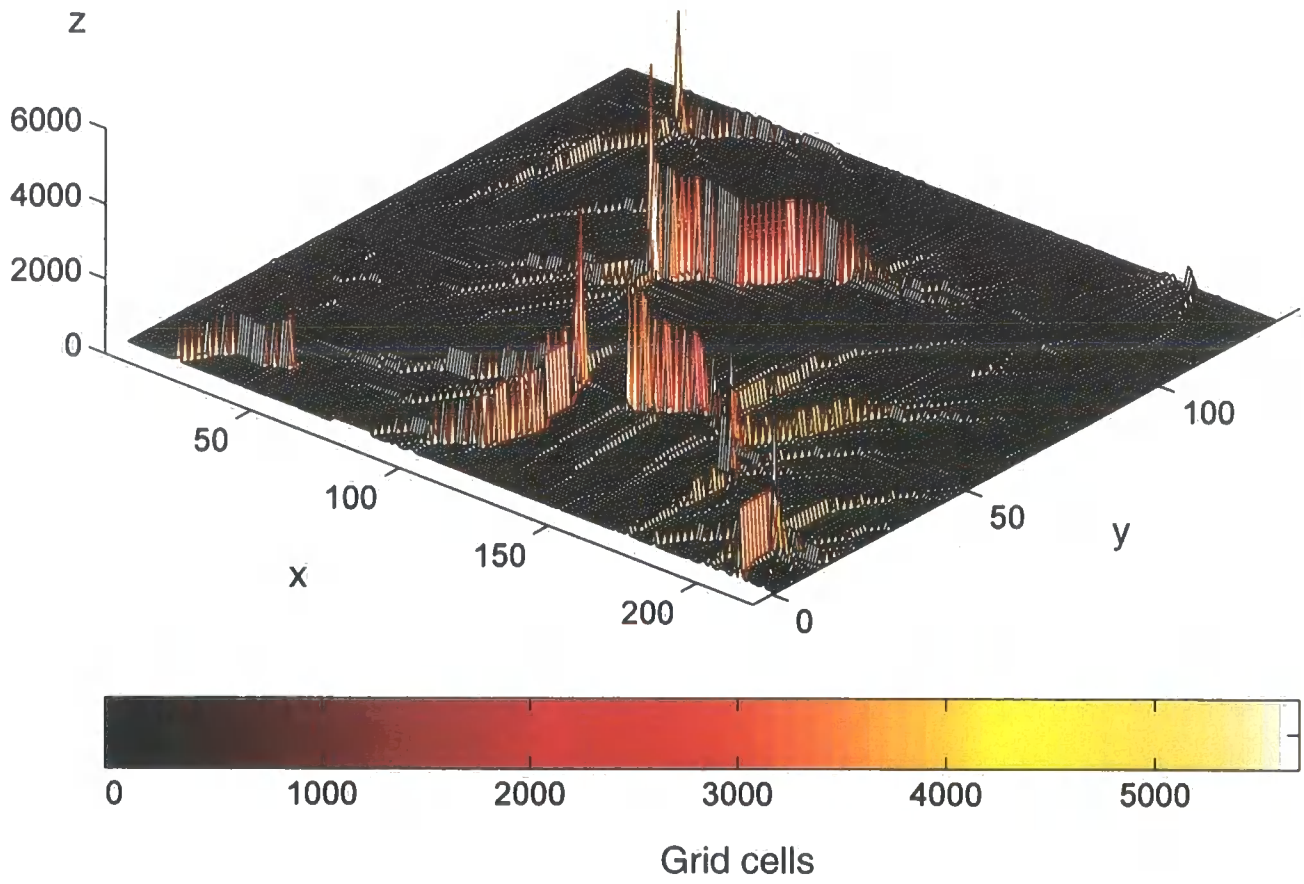

Figure 2.7. Ridge topography index

2.9. Discussion

The surfaces described in this section were modelled in order to test hypothetical relationships with surface climate. For example, slope aspect can influence surface temperature through the spatial and temporal distribution of insolation (section 5.1), and topographic drainage potential may be linked to the spatial occurrence of katabatic air flows (section 5.2). The *dist* variable may help to explain climatic patterns influenced by the orographic barrier of the Pennines (sections 5.4 and 6.5), while the *ridge* variable may improve modelling of wind speed at exposed sites (section 7.2). Each surface has been created to test specific *a priori* hypotheses concerning complexity of the landscape and its influence on surface climate.

Values of the modelled topographic variables can be obtained for any grid cell within the study area by interrogating the relevant surface within ARC/INFO. The effects of these topographical variables can then be tested by selecting locations within the study site where contrasting values of these modelled topographic variables occur. A sequence of experimental networks can be designed specifically for automatic weather stations to sample particular landscape features and allow assessment of their climatic effects.

The component of landscape variability captured by the *slope*, *shelter* and *drain* variables is similar but subtly different (Figures 2.2, 2.4 and 2.5). *Slope* is the first derivative of elevation (the rate of maximum change of elevation over horizontal distance) and is calculated from the elevation value of each individual grid cell and those of its eight nearest neighbours. *Shelter* (and *drain*) are also proportional to maximum slope, but within a user-specified neighbourhood, and only between higher (or lower) grid cells.

Autocorrelation coefficients between the *shelter* surfaces calculated at neighbourhoods between 0.2 and 1 km are high, ranging from +0.62 to +0.99. Autocorrelation between the *drain* surfaces calculated at the various neighbourhoods ranges from +0.59 to +0.99. The *drain* surfaces are slightly more autocorrelated than the *shelter* surfaces at smaller, more similar neighbourhoods; the correlation matrix for each variable at different neighbourhoods is shown in Table 2.1.

Table 2.1. Autocorrelation between *shelter* surfaces (italics) and *drain* surfaces (bold) calculated at a range of neighbourhoods

Neighbourhood (m)	200	300	400	500	600	700	800	900	1000
200	*	*0.94*	*0.86*	*0.79*	*0.74*	*0.69*	*0.65*	*0.62*	*0.59*
300	**0.95**	*	*0.96*	*0.91*	*0.85*	*0.80*	*0.76*	*0.73*	*0.70*
400	**0.89**	**0.97**	*	*0.97*	*0.93*	*0.89*	*0.85*	*0.82*	*0.79*
500	**0.83**	**0.92**	**0.98**	*	*0.98*	*0.95*	*0.92*	*0.88*	*0.86*
600	**0.77**	**0.86**	**0.93**	**0.98**	*	*0.99*	*0.96*	*0.93*	*0.91*
700	**0.72**	**0.81**	**0.89**	**0.95**	**0.98**	*	*0.99*	*0.97*	*0.95*
800	**0.68**	**0.77**	**0.84**	**0.91**	**0.95**	**0.99**	*	*0.99*	*0.97*
900	**0.65**	**0.73**	**0.81**	**0.87**	**0.92**	**0.96**	**0.99**	*	*0.99*
1000	**0.62**	**0.70**	**0.77**	**0.83**	**0.88**	**0.93**	**0.97**	**0.99**	*

Autocorrelation is especially high for similar sized neighbourhoods, and large neighbourhoods, but correlations are significant in all cases ($P < 0.01$). These high autocorrelation coefficients suggest that although landscape complexity may affect topo-climate at a range of scales (Tabony, 1985), it may be appropriate to use a single version of *shelter* or *drain* for any particular application to avoid problems of multicollinearity. The appropriate neighbourhood to use for particular climate modelling applications can be determined empirically by optimising regression statistics (sections 5.2 and 5.3).

The modelled topographic variables can be transformed, for example using logarithmic or power functions (Virtanen *et al.*, 1998) either to improve the fit of the data to an analytical distribution, or to optimise empirically observed relationships. Observed climate variables measured from each network of weather stations can be regressed on the topographic parameters for each station location in order to test for the occurrence of hypothesised relationships.

Chapter 3. Instrumentation

3.1. Recording the climate data

The automatic weather stations available for the project were of two different designs; Didcot Instruments (sourced from ELE International Ltd, Hemel Hempstead, UK), and Delta-T (sourced from Delta-T Devices Ltd, Cambridge, UK). All the AWS measure precipitation, wind speed, wind direction, solar radiation and air temperature. The Didcot Instruments stations also measure net radiation and wet-bulb air temperature. In addition to these variables, the ECN station at Moor House measures soil temperature (at 10 cm and 30 cm depth), surface wetness, and albedo.

Five stations were made available by the ECN specifically for the project, and were re-located to a series of experimental networks between September 1997 and March 2000. These five stations are all of the Didcot Instruments design and are referred to as "roving" AWS (Figure 3.1). The stations were numbered from 1 to 5 for identification. The sensors allocated to each individual AWS at the start of the project remained attached to that AWS for the duration; this precaution enabled the effect of any instrumentation problems to be traced back to previous networks. Data were also available from other *in situ* AWS within the Moor House nature reserve, at Moor House (location M, grid reference NY 75703280, 550 m elevation), Great Dun Fell summit (location G, NY 71003220, 845 m elevation), Knock Fell (location K, NY 71803130, 755 m elevation), High Carle Band (location H, NY 70903020, 600 m elevation) and Sink Beck (location S, NY 69902950, 465 m elevation). The locations of these *in situ* AWS are shown in Figure 1.2. These *in situ* stations were operated under other research programmes but data were made available to supplement the experimental data from the five roving stations. All AWS data were logged hourly. Precipitation data were logged as hourly totals (mm), wind direction data were logged as instantaneous observations made each hour, expressed as degrees clockwise from north. All other data were logged as hourly mean values, in units of m s^{-1} (wind speed), W m^{-2} (solar and net radiation) and ^{o}C (temperature).

Figure 3.1. A roving AWS deployed at the study site

Modern instrumentation and the use of remote data loggers imposes a distance between the measured system and the investigator (Bloom, 1996). A working knowledge of the system and the instruments is needed to enable awareness and identification of errors. Protocols exist for meteorological measurements at terrestrial sites within the UK Environmental Change Network (ECN) (Sykes and Lane, 1997), including notes on the installation and maintenance of automatic weather stations and the quality control of data. ECN protocols were followed to ensure the battery voltage within each logger remained adequate to prevent data loss. The domes on the solar and net radiation sensors were cleaned or replaced regularly, and the wick on each wet-bulb temperature probe was changed and the reservoir of de-ionised water refilled in accordance with the ECN guidelines.

Data errors can be classified as arising from problems of accuracy (the extent to which a true value is approximated), precision (repeatability of measurement), noise (output unrelated to the measured parameter), stability (sensor drift with time or with another variable), sensitivity (the magnitude of change of input causing a discernible change in output), resolution (the extent to which the scale of measurement is sub-divided), and response time (the lag associated with a change of input) (Bloom, 1996). Published tables are available suggesting maximum tolerable errors for AWS sensors (Linacre, 1992).

Cup anemometers may be insensitive to wind speeds if friction prevents rotation below a certain threshold (Unwin, 1980). Friction may also cause low readings at wind speeds above the threshold, and inertia may reduce sensitivity to gusts. An anemometer may not show a linear response over a range of wind speeds (Grace, 1996). Total errors of wind speed measurement should not exceed 2 m s^{-1} (or 10% above 20 m s^{-1}), and systematic instrument errors should be smaller than this (Linacre, 1992). The wind vane recording wind direction should have similarly low friction and inertia, and should record with an error of less than 20^{o} (Linacre, 1992).

The problems associated with the measurement of precipitation are diverse (Strangeways, 1996b), and the uncertainties inherent in estimating true precipitation from rain gauge catch are well documented in the literature (Reynolds, 1965). A representative catch can easily be confounded by poor exposure (Strangeways, 1996a). In addition, tipping bucket rain

gauges allow evaporation from the bucket between tips and the bearings on the bucket may be prone to sticking during prolonged dry periods (Linacre, 1992). Rainfall observations should have a total error no larger than 10%.

The thermometers installed on the AWS consist of a thermocouple, a pair of junctions between dissimilar metals (e.g. copper and constantan); the electrical output measured is proportional to temperature. The sensors are exposed in a screen 1 m above ground level. The response time to changing temperature is proportional to the mass of the sensor (Oke, 1978). Numerous other methods of deriving integrated estimates rely on temperature-dependent phenomena such as the diffusion of water through a polycarbonate resin capsule. The error associated with automatic temperature measurement should not exceed 1°C (Linacre, 1992).

The non-aspirated psychrometer consists of a paired dry-bulb and wet-bulb thermometer, the wet-bulb being covered by a water-soaked wick and indicating a lower temperature due to the loss of latent heat by evaporation, proportional to atmospheric humidity. The error of a water vapour pressure estimate should not exceed 1 hPa (Linacre, 1992). The wick must be clean and the reservoir full, the relationship between saturation vapour pressure and temperature on which psychrometry depends is only applicable for de-ionised water (Oke, 1978).

Incoming direct and diffuse solar radiation is measured by a Kipp pyranometer. A double glass dome above the sensor allows only short wave radiation to pass (wavelengths from 0.3 to 3 μ) and prevents heat exchange by convection (Pearcy, 1996). Similarly, the net radiation sensor measures total radiation including short-wave and long-wave. Black thermoelectric sensors with polyethylene shields are orientated towards ground and sky, measuring the difference between incoming and outgoing fluxes (Pearcy, 1996).

3.2. Standardising time code

Protocols for the quality control of AWS data (Sykes and Lane, 1997) were followed in order to identify erroneous data. Data files were routinely checked to identify missing, implausible or inconsistent observations. During preliminary analysis of the data a

discrepancy became apparent between the logger programs used by the two AWS manufacturers. Although both types of AWS record an hourly summary on the hour, Didcot Instruments loggers record midnight readings as 2400 GMT (day *j*) whereas the Delta-T loggers record the simultaneous reading as 0 GMT (day *j*+1). This was rectified by testing each hourly observation from a Delta-T AWS using the algorithm described in Figure 3.2. The correction was applied using a Fortran program that corrected the Delta-T AWS data to the Didcot Instruments format. The program changes the value of the variables describing the time of day and day of the year for all midnight observations. If necessary, the variable describing the year is also altered and the day of the year adjusted to account for leap years.

Sensitivity tests were undertaken to assess the effect of the inconsistent time coding on the daily data. Daily summaries of the hourly data were calculated both before and after correction of the time at midnight. The differences in the daily data due to the time coding discrepancy were quantified by calculating the root mean square error (RMSE) and the mean absolute error (MAE) between corrected and uncorrected data for each Delta-T station (Tables 3.1 to 3.4).

Table 3.1. The effect of the midnight time code discrepancy on daily data for Great Dun Fell (845 m), 23 September 1997 - 26 April 1998

Element	RMSE	MAE
Mean temperature	0.11 °C	-2.9×10^{-4} °C
Maximum temperature	0.18 °C	-0.5×10^{-2} °C
Minimum temperature	0.19 °C	-3.4×10^{-2} °C
Mean wind speed	0.30 m s^{-1}	-1.0×10^{-4} m s^{-1}
Total precipitation	0.61 mm	$+0.1 \times 10^{-2}$ mm

Table 3.2. The effect of the midnight time code discrepancy on daily data for Knock Fell (755 m), 31 October 1997 - 26 April 1998

Element	RMSE	MAE
Mean temperature	0.11 °C	-7.3×10^{-4} °C
Maximum temperature	0.16 °C	-1.1×10^{-3} °C
Minimum temperature	0.19 °C	-3.7×10^{-2} °C
Mean wind speed	0.24 m s^{-1}	$+1.1 \times 10^{-3}$ m s^{-1}
Total precipitation	0.78 mm	-1.0×10^{-3} mm

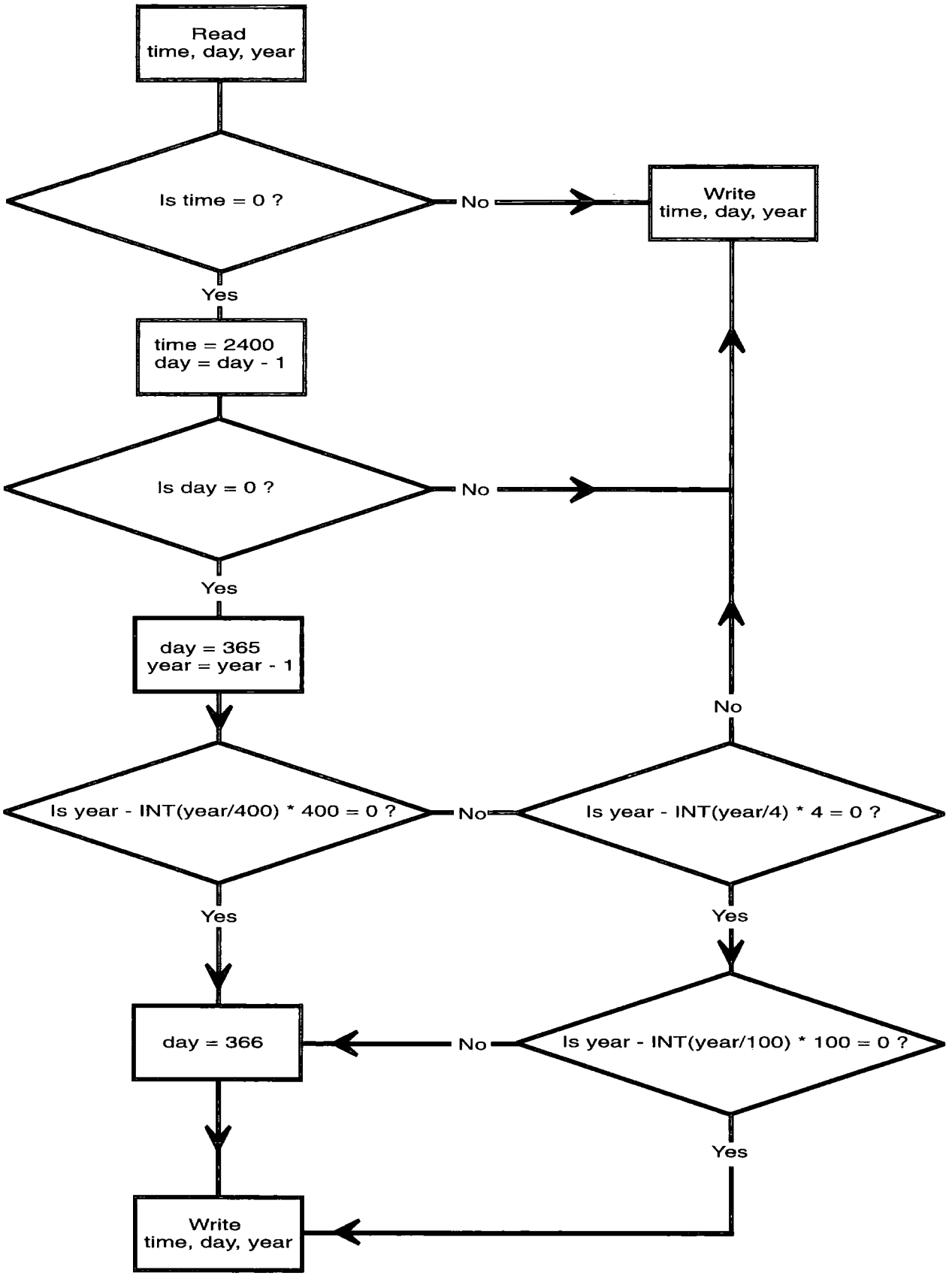

Figure 3.2. The algorithm used to standardise AWS time code

Table 3.3. The effect of the midnight time code discrepancy on daily data for High Carle Band (600 m), 23 September 1997 - 26 April 1998

Element	RMSE	MAE
Mean temperature	0.11 °C	-1.7×10^{-3} °C
Maximum temperature	0.17 °C	-7.9×10^{-3} °C
Minimum temperature	0.19 °C	-3.1×10^{-2} °C
Mean wind speed	0.12 m s^{-1}	-1.6×10^{-4} m s^{-1}
Total precipitation	0.82 mm	-4.4×10^{-4} mm

Table 3.4. The effect of the midnight time code discrepancy on daily data for Sink Beck (465 m), 30 October 1997 - 27 April 1998

Element	RMSE	MAE
Mean temperature	0.11 °C	-3.5×10^{-4} °C
Maximum temperature	0.15 °C	$+5.6 \times 10^{-4}$ °C
Minimum temperature	0.21 °C	-3.3×10^{-2} °C
Mean wind speed	0.17 m s^{-1}	-2.3×10^{-5} m s^{-1}
Total precipitation	0.92 mm	$+3.7 \times 10^{-4}$ mm

The root mean square error is a rigorous statistic which penalises large individual differences. The mean absolute errors are much smaller in magnitude, showing that the individual discrepancies are not systematically positive or negative. The biggest discrepancies for all stations are in daily minimum hourly mean temperature, followed by daily maximum hourly mean temperature. These quantities are dependent on a single hourly data point and may emphasise extreme individual values, unlike the other quantities which are a function of 24 data points. The larger differences for minimum temperature relate to the higher probability of minimum rather than maximum temperature occurring between 2300 and 2400, due to the diurnal cycle of radiation balance and its effect on air temperature. Although the magnitude of the effect of the time coding discrepancy is small, the corrections were implemented for all Delta-T AWS data to maintain consistency in data logging throughout the study site.

3.3. Calculating daily summaries

All calculations, analysis and modelling for the project use daily data. Daily summaries of the logged hourly data were extracted, using the standard civil day from midnight to midnight. Three separate temperature variables were extracted: daily mean temperature,

daily maximum temperature and daily minimum temperature (the mean, maximum and minimum of the 24 hourly observations respectively). The daily maximum, as defined here, is slightly lower (and the daily minimum slightly higher) than the true absolute diurnal temperature range.

The use of the standard civil day is consistent with conventional handling of climatological data (Meteorological Office, 1982). If observations of daily quantities are made at an arbitrary time (e.g. 0900 GMT) for the convenience of the human observer, such observations are always assigned to a specific calendar day (for example, 24 hour total precipitation and 24 hour maximum temperature are "thrown back" to the day prior to observation, while the 24 hour minimum air temperature is assigned to the day of observation). Probable errors associated with the use of different observing times have been estimated for observatory data (Glaisher, 1848), but such errors are insignificant compared to other sources of uncertainty in the context of the large climatic variations measured in space and time within the study site. Automated sampling allows daily summaries to be calculated accurately for a calendar day; such summaries are easier to compute and provide a more representative sample of conditions on any given day than fixed-hour summaries.

All temperature data were stored to a precision of 0.1 degree Celsius, precipitation data to a precision of 0.1 mm, wind speed to 0.1 m s^{-1}, wind direction to 1 degree, net radiation and solar radiation to 1 W m^{-2}. These levels of precision were chosen to represent the limit of reliable measurement and conform to ECN protocols (Sykes and Lane, 1997).

3.4. Standardising the AWS sensors

The five roving AWS were installed within 20 m of the ECN station on 18 September 1997 (Figure 3.3). Each AWS was located as uniformly as possible with respect to local radiation and wind exposure. For each AWS, the time period for which data were analysed was chosen to maximise the available data; for roving AWS 3 and 5, data were available from 18 September to 25 November 1997 while for all other stations the time period used is 18 September to 22 October 1997.

Figure 3.3. The five roving AWS installed at Moor House

Visual comparison of time series graphs of data measured by each sensor on different AWS allowed the identification of anomalous low wind speed data from one roving station, and anomalous solar radiation data from two of the roving stations. The wind speed data were rectified by replacing the anemometer with a new instrument. The calibration factors for the solar radiation sensors were found to be erroneous and were re-programmed using the correct values.

The daily mean, maximum and minimum temperature data sampled by the ECN station and each of the five roving AWS were compared visually using quantile-quantile plots (Figure 3.4 shows daily mean temperature data from roving AWS 2 and the ECN station as an example). The slight but consistent displacement of data points parallel to the line of equivalence is similar for maximum and minimum temperature, and for other roving stations. The displacement suggests that the difference in temperature measured by the official ECN station and each roving AWS is consistent across the range of observed values, and that the slight but systematic discrepancy can therefore be expressed as an additive constant.

The similarity between each pair of samples was quantified using the concordance correlation coefficient ρ_c (Lin, 1989). Whereas the Pearson correlation coefficient ρ can be used to test the relation between two measurement methods, with ρ reaching a value of ± 1 if two paired variables Y_1 and Y_2 lie on a straight line such that $Y_1 = a + bY_2$ even if $a \neq 0$ or $b \neq 1$ (Goudriaan, 1986), the extent to which two measurement methods are in absolute agreement (i.e. $Y_1 = Y_2$) can be tested more meaningfully using ρ_c. The statistic quantifies the agreement on a continuous measurement obtained by two methods, combining indices of both precision and accuracy to determine whether the observed data deviate significantly from the line of perfect concordance. Lin's coefficient increases in value as a function of accuracy, measured by the nearness of the data's reduced major axis to the line of perfect concordance, and as a function of precision, measured by the tightness of the data about its reduced major axis (Steichen, 1998). The coefficient ρ_c varies in value between +1 and -1 and is a more rigorous measure of agreement than ρ since $|\rho_c| \leq |\rho| \leq 1$. Each pair of

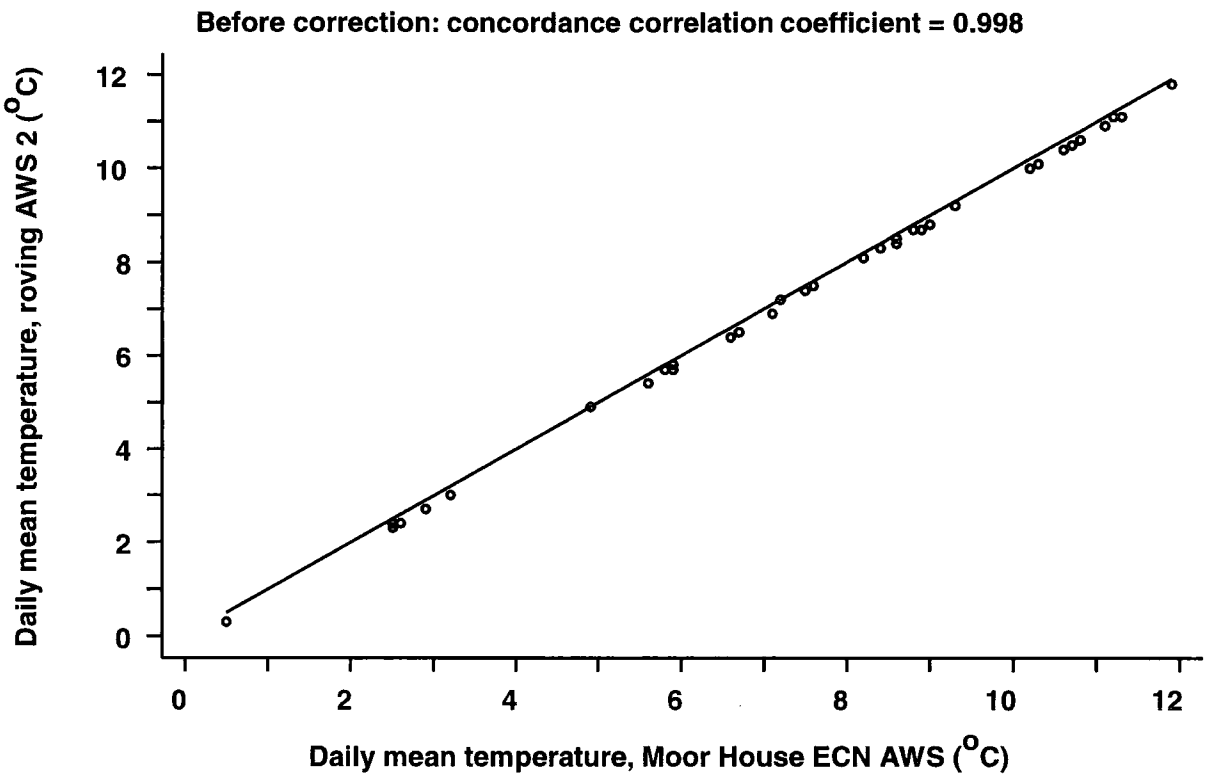

Figure 3.4. Quantile-quantile plot of daily mean temperature measured by roving AWS 2, before correction, against daily mean temperature measured by the ECN station at Moor House

observations must be in perfect concordance for ρ_c to equal 1. Daily data were compared for the ECN station and each roving AWS in turn. Corrections were applied iteratively and their effect quantified by calculating ρ_c. The procedure was repeated until the optimum correction constant was found, for which ρ_c reached a maximum value, as shown in Tables 3.5 to 3.7.

Table 3.5. Daily mean air temperature observed by roving AWS compared with data observed by the ECN Station at Moor House

Roving AWS	ρ_c (raw data)	correction (°C)	ρ_c (corrected data)
1	0.999	+0.1	1.0
2	0.998	+0.2	1.0
3	0.997	+0.2	0.999
4	0.999	+0.0	0.999
5	0.999	+0.1	1.0

Table 3.6. Daily minimum air temperature observed by roving AWS compared with data observed by the ECN Station at Moor House

Roving AWS	ρ_c (raw data)	correction (°C)	ρ_c (corrected data)
1	0.999	+0.1	1.0
2	0.999	+0.1	1.0
3	0.999	+0.2	1.0
4	0.999	+0.1	1.0
5	0.999	+0.0	0.999

Table 3.7. Daily maximum air temperature observed by roving AWS compared with data observed by the ECN Station at Moor House

Roving AWS	ρ_c (raw data)	correction (°C)	ρ_c (corrected data)
1	0.999	+0.1	0.999
2	0.998	+0.1	1.0
3	0.999	+0.0	0.999
4	1.0	+0.0	1.0
5	0.999	+0.1	1.0

The corrections identified by this method enable effective standardisation of the temperature data measured by the roving AWS. This is illustrated by Figure 3.5, which shows the quantile-quantile plot of daily mean temperature data from roving AWS 2 and the official Moor House ECN station (the same data as in Figure 3.4) after adjustment of

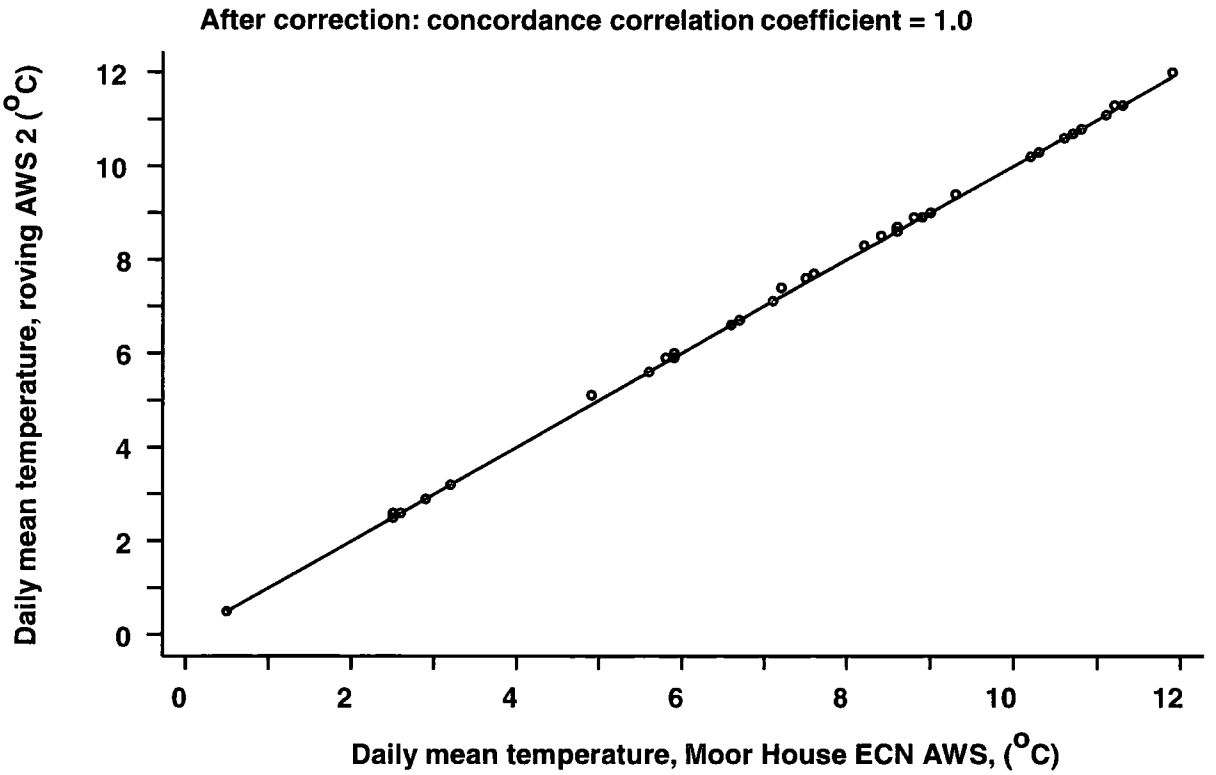

Figure 3.5. Quantile-quantile plot of daily mean temperature measured by roving AWS 2, after correction, against daily mean temperature measured by the ECN station at Moor House

the roving AWS data by the empirically-derived correction factor (+0.2°C). After correction, the data lie on the line of equivalence ($x = y$) indicating perfect concordance.

The five roving AWS were dismantled at Moor House and one station was erected next to each of the four *in situ* AWS. Roving AWS 1 was installed at Great Dun Fell summit, roving AWS 2 at High Carle Band, roving AWS 3 at Sink Beck and roving AWS 5 at Knock Fell (locations are shown in Figure 1.2). Roving AWS 4 was installed at Widdybank Fell in order to calibrate a fifth *in situ* AWS at that site. Data recording began on 26 November 1997 and continued until 12 January 1998. Daily mean, maximum and minimum temperature samples observed by each *in situ* AWS were compared to data measured simultaneously by the adjacent roving station, after adjustment of the data observed by the roving AWS using the appropriate empirically-derived correction factor. Systematic sensor discrepancies were identified for mean, maximum and minimum temperature using quantile-quantile plots, and the magnitude of appropriate correction factors was calculated iteratively, as previously described, by optimising the concordance correlation coefficient (Lin, 1989). The resulting corrections are presented below in Tables 3.8 to 3.10.

Table 3.8. Daily mean air temperature observed by *in situ* AWS compared with corrected data observed by roving AWS

In situ AWS	Roving AWS	ρ_c (raw data)	correction (°C)	ρ_c (corrected data)
G	1	0.991	+0.2	0.993
H	2	0.996	+0.1	0.998
S	3	0.997	+0.0	0.997
K	5	0.999	+0.0	0.999

Table 3.9. Daily minimum air temperature observed by *in situ* AWS compared with corrected data observed by roving AWS

In situ AWS	Roving AWS	ρ_c (raw data)	correction (°C)	ρ_c (corrected data)
G	1	0.993	+0.1	0.994
H	2	0.996	+0.0	0.996
S	3	0.994	-0.1	0.995
K	5	0.997	-0.1	0.999

Table 3.10. Daily maximum air temperature observed by *in situ* AWS compared with corrected data observed by roving AWS

In situ AWS	Roving AWS	ρ_c (raw data)	correction (°C)	ρ_c (corrected data)
G	1	0.993	+0.2	0.996
H	2	0.999	+0.1	0.999
S	3	0.996	-0.2	0.999
K	5	0.999	-0.1	1.0

The systematic discrepancy between temperature data measured by each pair of stations is never larger than ±0.2°C, and can be different for maximum, minimum and mean temperature data because of sensor behaviour at the extremes of the temperature distribution. Separate correction factors are therefore appropriate despite maximum, minimum and mean temperature all being recorded by the same sensor at each station; the optimisation of ρ_c is a robust and objective procedure.

The temperature data observed at Moor House range from -6.8 to 15.9°C during the calibration period of the five roving stations. The measured temperature range during the calibration of the remaining *in situ* stations was from -6.0 to 7.1°C at Great Dun Fell summit, from -5.5 to 7.5°C at Knock Fell, from -4.6 to 8.4°C at High Carle Band, and from -4.8 to 9.2°C at Sink Beck. The empirically-derived correction factors given in the tables above were applied to the daily data recorded by the AWS before any subsequent analysis. Time constraints necessitated the calculation of correction factors using data gathered during a relatively short period, although calibration was repeated for validation purposes (section 3.5).

3.5. Validation of sensor standardisation

After completion of the experimental data gathering, the five roving AWS were erected once again within 20 m of the Moor House ECN station from 12 March to 2 May 2000 as described in the previous section. Correction factors were re-calculated, using the same methodology, for maximum, minimum and mean daily temperature for each roving station in order to optimise the concordance correlation coefficient ρ_c between data measured by the roving station and the ECN AWS. The re-calculated corrections are presented below in

Tables 3.11 to 3.13, along with the optimised value of ρ_c and the change in the correction constants between the 1997 and 2000 calculations.

Table 3.11. Validation of the correction constants for daily mean air temperature observed by roving AWS

Roving AWS	ρ_c (raw data)	re-calculated correction (°C)	ρ_c (corrected data)	change in correction (°C)
1	0.997	+0.2	1.0	+0.1
2	0.997	+0.2	1.0	+0.0
3	0.993	+0.2	0.999	+0.0
4	1.0	+0.0	1.0	+0.0
5	0.992	+0.3	1.0	+0.2

Table 3.12. Validation of the correction constants for daily minimum air temperature observed by roving AWS

Roving AWS	ρ_c (raw data)	re-calculated correction (°C)	ρ_c (corrected data)	change in correction (°C)
1	0.996	+0.2	0.999	+0.1
2	0.994	+0.2	0.998	+0.1
3	0.989	+0.3	0.995	+0.1
4	0.998	+0.1	0.999	+0.0
5	0.995	+0.2	0.999	+0.2

Table 3.13. Validation of the correction constants for daily maximum air temperature observed by roving AWS

Roving AWS	ρ_c (raw data)	re-calculated correction (°C)	ρ_c (corrected data)	change in correction (°C)
1	0.997	+0.1	0.998	+0.0
2	0.996	+0.1	0.996	+0.0
3	0.996	+0.1	0.997	+0.1
4	0.998	+0.0	0.998	+0.0
5	0.992	+0.4	1.0	+0.3

The results presented above demonstrate that the sensor calibrations remained relatively consistent during the course of the experimental data gathering. Eighty percent of the sensor corrections re-calculated in 2000 are either identical to the original 1997 value, or within 0.1°C.

Minimum temperature data appear slightly more prone to sensor drift than maximum or mean temperature, as shown by the larger changes in the correction constants. This may be due to low temperatures approaching the limits of operational range of the sensors. A more probable explanation is the occurrence of micro-scale differences in radiation environment between the exposure of roving stations 1, 2, 3 and 5 during the calibration exercises in 1997 and 2000.

AWS 5 is the only station to show a systematic drift for maximum, minimum and mean temperature. The re-calculated corrections show that by the end of the project the temperature data recorded by this station were reading between 0.2 and 0.3°C too cold. A sensitivity study will test the effect of these corrections on observed spatial patterns of climate to determine the need for retrospective application of the re-calculated constants.

The two calibration exercises were undertaken in autumn and spring. Seasonal differences in the magnitude of the correction factors are not apparent at Moor House. This is probably due to the high exposure of the site, which causes a relatively low annual temperature range and reduces seasonal climatic differences. Seasonal corrections may need to be calculated for lower elevation sites where the thermal response of sensors to insolation could cause systematic differences in recorded temperature.

3.6. Standardising additional temperature loggers

Two Squirrel temperature loggers (sourced from Grant Instruments, Cambridge UK) were located with the sensors exposed adjacent to the dry-bulb temperature sensor of roving AWS 2 between 27 October and 24 November 1999 for calibration. Six sensors were set to record hourly temperature observations, from which daily mean, maximum and minimum values were calculated. The agreement between the Squirrel sensors and the AWS sensor is quantified using the concordance correlation coefficient as previously described (section 3.4) and the results are presented below in Tables 3.14 to 3.16. Additive correction constants are appropriate since the magnitude of the discrepancy is independent of the absolute temperature in each case. During the period of calibration, the temperature recorded by the AWS ranged from -4.0°C to 11.4°C.

Table 3.14. Daily mean temperature correction constants for Squirrel sensors

Sensor	ρ_c (raw data)	correction (°C)	ρ_c (corrected data)
1	0.998	0.1	1.0
2	0.999	0.1	0.999
3	0.998	0.2	1.0
4	0.995	0.3	0.999
5	0.998	-0.1	0.999
6	0.996	0.2	0.999

Table 3.15. Daily maximum temperature correction constants for Squirrel sensors

Sensor	ρ_c (raw data)	correction (°C)	ρ_c (corrected data)
1	0.997	0.1	0.998
2	0.998	0.0	0.998
3	0.997	0.1	0.998
4	0.995	0.2	0.998
5	0.996	-0.1	0.997
6	0.996	0.2	0.998

Table 3.16. Daily minimum temperature correction constants for Squirrel sensors

Sensor	ρ_c (raw data)	correction (°C)	ρ_c (corrected data)
1	0.994	0.2	0.996
2	0.996	0.1	0.996
3	0.994	0.2	0.996
4	0.991	0.2	0.996
5	0.996	-0.1	0.997
6	0.992	0.2	0.996

The magnitude of the correction factors is slightly larger than the initial corrections calculated for the roving AWS (section 3.4). The additive nature of the corrections required to standardise the sensors in each case indicates that the behaviour of all temperature sensors used in the project is similar, and consistent over the range of temperature over which the calibration exercises were performed.

3.7. Experimental networks

The five roving AWS were deployed in a series of temporary experimental networks, each designed to gather data with which to test for specific landscape-related effects on climate within the study site. The stations were run in each network for several months in order to

observe a representative sample of weather conditions at each location. The experimental networks are described below, in chronological order of operation.

3.7.1. Network 1

The five roving AWS were installed in a transect adjacent to the Trout Beck river valley between 30 January and 14 May 1998 (Figure 3.6). AWS 1 was located near the Tees bridge at the main entrance to the Moor House Reserve (grid reference NY 75943387, 540 m). AWS 2 was located near the fords over the Trout Beck (grid reference NY 75003317, 565 m). AWS 3 was located at the confluence of the Trout Beck and a tributary stream (grid reference NY 72653193, 650 m). AWS 4 was located in the bed of the Trout Beck valley below Hard Hill hush (grid reference NY 73603223, 595 m) and AWS 5 was located adjacent to Dun Fell hush (grid reference NY 71873183, 730 m). The resulting transect of roving AWS on the slope between the Pennine ridge and Moor House samples a horizontal distance of approximately 5 km.

The *in situ* AWS at the summit of Great Dun Fell (grid reference NY 71003220, 845 m), Knock Fell (grid reference NY 71803130, 755 m), High Carle Band (grid reference NY 70903020, 600 m) and Sink Beck (grid reference NY 69902950, 465 m) provide additional data from a transect sampling the western slopes of the reserve.

The first experimental network was designed primarily to sample the range of elevation within the study site. Previous work in the northern Pennines has used lapse rates derived from the difference between temperature observed at two individual stations; data from this network were used to test whether the lapse rate of temperature can be identified by regressing observed temperature on elevation. The Trout Beck valley was identified as a potential site for the accumulation of cold air during the development of katabatic drainage flow; this hypothesis can be tested using data from the network. These data can also be used to test the hypothesis that the Pennine ridge represents an orographic barrier to prevailing westerly weather systems, resulting in drier air and steeper lapse rates on eastern slopes within the study site, although such a process may operate at a spatial scale larger than that sampled by these transects.

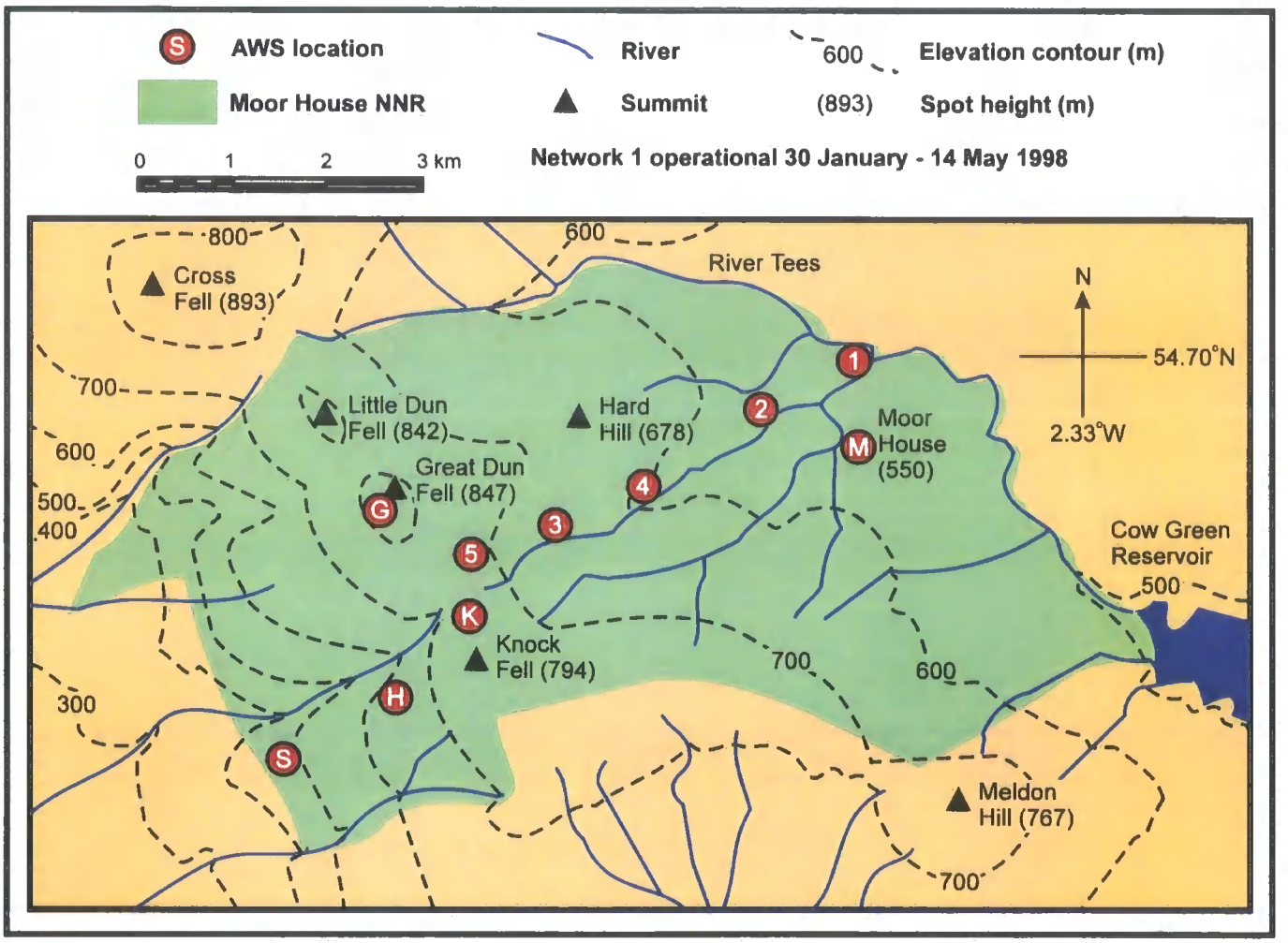

Figure 3.6. AWS locations during experimental network 1

3.7.2. Network 2

The second experimental network, illustrated in Figure 3.7, was designed primarily to sample data to test the hypothesis that systematic effects of slope aspect can be detected in temperature observations. Observations were required from contrasting slope aspects at a single elevation. The summit slopes of Great Dun Fell were selected, because a range of slope aspects are accessible at the 800 m contour. Preliminary grid references were selected for potential AWS locations to sample west, north, east and south-facing slopes on the flanks of Great Dun Fell at the required elevation, using the 1:25000 Ordnance Survey map. A slope aspect surface was calculated using the *aspect* function within the GRID program in ARC/INFO (see section 2.3), and values of elevation and aspect for grid cells in the vicinity of each of the four preliminary grid references were identified by interrogating the GIS surfaces. Four grid cells were chosen which met most closely the criteria of 800 m elevation and the required aspect. The topographic parameters for the chosen sites are presented in Table 3.17 below.

Table 3.17. Topographic parameters for AWS locations for network 2

AWS	O.S. Northing	O.S. Easting	Aspect (°)	Slope (°)	Elevation (m)
1	NY 70750	NY 32280	272.8	10.9	802.6
2	NY 70950	NY 32550	9.4	7.5	797.7
3	NY 71330	NY 32200	86.6	10.4	800.3
5	NY 71150	NY 31750	171.9	8.6	796.4

Roving AWS 1, 2, 3 and 5 were installed in the network on 19 May 1998 (AWS 4 remained at its previous location in the Trout Beck). The network remained operational until 11 October 1998. From 28 August until 11 October 1998, the Kipp pyranometers recording solar radiation were orientated parallel to the local slope instead of horizontally, to test whether the validation statistics for modelled solar radiation surfaces were thereby improved (section 6.6).

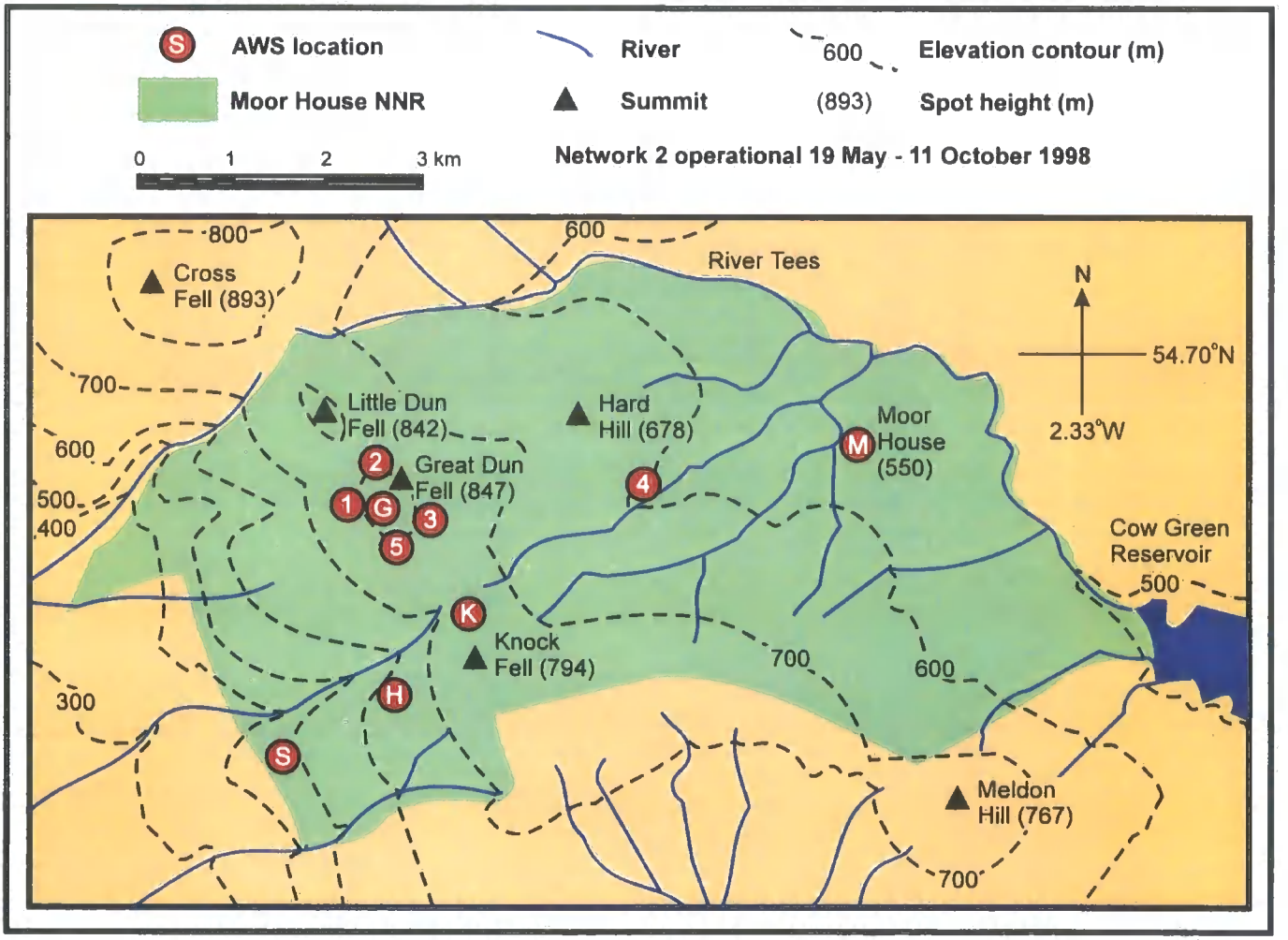

Figure 3.7. AWS locations during experimental network 2

3.7.3. Network 3

Between 7 November 1998 and 15 March 1999 the AWS were located in an experimental network designed primarily to identify and quantify the development of temperature inversions on the eastern slopes of the reserve between Great Dun Fell and Moor House. Roving AWS were installed along a 1 km long transect adjacent to Hard Hill Hush perpendicular to the Trout Beck valley. Roving AWS 1 was installed next to the lower slopes of Hard Hill hush (grid reference NY 73443249, 625 m). AWS 2 was installed on Hard Hill summit (grid reference NY 73123311, 670 m). AWS 3 was installed next to the upper slopes of Hard Hill hush (grid reference NY 73243287, 645 m). AWS 4 completed the transect, remaining in its existing location in the Trout Beck valley at the foot of Hard Hill hush (grid reference NY 73603223, 595 m). AWS 5 remained at 800 m on the southern slopes of Great Dun Fell. The network is illustrated in Figure 3.8.

Table 3.18 below shows elevation, location relative to the Pennine ridge (*dist*), ridge accumulation (*ridge*), topographic drainage potential (*drain*) calculated at a 500 m neighbourhood and *shelter* calculated at a 200 m neighbourhood for each AWS location used for Network 3.

Table 3.18. Topographic variables for the AWS locations, network 3

AWS	Elevation (m)	Dist (m)	Ridge (grid cells)	Drain (m)	Shelter (m)
S	465	1442.2	6	120.8	41.7
1	625	5916.9	4	34.4	16.6
2	670	5960.0	16	56.4	3.9
3	645	5935.7	7	53.3	24.8
4	600	5926.6	0	16.4	26.6

Two of the *in situ* AWS located on the Great Dun Fell radar station access road were removed by CEH towards the end of 1998, reducing the availability of data from the western side of the study site. The station at High Carle Band (grid reference NY 70903020) ceased operation on 23 October 1998 and the station at Knock Fell (grid reference NY 71803130) was removed on 16 December 1998.

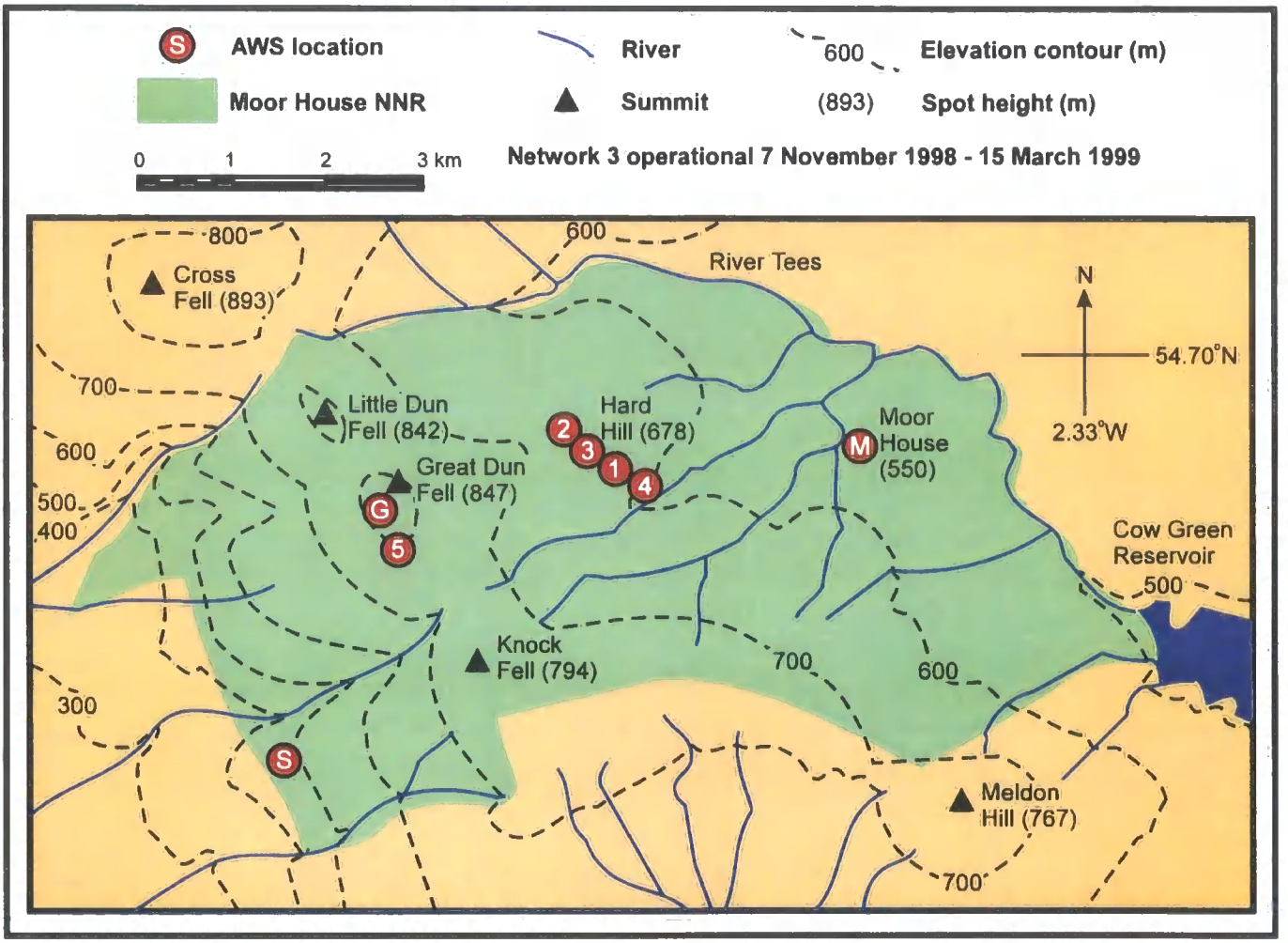

Figure 3.8. AWS locations during experimental network 3

3.7.4. Network 4

The fourth experimental AWS network was operational from 9 May to 29 September 1999 (Figure 3.9). The network was designed to validate the seasonal stability of spatial patterns identified during the operation of previous networks. Roving AWS 1 and 2 remained in their respective positions adjacent to the lower slopes of Hard Hill Hush (grid reference NY 73443249, 625 m) and on Hard Hill summit (grid reference NY 73123311, 670 m). AWS 3 was installed at High Carle Band (grid reference NY 70903020, 600 m) and AWS 4 was installed at Knock Fell (grid reference NY 71803130, 755 m) to compensate for the paucity of data to the west of the Pennine ridge resulting from the removal of the two *in situ* stations adjacent to the Radar Station access road. AWS 5 was installed at the Tees bridge (grid reference NY 75943387, 540 m). The *in situ* AWS at Great Dun Fell summit suffered prolonged operating problems and most data were not usable during the operation of this network. The roving AWS located at Knock Fell was therefore used as the high elevation base station in place of Great Dun Fell summit.

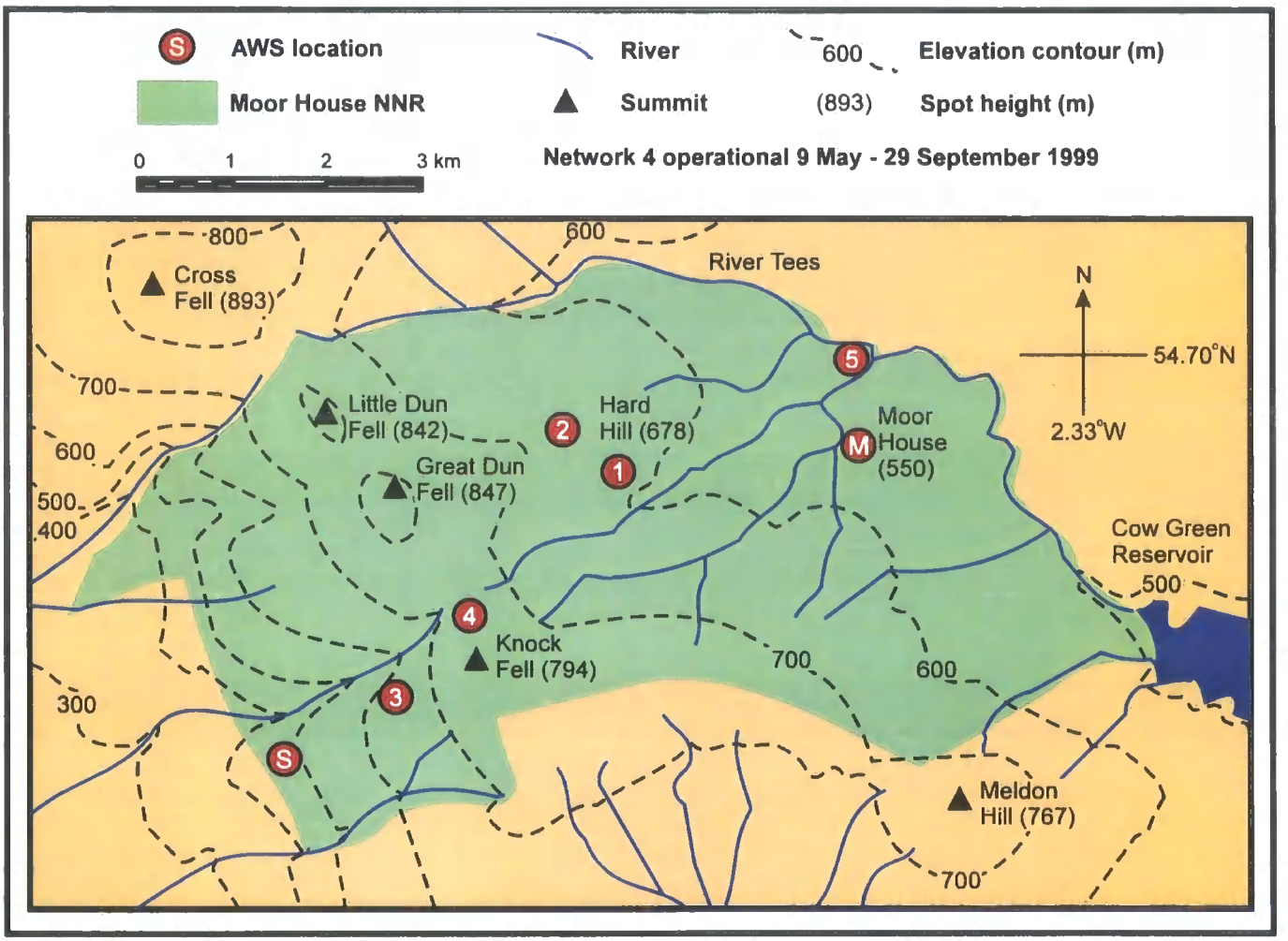

Figure 3.9. AWS locations during experimental network 4

3.7.5. Network 5

The final network (Figure 3.10) was designed to sample data with which to test models of spatial climatic behaviour within the reserve. AWS locations for the final network were chosen to sample previously unvisited locations to ensure the availability of independent data. The final network operated from 7 October 1999 until 8 March 2000. Roving AWS 1 was installed near an area of blanket bogs on the Trout Beck bridleway (grid reference NY 72233174, 680 m). AWS 2 was installed on the northern slopes of Hard Hill (grid reference NY 73033331, 665 m). AWS 3 was installed at Great Dun Fell summit to provide a back-up source of data for the failing *in situ* station at the summit (grid reference NY 71003220, 845 m). AWS 4 was installed on the access road to Silverband Mine, on the scarp slope south of Great Dun Fell (grid reference NY 70943099, 680 m) and AWS 5 was installed near a small conifer plantation at Dodgen Pot (grid reference NY 76553286, 545 m).

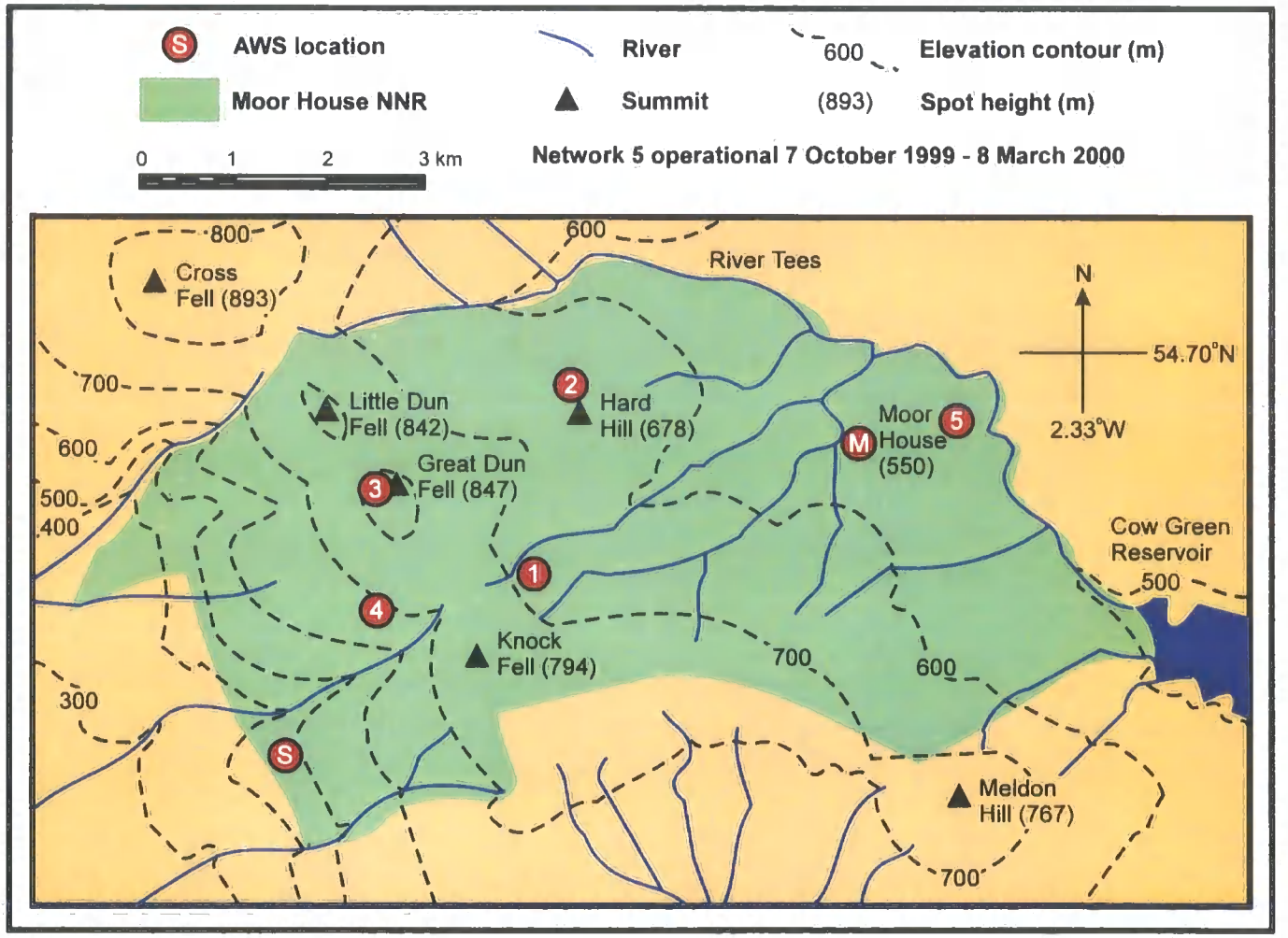

Figure 3.10. AWS locations during experimental network 5

3.7.6. Summary of network locations

Table 3.19 presents the co-ordinates and elevations of all the AWS locations used in the study. The locations associated with each network are also given.

Table 3.19. Co-ordinates and elevation of all AWS locations used in the experimental networks

Location	Network	OS Co-ordinates	Elevation (m)
M	1,2,3,4,5	NY 75703280	550
G	1,2,3,5	NY 71003220	845
H	1,2,4	NY 70903020	600
S	1,2,3,4,5	NY 69902950	465
K	1,2,4	NY 71803130	755
Bridge	1,4	NY 75943387	540
Fords	1	NY 75003317	565
Hardhill Hush	1,2,3	NY 73603223	595
Confluence	1	NY 72653193	650
Dun Fell Hush	1	NY 71873183	730
Great Dun Fell N	2	NY 70953255	800
Great Dun Fell E	2	NY 71333220	800
Great Dun Fell S	2,3	NY 71153175	800
Great Dun Fell W	2	NY 70753228	800
Hard Hill Summit	3,4	NY 73123311	670
Hard Hill Upper	3	NY 73243287	645
Hard Hill Lower	3,4	NY 73443249	625
Hard Hill N	5	NY 73033331	665
Silverband	5	NY 70943099	680
Dodgen	5	NY 76553286	545
Blanket Bogs	5	NY 72233174	680

3.8. Measuring location in the field

In order for the measured climate data to be used for modelling purposes, the values of topographic variables must be known for each AWS site. For this reason, before a roving station could be erected as part of an experimental network it was necessary to determine geographical location in the field with grid cell accuracy. For some locations, this can be achieved using the Ordnance Survey 1:25000 or 1:10000 maps. However, many of the sites chosen as AWS locations are distant from any landmarks, and a Global Positioning System (GPS) was used to achieve accurate measurements of location within the study site. The GPS used for the study was a hand-held unit (Garmin 12XL) sourced from Positioning Resources Ltd, Aberdeen, UK. The GPS is a multi-frequency receiver which continuously

tracks surface position using location and time signals transmitted by up to twelve geostationary satellites operated by the United States Department of Defence. The satellites are in a known orbit and so the GPS hand set can calculate the distance to each, using the time taken for transmitted microwave signals to reach the receiver. By combining this information for four or more satellites, geographical location can be derived (Cruddace and Clarke, 2000). Elevation data are also returned by the GPS, but the accuracy of elevation data is lower than for latitude and longitude. Elevation is therefore obtained for any location by interrogating the DTM at the relevant co-ordinates. The internal clock within the logger of each roving AWS was set to Universal Time (GMT) using the GPS time signals, and checked at monthly intervals.

The GPS equipment returns latitude and longitude co-ordinates to the nearest metre. However, the accuracy achieved by the system does not justify this level of precision. Although the manufacturer claims the unit is accurate to within 15 m, the accuracy of the transmitted location data available to civilian users was reduced by the Selective Availability Program, which incorporates deliberate inaccuracies into the broadcast information relating to the clock and orbit of each satellite.

The accuracy of the GPS equipment was determined empirically by making repeated measurements at a range of AWS locations between 1998 and 2000. The locations used were the roving AWS sites during experimental networks 1, 3 and 5 (see Figures 3.6, 3.8 and 3.10). Analysis of the resulting co-ordinates allows the variability of the GPS data to be quantified.

Each individual latitude or longitude measurement was expressed as an anomaly (in metres) from the mean value for all measurements made at that location. The mean value of repeated measurements of latitude and longitude at each location are inferred to be the "true" co-ordinates. Data from all three networks were used to calculate the mean value and standard deviation of the anomalies. The total number of individual observations was 164, and the mean value of the anomalies was +0.1 m. The fact that the mean anomaly value is so close to zero indicates that the GPS does not systematically overestimate or underestimate latitude or longitude. The standard deviation of the anomalies was 23.0 m.

In order to quantify formally the confidence attached to an individual GPS reading, the value for the 95% confidence interval can be found from properties of the normal distribution. The value of the 95% critical value is determined from Equation 3.1.

$$x_{95\%} = (1.96 \times sd) + \bar{x} \qquad 3.1$$

where: x_{95} = 95% critical value

sd = standard deviation of anomalies

$\bar{x}$ = mean value of anomalies

The empirically-determined 95% confidence interval for individual GPS fixes is therefore approximately ±45 m, i.e. 95% of GPS readings will be within 45 m of the true latitude and longitude. This figure is identical to published values quantifying the accuracy of GPS under Selective Availability (Cruddace and Clarke, 2000). The GPS equipment can therefore be used with reasonable confidence to assign any point within the study site to a specific 50 m × 50 m grid cell of the DTM, especially as accuracy can be further optimised by taking repeated GPS fixes on separate occasions and calculating the mean value as the best estimate of the location. This procedure is likely to achieve a substantial improvement in the accuracy associated with the GPS.

A GPS estimate of location is likely to be more accurate than an estimate made using a map and compass, particularly in featureless terrain or when poor visibility prevents the use of distant landmarks to ascertain compass bearings.

3.9. Discussion

Precautions have been taken to optimise data quality as a preliminary to the operation of experimental networks and throughout the subsequent gathering of spatial climate data. At the beginning of the project, faulty instruments and logger programs were identified and replaced. The sampling strategy was standardised for all AWS used for the project, so that daily summaries of hourly data can be used throughout. The adoption of existing ECN

protocols for data measurement ensures that a consistent methodology is used for all the AWS, and optimises the homogeneity of the data (Beard, Scott and Adamson, 1999). The clocks in the roving AWS were synchronised, and checked at regular periods throughout the project. The standardisation of the time code assigned to midnight observations ensures that data from all stations can be analysed consistently without introducing systematic bias.

Automatic data monitoring can be affected by at least three types of error, related to instrumentation, exposure and sampling (Linacre, 1992). The latter two types of error are controlled for in the methodology described in section 3.4 because data are only compared from pairs of adjacent AWS and all data are observed using a consistent sampling frequency. Instrumental error can be subdivided into random and systematic error. A total error of 1°C is suggested as the maximum tolerable error associated with automatic measurements of surface temperature (Linacre, 1992). The calibration procedure represents an explicit quantification of systematic instrumental error, and helps to minimise the total error associated with the observations. Thus although the magnitude of the calculated correction factors is within the specified accuracy of the sensors, the correction factors can nevertheless be applied to the observed data in order to optimise the accuracy with which subsequent spatial temperature differences can be modelled, using data measured simultaneously by the corrected temperature sensors.

Statistical comparison of temperature data sampled by adjacent weather stations has allowed the calculation of correction factors which compensate for small but systematic discrepancies in the response of individual sensors to ambient temperature. Having calculated corrections for five weather stations, their relocation adjacent to fixed stations elsewhere in the reserve allowed the correction of data from all weather stations within the study area, increasing the signal to noise ratio in the data measured by the network. The corrections appear robust and the magnitude of a correction for a specific temperature variable measured by a specific AWS seems generally stable in time.

The accuracy of the GPS equipment has been assessed and quantified, allowing the location of any data gathering undertaken within the study site to be specified with

confidence. Empirical data can therefore be analysed in conjunction with the digital terrain model and other spatially explicit data generated within the GIS.

Chapter 4. Temperature as a function of elevation

4.1. Lapse rates

The mechanism whereby altitude controls air temperature is discussed in section 2.2. The processes of adiabatic energy exchange also explain the fact that air temperature measured near the ground tends to vary as a function of surface elevation. The environmental lapse rate at which temperature is observed to fall with elevation varies with humidity and other air mass characteristics. The theoretical maximum rate of temperature decrease with height in stable conditions (the dry adiabatic lapse rate or DALR) is approximately -9.8×10^{-3} °C m^{-1} (a fall of 9.8°C for each kilometre increase in height). The environmental lapse rate can temporarily become steeper than the DALR during periods of strong surface heating (Barry, 1992). Lapse rates in saturated air are less steep than the DALR due to the release of latent heat during condensation. During stable atmospheric conditions when the air is poorly mixed, and especially at night, dense cool air may stratify near the ground surface causing shallow lapse rates or temperature inversions over a limited area. Katabatic density currents may develop as the layer of cold air at the surface flows downhill, controlled by the local topography (Simpson, 1999).

Observed mean environmental lapse rates in Britain are unusually steep (Manley, 1952) due to the progressive westerly circulation which often affects the British Isles, and due to the high frequency of polar-maritime air masses (Taylor, 1976). Despite the fact that the British uplands are small by world standards, the rapid fall of mean temperature with elevation makes areas of complex terrain such as the Moor Houses reserve ideal sites for the study of spatial patterns of temperature lapse rate.

4.2. Estimating lapse rates by regression using raw data

Data for the period from 30 January to 7 April and from 30 April to 14 May 1998 (gathered by network 1) were analysed as a single sample. Data for days between 8 and 29 April were removed from the analysis due to missing data from two of the roving AWS. Regression of daily temperature data on elevation results in the following relationships (Equations 4.1 to 4.3) for the transect of stations between the Tees bridge and Great Dun Fell.

$$tmp = -6.5 \times 10^{-3}(ele) + 7.87 \quad (R^2 = 0.04, n = 11952, t(ele) = -23.0, P < 0.01) \quad 4.1$$

$$tmx = -8.4 \times 10^{-3}(ele) + 11.17 \quad (R^2 = 0.05, n = 11952, t(ele) = -25.4, P < 0.01) \quad 4.2$$

$$tmn = -3.8 \times 10^{-3}(ele) + 3.66 \quad (R^2 = 0.01, n = 11952, t(ele) = -13.0, P < 0.01) \quad 4.3$$

where *tmx* = daily maximum hourly mean temperature (°C)

tmp = daily mean temperature (°C)

tmn = daily minimum hourly mean temperature (°C)

ele = elevation above sea level (m)

Data from the transect of four *in situ* AWS located to the west of Great Dun Fell were analysed using the same time period. The four stations sample elevations between 465 m and 845 m and cover a horizontal distance of approximately 4 km. The following relationships are apparent (Equations 4.4 to 4.6).

$$tmp = -7.3 \times 10^{-3}(ele) + 8.51 \quad (R^2 = 0.09, n = 7968, t(ele) = -28.0, P < 0.01) \quad 4.4$$

$$tmx = -7.7 \times 10^{-3}(ele) + 10.61 \quad (R^2 = 0.08, n = 7968, t(ele) = -26.2, P < 0.01) \quad 4.5$$

$$tmn = -6.9 \times 10^{-3}(ele) + 6.13 \quad (R^2 = 0.08, n = 7968, t(ele) = -27.0, P < 0.01) \quad 4.6$$

The mean lapse rate for each of the three daily temperature variables *tmp*, *tmx* and *tmn* can be interpreted from the slope coefficients of the above regression equations. The mean lapse rates are steepest for daily maximum temperature (-8.4×10^{-3} °C m^{-1} for the eastern

transect and -7.7×10^{-3} °C m^{-1} for the western transect), implying that the decrease of temperature with elevation is more rapid during day time. This is possibly due to elevation-dependent differences in insolation, or elevation-dependent differences in the proportion of insolation converted to sensible heat. For both transects, the lapse rate of minimum temperature is shallower than the lapse rate of either mean or maximum temperature. This is a consequence of the net loss of radiation from the ground surface at night, which allows cooling of air close to the ground. Minimum temperature may also be affected by occasional inversions, due to subsidence of cold air or heat loss from the surface. The lapse rate of mean temperature is intermediate between the lapse rate of maximum and minimum temperature for each transect. A systematic difference is apparent between the regressions for minimum temperature for the east and west of the Pennine ridge. The mean lapse rate of minimum temperature is much steeper on the western transect (-6.9×10^{-3} °C m^{-1}, compared to -3.8×10^{-3} °C m^{-1} for data measured simultaneously on the eastern transect). This result corroborates the hypothesis that the eastern slopes of the study site are prone to topographically influenced accumulation of cold air leading to anomalous low temperature minima.

The coefficient of determination (R^2) is low for each regression equation. This is partly due to the large day-to-day variability of temperature; Figure 4.1 illustrates that variability at timescales of two to three days can be as large as the amplitude of the annual cycle. Another reason for the poor performance of the regression models is the large day-to-day variability in lapse rate. Figure 4.2 shows that sporadic and short-lived occurrences of shallow lapse rate disrupt the usual strongly negative relationship between elevation and temperature. When the lapse rate is shallow or positive the effects on temperature distribution are unlikely to be spatially uniform, as topography will affect the accumulation or dispersal of cold air. The temporally-changing influence of topography on temperature also hinders the performance of the regression models. Lapse rates of minimum temperature may be particularly prone to the spatially-varying effects of katabatic air flow, and indeed the lowest R^2 value is for the regression of minimum temperature on elevation for the eastern transect, where shallow slopes may cause accumulation of cold air during calm nights.

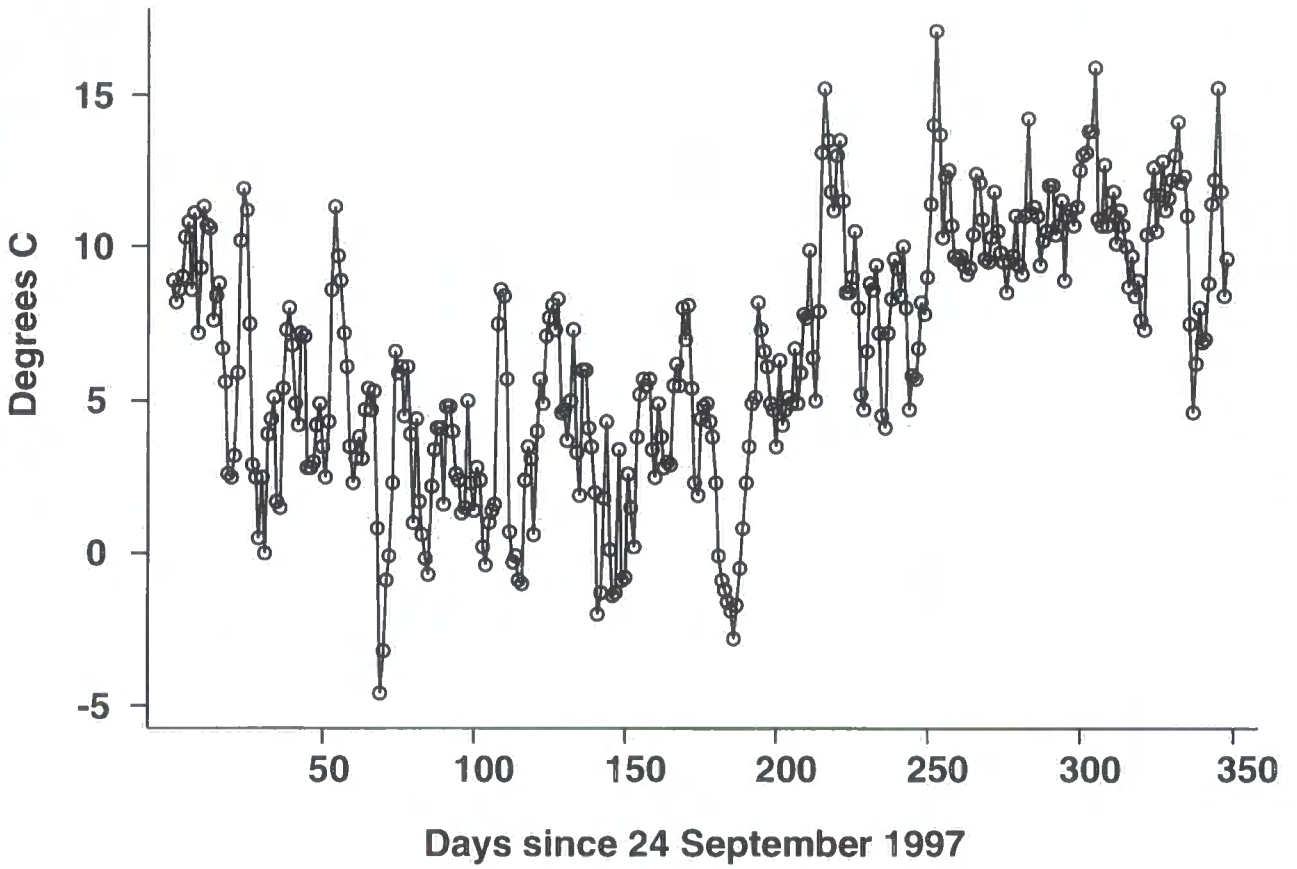

Figure 4.1. Variability of daily mean temperature at Moor House

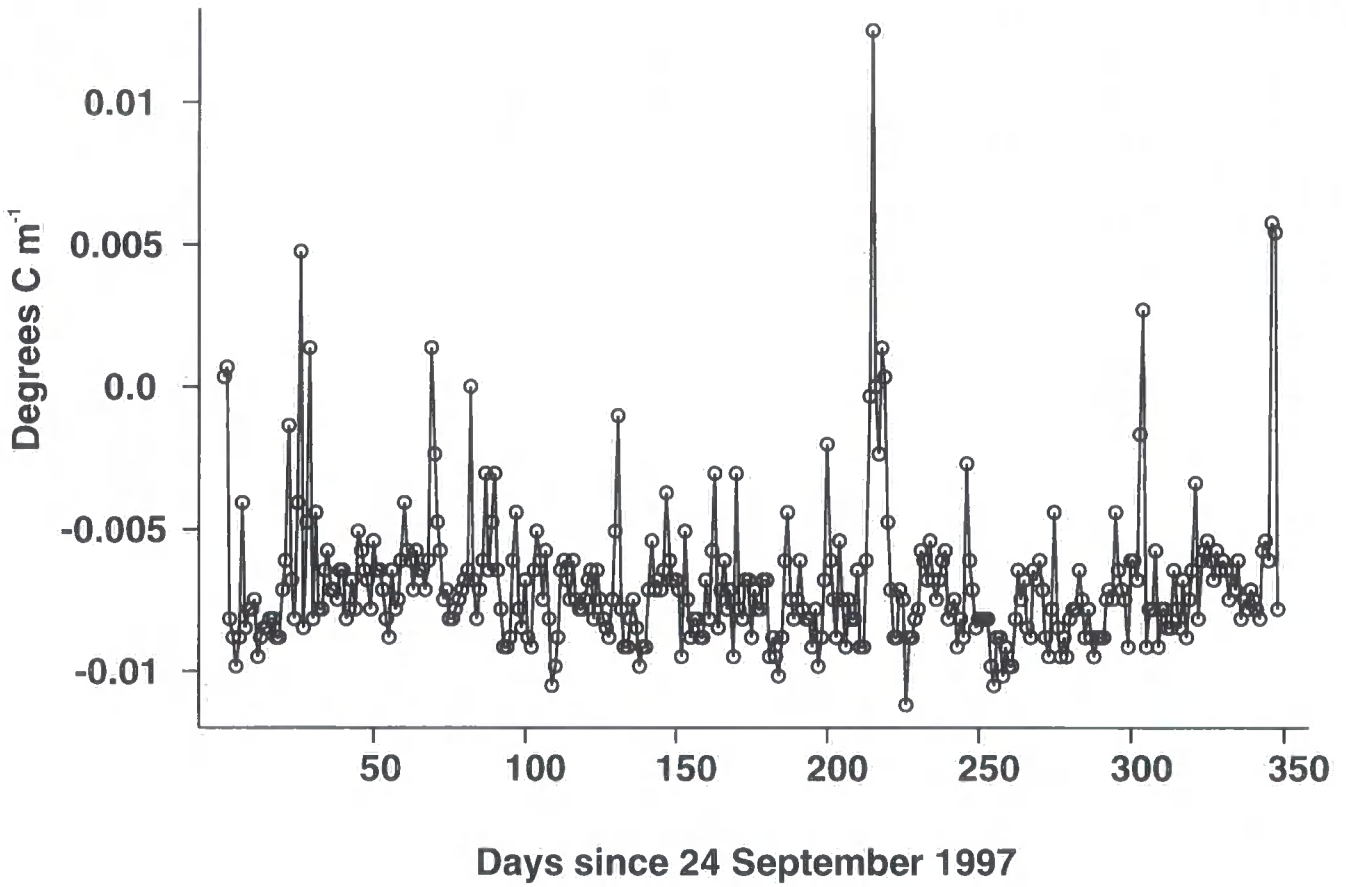

Figure 4.2. Variability of daily mean temperature lapse rate at Moor House

4.3. The effect of wind direction on lapse rates

Wind direction observed at the summit of Great Dun Fell has been used previously as an effective proxy variable for synoptic-scale atmospheric circulation in the northern Pennines (Pepin *et al.*, 1999). At a landscape-scale, the local wind direction measured at the summit is likely to be a more meaningful index of atmospheric circulation affecting the study site than indices calculated at a regional scale (Jenkinson and Collison, 1977), or estimated for the British Isles as a whole (Lamb, 1972). The interaction of the local air flow with the Pennine topography may cause systematic spatial differences in surface temperature due to the föhn effect, and to investigate this hypothesis the effect of summit wind direction on lapse rate was analysed for daily mean, maximum and minimum temperature.

Daily mean wind direction at Great Dun Fell summit (*dir*) was calculated as the arithmetic mean of the twenty four hourly wind directions and classified into one of four quadrants; north east ($dir < 90^{o}$), south east ($90^{o} \leq dir < 180^{o}$), south west ($180^{o} \leq dir < 270^{o}$) and north west ($270^{o} \leq dir \leq 360^{o}$). Separate regression models were calculated for each of the four wind directions for mean, maximum and minimum temperature (Tables 4.1 to 4.3).

Table 4.1. Relative effect of summit wind direction on lapse rates of mean temperature east and west of the Pennine ridge

Dir		
	Eastern transect	
NE	$tmp = -6.5 \times 10^{-3}(ele) + 7.45$	$R^2 = 0.23$, n = 1008, t(*ele*) = -17.4, $P < 0.01$
SE	$tmp = -4.2 \times 10^{-3}(ele) + 7.63$	$R^2 = 0.0$, n = 1872, t(*ele*) = -4.2, $P < 0.01$
SW	$tmp = -7.0 \times 10^{-3}(ele) + 8.03$	$R^2 = 0.05$, n = 8208, t(*ele*) = -21.0, $P < 0.01$
NW	$tmp = -7.2 \times 10^{-3}(ele) + 7.44$	$R^2 = 0.36$, n = 864, t(*ele*) = -22.0, $P < 0.01$
	Western transect	
NE	$tmp = -8.1 \times 10^{-3}(ele) + 8.81$	$R^2 = 0.45$, n = 672, t(*ele*) = -23.6, $P < 0.01$
SE	$tmp = -7.7 \times 10^{-3}(ele) + 10.49$	$R^2 = 0.05$, n = 1248, t(*ele*) = -8.1, $P < 0.01$
SW	$tmp = -7.1 \times 10^{-3}(ele) + 8.09$	$R^2 = 0.09$, n = 5472, t(*ele*) = -23.9, $P < 0.01$
NW	$tmp = -7.7 \times 10^{-3}(ele) + 7.83$	$R^2 = 0.57$, n = 576, t(*ele*) = -27.4, $P < 0.01$

Comparison of the slope terms indicates that the largest discrepancy in lapse rate occurs on days with south easterly winds, when lapse rates of mean temperature are substantially

steeper on the western transect than on the eastern transect (-7.7 × 10^{-3} °C m^{-1} compared to -4.2 × 10^{-3} °C m^{-1}). The constant in each regression model relates to mean temperature extrapolated to sea level, and the difference between the constant for western and eastern transects is largest for south easterly winds. This result indicates again that the spatial discrepancy in temperature is greatest for south easterly wind directions.

Table 4.2. Relative effect of summit wind direction on lapse rates of maximum temperature east and west of the Pennine ridge

Dir		
	Eastern transect	
NE	$tmx = -8.3 \times 10^{-3}(ele) + 10.63$	$R^2 = 0.11$, n = 1008, t(*ele*) = -11.4, P < 0.01
SE	$tmx = -7.1 \times 10^{-3}(ele) + 12.80$	$R^2 = 0.02$, n = 1872, t(*ele*) = -5.9, P < 0.01
SW	$tmx = -8.1 \times 10^{-3}(ele) + 10.61$	$R^2 = 0.06$, n = 8208, t(*ele*) = -22.9, P < 0.01
NW	$tmx = -1.33 \times 10^{-2}(ele) + 13.61$	$R^2 = 0.53$, n = 864, t(*ele*) = -31.5, P < 0.01
	Western transect	
NE	$tmx = -8.8 \times 10^{-3}(ele) + 11.00$	$R^2 = 0.26$, n = 672, t(*ele*) = -15.4, P < 0.01
SE	$tmx = -8.4 \times 10^{-3}(ele) + 13.86$	$R^2 = 0.05$, n = 1248, t(*ele*) = -8.0, P < 0.01
SW	$tmx = -7.2 \times 10^{-3}(ele) + 9.83$	$R^2 = 0.09$, n = 5472, t(*ele*) = -22.7, P < 0.01
NW	$tmx = -9.5 \times 10^{-3}(ele) + 10.51$	$R^2 = 0.72$, n = 576, t(*ele*) = -38.1, P < 0.01

Table 4.2 shows that on days when the summit wind direction has a westerly component lapse rates of daily maximum temperature are slightly steeper on the eastern slopes, and on days when wind direction has an easterly component lapse rates are steeper on western slopes. The spatial discrepancies in the lapse rate of maximum temperature are not as large as for mean temperature.

The relative steepness of lapse rate on leeward slopes is consistent with a föhn mechanism. The largest discrepancy occurs during south easterly winds, not during the prevailing south westerly wind direction as expected.

The effect of summit wind direction on lapse rates of minimum temperature is illustrated in Table 4.3.

Table 4.3. Relative effect of summit wind direction on lapse rates of minimum temperature east and west of the Pennine ridge

Dir		
	Eastern transect	
NE	$tmn = -1.9 \times 10^{-3}(ele) + 1.94$	$R^2 = 0.01$, n = 1008, t(*ele*) = -3.7, $P < 0.01$
SE	$tmn = 4.3 \times 10^{-5}(ele) + 1.42$	$R^2 = 0.0$, n = 1872, t(*ele*) = 0.1, $P = 0.96$
SW	$tmn = -5.4 \times 10^{-3}(ele) + 4.84$	$R^2 = 0.03$, n = 8208, t(*ele*) = -14.7, $P < 0.01$
NW	$tmn = 1.1 \times 10^{-3}(ele) - 0.76$	$R^2 = 0.0$, n = 864, t(*ele*) = 1.9, $P = 0.06$
	Western transect	
NE	$tmn = -8.0 \times 10^{-3}(ele) + 6.87$	$R^2 = 0.47$, n = 672, t(*ele*) = -24.2, $P < 0.01$
SE	$tmn = -6.0 \times 10^{-3}(ele) + 6.34$	$R^2 = 0.04$, n = 1248, t(*ele*) = -7.5, $P < 0.01$
SW	$tmn = -7.1 \times 10^{-3}(ele) + 6.16$	$R^2 = 0.08$, n = 5472, t(*ele*) = -22.4, $P < 0.01$
NW	$tmn = -5.6 \times 10^{-3}(ele) + 4.55$	$R^2 = 0.25$, n = 576, t(*ele*) = -13.9, $P < 0.01$

For all four wind direction quadrants, lapse rates of daily minimum temperature are substantially shallower on the eastern Trout Beck transect than on the western slopes. Large spatial discrepancies in the lapse rate of minimum temperature exist for all wind directions, and are consistent with the interaction of local topography with katabatic drainage of cold air. The proposed mechanism is that nocturnal radiation loss from the surface causes cooling of surface air, which flows katabatically as a density current. This cold air may tend to accumulate on the eastern slopes but disperse more rapidly from the western slopes due to topographic influences, exposing eastern slopes to lower temperature minima. The magnitude of the regression constants also show that minimum temperatures in the Trout Beck are relatively cold in all wind directions. One systematic effect of wind direction is apparent however; the spatial discrepancy in the lapse rate of minimum temperature is smallest on days with south westerly winds. South westerlies occur in the prevailing progressive conditions when high wind speeds and a well-mixed lower atmosphere prevent nocturnal heat loss and hinder development of the stable conditions necessary for the subsidence and accumulation of cold air. These observations provide further evidence in support of the hypothesis that katabatic drainage affects minimum temperature within the study site.

4.4. Lapse rates in wet-bulb temperature

Variation of wet-bulb temperature with elevation can also be modelled using a regression approach, in order to test the assumption that wet-bulb temperature may be modelled using lapse rates. For the five stations with wet-bulb temperature data, using the same time period described above, Equations 4.7 and 4.8 describe the relationship with elevation.

$$wet = -5.6 \times 10^{-3}(ele) + 6.68 \qquad 4.7$$
$$(R^2 = 0.02, n = 415, t(ele) = -2.5, P < 0.01)$$

$$tmp - wet = -1.3 \times 10^{-3}(ele) + 1.40 \qquad 4.8$$
$$(R^2 = 0.03, n = 415, t(ele) = -3.5, P < 0.01)$$

where *wet* = daily mean wet-bulb temperature (°C)

This relationship suggests that wet-bulb temperature can be modelled using lapse rates, although the R^2 values are low for reasons discussed in section 4.2. The mean wet-bulb depression (*tmp* - *wet*) falls with elevation (Equation 4.8), and because saturation vapour pressure varies with temperature, ambient vapour pressure will also tend to fall with increasing elevation (section 7.2).

Equations 4.7 and 4.8 also illustrate the fact that empirically calculated lapse rates can only be used to estimate temperature over a finite range of elevation values. If the above equations are used to extrapolate temperature for elevations above about 1200 m, the model becomes physically unrealistic, yielding estimates of wet-bulb temperature which systematically exceed estimates of dry-bulb temperature.

4.5. Estimating lapse rates by regression using anomalies

The regression analyses were repeated, expressing the observed daily value *S* at each station *i* as an anomaly *a* from the observed value at Moor House *MH*, calculated for each day *j* as described in Equation 4.9.

$$a_{ij} = S_{ij} - MH_j \qquad 4.9$$

Standardising the data removes the effects of day-to-day variability, and the power of elevation as a predictor of temperature within the reserve can be quantified by the improvement in the coefficient of determination for the above regressions. For all nine stations, on both the eastern and western transects, lapse rates can be estimated as follows, having first converted all daily data to anomalies from Moor House (Equations 4.10 to 4.12).

$$a_{tmp} = -7.1 \times 10^{-3}(ele) + 4.05 \qquad 4.10$$
$$(R^2 = 0.65, n = 747, t(ele) = -37.2, P < 0.01)$$

$$a_{tmx} = -8.2 \times 10^{-3}(ele) + 4.50 \qquad 4.11$$
$$(R^2 = 0.66, n = 747, t(ele) = -38.5, P < 0.01)$$

$$a_{tmn} = -5.5 \times 10^{-3}(ele) + 3.37 \qquad 4.12$$
$$(R^2 = 0.19, n = 747, t(ele) = -13.1, P < 0.01)$$

The coefficients of determination are increased, especially for mean and maximum daily temperature, by expressing the data as anomalies from a single base station. This result demonstrates that day-to-day variability in temperature is partly responsible for the poor predictive power of the regression relationships presented in section 4.2. The relatively poor coefficient of determination for minimum temperature anomalies (Equation 4.12) shows that lapse rates of minimum temperature are still relatively poorly modelled, despite conversion of the temperature observations to anomalies from a single base station. This illustrates a process affecting lapse rates of minimum temperature but not mean or maximum temperature, possibly the sporadic effects of katabatic air flow. In order to test for a spatial component to this effect, data from the two transects east and west of the Pennine ridge were analysed separately. For the stations to the west of the Pennine ridge, the results are as follows (Equations 4.13 to 4.15).

$$a_{tmp} = -7.3 \times 10^{-3}(ele) + 4.30 \quad (R^2 = 0.67, n = 332, t(ele) = -26.2, P < 0.01) \quad 4.13$$

$$a_{tmx} = -7.7 \times 10^{-3}(ele) + 4.11 \quad (R^2 = 0.67, n = 332, t(ele) = -25.9, P < 0.01) \quad 4.14$$

$$a_{tmn} = -6.9 \times 10^{-3}(ele) + 4.52 \quad (R^2 = 0.27, n = 332, t(ele) = -11.1, P < 0.01) \quad 4.15$$

For the stations on the Trout Beck transect east of the Pennine ridge, lapse rates for the same period calculated from the temperature anomalies are described in Equations 4.16 to 4.18.

$$a_{tmp} = -6.5 \times 10^{-3}(ele) + 3.67 \quad (R^2 = 0.65, n = 498, t(ele) = -30.6, P < 0.01) \quad 4.16$$

$$a_{tmx} = -8.4 \times 10^{-3}(ele) + 4.67 \quad (R^2 = 0.65, n = 498, t(ele) = -30.6, P < 0.01) \quad 4.17$$

$$a_{tmn} = -3.8 \times 10^{-3}(ele) + 2.05 \quad (R^2 = 0.12, n = 498, t(ele) = -30.6, P < 0.01) \quad 4.18$$

A comparison of Equations 4.15 and 4.18 shows that the relationship between minimum temperature and elevation is particularly weak on the eastern side of the Pennine ridge (the mean lapse rate of minimum temperature for the eastern transect is -3.8×10^{-3} °C m^{-1}, whereas on the other side of the ridge during the same period the lapse rate is -6.9×10^{-3} °C m^{-1}, and the R^2 statistic is also higher). This is evidence that the development of temperature inversions affects the Trout Beck valley more than the western slopes.

Despite the improvement in performance resulting from the use of temperature anomalies, the regression models described by Equations 4.10 to 4.18 still suffer because they quantify the mean lapse rate as a single quantity (the slope term) for each sample, whereas in reality the lapse rate varies from day to day, especially for minimum temperature. Daily lapse

rates can be calculated using data measured simultaneously at two base stations within the study site. The difference in elevation between the two base stations must be sufficiently large to sample a range of temperature, and the locations must be representative with respect to topographic and micro-climatic exposure. The two AWS sites chosen as base stations for the calculation of lapse rates were the ECN site at Moor House, and the Great Dun Fell summit station. These base stations are located 4.8 km apart, with an elevation difference of 295 m.

For each day, the temperature difference between Great Dun Fell summit AWS and the ECN Moor House AWS was found and a linear lapse rate was calculated. The procedure is shown in Equation 4.19 for mean temperature. Linear lapse rates can be calculated for maximum and minimum temperature using the same method.

$$lr_{tmp} = \frac{tmp_{GDF} - tmp_{MH}}{295} \qquad 4.19$$

where lr_{tmp} = lapse rate (°C m^{-1})

tmp_{GDF} = observed temperature at Great Dun Fell summit (°C)

tmp_{MH} = observed temperature at Moor House (°C)

295 = elevation difference between the base stations (m)

The importance of the variability of daily lapse rate can be seen by including the lapse rate of mean (lr_{tmp}), maximum (lr_{tmx}) or minimum temperature (lr_{tmn}) as an explanatory variable in the appropriate regression model, using data from all stations (Equations 4.20 to 4.22).

$$a_{tmp} = -7.1 \times 10^{-3}(ele) + 154.8(lr_{tmp}) + 5.01 \qquad 4.20$$

($R^2 = 0.85$, n = 747, t(ele) = -56.7, t(lr_{tmp}) = 31.4, $P < 0.01$)

$$a_{tmx} = -8.2 \times 10^{-3}(ele) + 100.4(lr_{tmx}) + 5.27 \qquad 4.21$$

($R^2 = 0.77$, n = 747, t(ele) = -46.1, t(lr_{tmx}) = 18.1, $P < 0.01$)

$$a_{tmn} = -5.5 \times 10^{-3}(ele) + 143.4(lr_{tmn}) + 3.96 \qquad 4.22$$

($R^2 = 0.60$, n = 747, t(ele) = -18.8, t(lr_{tmn}) = 27.9, $P < 0.01$)

The inclusion of the daily lapse rate in the regression models results in an improvement in R^2 from 0.65 to 0.85 for mean temperature, from 0.66 to 0.77 for maximum temperature, and from 0.19 to 0.60 for minimum temperature. The increase in model performance due to the inclusion of lapse rate variations is thus greatest for minimum temperature, although the final model is still poorer than for mean or maximum temperature. These results show that the relationship of daily minimum temperature with elevation is more complex than that of daily mean and maximum temperature. This may be partly due to the predominantly nocturnal occurrence of katabatic flows of cold air which can disrupt or invert lapse rates. Chapter 5 will address whether this effect is restricted to the Trout Beck valley, or whether the effect extends to wider areas within the Moor House reserve.

4.6. Modelling temperature using daily lapse rates

Regression of temperature, or temperature anomalies, on elevation elucidates systematic differences between the mean lapse rate of daily mean, maximum and minimum temperature, and also spatial differences between separate transects of data. The models described in section 4.5 could be used to obtain a spatial estimate of daily temperature anomalies across the study site. However, the application of the regression approach for modelling daily surfaces of temperature is limited due to the inability of the method to capture day-to-day variability of temperature and lapse rate within the time period over which a regression model is calibrated. A regression approach will, by definition, produce estimates close to the mean of the calibration period, and without the full variability of the true data. The resulting time series would be unrealistically smooth. The high frequency variability of lapse rate, including the sporadic occurrence of temperature inversions (Figure 4.2) is one of the defining climatic characteristics of the study site. To overcome these limitations, a method was developed whereby daily lapse rate is explicitly measured, and this variability is included in the spatial temperature model for each day.

The linear lapse rate calculated using Equation 4.19 was used to model a daily temperature surface (*TEMP*) across the study site using the DTM within the ARC/INFO GIS. The

procedure is shown for mean temperature in Equation 4.23; the same procedure can be used for maximum and minimum temperature.

$$TEMP = lr_{tmp}[DTM - 550] + tmp_{MH} \qquad 4.23$$

As an illustration, daily mean temperature data for 20 November 1998 were used to model temperature across the study site. Mean temperature for the day was 2.2°C at Moor House and -0.2°C at Great Dun Fell. The resulting linear lapse rate is -8.14×10^{-3} °C m^{-1}, which results in spatial temperature estimates across the study site ranging from -0.5°C at the summit of Cross Fell to 4.5°C at the foot of the Pennine scarp slope (Figure 4.3). For modelling purposes, an advantage of using a model based on only two base stations is the increased availability of independent data from the other stations for validation. Data from stations not used to calculate the lapse rate can be expressed as daily residuals from the linear lapse rate model to quantify the performance of the model.

For all stations on the reserve, daily mean, minimum and maximum temperature data were calculated using the first experimental network. Linear lapse rates of mean, minimum and maximum temperature were calculated for each day based on the daily data from Moor House and Great Dun Fell summit using Equation 4.19, and the daily lapse rates were used to estimate temperature over the reserve using Equation 4.23. Observed data from independent stations were used to validate the model. The mean differences shown in Table 4.4 are calculated by subtracting the modelled temperature from the observed temperature. A negative residual indicates that the model overestimates temperature, and vice versa.

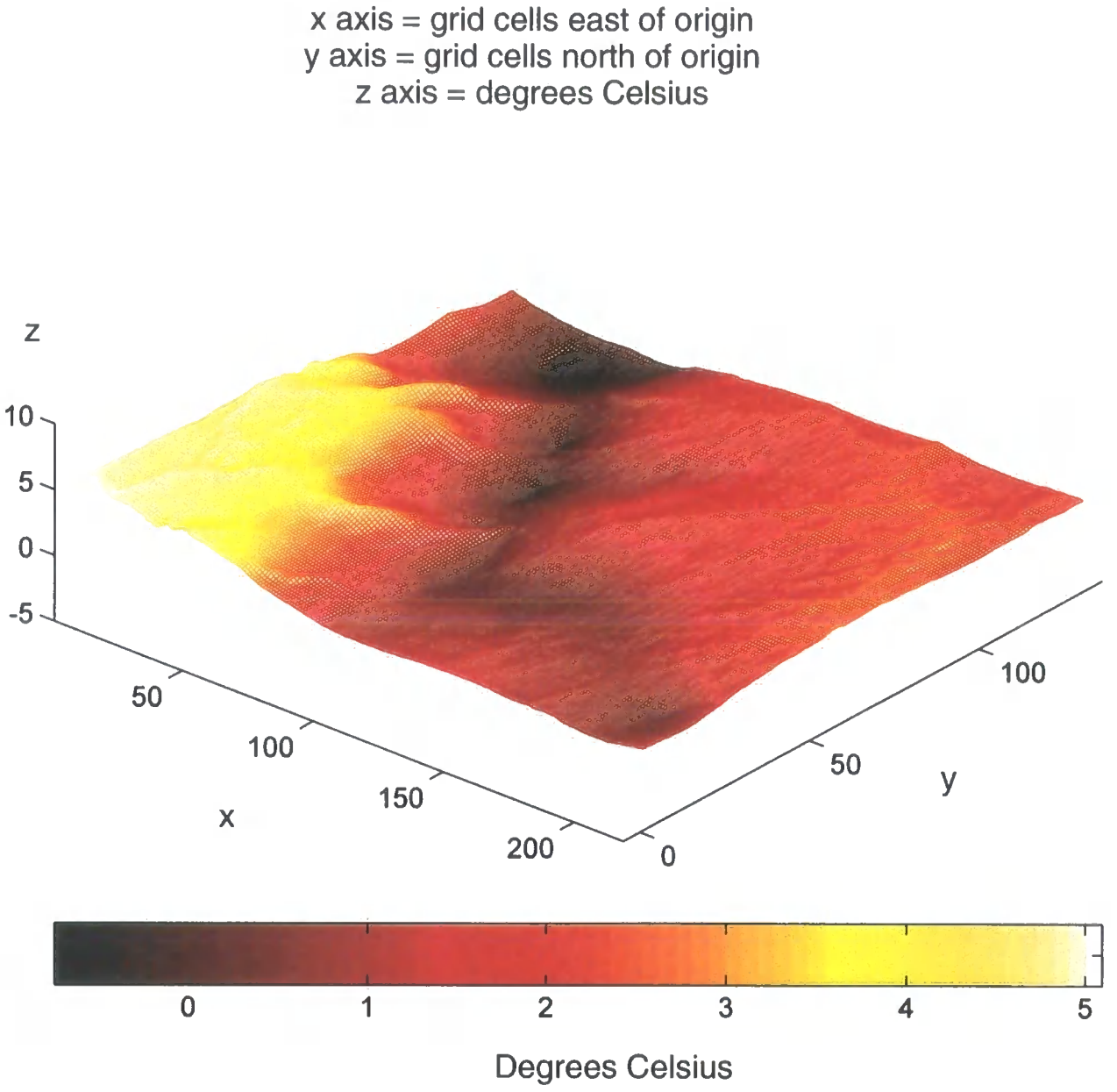

Figure 4.3. Modelled daily mean air temperature
20 November 1998

Table 4.4. Mean residuals from the linear lapse rate model

AWS	Mean temperature mean residual, °C	Maximum temperature mean residual, °C	Minimum temperature mean residual, °C
1	0.0	0.1	-0.1
2	0.2	0.3	-0.1
3	0.0	-0.2	0.1
4	0.0	0.0	0.0
5	-0.1	-0.2	0.1
K	0.0	-0.3	0.1
H	0.2	0.0	0.7
S	0.4	-0.1	1.0

The magnitude and sign of the mean residual for each AWS relates to the systematic performance of the model at estimating temperature at each site. Overestimates of maximum temperatures (negative residuals) may indicate a low Bowen ratio where validation sites are in wet locations, and the process of evaporation uses energy which would otherwise cause increased daytime temperature.

Table 4.5. Root mean square residuals from the linear lapse rate model

AWS	Mean temperature RMSE, °C	Maximum temperature RMSE, °C	Minimum temperature RMSE, °C
1	0.1	0.3	0.5
2	0.2	0.5	0.4
3	0.3	0.2	0.3
4	0.2	0.4	0.5
5	0.2	0.4	0.4
K	0.2	0.5	0.3
H	0.7	0.5	1.5
S	0.9	0.8	2.1

The root mean square residuals relate to the variability around the mean value, and indicate that the model predicts mean temperature best and minimum and maximum temperature less well at most sites. The validation statistics for High Carle Band and Sink Beck show that the model appears to underestimate mean and minimum temperatures west of the Pennine crest. One possible explanation is that these validation sites are the most distant from the base stations used to calibrate the model, the stations in the Trout Beck being located between Moor House and Great Dun Fell. Another possible explanation is that the performance of the linear lapse rate model weakens when used to extrapolate outside the

elevation range over which it was calibrated (Sink Beck is the lowest station on the reserve at 465 m). Another hypothesis is that the residuals from the model are systematic, and the magnitude of the residuals can be explained as a function of local topography at each validation site.

The residuals from the lapse rate model will be analysed in relation to topographic variables, in order to test for systematic behaviour (Chapter 5). The simple linear model outlined above may thus be improved by incorporating spatial patterns of temperature anomalies related to landscape-scale processes, identified using results from a range of experimental AWS transects.

4.7. Soil temperature

The dependence of soil temperatures on elevation can be described using lapse rates (Barry, 1992), as for air temperature. Although physical characteristics such as texture, heat capacity, moisture content and vegetation height can affect soil temperature (Green, Harding and Oliver, 1984), these influences are not as important as atmospheric controls (Gloyne, 1971). Previous work has identified a large seasonal range in the lapse rate of soil temperature; in the northern Pennines this range can exceed 10^{-2} °C m^{-1} (Green and Harding, 1979).

In order to test whether the lapse rate of soil temperature could be identified empirically within the study site, and if so, whether the lapse rate can be used to model spatial variations in soil temperature, the two Squirrel temperature loggers were installed at Grid References NY 372650 531928 (650 m) and NY 371642 531751 (750 m) on the Trout Beck on 14 December 1999. Sensors attached to each logger were exposed at 30 cm and 10 cm depth within the soil in the same configuration as used at the base stations at Moor House and Great Dun Fell. The loggers were left to record hourly temperature data until 18 January 2000. Daily mean temperature data only were used; daily maxima and minima were not calculated due to the reduced diurnal temperature range within the soil. Soil temperature data from Moor House and Great Dun Fell were used to model the linear lapse rate of soil temperature at both soil depths for each day using Equation 4.19.

The lapse rates calculated using the data from the two base stations are shallow. The data measured at 10 cm depth give a mean lapse rate of -1.5×10^{-4} °C m^{-1}, and the data measured at 30 cm depth give a mean lapse rate of -1.7×10^{-3} °C m^{-1}. These compare to a much steeper lapse rate of -6.2×10^{-3} °C m^{-1} for mean air temperature during the same period, and are consistent with previous findings for soil temperature lapse rate during winter in northern England (Green and Harding, 1979).

Spatial estimates of soil temperature were obtained for both soil depths using Equation 4.23, and data from the Squirrel temperature loggers were expressed as residuals from the lapse rate model. The validation data are presented in Table 4.6.

Table 4.6. Mean and root mean square residuals from the linear lapse rate model for soil temperatures at two elevations and two soil depths

Soil depth (cm)	10		30	
Elevation (m)	650	750	650	750
Mean residual (°C)	0.1	-0.2	0.4	0.2
RMSE residual (°C)	0.4	0.3	0.5	0.3

The lapse rate model tends to underestimate soil temperature, except at the higher site where temperature at 10 cm depth is overestimated by 0.2°C. The relative warmth at 30 cm depth at both validation sites may be due to soil type. The soil has previously been characterised as a cambic stagnohumic gley (Briones *et al.*, 1997) although differences are apparent within the study site; the soil in the Trout Beck valley has peaty clay characteristics with low thermal diffusivity (Green and Harding, 1979) compared to the more loamy soil at Moor House and the thinner gleyic brown earth soil at Great Dun Fell summit (Fitter *et al.*, 1999). In addition, the peat at the 650 m site is particularly wet and the large model residual at 30 cm depth may be due to the increased specific heat capacity and thermal inertia associated with waterlogged soil.

The study site was also affected by sporadic snow cover during the data gathering, although the spatial and temporal occurrence is not known. The high emissivity and albedo of snow, as well as its insulating effect which hinders energy fluxes between the soil and atmosphere, may all cause anomalous soil temperatures under snow cover.

The performance of the model would be weakened if observed soil temperatures were to fall below zero, because the freezing of soil water releases latent heat and slows any subsequent fall in temperature. This process did not affect the measured data however, as temperatures remained above freezing at both soil depths at all four sites for the duration. The upper soil horizon may freeze on exposure to very cold air, but the empirical data from the study site support previous findings that soil temperature at measurement depths rarely falls below 0°C (Green and Harding, 1979), although it may frequently fall to within one or two degrees Celsius.

Previous work has found that soil temperature falls particularly rapidly with elevation in summer. Lapse rates can become steeper than -1.2×10^{-2} °C m^{-1} in the northern Pennines during summer (Green and Harding, 1979) due to relatively stronger evaporative cooling of moist upland soils (Oliver, 1962). If the base stations used to calculate lapse rates sample this environmental gradient, the linear model of soil temperature will be more applicable during summer and elevation can be used as a powerful predictor of growing season soil temperature. However, the empirical data suggest that lapse rates do not reach these extremes within the study site. The monthly mean lapse rate of 10 cm soil temperature was -6.8×10^{-3} °C m^{-1} during both June and July 1998, and -6.1×10^{-3} °C m^{-1} during August 1998, calculated using data from Moor House and Great Dun Fell. These lapse rates are no steeper than lapse rates of mean air temperature. The explanation may be that while most previous analyses of soil temperature lapse rates in Britain have used data from a lowland base station and an upland base station, with the upland station rarely located above 400 m (Green and Harding, 1979), the measurements in the current study were all made at or above 550 m. Comparison of the steep lapse rates described previously and the shallower lapse rates measured within the Moor House reserve suggests that the strongest elevation dependence of soil temperature occurs in relatively lowland regions, whereas at exposed upland sites the relationship is less profound, although still systematic.

The linear lapse rate model provides a useful approximation of soil temperatures within the reserve. The residuals from the soil temperature model are of the same order of magnitude as for the mean air temperature model. Figure 4.4 shows the modelled surface for mean

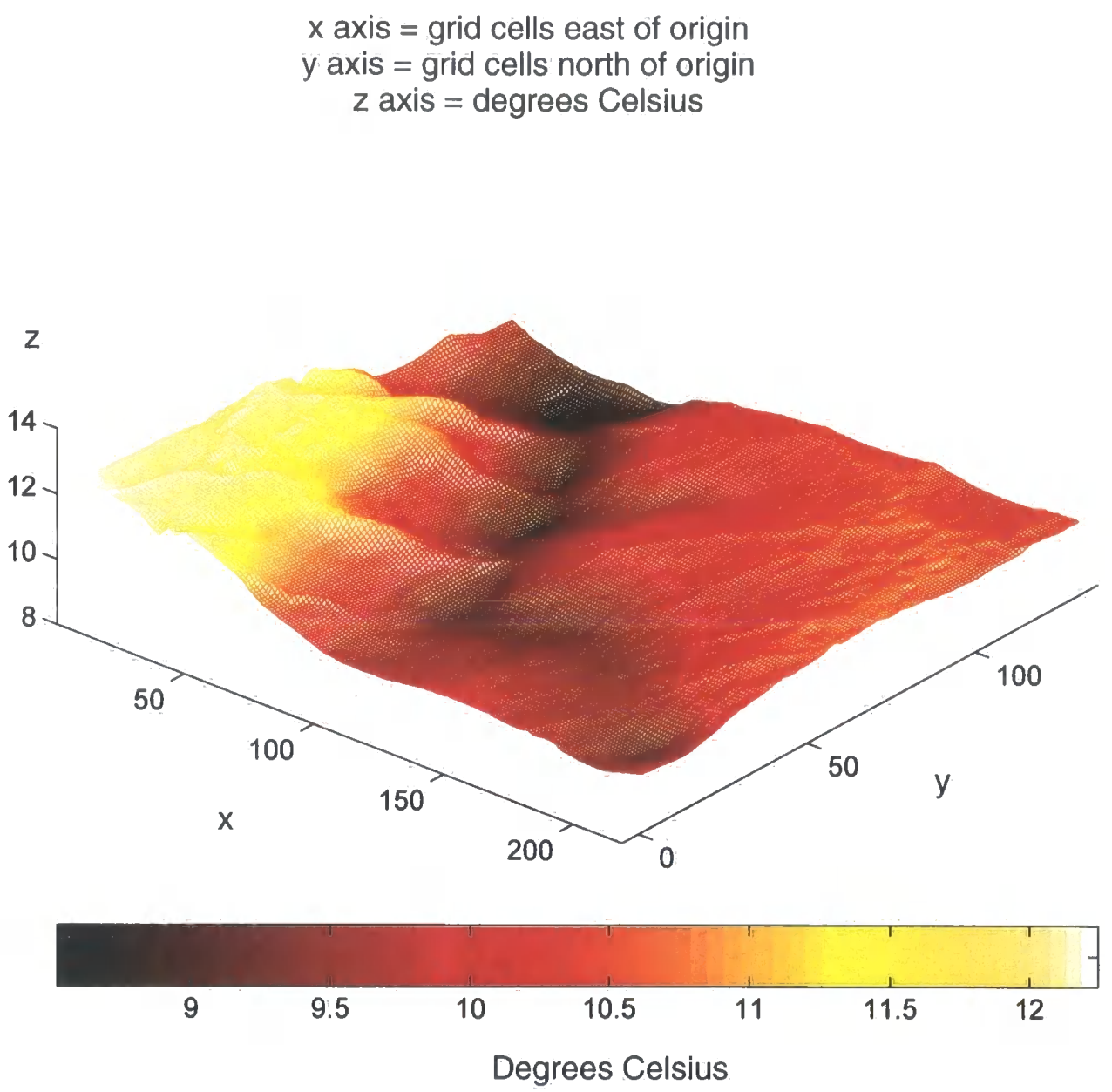

Figure 4.4. Modelled daily mean soil temperature (10 cm depth) 1 June 1998

soil temperature at 10 cm depth on 1 June 1998. The mean value was 8.8 °C at Great Dun Fell and 10.4 °C at Moor House, giving a lapse rate of -5.4×10^{-3} °C m^{-1}, resulting in a range of modelled values of soil temperature from 8.5°C at Cross Fell to 11.9°C at the base of the Pennine scarp slope.

4.8. Modelling lapse rates using data from a single AWS

The work described in section 4.6 concentrates on using two base stations to measure explicitly daily temperature lapse rates. Previous work suggests that lapse rates can be modelled using data from an individual station (Pepin *et al.*, 1999), which might allow estimation of temperature surfaces using a single AWS. The analyses described below assess whether two base stations are necessary, or whether lapse rates can be estimated from data measured at a single AWS.

For the period from 24 September 1997 to 23 September 1998, daily lapse rates of mean temperature (lr_{tmp}, °C m^{-1}), maximum temperature (lr_{tmx}, °C m^{-1}) and minimum temperature (lr_{tmn}, °C m^{-1}) were calculated using data from Moor House and Great Dun Fell summit using Equation 4.19. The lapse rate was used as the dependent variable in regression models using AWS observations from the Moor House station. Daily mean, maximum and minimum temperature (*tmp*, *tmx* and *tmn*, °C) were calculated from the Moor House data, as were daily mean solar radiation (*solar*, W m^{-2}), net radiation (Q_n, W m^{-2}), wet-bulb air temperature (*wet*, °C), and wind speed (*wind*, m s^{-1}). Diurnal temperature range (*dra*, °C, defined as *tmx* - *tmn*) was also calculated as well as the difference between daily mean and daily minimum temperature (*diff*, °C). Saturation vapour pressure (e_s, hPa) was modelled as a function of mean temperature using Equation 4.24 (Murray, 1967).

$$e_s = 6.108 \times \exp\left(\frac{17.27(tmp)}{tmp + 237.3}\right) \qquad 4.24$$

Daily mean vapour pressure (*vap*, hPa) was calculated from the wet-bulb depression (*tmp* - *wet*) using Equation 4.25. In the absence of atmospheric pressure data, the factor

0.8 hPa $^{o}C^{-1}$ can be used for unventilated thermometers at the elevations sampled within the study site (Linacre, 1992).

$$vap = e_s - 0.8(tmp - wet) \qquad 4.25$$

The ratio of *vap* to e_s was also calculated to give relative humidity (*rh*, %). Using data for the complete year, the individual predictor variables were tested separately in univariate regression models to identify which exerts the strongest control on the lapse rate. The most successful models for mean, maximum and minimum temperature lapse rates are given in Equations 4.26 to 4.28. Numerically small lapse rate values correspond to steep lapse rates where temperature falls rapidly with an increase in elevation, whereas numerically large lapse rate values correspond to shallow lapse rates (a positive lapse rate value indicates a temperature inversion).

$$lr_{tmp} = 4.09 \times 10^{-4}(dra) - 0.01 \qquad 4.26$$
$$(R^2 = 0.20,\ n = 348,\ t(dra) = 9.4,\ P < 0.01)$$

Lapse rates of mean temperature are steepest on days with a small diurnal temperature range. Such conditions coincide with periods of well mixed cloudy atmosphere and mobile air flow. At these times maximum temperature remains low due to small insolation inputs, while minima remain high due to reduced radiation losses.

$$lr_{tmx} = -2.17 \times 10^{-5}(solar) - 0.01 \qquad 4.27$$
$$(R^2 = 0.25,\ n = 348,\ t(solar) = -10.9,\ P < 0.01)$$

Steep maximum temperature lapse rates coincide with high insolation, indicating that the mechanism for the development of the steep lapse rates is solar heating affecting lower elevations more than higher elevations. This is due to the greater moisture availability at higher elevations, which allows a larger proportion of the surface energy budget to be converted to latent heat as the moisture is evaporated. At lower elevations, the relatively

dry surface causes a larger proportion of available energy to be converted to sensible heat, raising the daytime temperature.

$$lr_{tmn} = 3.07 \times 10^{-3}(diff) - 0.01 \qquad 4.28$$
$$(R^2 = 0.70, n = 348, t(diff) = 28.2, P < 0.01)$$

The positive gradient of the *diff* variable in the regression on minimum temperature lapse rate indicates that large lapse rates (e.g. inversions) tend to occur when minimum temperature falls substantially below mean temperature. The significance of the *diff* variable (a function of mean temperature), as opposed to the *dra* variable (a function of maximum temperature) in explaining variance in minimum temperature lapse rates demonstrates that development of shallow lapse rates is primarily a nocturnal process, driven either by radiation loss from the surface or subsidence of cold air from higher levels. The R^2 value shows that the predictive power of the regression model is substantially better for lapse rates of minimum temperature than for mean or maximum temperature.

In order to test for seasonal variation in the influence of the predictor variables on lapse rates, data were analysed from a summer sub period between April 1 and September 30. The best individual predictor variable in each case was re-calculated and the results are presented in Equations 4.29 to 4.31.

$$lr_{tmp} = 4.96 \times 10^{-4}(dra) - 0.01 \qquad 4.29$$
$$(R^2 = 0.27, n = 183, t(dra) = 8.3, P < 0.01)$$

$$lr_{tmx} = -1.97 \times 10^{-5}(solar) - 0.01 \qquad 4.30$$
$$(R^2 = 0.18, n = 183, t(solar) = -6.2, P < 0.01)$$

$$lr_{tmn} = 3.32 \times 10^{-3}(diff) - 0.01 \qquad 4.31$$
$$(R^2 = 0.75, n = 183, t(diff) = 23.1, P < 0.01)$$

For lapse rates of mean, maximum and minimum temperature, the single variable identified as most significant is the same for the summer period as for the full year's data. The sign

and magnitude of the regression coefficients show that the relative effects of the explanatory variables are also consistent. Prediction of lapse rates is better during summer for minimum and mean temperature, with a stronger dependence of the lapse rate on the temperature variable (*diff* and *dra* respectively) than during the complete year.

Data were analysed from a winter sub period between October 1 and March 31. The best individual predictor variable in each case was re-calculated and the results are presented in Equations 4.32 to 4.34.

$$lr_{tmp} = -4.74 \times 10^{-4}(wind) - 0.0 \qquad 4.32$$
$$(R^2 = 0.23, n = 165, t(wind) = -7.0, P < 0.01)$$

$$lr_{tmx} = -5.68 \times 10^{-5}(Q_n) - 0.01 \qquad 4.33$$
$$(R^2 = 0.16, n = 165, t(Q_n) = -5.5, P < 0.01)$$

$$lr_{tmn} = 2.69 \times 10^{-3}(diff) - 0.01 \qquad 4.34$$
$$(R^2 = 0.55, n = 165, t(diff) = 14.1, P < 0.01)$$

During winter, net radiation performs slightly better than solar radiation as a predictor variable for maximum temperature lapse rate (t = -5.5 and t = -5.3 respectively), indicating that when solar radiation is weak the daily balance of energy fluxes to and from the ground surface is more important than insolation alone. Wind speed is the primary predictor variable influencing mean temperature lapse rates during winter, with high wind speed corresponding to steep lapse rates and indicating a mixed mobile airflow, corroborating the inferences drawn from Equation 4.28.

Stepwise selection was used to identify optimum combinations of variables explaining variance in the lapse rate data. The threshold significance level for removal of variables from the model is P = 0.002, and the threshold for addition of variables is P = 0.001. The *diff* and *dra* variables were automatically removed from all models due to multicollinearity. The results for mean, maximum and minimum temperature using the full data set are shown in Tables 4.7 to 4.9.

Table 4.7. Variables selected by stepwise regression model explaining variance in lapse rate of daily mean temperature ($R^2 = 0.45$)

Variable	Coefficient	t - statistic
solar radiation	-1.70×10^{-5}	-8.005
minimum temperature	-6.39×10^{-4}	-6.756
maximum temperature	8.00×10^{-4}	6.077
vapour pressure	1.15×10^{-3}	5.568
wind speed	-2.61×10^{-4}	-4.509
mean temperature	-8.76×10^{-4}	-3.818
constant	-1.43×10^{-2}	-11.524

Steep mean temperature lapse rates appear to correspond to a relatively greater solar heating effect at lower elevations, as well as high minimum and low maximum temperatures (implying a small diurnal range as identified by the univariate model in Equations 4.26 and 4.29).

Table 4.8. Variables selected by stepwise regression model explaining variance in lapse rate of daily maximum temperature ($R^2 = 0.30$)

Variable	Coefficient	t - statistic
solar radiation	-2.18×10^{-5}	-7.345
relative humidity	1.91×10^{-4}	3.994
minimum temperature	-4.31×10^{-4}	-3.836
mean temperature	4.51×10^{-4}	3.695
constant	-2.59×10^{-2}	-5.510

Steep lapse rates of maximum temperature appear to correspond to strong insolation and low relative humidity. This result corroborates the hypothesis that steep lapse rates of maximum temperature occur due to greater availability of surface moisture at high elevation sites. When humidity is low, evaporation will be more intense, increasing the discrepancy in Bowen ratio between high and low elevations and thus steepening the lapse rate.

Table 4.9. Variables selected by stepwise regression model explaining variance in lapse rate of daily minimum temperature ($R^2 = 0.75$)

Variable	Coefficient	t - statistic
minimum temperature	-3.16×10^{-3}	-23.857
mean temperature	3.11×10^{-3}	21.594
wind speed	-6.49×10^{-4}	-6.954
solar radiation	-1.34×10^{-5}	-4.322
constant	-7.76×10^{-3}	-12.020

The regression model shows that mean and minimum temperature are the two most significant variables affecting minimum temperature lapse rates. The sign of the coefficients shows that inversions correspond to days with high mean and low minimum temperatures (corroborating the effect of the *diff* variable identified in the univariate models in Equations 4.28, 4.31 and 4.34). Low wind speeds also correspond to shallow lapse rates.

The stepwise selection procedure was repeated for the summer period previously described, the results are presented in Tables 4.10 to 4.12.

Table 4.10. Variables selected by stepwise regression model explaining variance in lapse rate of daily mean temperature for the summer sub-period ($R^2 = 0.50$)

Variable	Coefficient	t - statistic
maximum temperature	1.01×10^{-3}	13.265
minimum temperature	-9.01×10^{-4}	-12.203
solar radiation	-1.83×10^{-5}	-5.204
relative humidity	2.07×10^{-4}	3.749
constant	-3.07×10^{-2}	-5.518

The explained variance is slightly higher for the summer sub-period. The three most important variables in the full year model also appear as the best predictors for the summer sample, although in different rank order.

Table 4.11. Variables selected by stepwise regression model explaining variance in lapse rate of daily maximum temperature for the summer sub-period (R^2 = 0.18)

Variable	Coefficient	t - statistic
solar radiation	-1.97×10^{-5}	-6.204
constant	-6.84×10^{-3}	-14.032

Solar radiation is the most important predictor of the lapse rate of maximum temperature, as for the full year model, although the explained variance is low during summer.

Table 4.12. Variables selected by stepwise regression model explaining variance in lapse rate of daily minimum temperature for the summer sub-period (R^2 = 0.78)

Variable	Coefficient	t - statistic
minimum temperature	-3.86×10^{-3}	-22.388
mean temperature	3.93×10^{-3}	21.184
solar radiation	-2.38×10^{-5}	-5.121
constant	-1.20×10^{-2}	-15.184

The effects of minimum and mean temperature are consistent during summer, but solar radiation replaces wind speed as the third most important variable. Summer inversions thus tend to develop when insolation is low, maintaining a negative surface energy balance. The predictive power of the model is highest during summer.

The stepwise selection procedure was repeated for the winter period previously described, the results are presented in Table 4.13 to 4.15.

Table 4.13. Variables selected by stepwise regression model explaining variance in lapse rate of daily mean temperature for the winter sub-period (R^2 = 0.52)

Variable	Coefficient	t - statistic
mean temperature	-2.00×10^{-3}	-8.612
wind speed	-3.97×10^{-4}	-6.953
maximum temperature	8.54×10^{-4}	6.679
vapour pressure	1.75×10^{-3}	5.362
solar radiation	-1.38×10^{-5}	-3.445
constant	-1.55×10^{-2}	-8.157

The influence of both mean temperature and wind speed on lapse rates of mean temperature is greater during winter, with larger values of both variable associated with steep lapse rates. The effect of solar radiation is greatly reduced during winter.

Table 4.14. Variables selected by stepwise regression model explaining variance in lapse rate of daily maximum temperature for the winter sub-period (R^2 = 0.24)

Variable	Coefficient	t - statistic
net radiation	-4.67×10^{-5}	-4.418
relative humidity	2.34×10^{-4}	4.326
constant	-2.92×10^{-2}	-5.606

Net radiation becomes more important than solar radiation during winter, as previously identified by Equation 4.33.

Table 4.15. Variables selected by stepwise regression model explaining variance in lapse rate of daily minimum temperature for the winter sub-period (R^2 = 0.70)

Variable	Coefficient	t - statistic
minimum temperature	-2.27×10^{-3}	-13.609
vapour pressure	3.32×10^{-3}	10.449
wind speed	-6.63×10^{-4}	-6.716
relative humidity	-3.15×10^{-4}	-4.794
solar radiation	-4.76×10^{-5}	-3.493
net radiation	7.44×10^{-5}	3.152
constant	7.18×10^{-3}	1.178

Minimum temperature is once again the best explanatory variable for minimum temperature lapse rates, although predictive power is reduced during winter.

Splitting the data into separate sub-periods shows that separate processes can dominate at different times of year. For example, the seasonal analyses suggest that solar radiation is the most important predictor of maximum temperature lapse rate during summer, while net radiation performs better during winter.

The optimum coefficient of determination for any of the models described above is 78%, for the stepwise selection model for minimum temperature lapse rate during summer.

However, this model is only slightly better than Equation 4.31, which uses the *diff* variable alone and achieves an R^2 coefficient of 75%. The univariate model may be preferable due to its simplicity, seasonal stability and the fact that the effect of the explanatory variable can be easily explained in terms of a physical mechanism. In contrast, the physical meaning of a model fitted using stepwise selection can be unclear, and the statistical influence of a given combination of variables may not be repeatable experimentally. Models identified using stepwise methods have a higher risk of capitalising on chance features of the data. Better models and understanding of the data are likely to arise from analysis based *a priori* on theoretical processes.

Minimum temperature is the only one of the three temperature variables for which the daily lapse rate can be estimated with any useful degree of accuracy, and much of the day-to-day variability would be lost if these regression equations were used to model daily lapse rates. The results presented in section 4.8 demonstrate the need for two base stations to measure the daily variation of temperature with elevation, since all subsequent spatial modelling of temperature depends upon the accurate quantification of lapse rate.

4.9. Discussion

Despite energy exchanges between the surface and atmosphere that complicate the relationship between altitude and air temperature, elevation remains a primary control on surface temperature. The results described in this chapter corroborate hypotheses 1a and 1b, that elevation above sea level can be used to predict daily air temperature and soil temperature within the study site. Mean lapse rates can be estimated from the slope parameter of regression equations where temperature (or temperature anomalies) are modelled as a function of elevation. Lapse rates estimated in this way are comparable to theoretical values, and also agree well with previously-published mean values for the northern Pennines (Harding, 1979a) and other sites in northern England (Green and Harding, 1979).

The transect east of Great Dun Fell shows shallower lapse rates of minimum temperature than the western transect. Coefficients of determination are also systematically lower for the eastern transect than for the western transect, which may imply that accumulation of

cold air during the development of katabatic air flow obscures the primary effects of elevation on minimum temperature on shallow eastern slopes within the study site.

A criterion of the project was that analysis should be limited to data measured within the study site, to minimise the data requirements for the developed models. Wind direction at Great Dun Fell summit provides information relating to atmospheric circulation, which is important because lapse rates can be affected by synoptic-scale air mass characteristics (Manley, 1945), and spatial patterns of surface temperature may also vary as air flow in the free atmosphere interacts with topography. The sub-division of data according to wind direction on Great Dun Fell summit shows that the spatial behaviour of mean temperature is markedly different for south easterly wind directions. Summit wind direction is thus a useful variable, as it allows the identification of a sporadic topo-climatic process. There is no evidence to support the initial hypothesis that interaction between the Pennine ridge and prevailing westerly winds causes systematic spatial temperature differences, but systematic differences are apparent for south easterly winds.

Two hypothetical processes were proposed to explain the discrepancy in the lapse rate of mean temperature between windward and leeward slopes on days with south easterly wind direction. The föhn effect was discussed in section 2.7; a second possible mechanism relates to the advection of relatively cold air across the study site from the North Sea or continental Europe on south easterly winds. A cool air mass may gain heat at its base as it travels over a warmer land surface, causing the spatial temperature gradient measured across the study site. This effect would be seasonally dependent, as the relative thermal characteristics of the source regions vary between winter and summer (Joyce, 2000). Investigation of these mechanisms is discussed further in section 6.5.

The attempt to model daily lapse rate using data from a single AWS (section 4.8) shows that two base stations are necessary. Although a reasonable estimate can be obtained for daily lapse rate of minimum temperature using one station, it is essential to optimise the variability of temperature and lapse rate captured in the daily climate surfaces. Data from the two base stations at Moor House and Great Dun Fell summit will be used to calculate daily linear lapse rates, and data from independent stations will be used for validation.

Residuals from the linear lapse rate model will be modelled as a function of topographic variables to improve the spatial models.

Chapter 5. Other topographic controls on temperature

5.1. Slope aspect

The primary mechanism whereby slope aspect can influence surface temperature through variations in direct-beam solar irradiance is discussed in section 2.4. Landscape-scale examples include discrepancies in mean maximum air temperature between north and south aspects in forested catchments in Idaho (Furman, 1978) and the Appalachian mountains (Bolstad *et al.*, 1998). Spatial variation in temperature anomalies was also identified around an isolated summit during a sunny day, responding to changes in solar altitude and azimuth (Fujita, Baralt and Tsuchiya, 1968).

The complex terrain of the Moor House reserve necessitates the quantification of slope-related temperature effects, and the second experimental network was designed to measure data to test for their occurrence. Between 19 May and 11 October 1998, four roving AWS were installed at 800 m elevation, on north, east, south and west-facing slopes on Great Dun Fell. Slope aspect was calculated using the digital terrain model and the *Aspect* function in ARC/INFO as described in section 2.3. Grid cells with the appropriate elevation and aspect attributes were identified by interrogating the DTM and the *aspect* surface. The roving AWS were installed at co-ordinates corresponding to these grid cells; locations were verified in the field using GPS. Data were discarded for the period between 18 and 28 August due to data problems arising from a faulty cable, which was subsequently replaced.

The daily temperature data from Moor House and Great Dun Fell summit were used to calculate lapse rates (Equation 4.19) and the daily lapse rates were then used in conjunction with the temperature observed at Moor House to model mean, maximum and minimum temperature (Equation 4.23). The observed temperature from each roving AWS was compared to the modelled value using the concordance correlation coefficient. The residuals from the lapse rate model were calculated by subtracting the modelled temperature from the observed temperature, and are presented in Tables 5.1 to 5.3.

Table 5.1. The effect of aspect on daily mean temperature

AWS	Aspect	Concordance correlation coefficient	Mean residual (°C)
1	West	0.996	-0.1
2	North	0.998	-0.1
3	East	0.996	-0.1
5	South	0.993	-0.1

Table 5.2. The effect of aspect on daily maximum temperature

AWS	Aspect	Concordance correlation coefficient	Mean residual (°C)
1	West	0.987	0.0
2	North	0.996	-0.2
3	East	0.983	-0.1
5	South	0.982	0.0

Table 5.3. The effect of aspect on daily minimum temperature

AWS	Aspect	Concordance correlation coefficient	Mean residual (°C)
1	West	0.995	0.0
2	North	0.994	-0.1
3	East	0.994	0.0
5	South	0.990	-0.1

For daily mean and minimum temperature, the mean modelled values are all within 0.1°C of the actual values. The residuals in Table 5.2 suggest that the north-facing slope may experience slightly lower maxima than other aspects, which is consistent with the reduced insolation received on a shallow north facing slope at this latitude during summer. Nevertheless the concordance correlation coefficients are high in all cases and the mean residuals are small, showing that the modelled and observed data are in close agreement, and that the theoretical effects of slope aspect on air temperature are not observed.

It is possible that slope aspect does not influence air temperature due to the moist surface conditions prevailing at this upland site. Available surface moisture will lead to a low Bowen ratio, with greater proportion of available energy expended as latent heat. A second explanation relates to the extreme exposure and elevation of the study site. The high mean wind speeds occurring at the locality will also tend to cause efficient mixing of air in the boundary layer. Strong advection will prevent any local differences in surface radiation budget affecting measured temperature, because air in proximity to the ground will be

transported away from a slope before any substantial aspect-related differences in air temperature can develop.

Any systematic temperature effects which may be attributable to slope aspect are minor and inconclusive, and the *aspect* variable will therefore not be included as a predictor variable in the subsequent development of spatial temperature models.

5.2. Topographic shelter

The mechanisms whereby topographic shelter can influence surface climate are described in section 2.5, along with the derivation of the *shelter* variable. The *shelter* values corresponding to the AWS locations were calculated at a range of neighbourhoods from 0.2 to 1.0 km and are shown in Table 5.4.

Table 5.4. Values of *shelter* (m) calculated at nine neighbourhoods, for DTM cells containing AWS during operation of network 1

AWS	200 m	300 m	400 m	500 m	600 m	700 m	800 m	900 m	1 km
M	26.8	29.0	29.8	34.5	39.7	46.3	52.8	57.2	60.5
H	46.7	61.7	79.3	85.1	100.3	118.8	151.2	164.1	171.3
S	41.7	54.1	66.7	83.4	102.3	114.6	127.3	138.8	151.4
K	14.5	20.7	27.9	43.8	61.3	83.6	89.3	95.1	95.1
1	14.8	27.1	36.9	44.9	55.1	63.8	67.6	68.5	70.5
2	21.3	23.3	28.2	32.0	34.8	39.7	50.0	53.5	56.1
4	26.6	36.2	42.3	55.0	67.0	75.9	79.3	85.6	94.3
3	22.0	42.4	56.1	66.0	74.0	94.3	112.4	120.7	124.3
5	29.1	38.8	49.7	67.4	85.9	103.3	111.1	112.9	112.9

The *shelter* variable, calculated at different neighbourhoods, was included in multiple regression models to assess its ability to improve the explanation of temperature variance. Temperature anomalies were regressed on elevation, lapse rate and *shelter*. For mean temperature, the inclusion of a *shelter* variable results in no increase in the R^2 statistic, while for maximum and minimum temperature, the inclusion of *shelter* results in an increase from 0.77 to 0.78 and from 0.60 to 0.62 respectively.

The topographic shelter variable reaches a maximum significance at a neighbourhood of 200 m, with shelter increasing minimum temperature. This effect is consistent with a

reduced rate of net radiation loss from sheltered sites. However, the effect was small and the shelter variable will not be used as a predictor of temperature for daily surfaces.

5.3. Topographic drainage potential

The mechanism of katabatic density flow of cold air down slope and the potential effects on minimum temperatures are described in section 2.6, along with the calculation of the *drain* variable. The values of the variable, calculated at nine geographical neighbourhoods, are presented in Table 5.5 for the AWS locations during the first experimental network.

Table 5.5. Values of *drain* (m) calculated at nine neighbourhoods, for DTM cells containing AWS during operation of network 1

	200 m	300 m	400 m	500 m	600 m	700 m	800 m	900 m	1000 m
G	58.4	78.3	93.7	119.1	154.8	166.9	187.1	201.2	217.7
H	91.5	112.0	126.6	140.9	169.9	182.0	190.6	200.3	206.6
S	41.5	64.9	95.9	120.8	124.6	130.1	141.9	153.8	167.3
K	31.1	60.8	72.2	94.4	132.6	154.8	171.8	206.7	224.2
1	10.0	11.8	12.7	12.7	12.7	12.7	13.8	13.8	13.8
2	13.0	14.0	15.8	17.8	20.5	23.9	25.1	25.3	29.9
3	10.4	18.0	24.2	30.4	36.2	41.9	46.0	51.0	52.6
4	8.2	8.2	9.4	16.4	18.2	18.2	19.3	21.6	28.1
5	29.1	42.3	53.1	62.8	71.1	78.5	85.7	89.4	94.7

Topographic drainage potential is largest at the sites west of the Pennine crest, and smallest at the locations of the roving AWS between Great Dun Fell and Moor House. The variation within the study site of the *drain* variable calculated at a 500 m neighbourhood is illustrated in Figure 2.5. The values of *drain* increase with the size of the geographical neighbourhood, especially on long slopes. Autocorrelation of *drain* calculated at different neighbourhoods is high, as discussed in section 2.8.

The *drain* variable, calculated at different neighbourhoods, was included in multiple regression models to assess its ability to improve the explanation of temperature variance. Temperature anomalies were regressed on elevation, lapse rate and topographic drainage potential. For mean temperature, the results are shown in Table 5.6; the R^2 value prior to the inclusion of a drainage variable is 0.85.

Table 5.6. Improvement in the explained variance of mean temperature achieved by including a topographic drainage potential variable

Neighbourhood (m)	R^2 statistic	t statistic	probability value
200	0.86	5.77	0.0
300	0.86	5.99	0.0
400	0.86	6.21	0.0
500	0.86	6.22	0.0
600	0.86	6.13	0.0
700	0.86	6.07	0.0
800	0.86	6.08	0.0
900	0.86	5.83	0.0
1000	0.86	5.81	0.0

For mean temperature the most significant *drain* variable is at a 500 m neighbourhood, with a *t* statistic of 6.22. The inclusion of this variable in the regression model achieves a slight improvement in R^2 from 0.85 to 0.86.

For maximum temperature, the results are shown in Table 5.7; the R^2 value prior to the inclusion of a *drain* variable is 0.77.

Table 5.7. Improvement in the explained variance of maximum temperature achieved by including a topographic drainage potential variable

Neighbourhood (m)	R^2 statistic	t statistic	probability value
200	0.77	-0.07	0.95
300	0.77	-1.29	0.20
400	0.77	-1.82	0.07
500	0.77	-2.10	0.04
600	0.77	-1.94	0.05
700	0.77	-2.10	0.04
800	0.77	-2.14	0.03
900	0.77	-2.47	0.01
1000	0.77	-2.46	0.01

For maximum temperature the *drain* variable achieves no improvement in the R^2 statistic at any neighbourhood.

For minimum temperature, the results are shown in Table 5.8; the R^2 value prior to the inclusion of a *drain* variable is 0.60.

Table 5.8. Improvement in the explained variance of minimum temperature achieved by including a topographic drainage potential variable

Neighbourhood (m)	R^2 statistic	t statistic	probability value
200	0.63	7.51	0.0
300	0.64	8.35	0.0
400	0.64	8.91	0.0
500	0.64	9.06	0.0
600	0.64	8.71	0.0
700	0.64	8.64	0.0
800	0.64	8.62	0.0
900	0.64	8.43	0.0
1000	0.64	8.37	0.0

The most convincing result of all the tests using the *drain* variable is the effect on minimum temperature of topographic drainage at a 500 m neighbourhood. The *drain* variable calculated at this neighbourhood results in the most significant improvement in R^2, from 0.60 to 0.64. The value of the *t* statistic is optimised at 9.06, also for the 500 m neighbourhood, providing further evidence for a process operating at a specific landscape-scale. The positive sign of the *t* statistic indicates that higher values of *drain* are associated with higher minimum temperatures. The 500 m neighbourhood was used for all subsequent applications using the *drain* variable.

In addition to fitting multiple regression models to assess the effect of topographic drainage potential, the residuals from the daily linear lapse rate model can also be analysed to quantify the influence of *drain* at each validation site. The model residuals were calculated for each site and regressed on *drain*, the results are given in Equation 5.1.

$$residual_{tmn} = 6.79 \times 10^{-3}(drain) - 0.20 \qquad 5.1$$

($R^2 = 0.69$, n = 8, t(*drain*) = 4.1, P = 0.006)

This approach confirms the systematic relationship between topographic drainage potential and minimum temperature. Positive residuals occur where the model underestimates true minimum temperature, and tend to coincide with sites where *drain* is large. Minimum temperature residuals can also be modelled as a function of *drain* using a non-linear

relationship. The Tablecurve 2D software (SPSS) was used to fit the optimum curve to the data, the equation of the line is shown in Equation 5.2.

$$residual_{tmn} = -4.65 \times 10^{-2} + 9.43 \times 10^{-6}(drain)^2 \times \ln(drain) \qquad 5.2$$
$$(R^2 = 0.77,\ n = 8,\ t(drain^2) = 1.8,\ t(\ln drain) = 0.02,\ P = 0.02)$$

The explained variance rises from 0.69 to 0.77 using the non-linear model. This represents an improvement for the range of observed values over which the model was calibrated where *drain* is between zero and 141 m, and the residuals are between -0.2 and 1.0°C. However, the log term in the non-linear model causes unrealistically high estimates of residuals for large values of *drain* outside the calibration range (a site with a *drain* value of 230 m, such as occurs at the top of the Pennine scarp slope, has an estimated residual value of 1.4°C using Equation 5.1, but this rises to 2.7°C using Equation 5.2). For modelling purposes, a linear relationship may thus provide better estimates over a wider data range.

In terms of a physical mechanism, these statistical results corroborate the hypothesis that katabatic density flows of cold air interact with the surface topography. When katabatic air flow occurs, large topographic drainage potential away from a site leads to relatively high minimum temperatures by allowing the removal of cold air. Sites with small values of *drain* cause dense cold air to accumulate, leading to relatively low minimum temperatures.

The above relationships quantify the effects of topographic drainage potential for all days. If, as hypothesised, the causal mechanism is the interaction between topography and katabatic air flow, the effects should only be apparent on days when katabatic flow occurs. Density flow of cold air down hill will disrupt the general pattern of temperature decrease with elevation, therefore the occurrence of a shallow minimum temperature lapse rate may indicate that the effect of topographic drainage is important on that day.

In order to test the hypothesis that the *drain* variable has greater explanatory power on days with shallow minimum temperature lapse rates, the data from the first experimental network were divided into five samples according to the percentiles of the daily minimum temperature lapse rates. Days with the steepest 20% of lapse rates formed the first sample,

with minimum temperature lapse rates steeper than -7.12 × 10^{-3} °C m^{-1}. Days with the next steepest 20% of lapse rates (between -7.12 × 10^{-3} °C m^{-1} and -6.44 × 10^{-3} °C m^{-1}) formed the second sample, while the third, fourth and fifth samples contain days with lapse rates between -6.44 × 10^{-3} °C m^{-1} and -5.42 × 10^{-3} °C m^{-1}, between -5.42 × 10^{-3} °C m^{-1} and -2.03 × 10^{-3} °C m^{-1}, and shallower than -2.03 × 10^{-3} °C m^{-1} respectively. The mean residuals from the linear lapse rate model are shown for each sub-sample in Table 5.9.

Table 5.9. Mean minimum temperature residuals (°C) for five percentiles of lapse rate at the eight independent AWS during the operation of experimental network 1

Percentile	1	2	3	4	5	S	H	K
0-20%	0	0	0	0.1	0	-0.1	0	0
20-40%	-0.1	-0.2	0	0	-0.1	0.2	0.1	-0.1
40-60%	0	0.1	0.1	0.2	0	0.2	0.2	0
60-80%	-0.2	0	0.3	0.1	0.1	0.9	0.5	0
80-100%	-0.4	-0.3	0.3	-0.2	0.7	4.1	2.9	0.5

The results confirm that for days with steep lapse rates, when minimum temperature decreases relatively rapidly with elevation (e.g. the 0-20% sample, representing lapse rates steeper than -7.12 × 10^{-3} °C m^{-1}), the linear lapse rate model performs well, with very small residuals at all validation sites. Conversely, for the shallowest lapse rates (e.g. the 80-100% sample representing lapse rates shallower than -2.03 × 10^{-3} °C m^{-1}, and including inversions of minimum temperature) residuals are larger especially for sites on the scarp slope. The values of the residuals can be modelled in terms of topographic drainage potential, as shown in Equations 5.3 to 5.7. The regressions are presented in percentile-order from the steepest lapse rates (Equation 5.3) to the shallowest lapse rates (Equation 5.7).

$$residual_{tmn} = -5.7 \times 10^{-4}(drain) + 0.04 \qquad 5.3$$
$$(R^2 = 0.30, n = 8, t(drain) = -1.6, P = 0.16)$$

$$residual_{tmn} = 1.7 \times 10^{-3}(drain) - 0.13 \qquad 5.4$$
$$(R^2 = 0.43, n = 8, t(drain) = 2.1, P = 0.08)$$

$$residual_{tmn} = 6.0 \times 10^{-4}(drain) + 0.06 \qquad 5.5$$
$$(R^2 = 0.10, n = 8, t(drain) = 0.8, P = 0.43)$$

$$residual_{tmn} = 4.8 \times 10^{-3}(drain) - 0.09 \quad 5.6$$
$$(R^2 = 0.50, n = 8, t(drain) = 2.5, P = 0.05)$$

$$residual_{tmn} = 2.85 \times 10^{-2}(drain) - 0.82 \quad 5.7$$
$$(R^2 = 0.77, n = 8, t(drain) = 4.5, P = 0.004)$$

The relationships presented in Equations 5.3 to 5.7 show that the *drain* variable has a greater effect for shallower lapse rates, with the strongest relationship ($R^2 = 0.77$) for the sub-sample of shallowest lapse rates. The effect of *drain* is statistically significant for this sub-sample ($t = 4.5$, $P < 0.01$), indicating that when the lapse rate of minimum temperature is shallower than -2.03×10^{-3} °C m^{-1}, topography exerts a systematic and quantifiable effect on minimum temperature. These results suggest that Equation 5.7 could be used to model minimum temperature residuals. These modelled residuals could be used as correction values on days with a shallow lapse rate, by adding the residuals to the minimum temperature surface generated using the linear lapse rate model.

The third experimental network (Figure 3.8) was designed to measure data to test the model further. The network includes four AWS installed in a 1 km transect between Hard Hill (670 m) and the Trout Beck valley (600 m). These stations are thus not only in close geographical proximity, but also cover a relatively small range of elevation. Within the transect, *drain* values range from 16.4 m to 56.4 m, the sampling of data from this network will thus provide a rigorous test of the ability of the *drain* variable to explain variance in the residuals from the linear lapse rate model.

Data from the base stations at Great Dun Fell and Moor House were used to model the daily lapse rate of minimum temperature, and the data from the other stations were calculated as residuals from the temperature predicted by the lapse rate at each relevant elevation. The residuals are presented in Table 5.10.

Table 5.10. Mean residuals of minimum temperature from network 3

AWS	Mean minimum temperature residual (°C)
1	0.1
2	0.1
3	0.0
4	0.2
S	0.5

The mean residuals from the linear lapse rate model are substantially larger for the Sink Beck validation station to the west of the study site where topographic drainage potential is large. The data were used to test whether Equation 5.7, calibrated for network 1, can explain minimum temperature residuals for shallow lapse rate conditions for an independent sample. Equation 5.7 was used to estimate the residuals from the linear lapse rate model. The actual and predicted residuals are shown in Table 5.11.

Table 5.11. Predicting the behaviour of mean daily minimum temperature residuals using the *drain* variable, for the shallowest 20% of lapse rates

AWS	Actual minimum temperature residual, °C	Predicted minimum temperature residual, °C
S	2.5	2.6
1	0.4	0.2
2	0.6	0.8
3	0.6	0.7
4	0.2	-0.3

Table 5.11 shows that the observed minimum temperature residuals are much larger at the Sink Beck station. The *drain* variable correctly estimates the relative magnitude of the residuals at this site with large topographic drainage potential; the correlation between the actual and predicted residuals is 0.97 ($P < 0.01$). The validation uses independent data measured between November and March, as opposed to the Network 1 which was in operation from February to May. The validation sites are likely locations for topographically-influenced temperature inversions to occur, and the stations were located in close proximity to provide a rigorous test of the *drain* variable. The results suggest that *drain* is a meaningful predictor of minimum temperature residuals. For the third experimental network, the relationship between residuals and *drain* is shown in Equation 5.8.

$$residual_{tmn} = 9.90 \times 10^{-3}(drain) - 0.18 \qquad 5.8$$
$$(R^2 = 0.89, n = 5, t(drain) = 6.1, P = 0.009)$$

Data from the fourth experimental network can be used to test the previously identified relationship between *drain* and the magnitude of minimum temperature residuals on days with shallow minimum temperature lapse rates. The relationship between the variables is given in Equation 5.9.

$$residual_{tmn} = 3.21 \times 10^{-2}(drain) - 0.63 \qquad 5.9$$
$$(R^2 = 0.74, n = 5, t(drain) = 2.9, P = 0.061)$$

The relationship for the data from the final experimental network is shown in Equation 5.10.

$$residual_{tmn} = 3.50 \times 10^{-2}(drain) - 0.83 \qquad 5.10$$
$$(R^2 = 0.88, n = 5, t(drain) = 4.9, P = 0.04)$$

These relationships corroborate the hypothesis that topographic drainage potential can be used to quantify the magnitude of minimum temperature anomalies. The effect of topographic drainage potential has been tested using data from experimental networks sampling a range of locations and time periods. Aggregation of data from all the experimental networks gives the relationship shown in Equation 5.11 and illustrated in Figure 5.1.

$$residual_{tmn} = 2.90 \times 10^{-2}(drain) - 0.74 \qquad 5.11$$
$$(R^2 = 0.71, n = 22, t(drain) = 7.0, P < 0.01)$$

The results suggest that effects of topographic drainage potential are predictable and can be modelled using the empirical relationship. The modelled residuals can be added to the linear lapse rate model estimated from the two base stations. As an illustration, the modelled minimum temperature surface for 3 February 1998 is shown in Figure 5.2.

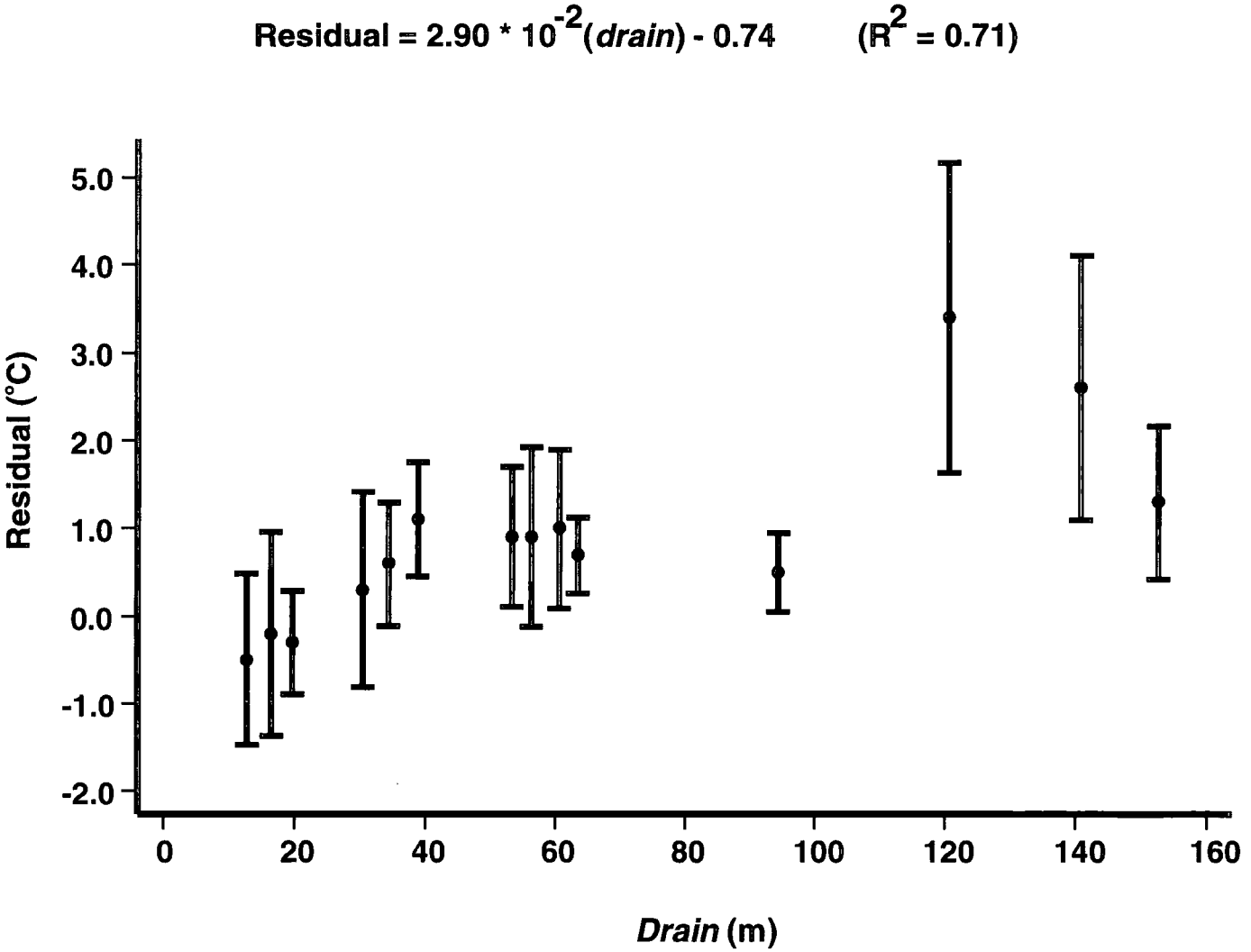

Figure 5.1. Plot of daily minimum temperature residuals from the linear lapse rate model against topographic drainage potential, for minimum temperature lapse rates shallower than $-2.03 * 10^{-3}$ °C m^{-1}. Data are from all experimental networks, one standard deviation is shown.

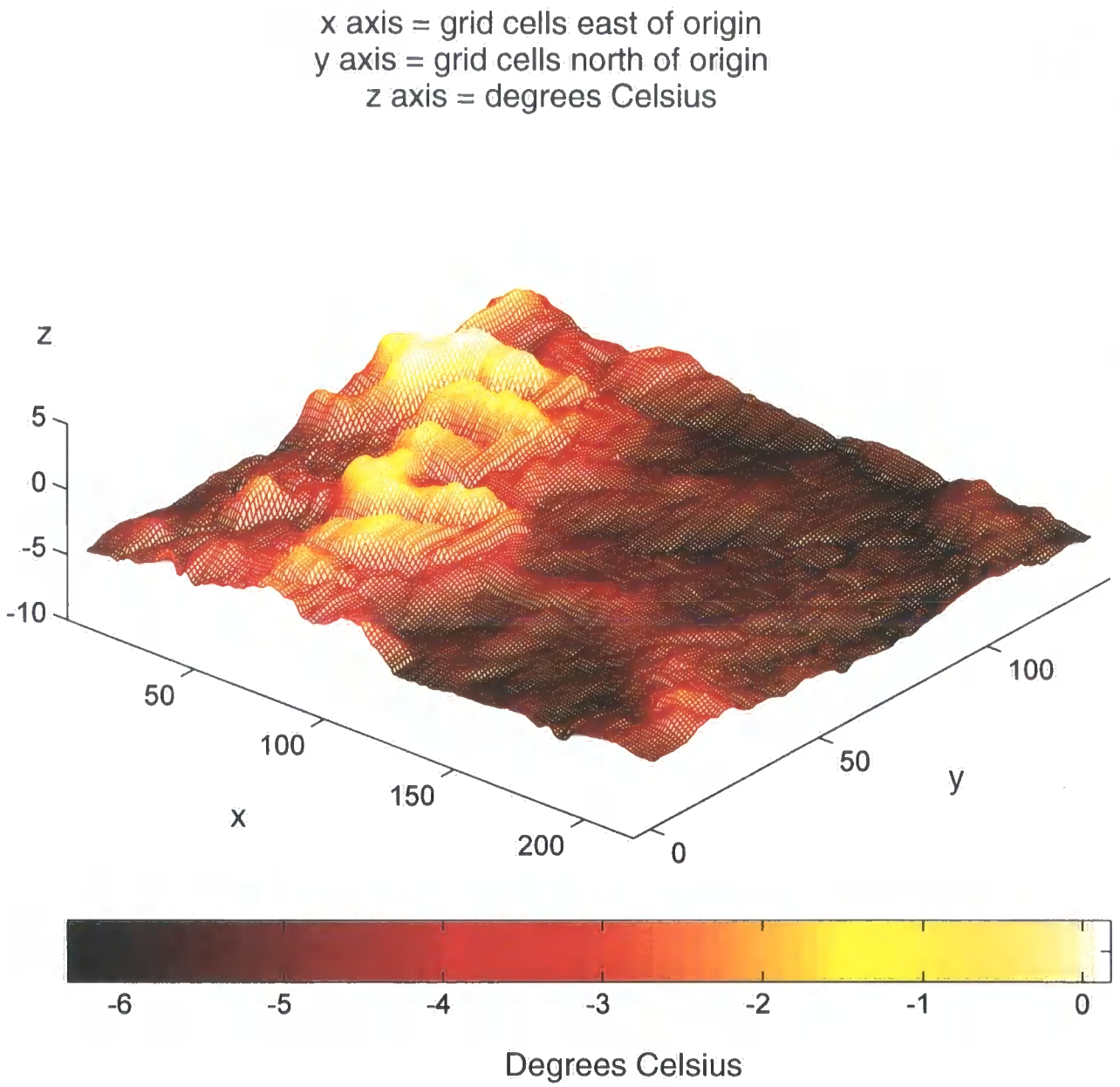

Figure 5.2. Modelled daily minimum air temperature
3 February 1998

Minimum temperature was -5.5°C at Moor House and -5.9°C at Great Dun Fell. The highest modelled temperature occurs where topographic drainage potential is large, with values of 0.0°C at the top of the scarp slope. Modelled temperature falls to -6.0°C on the eastern slopes where cold air is trapped. This pattern is superimposed on the underlying elevation relationship, which is weak on this particular day because the lapse rate is close to zero (-1.36×10^{-3} °C m^{-1}).

5.4. Distance relative to the Pennine ridge

Discrepancies were identified in the lapse rate of daily mean temperature between transects east and west of the Pennine ridge on days with south easterly wind direction. The *dist* variable was created to describe geographical location on an axis perpendicular to the Pennine ridge (Chapter 2). Within the study site, the location of any grid cell can be quantified relative to the ridge, and this variable can be used to model the spatial variability of mean temperature residuals.

Residuals from the linear lapse rate model for mean temperature were subdivided into four samples according to the summit wind direction, and residuals were regressed on the transformed *dist* variable. The resulting relationships are shown in Equation 5.12 (south westerly quadrant), Equation 5.13 (north westerly quadrant), 5.14 (north easterly quadrant) and Equation 5.15 (south easterly quadrant).

$$residual_{tmp} = 210883.2(dist)^{-2} + 0.0 \qquad 5.12$$
$$(R^2 = 0.10, n = 8, t(dist^{-2}) = 0.8, P = 0.439)$$

$$residual_{tmp} = 752663.8(dist)^{-2} + 0.08 \qquad 5.13$$
$$(R^2 = 0.34, n = 8, t(dist^{-2}) = 1.8, P = 0.13)$$

$$residual_{tmp} = 1147093.0(dist)^{-2} - 0.03 \qquad 5.14$$
$$(R^2 = 0.65, n = 8, t(dist^{-2}) = 3.4, P = 0.015)$$

$$residual_{tmp} = 3063631.0(dist)^{-2} + 0.01 \qquad 5.15$$
$$(R^2 = 0.84, n = 8, t(dist^{-2}) = 5.6, P = 0.001)$$

Equation 5.15 shows that on days with a south easterly wind direction, 84% of the remaining variance in mean temperature not explained by the linear lapse rate model can be accounted for by geographical location relative to the Pennine crest. An inverse-square relationship can be used to model the spatial decay of the effect, and the transformation improves the statistical significance of the *dist* variable ($|t|$ = 5.6 compared to $|t|$ = 2.5). However, the non-linear relationship results in unrealistically large modelled residuals in the south western corner of the study site, where values of *dist* are small. For this reason, the un-transformed *dist* variable is likely to be a better predictor of temperature residuals; the relationship with the temperature residuals is shown in Equation 5.16.

$$residual_{tmp} = -1.53 \times 10^{-4}(dist) + 1.09 \qquad 5.16$$

(R^2 = 0.51, n = 8, t(*dist*) = -2.5, P = 0.047)

The ability of the transformed and un-transformed *dist* variable to estimate temperature residuals can be tested using independent data. Equations 5.15 and 5.16 were used to simulate the magnitude of the residual for each site used for the third experimental network. The observed mean residuals and the predicted residuals are shown in Table 5.12.

Table 5.12. Predicting the behaviour of mean temperature residuals using position relative to the Pennine crest, for days with SE wind direction

AWS	Actual mean residual (°C)	Predicted residual, Equation 5.15 (°C)	Predicted residual, Equation 5.16 (°C)
S	0.5	1.5	0.4
1	0.1	0.1	0.0
2	0.1	0.1	0.0
3	0.0	0.1	0.0
4	0.1	0.1	0.0

Using this set of independent data, Equation 5.15 over-estimates the temperature anomalies for the Sink Beck site to the west of the study site. Equation 5.16 successfully models the warm anomaly at Sink Beck, the anomalies are estimated correctly to within 0.1°C at each validation site. Using the data from the third experimental network, the regression of mean

temperature residuals on distance for south easterly wind directions is shown in Equation 5.17.

$$residual_{tmp} = -9.46 \times 10^{-5}(dist) + 0.63 \qquad 5.17$$
$$(R^2 = 0.93, n = 5, t(dist) = -7.6, P = 0.005)$$

Equation 5.17 confirms that the effects of distance are systematic, although the explained variance is artificially high because the four AWS located on Hard Hill during this network all have very similar *dist* values. The data gathered during the operation of the fourth experimental network cannot be used to test the effects of the *dist* variable, due to the absence of AWS data from the summit site. For the final experimental network, the relationship is shown in Equation 5.18.

$$residual_{tmp} = -1.0 \times 10^{-4}(dist) + 0.56 \qquad 5.18$$
$$(R^2 = 0.87, n = 5, t(dist) = -5.4, P = 0.012)$$

Aggregation of data from all the experimental networks gives the relationship shown in Equation 5.19 and illustrated in Figure 5.3.

$$residual_{tmp} = -1.23 \times 10^{-4}(dist) + 0.82 \qquad 5.19$$
$$(R^2 = 0.51, n = 18, t(dist) = -4.1, P = 0.001)$$

The *dist* variable quantifies location relative to the Pennine ridge, and the residuals of mean temperature from the linear lapse rate model can be estimated as a function of this variable on days with south easterly wind direction. As an illustration, the modelled mean temperature surface for 19 November 1998 is shown in Figure 5.4. Mean wind direction at Great Dun Fell summit was 144°, within the south easterly quadrant, signalling the need to model the pattern of temperature with distance from the Pennine ridge. Mean temperature was 0.6°C at Moor House and -1.2°C at Great Dun Fell summit, giving a lapse rate of -6.1×10^{-3} °C m^{-1}. The modelled residuals are superimposed on the underlying elevation relationship, the final modelled temperature surface ranges from 3.2°C at the foot of the

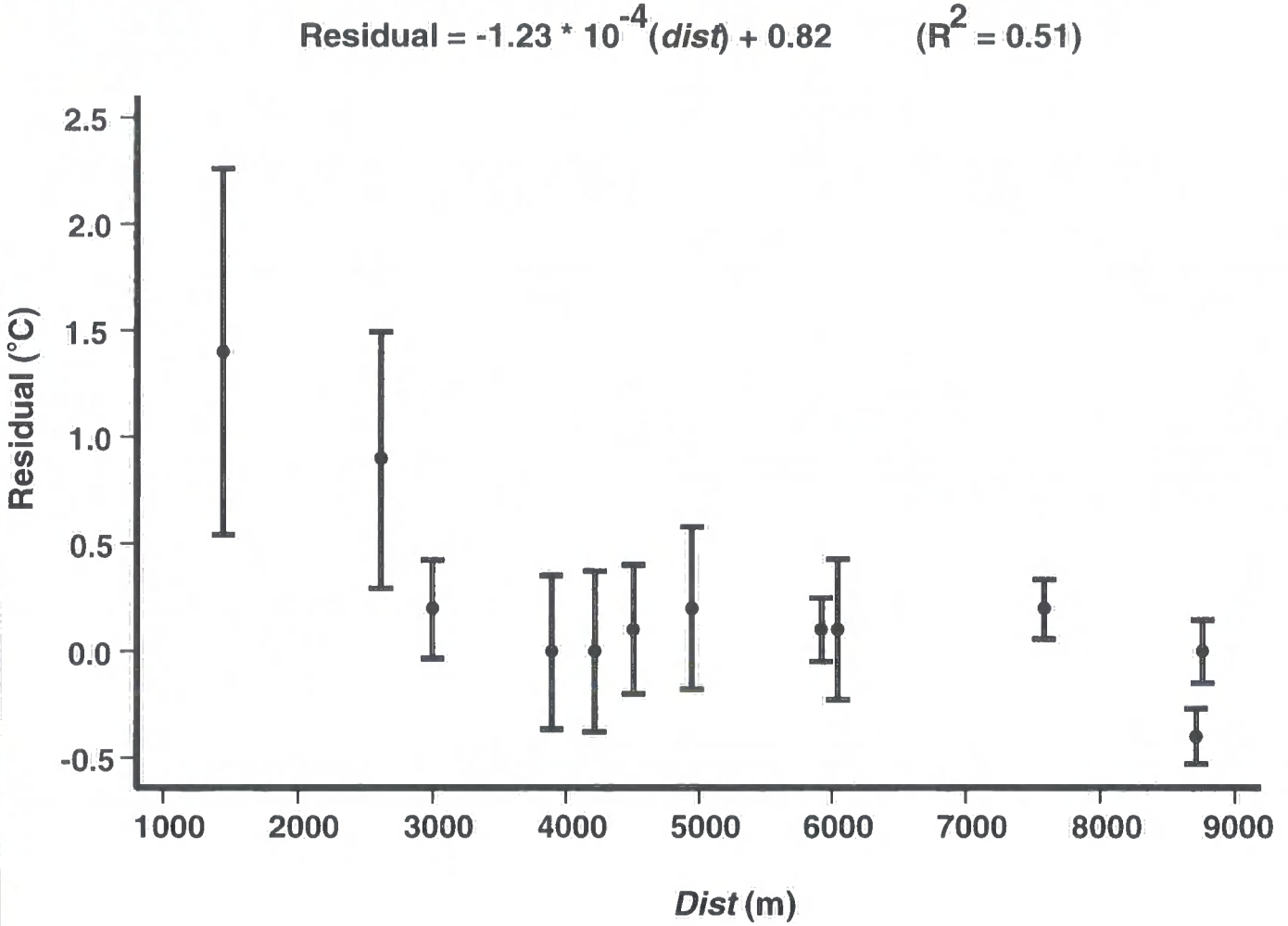

Figure 5.3. Plot of daily mean temperature residuals from the linear lapse rate model against distance relative to the Pennine ridge, for south easterly wind directions. Data are from all experimental networks, one standard deviation is shown.

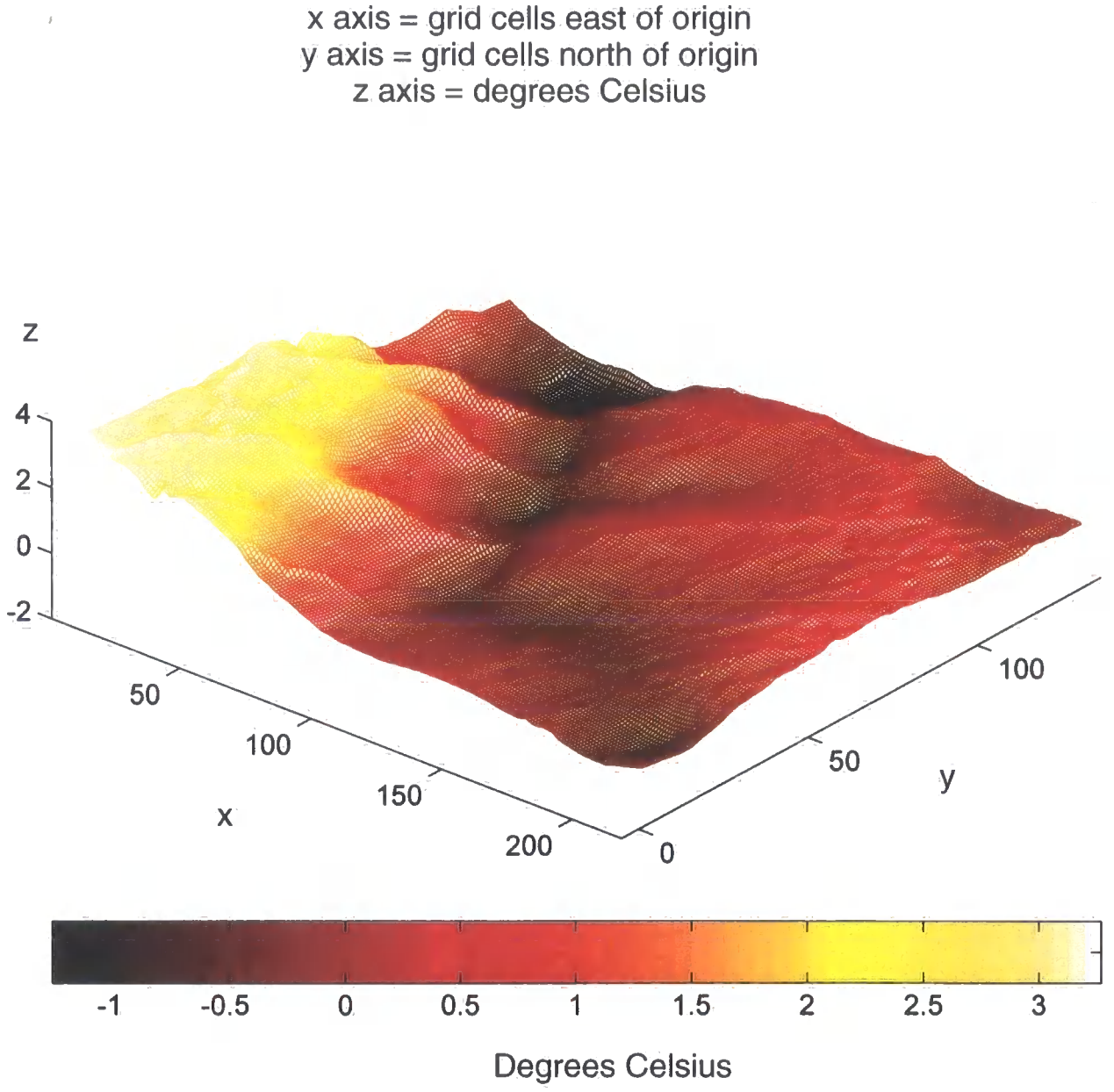

Figure 5.4. Modelled daily mean air temperature
19 November 1998

scarp slope to -1.3°C at Cross Fell. The surface is primarily determined by elevation, but there is also a secondary temperature gradient along the axis perpendicular to the Pennine ridge, with temperatures enhanced to the south west and reduced to the north east.

5.5. Discussion

Despite the theoretical mechanisms that link slope aspect to surface air temperature, the data from the second experimental network do not provide conclusive evidence for any effect. Hypothesis 2, that daily air temperature varies systematically with slope aspect, can thus be refuted. The prevailing cloudy conditions within the study site reduce direct-beam solar radiation, while the low Bowen ratio associated with moist upland sites will tend to partition only a small proportion of any surplus surface energy to sensible heat. The exposure of the study site results in active advection and consequently the flow of air in the boundary layer prevents any spatial discrepancies in surface radiation budget from exerting a systematic influence on air temperature.

The evidence for any effect of topographic shelter on temperature is similarly inconclusive. The data suggest that topographic shelter in close proximity to a site may increase minimum temperature, possibly by reducing the nocturnal loss of infra-red radiation. Only a very small increase in explained temperature variance was achieved using the *shelter* variable, refuting hypothesis 3 that the presence of higher-elevation terrain within a localised geographical neighbourhood affects daily air temperature. The *shelter* variable was not included as a predictor for modelling the daily temperature surfaces.

Topographic drainage potential exerts a systematic effect on minimum temperature, corroborating hypothesis 4. The strongest effect on temperature occurs at a 500 m neighbourhood. The 500 m *drain* variable alone should be used in subsequent analysis, due to the strong autocorrelation of the variable between neighbourhoods. The effect of *drain* on residuals of minimum temperature is apparent in the mean data for all days, although the effect is much stronger on days with a shallow lapse rate of minimum temperature. The sub-division of the data by lapse rate suggests that a lapse rate of minimum temperature of -2.03×10^{-3} °C m^{-1} represents a threshold for the development of katabatic cold air drainage within the study site. The effects of katabatic density currents

are apparent when the lapse rate of minimum temperature is weakly negative, as well as during temperature inversions when lapse rates are positive.

The frequency of calm clear nights conducive to surface radiation loss has been noted previously within the study site (Manley, 1980). The occurrence of a shallow lapse rate provides a clear indication of conditions conducive to the development of katabatic density currents of cold air. The shallow long profile of the upper River Tees and the topographical constriction of the valley were identified as possible influences on the katabatic flow of air (Manley, 1943). The results shown here corroborate these findings and allow spatial modelling of the effects of landscape on minimum temperature. The interaction effects of topography and katabatic air flows are likely to be scale-dependent. The model can account for observed spatial temperature patterns; for example, the occasional occurrence of relatively warm minima on the steep scarp slopes west of the Pennine ridge coinciding with cooler minima at lower elevations within the Eden Valley.

Geographical location relative to the orographic barrier of the Pennine ridge, described using the *dist* variable, improves the explanation of daily mean temperature, corroborating hypothesis 5. Location relative to the Pennine ridge influences temperature on days with south easterly wind, such that mean temperature is enhanced with increasing distance to the south west of the ridge, and reduced with increasing distance north east. The gradient of temperature residuals with the *dist* variable is consistent for all experimental networks regardless of the time of year, although the relative thermal characteristics of the source regions from which south easterly winds originate (i.e. the North Sea and continental Europe) vary seasonally (Manley, 1952). An advection mechanism, whereby cool air gains heat as it flows over a warmer surface, can thus be rejected as a possible explanation for the effect of *dist* on temperature. Further evidence against the advection hypothesis is the fact that the temperature gradient is steep over a small geographical distance, suggesting a mechanism involving the Pennine ridge itself rather than a gradual regional-scale warming.

Another hypothesis is available to explain the dependence of temperature residuals on the *dist* variable. The proposed mechanism is a föhn effect, whereby air flowing from the south east is forced to rise over the Pennines where it reaches saturation and causes a

gradient in humidity and temperature lapse rate between windward and leeward slopes of the Pennine ridge. Greater cloudiness on the more humid windward slopes may also lead to stronger insolation on lee slopes, causing a more positive energy budget and increased sensible heat flux. The lack of evidence for any föhn effect for westerly wind directions may be due to the fact that the prevailing westerly air masses are well mixed and travel at relatively high velocity. Any discrepancy in environmental lapse rate and humidity associated with these air masses crossing the Pennine ridge is unlikely to coincide with the precise location of the topographic barrier, but may be displaced downwind. A systematic effect may exist, but only at a spatial scale larger than that sampled within the Moor House study site.

Both the effect of the *drain* variable on minimum temperature residuals and the effect of the *dist* variable on mean temperature residuals can be modelled as linear relationships. Although log or power functions may improve the fit within the observed range of data values, for predictive purposes a linear model captures the temperature behaviour and restricts the estimated values to realistic limits within the study site.

The use of validation data from a series of independent experimental networks confirms that the behaviour of the temperature residuals with respect to the topographic variables is consistent for different times of year. The criterion adopted for the inclusion of the modelled effects of *drain* (the threshold lapse rate of minimum temperature) was consistent for the validation networks, despite the common perception that the development of katabatic cold air drainage flows and the subsequent occurrence of shallow lapse rates and temperature inversions is a predominantly winter phenomenon (Whiteman, Bian and Sutherland, 1999). Similarly the criterion for the modelling of the effects of *dist* (a summit wind direction between 90^{o} and 180^{o}) was also seasonally consistent.

The use of two base stations is critical for the modelling methodology. The accuracy of the daily lapse rate data must be optimised in order to achieve useful temperature estimates from the lapse rate model, and to apply the criterion for the inclusion of topographic drainage effects. The lapse rate of minimum temperature can be modelled using data from Moor House AWS alone, but measurements from a pair of stations are necessary to capture

the full variability. Also, wind direction must be measured on a summit site where the regional circulation is affected as little as possible by interaction with the topography.

The methods developed for modelling daily surfaces of mean, maximum and minimum temperature are based on the daily temperature and lapse rate measurements. The large day-to-day variability of temperature and lapse rate are important characteristics of the climate of the study site, and are captured fully in the sequence of daily temperature surfaces. Quantification of topo-climatic processes affecting daily mean and minimum temperature provides further information about the subtle spatial and temporal patterns of surface climate at a landscape scale.

Chapter 6. Solar radiation modelling

6.1. Methods of estimation

Solar radiation provides the energy necessary for photosynthesis in plants and is the primary source of energy for ecosystems. The effects of solar radiation can be tested experimentally by controlling other climatic variables, demonstrating that solar radiation may be a limiting factor in particular stages of plant development. For example, root growth may respond primarily to the flux of photosynthetically-active radiation to the surface (Fitter *et al.*, 1999) and in lentil (*Lens culinaris*) the time taken from flowering until full leaf development is proportional to solar radiation (McKenzie and Hill, 1989).

The flux of solar radiation received at the surface can be measured using a pyranometer or estimated from other meteorological variables such as temperature and precipitation (Thornton, Hasenaur and White, 2000) or cloud cover (Supit and van Kappel, 1998) and diurnal temperature range (Hunt, Kuchar and Swanton, 1998). Alternatively, the surface irradiance can be modelled mechanistically. The extra-terrestrial irradiance (Q_a, W m^{-2}) represents the theoretical solar radiation flux to a flat surface perpendicular to the sun in the absence of any atmospheric attenuation or scattering, and is a useful quantity for predicting ground level solar radiation (Burman and Pochop, 1994). Q_a can be modelled as a function of latitude, day of the year, time of day and the solar constant.

As a first step to calculating Q_a, the solar declination d must be estimated. Solar declination describes the seasonally varying latitude of the path of the sun relative to the equator. The solar declination varies between 23.45° at the June solstice and -23.45° at the December solstice (Linacre, 1992), and can be calculated using Equation 6.1 (Cooper, 1969).

$$d = 23.45 \sin\left(\frac{360}{365.25} Nm\right) \qquad 6.1$$

where d = solar declination (degrees)

Nm = time elapsed since the March equinox, March 21 (days)

For solar modelling purposes time of day is measured by the solar hour angle (H, degrees) which is the difference in time from solar noon, expressed as fifteen degrees per hour of difference (Linacre, 1992). The hour angle is negative before solar noon and positive thereafter. The solar hour angle at sunset is calculated using Equation 6.2.

$$\cos H_s = -\tan A \tan d \qquad 6.2$$

where H_s = time at sunset, hour angle (degrees)

A = latitude (degrees)

Due to the slightly elliptical orbit of the earth, a numerical correction is needed to estimate Q_a (Brock, 1981). The periodic function given in Equation 6.3 (Duffie and Beckman, 1980) can be used to model the earth-sun distance correction, which varies during the year. The correction (se) assumes that the radiation intensity varies inversely with the square of distance.

$$se = 1 + 3.44 \times 10^{-2} \cos\left(\frac{360(Nm + 80)}{365.25}\right) \qquad 6.3$$

The extra-terrestrial irradiance Q_a can then be modelled using Equation 6.4.

$$Q_a = 1360\pi(Hs \times \sin A \sin d + \cos A \cos d \sin Hs)se \qquad 6.4$$

where 1360 W m^{-2} = solar constant (Peixoto and Oort, 1992)

Mechanistic modelling of solar radiation received at a site on the surface requires further quantification of slope geometry and the position of the sun in the sky, which varies with time of day. Solar altitude (the angle of the sun above the horizon) and solar azimuth (the angle of the sun clockwise from north) can be calculated using Equations 6.5 and 6.6 (Monteith and Unsworth, 1990).

$$\sin sa = \sin d \sin A + \cos d \cos A \cos H \qquad 6.5$$

where sa = solar altitude (degrees)

$$\cos az = \frac{(\sin d - \sin A \sin sa)}{\cos A \cos sa} \qquad 6.6$$

where az = solar azimuth (degrees)

The flux density of direct-beam solar radiation can then be modelled explicitly. The cosine law of illumination given in Equation 1.3 provides the basis for the trigonometrical relationships between slope geometry and solar geometry, which can be used to estimate direct insolation for a surface location (Equation 6.7). Q_a provides an approximation of the insolation received by a slope perpendicular to the solar beam.

$$K\downarrow = Q_a \cos(slope)\sin(sa) + \sin(slope)\cos(sa)\cos(az - aspect) \qquad 6.7$$

The flux density of solar radiation reaching the ground surface is always less than Q_a, due to the attenuation of radiation by the atmosphere. Some of the radiation passing through the atmosphere is absorbed (Oliver, 1981), particularly at wavelengths shorter than 0.3 μ (by ozone) and wavelengths between 0.9 and 2.1 μ (by water vapour and carbon dioxide). Gas molecules may also scatter sunlight, complicating the geometrical relationships described in Equation 6.7. The high albedo of cloud tops may cause incoming solar radiation to be reflected back into space. The turbidity of the atmosphere varies in space and time. Mechanistic solar radiation models assign a value to the atmospheric transmissivity (Lowry, 1980). For example, the LOWTRAN-7 method (Kneizys *et al.*, 1988) models the atmosphere in 33 separate layers, quantifying temperature as well as the content of water vapour, aerosols, particulates and radiatively-active gases for each layer. One of six atmospheric models is applied depending on season (North, 1994), but these parameterisations are more applicable for seasonal or annual integrations of radiation than for daily modelling. At the higher temporal resolutions required for many ecological

applications, the variability of fluxes associated with day-to-day weather must be accounted for. Effects of terrain shading are also difficult to model using a mechanistic approach, and the accuracy of modelled fluxes will thus be compromised at sites shadowed by the surrounding landscape. This poses particular problems in complex terrain.

6.2. Solar radiation modelling using ARC/INFO

A GIS-based method was developed for modelling daily surfaces of solar radiation, taking into account topographical variability and the high-frequency variability in cloudiness that is poorly modelled using a deterministic approach. The GIS is well suited to context operations, in which the effects of processes determined by the values of neighbouring grid cells can be modelled. The GIS can thus include the effects of terrain shadowing, by calculating areas within the study site shaded by neighbouring terrain for any given value of solar altitude and azimuth.

The latitude of the study site is taken as a constant (54.68°N) for modelling purposes. This latitude is representative of the Moor House reserve as a whole, and is approximately 1 km south of the Moor House AWS. Values of latitude for the area covered by the DTM range from approximately 54.72 to 54.60°N.

Within each individual day, the interaction between slope geometry and solar geometry changes between sunrise and sunset. Where solar radiation estimates are required at a daily resolution, previous work has identified that representative daily values can be obtained by Gaussian integration (Goudriaan, 1986). A five-point method is described (Leuning *et al.*, 1995) in which discrete calculations are made when five specified fractions of daylight duration have elapsed, and a weighted average is taken. If Gaussian fraction 0.0 represents sunrise and Gaussian fraction 1.0 represents sunset, calculations should be made at Gaussian fractions 0.04691, 0.23075, 0.5, 0.76925 and 0.95309 of daylight duration and multiplied respectively by weights 0.11846, 0.23931, 0.28444, 0.23931 and 0.11846 (Leuning *et al.*, 1995). These five weighted samples can then be summed to obtain a daily value. Since Gaussian fraction 0.0 (sunrise) corresponds to $-H_s$ and Gaussian fraction 1.0 (sunset) corresponds to H_s, the Gaussian fractions of daylight duration given above can be converted to solar hour angle by Equation 6.8.

$$H_{gd} = -\left(1.0 - \frac{gd}{0.5}\right) H_s \qquad 6.8$$

where H_{gd} = hour angle for sampling

gd = Gaussian fraction of daylight duration for sampling

The corresponding proportions of day length, H_{gd}, at which the five calculations should be made are therefore equal to -0.90618(H_s), -0.5385(H_s), 0.0(H_s), 0.5385(H_s) and 0.90618(H_s).

For each day of the year, *sa* and *az* were calculated at the five fractions of daylight duration using Equations 6.5 and 6.6. The Grid function *Hillshade* in ARC/INFO was used to calculate five illumination surfaces for each day of the year, using the DTM and the values of *sa* and *az*. The output is a surface of relative illumination with cell values ranging from 0 to 255. A mean illumination surface, *SOLAR1*, is calculated for each day as the mean of the five surfaces using the appropriate Gaussian weights. The maximum cell value occurring within *SOLAR1* is identified, and the surface is scaled to produce a theoretical daily baseline surface *SOLAR2* using Equation 6.9.

$$SOLAR2 = \frac{SOLAR1}{[SOLAR1]_{MAX}} Q_a \qquad 6.9$$

where *SOLAR1* = daily mean of five weighted illumination surfaces

$[SOLAR1]_{MAX}$ = maximum cell value within the surface *SOLAR1*

SOLAR2 = daily baseline solar radiation surface (W m^{-2})

SOLAR2 provides an estimate of interaction between the extra-terrestrial irradiance and the topographical variability within the study site. A scaling factor is calculated to adjust for the difference between Q_a and the observed value at Moor House. The observed daily solar

radiation at Moor House (*solar*) is divided by the cell value corresponding to Moor House within *SOLAR2* to derive a new surface, as shown in Equation 6.10.

$$SOLAR3 = \frac{solar}{[SOLAR2]_{MH}} SOLAR2 \qquad 6.10$$

where *SOLAR3* = final daily solar radiation surface (W m^{-2})

solar = observed daily solar radiation at Moor House (W m^{-2})

$[SOLAR2]_{MH}$ = cell value corresponding to Moor House in *SOLAR2* (W m^{-2})

The resulting surface *SOLAR3* gives an estimate of solar radiation, as received at the surface. The radiation amounts are scaled to observed values.

The AWS pyranometers measure the daily flux of solar radiation received at the surface, providing data to validate the model estimates. The model performance was tested using data from the experimental networks. The observed daily solar radiation value observed by the pyranometer of each AWS was compared to the modelled value for the relevant grid cell. The RMSE is 34.2 W m^{-2} (network 1), 43.7 W m^{-2} (network 3), 36.3 W m^{-2} (network 4) and 40.0 W m^{-2} (network 5). Data from network 2 were used for separate analyses (section 6.6). Figure 6.1 shows the relationship between observed and modelled solar radiation. The quantile-quantile plot shows the model overestimates the true solar radiation, and the overestimate varies non-linearly according to the solar radiation flux. The correlation coefficient between observed and modelled data is 0.92, the concordance correlation coefficient is 0.87, and the RMSE for all data is 38.0 W m^{-2}.

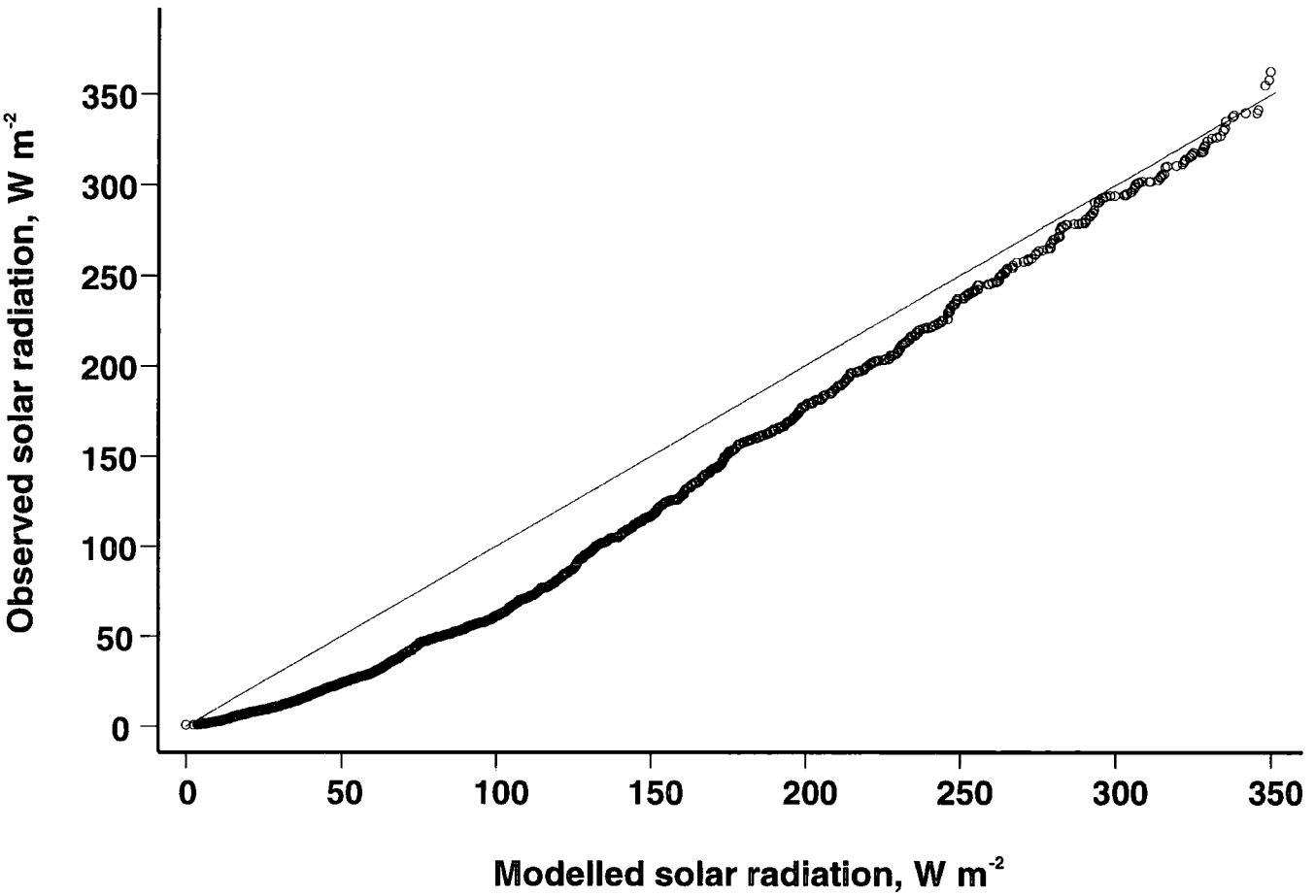

Figure 6.1. Quantile-quantile plot of observed daily solar radiation against modelled daily solar radiation, for all experimental networks.

6.3. Modelling the effects of cloudiness

The flux of solar radiation reaching the surface varies greatly between clear and cloudy days, and overcast conditions also affect the relative contribution of direct-beam and diffuse radiation (Gueymard, 1987). Previous approaches to modelling cloudiness require explicit measurement of the direct and diffuse components of solar radiation using a pyranometer fitted with a shade ring (Oliver, 1992). This instrumentation was unavailable at the study site.

The solar radiation totals modelled by each *SOLAR3* surface are reduced on cloudy days, by scaling the grid cell values to the observed solar radiation value at Moor House using Equation 6.10. However, the spatial variability arising from slope geometry remains unmodified. This is unrealistic, because a greater proportion of solar radiation reaching the surface on cloudy days will be scattered or diffuse as the direct solar beam is almost completely extinguished (North, 1994). The influence of interaction between slope and solar geometry will therefore not be as great on cloudy days. This is modelled by smoothing the daily *SOLAR3* surfaces by a variable amount, the degree of smoothing depending on the cloudiness on the day in question.

Cloudiness is not measured by the AWS but can be estimated from the ratio of observed solar radiation at Moor House (*solar*) to the extra-terrestrial irradiance Q_a. This ratio has been used previously to model the importance of the direct and diffuse components of the solar radiation flux (Oliver, 1992). The ratio of these terms provides an index of atmospheric turbidity *turb* and was estimated using Equation 6.11.

$$turb = \frac{Q_a}{solar} \qquad 6.11$$

The theoretical range of values for *turb* is from 1 when *solar* approaches the clear-sky value, to infinity when *solar* tends to zero on very dull days. In reality, observed solar radiation at the surface does not reach the extra-terrestrial value; values of *turb* at Moor House are all greater than 1.4. A new surface *SOLAR4* is generated using Equation 6.12.

$$SOLAR4 = solar - \left(\frac{solar - SOLAR3}{turb} \right) \qquad 6.12$$

Each individual grid cell value in the *SOLAR3* surface is adjusted towards the observed Moor House value (*solar*), the amount of adjustment is greater on cloudy days, when *turb* is larger. On a very sunny day when solar radiation totals are high the smoothing is relatively slight, whereas on a very overcast day the smoothing is relatively strong. The spatial homogeneity of the resulting surface is proportional to *turb*, so that on cloudy days the effect of slope geometry on solar radiation totals is less marked than on sunny days.

The effect of smoothing the surfaces on model performance was tested by repeating the validation described in section 6.2. The difference was calculated between observed measurements from each AWS for each day and the smoothed value for the corresponding grid cell. The improvement in the model arising from smoothing for cloudiness is quantified in Table 6.1.

Table 6.1. Improvement in solar radiation model due to smoothing for cloudiness

Network	RMSE, W m^{-2} (unsmoothed)	RMSE, W m^{-2} (smoothed)
1	34.2	29.0
3	43.7	30.6
4	36.3	34.6
5	40.0	19.4

The substantial improvement in model performance for the four experimental networks suggests that the smoothing filter provides a useful correction for varying cloud conditions during a range of seasons. Figure 6.2 shows a quantile-quantile plot of observed solar radiation against modelled solar radiation smoothed for cloudiness. The fit to the observed data is improved, although the model still overestimates the true value. The correlation coefficient and concordance correlation coefficient are improved to 0.94 and 0.92 respectively, and the RMSE for all data is 30.4 W m^{-2}.

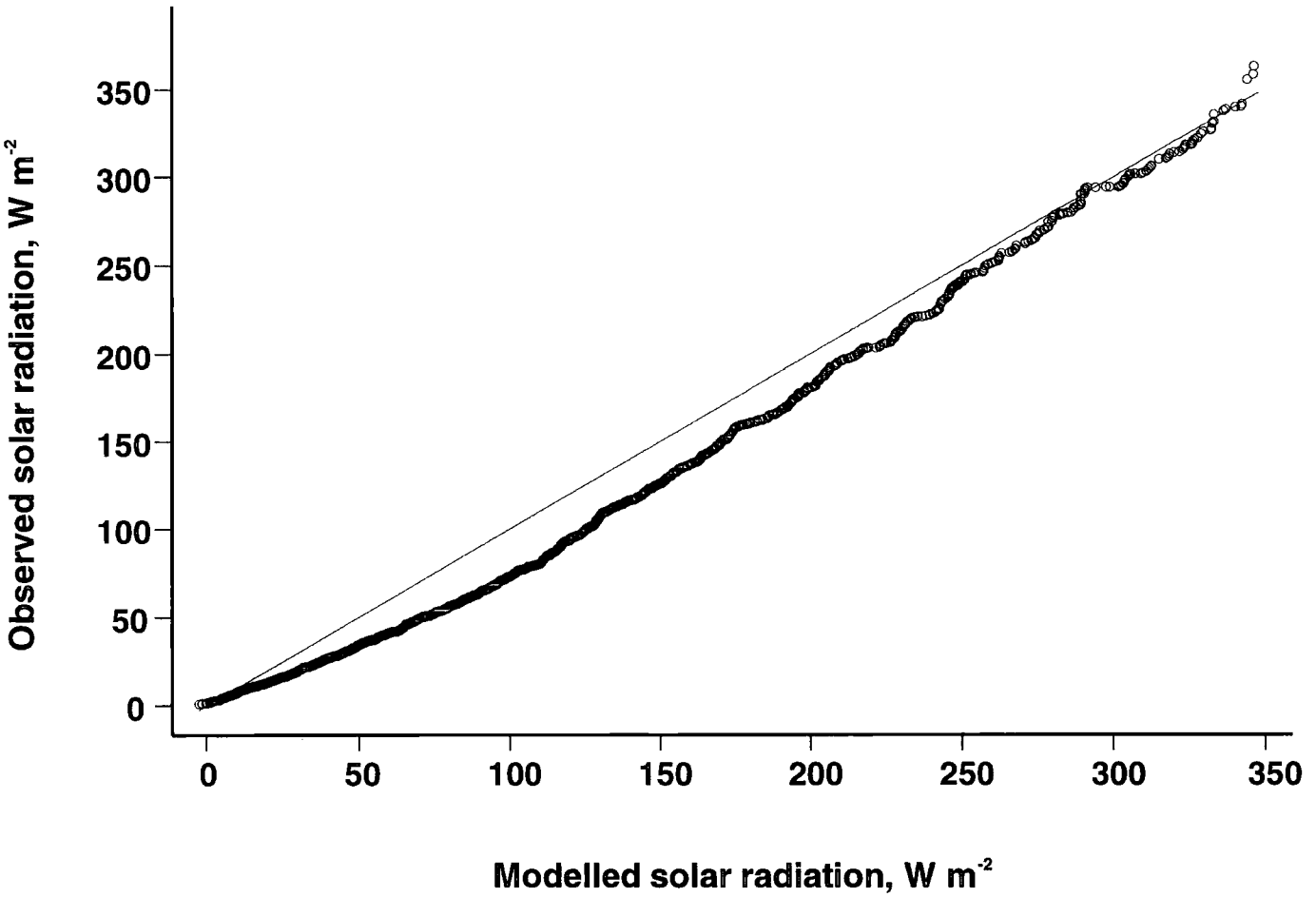

Figure 6.2. Quantile-quantile plot of observed daily solar radiation against modelled daily solar radiation smoothed for cloudiness, for all experimental networks.

6.4. Modelling the effects of daylight duration

Comparison of observed solar radiation against smoothed modelled solar radiation shows that despite the relatively small residuals, the model systematically over-estimates the true radiation amount.

The systematic overestimation of actual solar radiation by the model was quantified by calculating for each day and each station the empirical ratio (*ratio*) of observed to smoothed modelled radiation, as shown in Equation 6.13.

$$ratio = \frac{observed}{smoothed} \qquad 6.13$$

where *observed* = observed solar radiation at validation sites

smoothed = smoothed modelled radiation at validation sites

The mean values of ratio are shown in Table 6.2 for all experimental networks.

Table 6.2. Quantification of the systematic overestimate of modelled solar radiation for all experimental networks

Network	Season	mean value of ratio
1	January - May	0.79
2	May - October	0.81
3	November - March	0.64
4	May - September	0.93
5	October - February	0.71

Table 6.2 suggests that *ratio* varies seasonally, with values reaching a maximum during summer (e.g. networks 2 and 4) and a minimum during winter (e.g. networks 3 and 5). If the value of *ratio* can be modelled instead of calculated empirically, a further improvement in the solar radiation estimates may be achieved. The value of *ratio* can be modelled as a function of daylight duration (*light*, hours), which can be calculated as described by Equation 6.14 (Linacre, 1992).

$$light = \frac{H_s}{7.5} \qquad 6.14$$

Daylight duration varies from 17.0 hours at the summer solstice to 7.0 hours at the winter solstice at the latitude of Moor House. The correction factor η was modelled for each day as the ratio of *light* to the summer solstice value, as shown in Equation 6.15.

$$\eta = \frac{light}{17.0} \qquad 6.15$$

Modelled values of η range between 0.41 and 1.0. The smoothed modelled solar radiation surfaces are multiplied by the daylight duration correction factor η to give a final modelled value. Figure 6.3 shows a quantile-quantile plot of observed solar radiation against modelled solar radiation smoothed for cloudiness and corrected for daylight duration. The fit to the observed data is greatly improved. The correlation coefficient and concordance correlation coefficient are both 0.94, the RMSE for all data is 24.6 W m^{-2}.

The model incorporating the smoothing and η correction can be applied to spatialise solar radiation estimates for the study site, using observed pyranometer data from Moor House AWS alone. An alternative to the model, also using data from a single station, would be to apply the daily Moor House observations as a single spatial estimate throughout the study site. To test whether the validation data agree more closely with the modelled values or with the Moor House data, daily solar radiation observations from each validation station were expressed as anomalies from the Moor House value as described in Equation 4.9, and the anomalies were compared with the model residuals. The results are shown in Table 6.3.

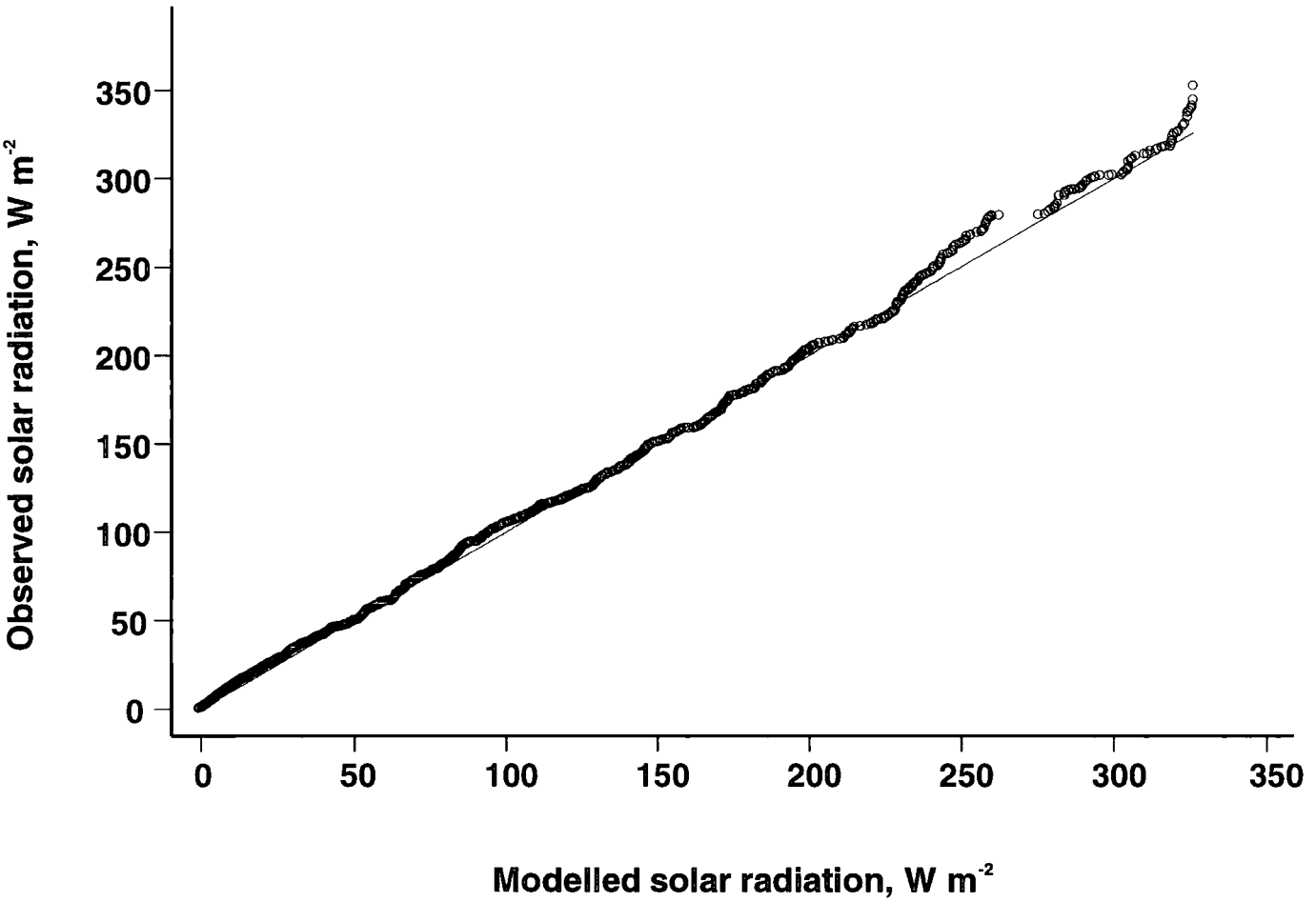

Figure 6.3. Quantile-quantile plot of observed daily solar radiation against modelled daily solar radiation smoothed for cloudiness and adjusted for daylight duration, for all experimental networks.

Table 6.3. Comparison of validation data with modelled solar radiation values and values observed at Moor House AWS

Network	Moor House anomaly (RMSE, W m^{-2})	Model residual (RMSE, W m^{-2})
1	26.0	23.9
2	37.5	36.3
3	11.6	11.2
4	33.4	31.9
5	15.3	11.8

The model incorporating the smoothing and η correction consistently provides a better estimate of true daily solar radiation within the study site than the observed Moor House value. The result provides evidence that the model is successful at quantifying both day-to-day variations in insolation (including cloudiness) and spatial variations in topographic effects on flux density and terrain shading.

As an example, Figure 6.4 shows modelled solar radiation for 15 August 1998, smoothed for cloudiness and corrected for daylight duration. The modelled flux density of solar radiation ranges from 140 W m^{-2} on slopes shaded by higher ground to the south, such as the areas immediately to the north of Meldon Hill and Great Dun Fell, to 210 W m^{-2} on slopes orientated perpendicular to the direction of the sun at noon, such as the southern slopes of Cross Fell.

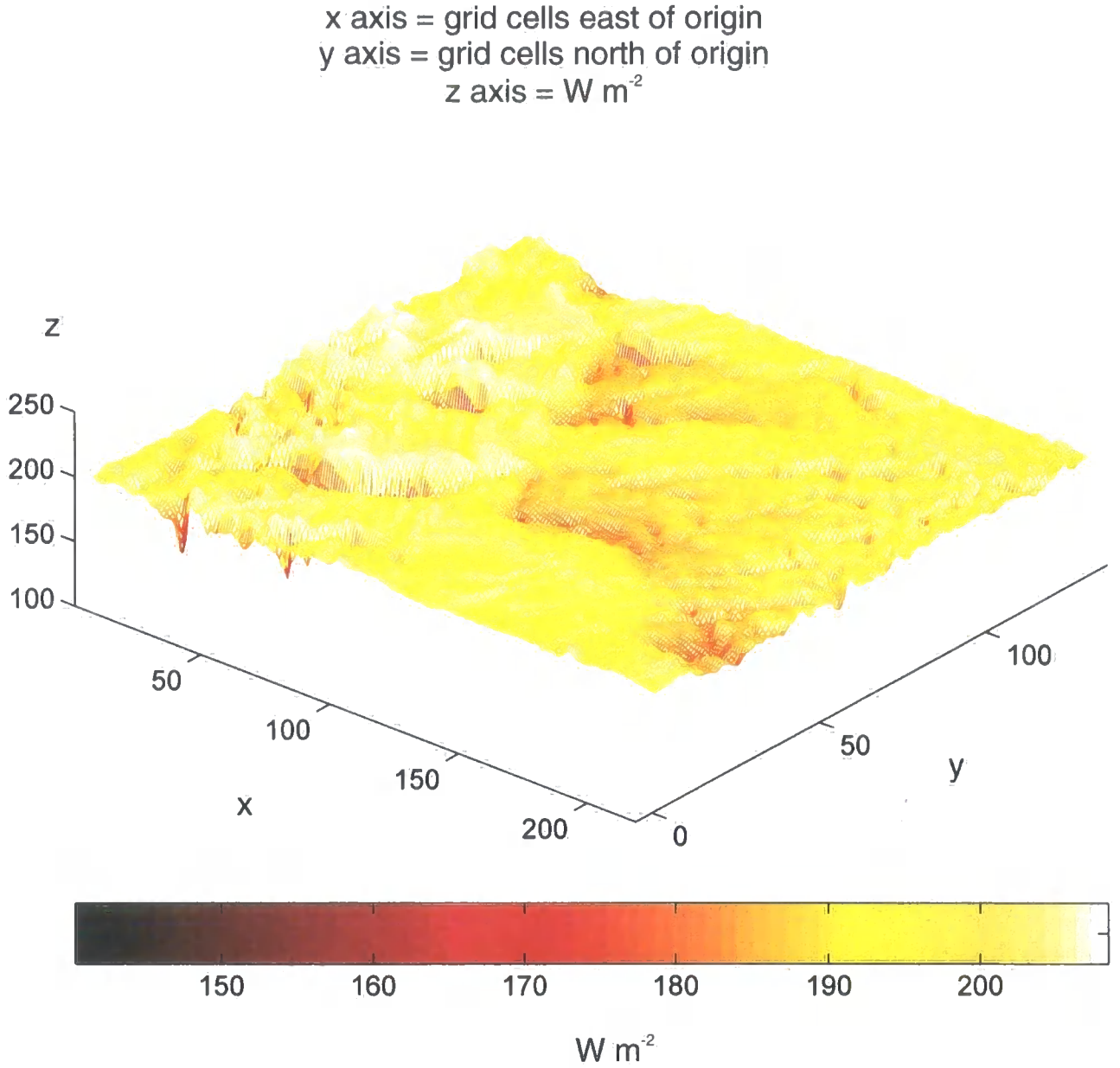

Figure 6.4. Modelled solar radiation
15 August 1998

6.5. Systematic spatial behaviour in model residuals

The residuals from the solar radiation model at individual validation stations were calculated in order to assess whether variance left unexplained by the model could be accounted for. The residuals from the model are shown in Table 6.4.

Table 6.4. Residuals from individual validation stations, Network 1

AWS	RMSE from model W m^{-2}
S	41.5
H	36.5
K	23.4
1	17.0
2	15.0
3	18.7
4	14.0
5	23.5

The mean residuals from the stations on the western slope (Sink Beck, High Carle Band and Knock Fell) are larger than those from the roving stations. The data were used to investigate the hypothesis that this pattern is due to the interaction of the Pennine ridge with prevailing wind flow. The residuals were re-calculated separately for days with easterly winds (*dir* between 0 and 180) and westerly winds (*dir* between 180 and 360). The mean residuals are shown in Table 6.5.

Table 6.5. Mean absolute error (W m^{-2}) at individual validation stations for separate wind directions

AWS	days with E wind	days with W wind
S	79.2	-9.2
H	65.3	-9.6
K	22.6	-12.8
1	18.2	7.7
2	18.1	4.1
3	18.5	-7.8
4	14.9	-5.2
5	21.0	-14.0

For days with easterly winds, a strong pattern is apparent in the residuals which can be largely explained by position relative to the Pennine ridge, using the *dist* variable

previously used to explain variability in the mean temperature residuals. The relationship is shown in Equation 6.16.

$$residual = -7.9 \times 10^{-3}(dist) + 71.2 \qquad 6.16$$
$$(R^2 = 0.41, n = 8, t(dist) = -3.0, P = 0.025)$$

The result indicates that under easterly winds the western slopes are sunnier than eastern slopes. This analysis clarifies the previously identified relationship between mean temperature residuals and geographical location on days with a south-easterly wind direction, when lapse rates of mean temperature are relatively steep on western slopes. The spatial pattern in the solar radiation residuals provides clear corroboration for the föhn mechanism, the relatively sunny and warm conditions west of the Pennine ridge under easterly or south-easterly winds are consistent with a discrepancy in saturation and lapse rate arising from the föhn effect.

6.6. Effects of pyranometer exposure

The modelling of solar radiation received across a complex landscape relies on the interaction of solar and slope geometry. However, the conventional horizontal exposure of the Kipp pyranometers used to measure validation data ignores the local slope. Solar radiation models incorporating topographic complexity may be better validated by pyranometers orientated parallel to the local slope (Oliver, 1992). In order to test this hypothesis, on 28 August 1998 the mast of each roving AWS was adjusted from vertical to an orientation perpendicular to the local topographic gradient. The appropriate local gradient was identified by interrogating the relevant co-ordinates of the modelled *slope* surface described in section 2.2. The solar radiation data from the second experimental network can thus be split into one half measured with pyranometers horizontal, and one half with pyranometers parallel to the local slope. Comparison of the validation statistics can clarify any differences. The difference between observed and modelled solar radiation was calculated for each station for each subsample and the results are shown in Table 6.6.

Table 6.6. Model validation statistics (RMSE, W m^{-2}) for experimental network 2

Exposure	Unsmoothed	Smoothed	Smoothed and η corrected
Horizontal	51.6	48.6	38.8
Parallel to slope	34.9	29.1	28.0

The smoothing and η correction procedures results in improved validation statistics, corroborating the finding that the smoothing filter helps to model spatial variability of solar radiation in response to cloudiness and that the model can be adjusted to take account of systematic seasonal variations in daylight duration.

The validation statistics for the modelled surfaces (both before and after smoothing) are better for the sample when pyranometers were arranged parallel to the local slope than for the conventional horizontal arrangement. The difference in validation results between the two sub-samples suggests that the orientation of the pyranometers relative to the slope is important for obtaining a realistic validation of modelled solar radiation, where the model incorporates the effects of slope geometry.

Despite this result, parallel pyranometer exposure was not implemented. It was not feasible to alter the pyranometer exposure of the AWS operated under other research programs, and in order to maintain a consistent data sampling strategy throughout all stations within the study site the conventional horizontal arrangement was used for all AWS for the remaining duration of the project.

6.7. Discussion

Although the solar radiation modelling technique is empirical rather than process-based, the validation statistics compare favourably with published results for other estimation models at other sites, e.g. RMSE of 47.5 W m^{-2} for a site in Ontario, Canada (Hunt *et al.*, 1998), 43.8 W m^{-2} for complex terrain in Spain (Olmo *et al.*, 1999) or 28.7 W m^{-2} for daily radiation estimates at a range of European sites (Supit and van Kappel, 1998). Alternative methodologies suffer at fine time steps due to the need to parameterise the attenuation of radiation by the atmosphere. The method described here achieves consistent spatial

estimates of daily solar radiation, refuting previous suggestions that ecological applications require site-specific daily measurements (Brock, 1981).

The method avoids the need for the user to run complex programs modelling the interactions of slope and solar geometry, because the ARC/INFO *hillshade* routine accounts for these in the estimate of spatial variability of illumination over the surface for each day. The need to parameterise atmospheric transmissivity is also avoided by smoothing the modelled surfaces to adjust for cloudiness.

Despite the complexity of the mechanistic approach applied in models such as LOWTRAN-7 (Kneizys *et al.*, 1988), variations in atmospheric transmissivity associated with cloudiness are still a dominant source of error in resulting estimates of solar radiation (North, 1994). These errors increase as the modelling time-step decreases. In the model described here, the *turb* variable and correction factor η avoid the need for these parameterisations, accounting for daily cloudiness, daylight duration and the varying atmospheric path length which causes attenuation to vary throughout the year (Barry, 1992).

In theory, radiation flux density increases with altitude in a clear dry atmosphere (Barry, 1992) due to a reduction in scattering (North, 1994). The predictive power of mechanistic solar radiation models generally weaken at high elevations (Scheifinger and Kromp-Kolb, 2000). Pyranometer observations in England and Wales show that at a regional scale, insolation in British uplands decreases with elevation due to increased cloudiness (Harding, 1979b) and within an individual upland area solar radiation receipt tends to be uniform regardless of elevation, especially above about 500 m. The results of the present study corroborate these latter findings. Within the study site the residuals from the modelled solar radiation surfaces show no systematic relationship with elevation.

The relatively sunny conditions west of the Pennine ridge correspond to warm temperature anomalies in the same location for easterly wind directions. Although the effects of *dist* on solar radiation residuals and mean temperature residuals reach maximum significance at slightly different wind directions, the processes are consistent. This result corroborates the

föhn effect hypothesis, with the spatial discrepancy in humidity east and west of the Pennines explaining the anomalies of both solar radiation and temperature. The föhn hypothesis can only be tested using experimental network 1, because no other network has the necessary transects east and west of the Pennine ridge combined with summit wind direction data. The anomalous conditions identified for easterly wind directions may also provide information about the helm phenomenon, recognised locally by a cloud cap above the summits developing during easterly winds, with clear skies above the Eden valley (Manley, 1936). It is likely, however, that the helm phenomenon is a manifestation of processes operating at a larger spatial scale than that sampled by the experimental networks within the Moor House study site.

The results from section 6.6 show that if validation data are measured by pyranometers orientated parallel to the local slope, a closer fit is achieved between observed and modelled data. Model estimates of solar radiation are dependent on slope geometry and so parallel pyranometer exposure allows a more realistic test of the model. Parallel pyranometer exposure was not implemented for logistical reasons, but it is likely that the performance of the model at a landscape-scale is better than the validation statistics suggest for other experimental networks. The installation of AWS is impossible on slopes steeper than about 15°, so validation data are unavailable for such terrain although data from the second experimental network suggest that model performance may be relatively good on steep slopes.

The data from successive experimental networks have allowed the model estimates to be incrementally improved. The validation data agree better with the modelled values than with the Moor House observations, demonstrating that the model produces a useful estimate of daily solar radiation within the study site. The modelling method is quick and effective to use, allowing sequences of daily spatial solar radiation estimates to be easily prepared for ecological applications.

Chapter 7. Moisture budget modelling

7.1. Ecological importance of moisture availability

Moisture-related climate variables are of critical importance to plant growth, determining the potential soil moisture deficit (Jones and Thomasson, 1985). The exchange of gases through leaf stomata necessary for photosynthesis cannot occur without transpiration of water vapour. The rate of transpiration from plants varies with atmospheric conditions including temperature, humidity, radiation and wind speed.

Various quantities may be used to describe the water vapour content of the atmosphere, although conversion between different quantities requires simultaneous temperature data. Saturation vapour pressure (e_s) is defined as the equilibrium vapour pressure where the rate at which molecules leave a water surface is equal to the rate at which molecules enter the water surface, and is a function of temperature only. The method for calculating e_s given in Equation 4.24 provides acceptable estimates at temperatures up to 90°C with errors below 0.11% (Burman and Pochop, 1994). The ambient vapour pressure (*vap*) is the partial pressure caused by water molecules in the atmosphere, and can be estimated using Equation 4.22.

Evapotranspiration describes the combined process of evaporation from the ground surface and transpiration through plant tissue (Burman and Pochop, 1994), while potential evapotranspiration (*PE*) is defined as the water transpired by a short green crop completely covering the ground, amply supplied with water (Penman, 1948) and not limited by disease or fertility (Burman and Pochop, 1994). Annual totals of *PE* in the British uplands are commonly under 300 mm (Jones and Thomasson, 1985), although actual values vary with vegetation type. The inter-annual variability of *PE* within Britain is much lower than that of precipitation (Jones and Thomasson, 1985).

The rate of evaporation from a surface is dependent on both radiant energy flux and the effective ventilation of a surface (Penman, 1948). Combination equations which account for both energy balance and aerodynamic terms are the most appropriate methods for estimating potential evapotranspiration, if adequate climatic data are available (Burman

and Pochop, 1994). Various calibrations of Penman's original method have been developed. Equations are commonly calibrated using empirical coefficients calculated for specific locations, surfaces or crops. In the absence of an equation calibrated specifically for the study site two alternative equations based on combination methods were used; the original combination method (Penman, 1948), and a version of the Penman equation which includes a physically-derived aerodynamic coefficient to account for moderate surface roughness encountered in British environments (Thom and Oliver, 1977). The methods are described in Equation 7.1.

$$PE = \frac{\Delta Q_n + b\gamma(Ea)}{\Delta + c\gamma} \qquad 7.1$$

where PE = potential evapotranspiration (mm day^{-1})

Δ = slope of the saturation water vapour pressure versus temperature curve

γ= psychrometric coefficient (hPa $^{o}C^{-1}$).

b = 1.0 (Penman, 1948), or 2.5 (Thom and Oliver, 1977).

c = 1.0 (Penman, 1948), or 2.4 (Thom and Oliver, 1977).

$$Ea = 0.26(vpd) \times \left(1 + \frac{0.093wind}{100}\right) \qquad 7.2$$

where $vpd = e_s$ - vap, hPa

The original Penman equation tends to underestimate PE during winter (Thom and Oliver, 1977), and the adjustment to the coefficients b and c serves to increase estimates above those of the original method during winter and to reduce estimates in summer. Long term average values were calculated using data for Durham Observatory (54.8°N, 1.6°W, 102 m); mean annual values of PE for the period 1987-1995 are 2.3 mm day^{-1} (Penman, 1948) and 2.0 mm day^{-1} (Thom and Oliver, 1977). Comparison with maps of long-term mean annual PE for the UK (Goudie and Brunsden, 1994) suggests the latter method gives the better estimate. The latter method (Thom and Oliver, 1977) is also the suggested technique

for the estimation of *PE* cited by the Soil Survey of England and Wales (Jones and Thomasson, 1985).

7.2. The relationship of *PE* with topography

Previous work has found that *PE* decreases with elevation within the British Isles (Smith, 1976). Analysis of monthly data shows the magnitude of the lapse rate varies from around -3.5×10^{-2} mm m^{-1} in April and May, to approximately -1.0×10^{-2} mm m^{-1} in November and December (Smith, 1976). The dependence of *PE* on elevation is thus strongest during late spring and weakest in winter.

As a preliminary to investigating the relationship between PE and elevation within the study site, the elevation dependence of the climate variables used to estimate PE was analysed. Temperature and vapour pressure vary fundamentally with elevation; the dependence of temperature was discussed in Chapter 4. To assess the variation of vapour pressure and wind speed with elevation, daily values were calculated at each independent AWS and expressed as anomalies (a_{vap} and a_{wind}) from the simultaneous daily values measured at Moor House, as described in Equation 4.9. Using data from experimental network 3, the relationship between vapour pressure anomalies and elevation is shown in Equation 7.3.

$$a_{vap} = -2.12 \times 10^{-3}(ele) - 1.03 \qquad 7.3$$

($R^2 = 0.50$, n = 774, t(*ele*) = 28.0, $P < 0.01$)

The regression shows that vapour pressure falls with increasing elevation. The strength of the relationship arises partially from the fact that vapour pressure is dependent on temperature, as warm air has a higher saturation vapour pressure. Vapour pressure deficit is a more meaningful measure of humidity for ecological systems, and also decreases as a function of elevation as shown in Equation 7.4, although the elevation dependence is not as strong.

$$a_{vpd} = 1.14 \times 10^{-3}(ele) - 0.71 \qquad 7.4$$

($R^2 = 0.25$, n = 774, t(*ele*) = 16.3, $P < 0.01$)

The decrease in vapour pressure with elevation is usually expressed as an exponential function (Reitan, 1963). The Tablecurve 2D software (SPSS) was used to fit the optimum exponential curve to the data, the resulting relationships are shown in Equations 7.5 and 7.6 for vapour pressure and vapour pressure deficit respectively.

$$a_{vap} = -9.79 \times 10^{-3} \exp\left(\frac{-ele}{-195.09}\right) \qquad 7.5$$

($R^2 = 0.59$)

$$a_{vpd} = -1.86 \times 10^{-3} \exp\left(\frac{-ele}{-172.31}\right) \qquad 7.6$$

($R^2 = 0.50$)

Elevation can also explain a proportion of the variance in wind speed anomalies. The relationship is given in Equation 7.7, and shows that wind speed increases with elevation.

$$a_{wind} = 1.74 \times 10^{-2}(ele) - 10.18 \qquad 7.7$$

($R^2 = 0.37$, n = 695, t(*ele*) = 20.0, $P < 0.01$)

The *ridge* variable can also be used to explain variance in wind speed anomalies, as shown in Equation 7.8.

$$a_{wind} = 1.62 \times 10^{-1}(ridge) - 0.73 \qquad 7.8$$

($R^2 = 0.53$ n = 7695, t(*ridge*) = 27.9, $P < 0.01$)

Wind speed is thus also higher at sites exposed on ridges. Elevation is highly correlated with the *ridge* variable ($\rho = 0.92$), and the two variables cannot be combined meaningfully in a bivariate regression model due to multicollinearity.

Modelled values of *PE* (Thom and Oliver, 1977) can also be regressed on elevation, as shown in Equation 7.9.

$$a_{PE} = -1.26 \times 10^{-3}(ele) - 0.81 \qquad 7.9$$

$$(R^2 = 0.32 \text{ n} = 695, \text{t}(ele) = -7.3, P < 0.01)$$

The assumption that *PE* decreases with increasing elevation, creating a lapse rate in PE, appears valid. In order to test the theoretical linear lapse rate in *PE*, data from the base stations at Moor House and Great Dun Fell were used to calculate daily *PE* at the two sites, using both versions of Equation 7.1. A daily lapse rate was calculated (Equation 4.19) using the base station values for each method, and spatial estimates of *PE* were obtained using Equation 4.23. The estimates were validated using independent data from roving AWS. Data from the Delta-T AWS could not be used due to the lack of wet-bulb temperature observations and net radiation observations. Operating problems during the first two experimental networks prevent the use of those data.

Table 7.1. Validation statistics (RMSE, mm day^{-1}) for *PE* estimates using two versions of the Penman equation

Network	Penman, 1948	Thom and Oliver, 1977
3	0.40	0.20
4	2.28	0.93
5	0.57	0.13

The calibration that includes the aerodynamic adjustment (Thom and Oliver, 1977) gives the smallest errors for the three networks, which sample both summer and winter conditions. The results corroborate tests using long-term data from Durham Observatory

and published values of *PE* (Goudie and Brunsden, 1994). The Thom and Oliver (1977) method was adopted for all subsequent *PE* modelling within the study site.

The observed lapse rates of *PE* were compared with published values for the UK. Mean summer (May to September) lapse rates were previously estimated at -2.8×10^{-2} mm m^{-1} (Jones and Thomasson, 1985). The corresponding value calculated from the experimental networks is -6.6×10^{-2} mm m^{-1}. The result confirms that *PE* depends on elevation, and that the observed relationship within the study site is stronger than that calculated for stations at lower elevations elsewhere in Britain.

The mean modelled values of *PE* for the lower and upper base station are presented in Table 7.2.

Table 7.2. Mean modelled values of PE (mm day^{-1})

Network	Lower Base Station	Upper Base Station
3	0.16	0.07
4	2.43	1.99
5	0.15	0.13

The values shown above give the expected result that *PE* is higher in summer (network 4) than in winter (networks 3 and 5) due to enhanced mean temperature and vapour pressure deficit. The data also show a general inverse relationship between *PE* and elevation. Due to the complexity of the relationship between the individual input variables and *PE*, the theoretical decrease in *PE* with elevation may not be applicable on individual days. For example, on a day with a strong temperature inversion wind speed may be negligible, with net radiation and temperature increasing with elevation, causing *PE* to increase with elevation. Nevertheless, if the lapse rate of *PE* is calculated on a daily basis the prevailing spatial pattern of *PE* could still be estimated meaningfully as a linear function of elevation.

Modelled daily *PE* for 6 March 2000 is shown in Figure 7.1 as an example. The *PE* total estimated using the Thom and Oliver method was 0.9 mm at Moor House and 0.4 mm at Great Dun Fell, giving a lapse rate of -1.69×10^{-3} mm m^{-1}. Modelled values in the *PE* surface range between 0.3 mm at Cross Fell, and 1.4 mm at the foot of the scarp slope.

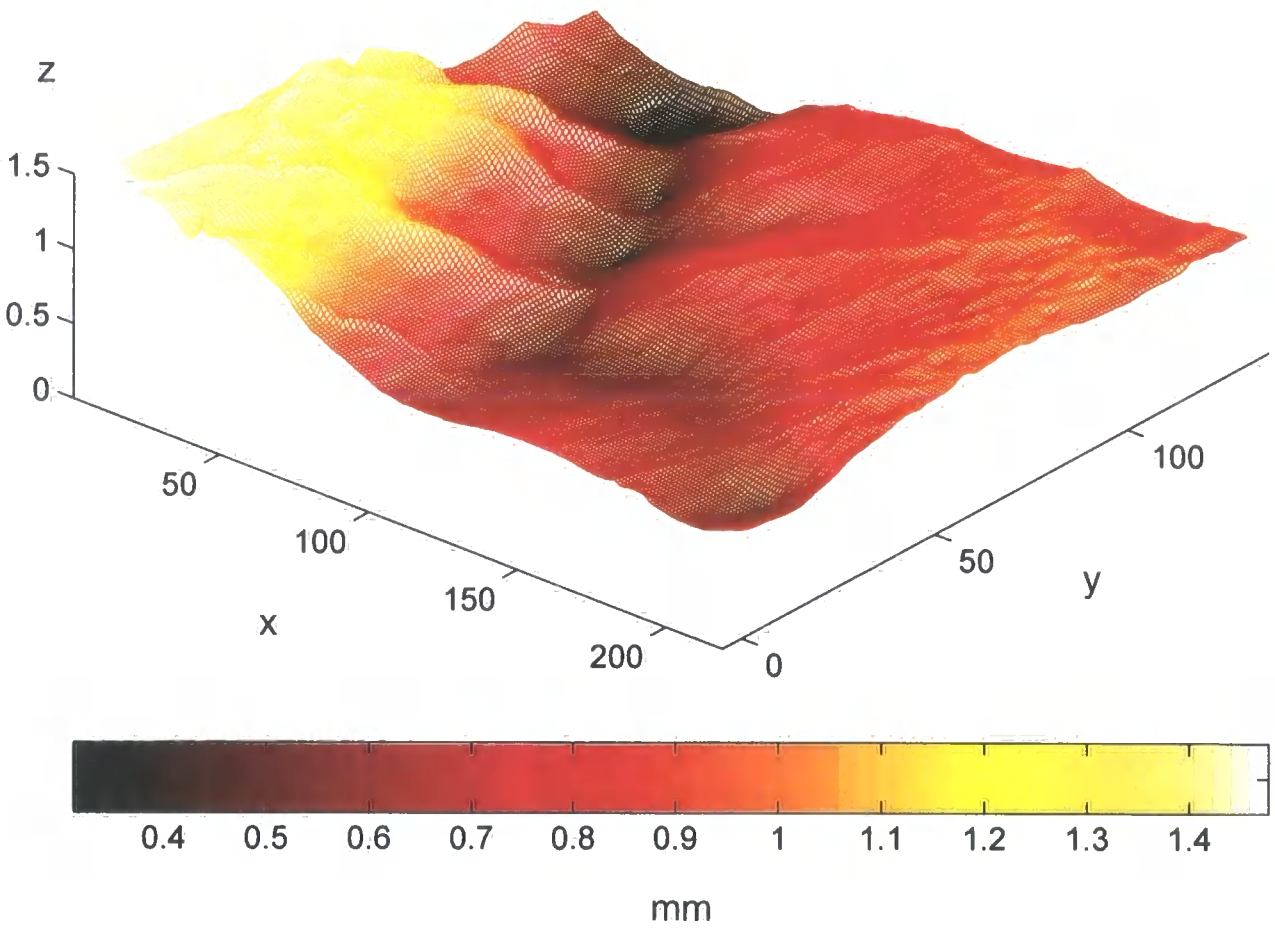

Figure 7.1. Modelled potential evapotranspiration
6 March 2000

7.3. Spatial estimates of precipitation

Previous work suggests that precipitation increases strongly with elevation in mid-latitude climates (Barry, 1992). Significant correlations exist between precipitation and elevation using monthly data, especially in summer (Taylor, 1996). Published rates of precipitation increase with elevation for Great Britain range from 0.8 mm m^{-1} to 3.0 mm m^{-1} at windward sites exposed to prevailing westerly weather systems (Salter, 1918). Other studies suggest that the elevation of surrounding terrain exerts a more important control on precipitation than local site elevation (Chuan and Lockwood, 1974).

Daily precipitation totals were calculated for all AWS and regressed on elevation. The analysis was refined in four stages shown below:

1. Precipitation data were used from all experimental networks.

2. Separate regressions were undertaken for transects east and west of the Pennine ridge using data from the first experimental network.

3. The data were also split into four quadrants according to the daily wind direction at the summit of Great Dun Fell and analysed using separate regressions.

4. Days recording a precipitation catch smaller than 0.1 mm were excluded from the analysis.

No systematic relationship could be identified between precipitation and elevation for any of the analyses described above. In all cases, the explained variance in the precipitation data was less than 5%. Similarly, no relationship could be identified between precipitation and the *shelter*, *drain* or *dist* variables.

7.4. Discussion

For ecological applications, *PE* is best modelled using combination methods which account for radiative and aerodynamic influences on the evaporation process. Other methods may

be appropriate at larger scales (Thornthwaite, 1948), but daily estimates of *PE* for ecological applications require explicit modelling of the physical processes. One disadvantage of combination methods is the large data requirements, *PE* could not be estimated using data from the Delta-T AWS due to the lack of wet-bulb temperature and net radiation measurements. No data were available relating to soil heat flux, and this variable was not included in the algorithms used to calculate *PE*. Soil heat flux is small compared to other components of the energy balance and its omission has a negligible effect on final estimates (Burman and Pochop, 1994). Validation of the estimates using independent data suggests the method of Thom and Oliver (1977) is most appropriate for calculating *PE* at a daily time step, if the necessary atmospheric variables are available. The results of the *PE* analysis confirm that spatial estimates can be modelled using elevation as a predictor variable, corroborating hypothesis 1c.

The analyses of the precipitation data show no evidence for any systematic relationship between precipitation and elevation within the study site (refuting hypothesis 1d), nor between precipitation and any other topographic variable. It is possible that precipitation within the study site does not vary systematically with elevation, due to variations in micro-scale exposure overwhelming any systematic landscape-scale effects. Precipitation is inherently more variable than most other climatic elements (Linacre, 1992), hindering the identification of spatial pattern. Clarification of the extent to which landscape influences precipitation is also prevented by the fact that rain gauge observations are often inaccurate; errors associated with precipitation measurement can often reach 10 to 20% (Mackey *et al.*, 1996). Turbulent interaction between a rain gauge and the local air flow may reduce the measured catch. The tipping bucket rain gauges must be perfectly horizontal to measure an accurate catch, but it is difficult to install and maintain the gauges of the roving AWS horizontally at the exposed windy vegetated sites of the experimental networks.

The frequent occurrence of snow within a study site further confounds the measurement of precipitation, particularly in complex terrain (Taylor, 1996). The catch of snow is generally reduced relative to the true precipitation by the interaction of wind eddies with the rain gauge, especially when snow is blowing and drifting (Archer and Stewart, 1995). Snow may also bridge the gauge orifice and prolonged low temperature may cause an

unknown time lag between a precipitation event and its eventual measurement. The duration of lying snow is ecologically important due to its effects on radiation and temperature regimes in the vegetation and soil (Walton, 1982). The drifting of fallen snow and the complexity of processes affecting melting, sublimation and metamorphosis (Perla and Martinelli, 1976) introduce further uncertainties to the understanding of the hydrological regime during winter (Essery and Pomeroy, 1999).

With the existing uncertainties associated with precipitation measurement, low confidence should be attached to any spatial pattern of precipitation within the study site. The hypothesis of a linear lapse of precipitation with elevation within the site can neither be firmly corroborated nor refuted, due to problems associated with the accurate measurement of precipitation. In the absence of any evidence for topographic controls on precipitation, the best method for modelling daily precipitation surfaces is to use an average of the catch received at the Moor House and Great Dun Fell base stations.

Chapter 8. Ecological applications

8.1. Ecosystem Dynamics Models

The climate surfaces generated by the methods described are produced at high spatial resolution (50 m grid cells), and consecutive surfaces are produced at a daily time step. The methodology can therefore produce time series of spatial climate data suitable for use as input to ecosystem dynamics models, such as programs which simulate plant growth based on climatic input data. At a landscape scale, the relationship between surface climate, plant growth and species distribution can be modelled.

8.2. Temperature sums and means

Temperature is the main control on ecological productivity in the uplands (Harding, 1979b), as such the temperature surfaces may be particularly applicable to ecological problems such as species distribution or phenology. Consecutive daily surfaces may be summed or integrated to provide spatial climate information for longer time periods depending on the specific ecological application. The average of consecutive daily surfaces can be calculated, as an example mean daily soil temperature at 10 cm depth is shown for the month of June 1998 in Figure 8.1. The mean soil temperature was 11.2°C at Moor House and 9.2°C at Great Dun Fell, giving a lapse rate of -6.8×10^{-3} °C m^{-1}.

Another useful variable that can be derived is accumulated thermal time above a temperature threshold. Accumulated temperature is the best climatic indicator of shoot extension rate (Squire, 1981) and time from sowing to emergence in crop plants (McKenzie and Hill, 1989). Heat accrued over time is also a useful measure of development in insects (Gullan and Cranston, 1996).

As an example, degree days above 5°C were summed for the study region for April 1998. Days with mean temperature below the threshold do not affect the accumulated temperature sum. Daily grids of temperature surplus above the threshold were created using the *Con* function in ARC/INFO, which allows conditional evaluation of gridded data

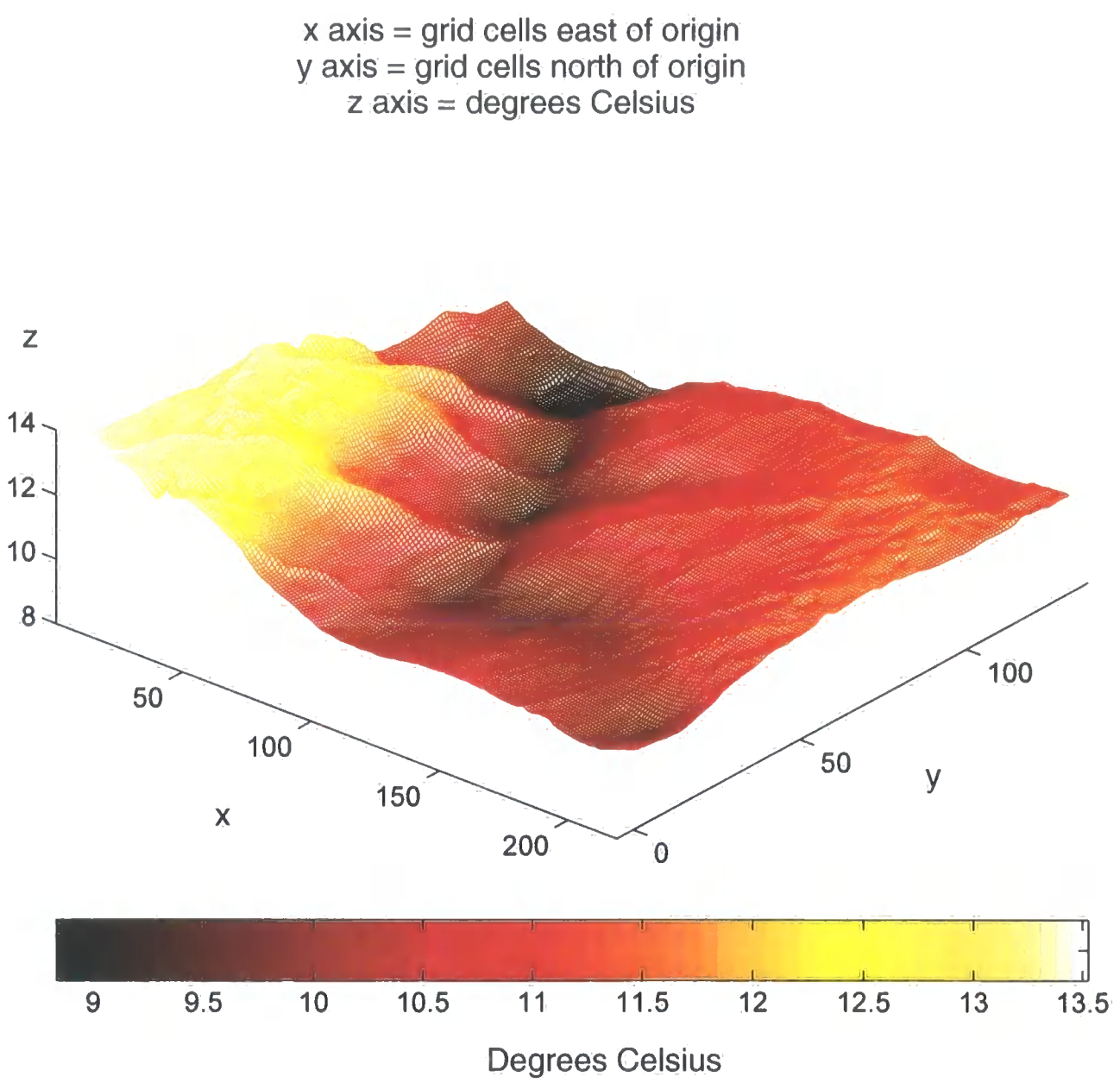

Figure 8.1. Modelled monthly mean soil temperature at 10 cm depth
June 1998

on a cell-by-cell basis. The function was used to create a new grid for each day using the algorithm described in Figure 8.2. The resulting grids were then summed to give a final surface of accumulated temperature above 5°C for April 1998 (Figure 8.3). The temperature sum ranges from zero degree days on the summits of the Pennine ridge, to 45 degree days at the foot of the scarp slope in the Eden valley. The procedure was repeated for May 1998; the spatial distribution of the temperature sum variable is similar (Figure 8.4), but with values ranging from 80 to 170 degree days. The entire region experienced an increase in accumulated thermal time during May compared to April 1998, but the increase was markedly smaller at higher elevations. The gradient of the relationship between thermal time and elevation is determined by the mean temperature lapse rate on each day. Daily surfaces of mean temperature must be calculated before integrating the data into longer-term summaries, in order to include the effects of high frequency variability captured by the daily model.

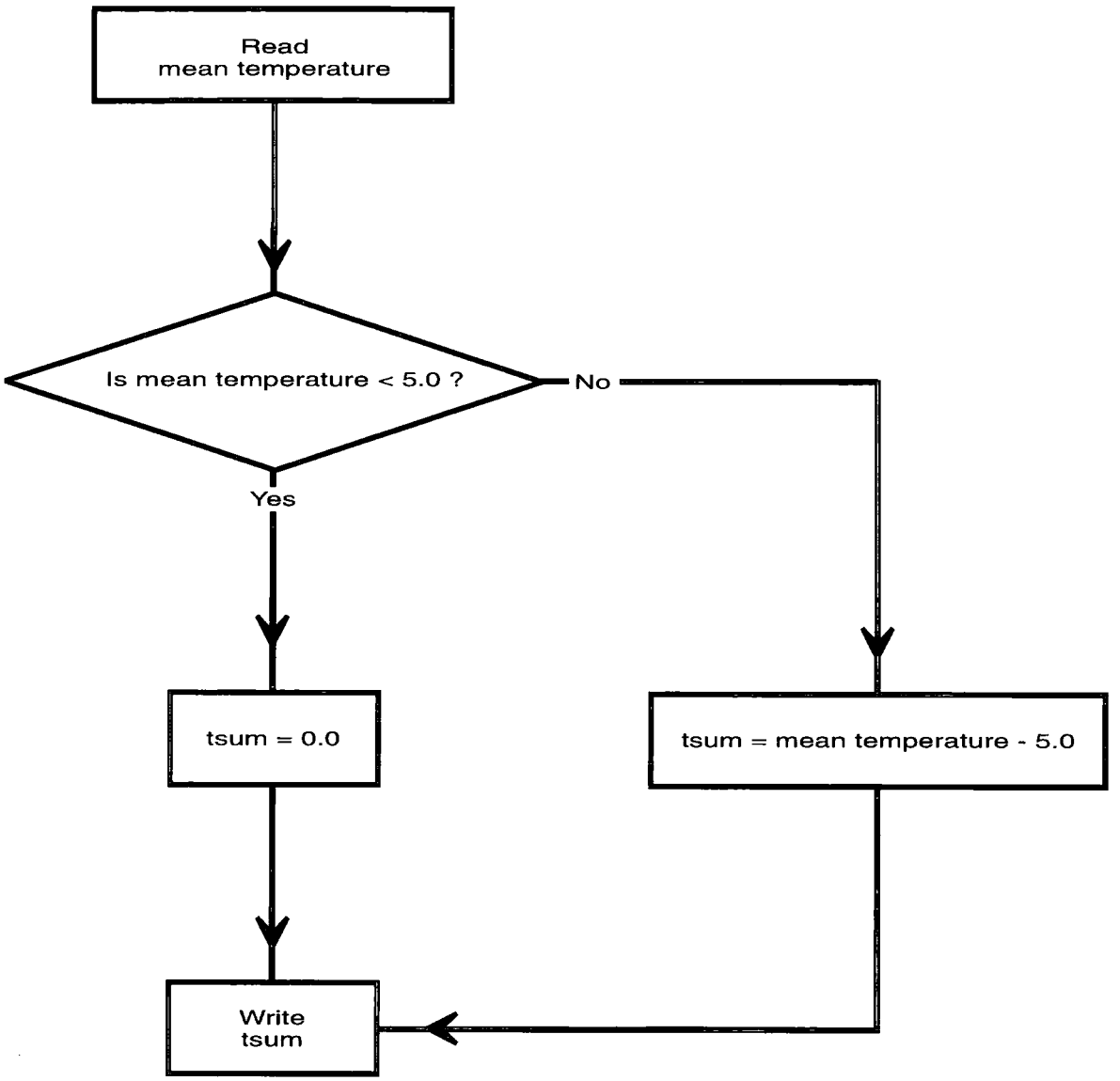

Figure 8.2. The algorithm used to determine daily temperature above 5°C

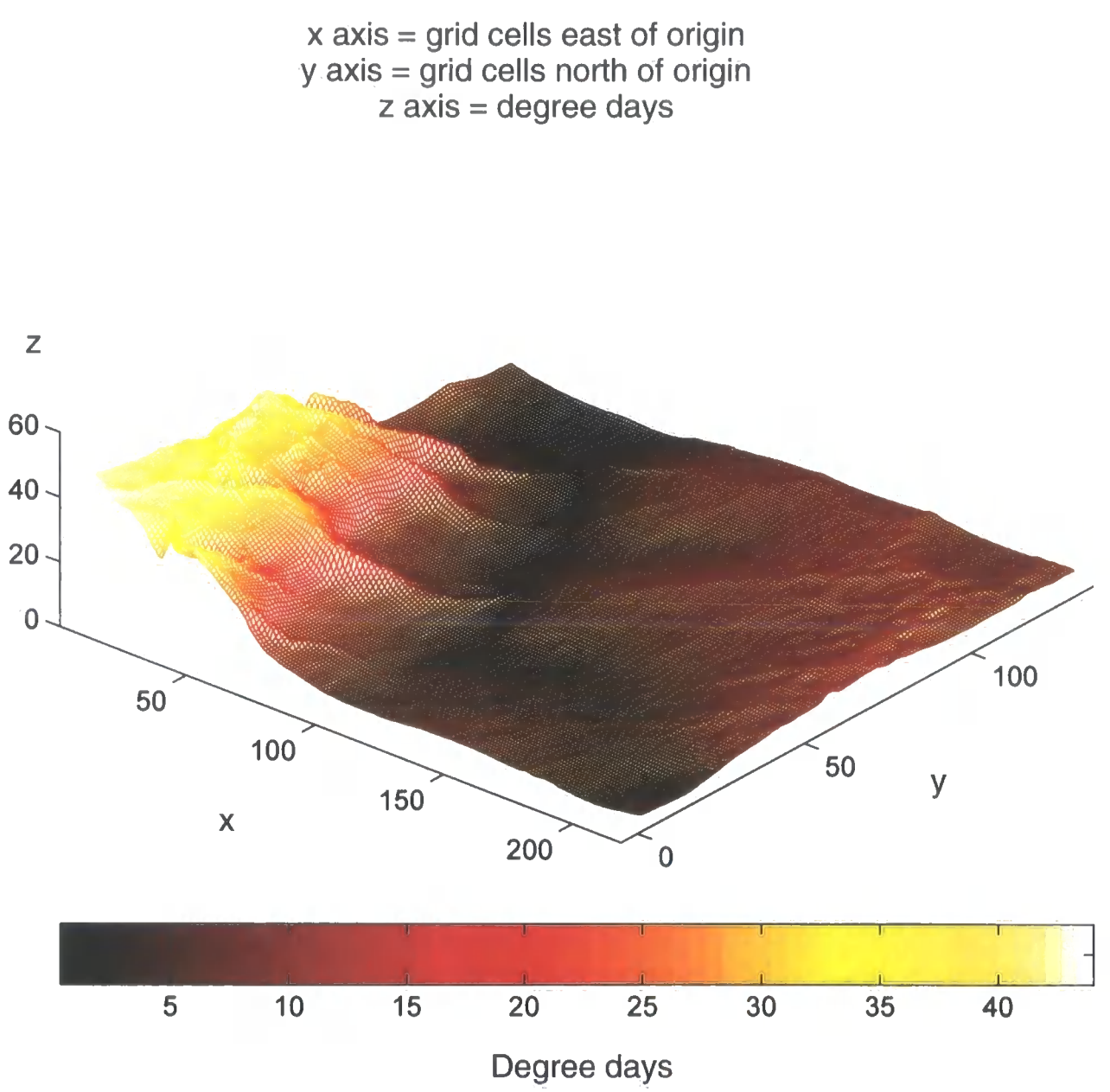

Figure 8.3. Modelled accumulated air temperature above 5 degrees Celsius April 1998

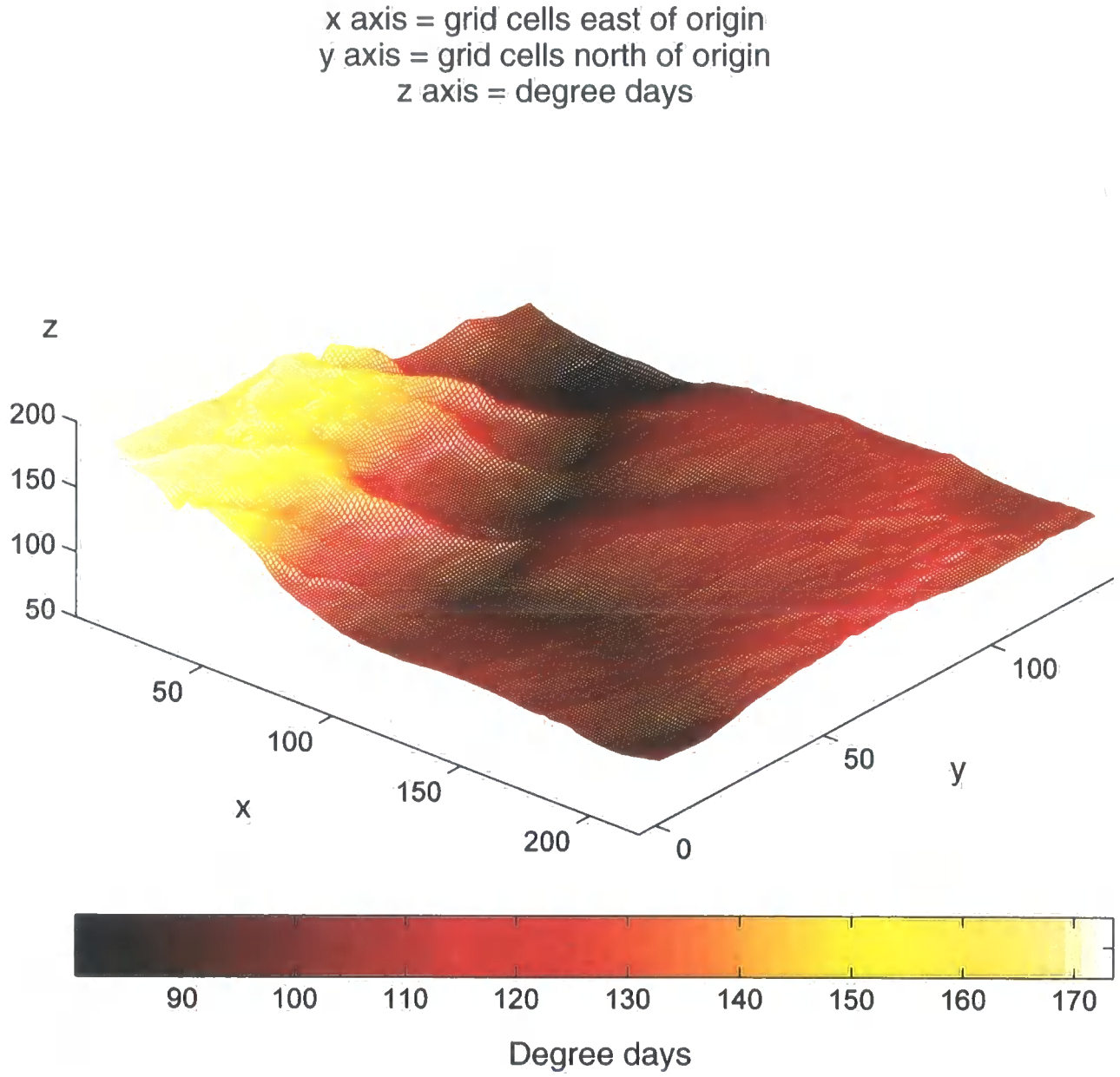

Figure 8.4. Modelled accumulated air temperature above 5 degrees Celsius May 1998

8.3. Frost

Frost is a climatic variable of ecological importance, for example the occurrence of frost in complex elevated terrain can be closely related to plant mortality (Lindkvist and Chen, 1999). The distribution of daily minimum temperature has been shown to be affected by elevation but also on occasion by topographical drainage potential, making the distribution of frost occurrence spatially complex. The calculation of surfaces of frost occurrence provides an ecological application for the minimum temperature surfaces. The months of April and May 1998 were used for illustration. The *Con* function in ARC/INFO was used again to produce intermediate surfaces. The function was used to create a new grid for each day, in which each cell is assigned a value of 1 if the daily minimum air temperature is zero degrees or less, or a value of 0 if the daily minimum air temperature is greater than zero (Figure 8.5). The resulting grids were then summed for each month to give final surfaces of air frost occurrence (Figures 8.6 and 8.7).

During April 1998, the model suggests that the upland areas to the east of the Pennine ridge experienced the highest frequency of air frosts, up to 16 occurrences. This pattern occurs because on 23 of the 30 days in the month, the lapse rate of daily minimum temperature was strongly negative and elevation alone was used as a predictor of temperature. The monthly mean daily minimum air temperature at Moor House was 0.0°C, ambient temperatures were thus low enough on most nights during April 1998 to bring the freezing level below the Pennine summits. On 7 days however, the lapse rate of minimum air temperature exceeded the threshold at which topographic drainage potential is included in the model. This explains the distribution of the highest frost frequencies in areas where elevation is high and topographic drainage potential is low. In these regions, the cooling effect of high elevation (on days with strong negative lapse rates) is compounded by the ponding of subsiding cold air (on days with weak lapse rates and temperature inversions).

During May 1998, the frequency and spatial distribution of modelled air frosts is very different (Figure 8.7). The warmer monthly mean daily minimum air temperature (4.4°C at Moor House) did not bring the freezing level regularly below the Pennine summits, and the

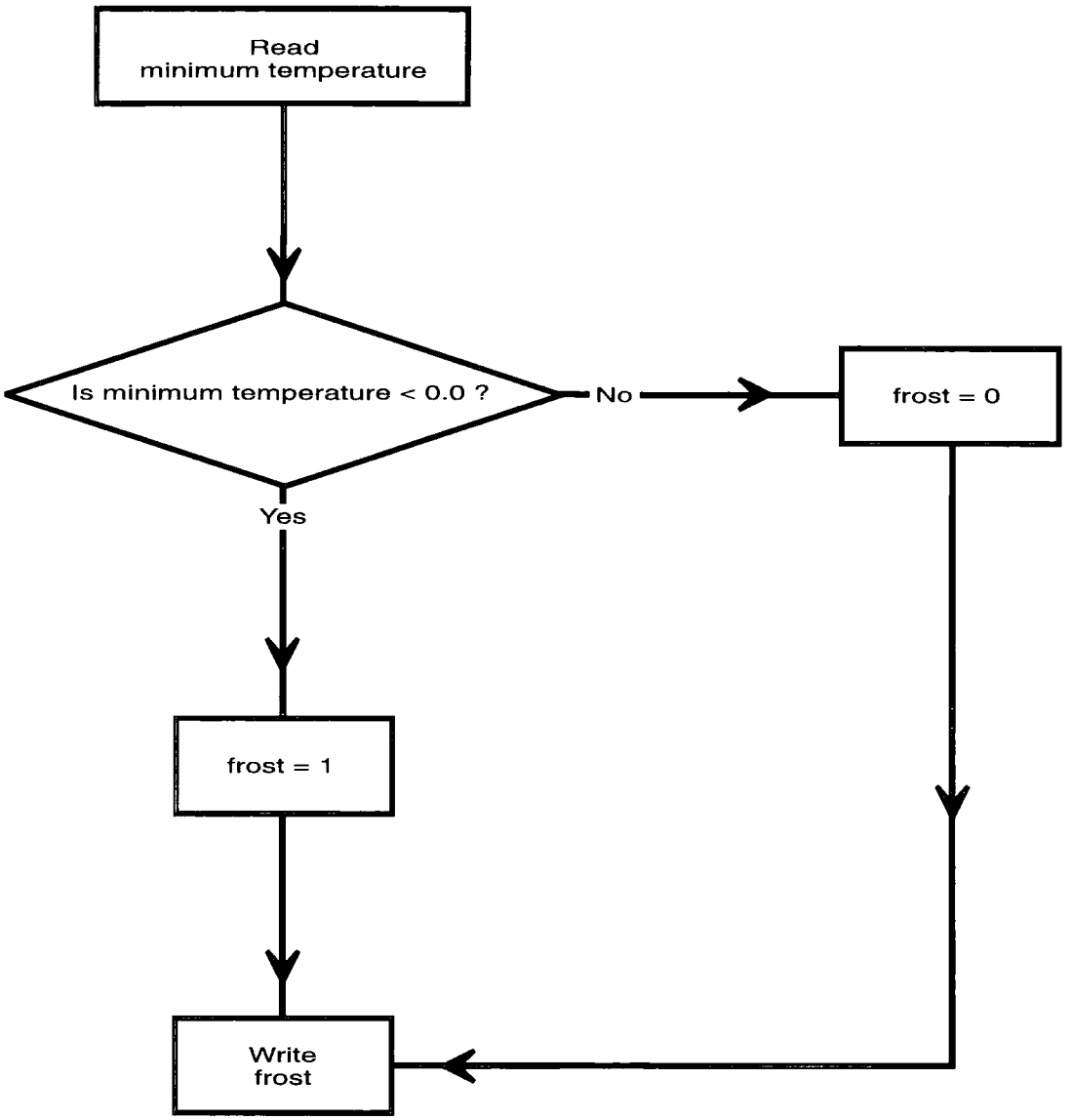

Figure 8.5. The algorithm used to determine daily frost occurrence

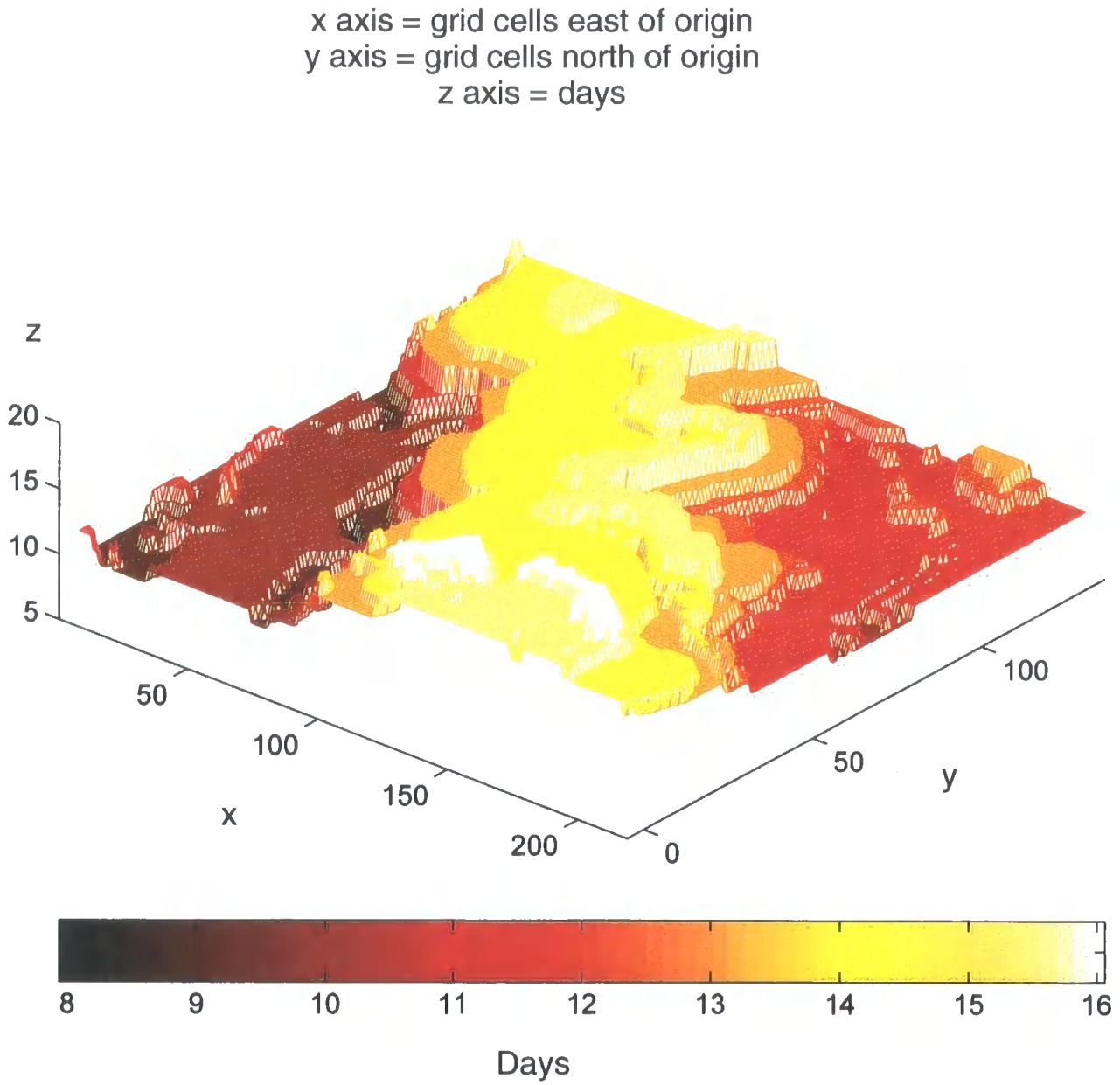

Figure 8.6. Modelled frequency of air frost
April 1998

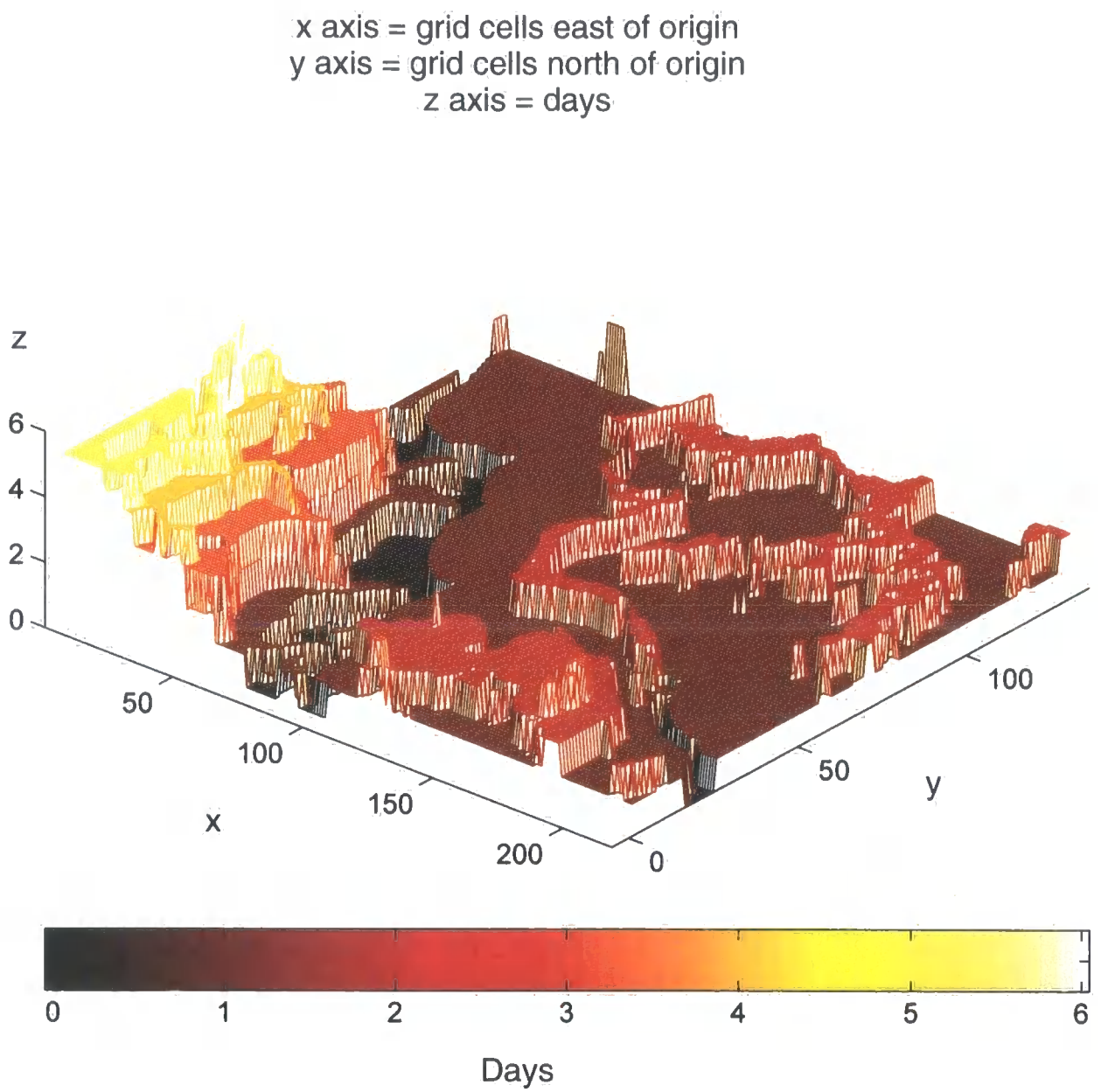

Figure 8.7. Modelled frequency of air frost
May 1998

highest elevations do not coincide with the most frequent frosts. Lapse rates of minimum air temperature were shallow enough on ten days for the effect of topographic drainage potential to be included in the temperature model. The effect is visible where areas of high topographic drainage potential on the scarp slope to the west of the Pennine ridge remained frost-free throughout the month. The distribution of the most frequent modelled air frosts (6 days) at the lowest elevations is due to the occurrence of temperature inversions.

Surfaces of air frost frequency were also generated for April and May 1999. Monthly mean daily minimum air temperature during April 1999 at Moor House was 0.9°C and lapse rates were shallow enough for topographic drainage potential to be included in the model on 11 days. The highest air frost frequencies (14 days) are found both at the highest elevations and in regions of low topographic drainage potential (Figure 8.8). During May 1999, monthly mean daily minimum air temperature at Moor House was 4.1°C, and lapse rates exceeded the threshold for inclusion of topographic drainage potential on only 3 days. The frost distribution for the month is primarily controlled by elevation and strong negative lapse rates (Figure 8.9), with topographic drainage only exerting a slight influence.

In addition to air temperature, ground surface temperatures are also of interest to ecologists. Only one AWS within the study site recorded grass minimum temperature, on the summit of Great Dun Fell after November 1998. Daily minimum air temperature and daily grass minimum temperature (*gra*, °C) were calculated from this station and a regression relationship was fitted between the two variables (Equation 8.1).

$$gra = 0.64(tmn) - 1.65 \qquad 8.1$$
$$(R^2 = 0.58, n = 6264, t(tmn) = 78.6, P < 0.01)$$

The relationship allows an approximate estimation of grass minima from air minima. For April 1998, grass minimum temperature surfaces were calculated from the air minimum temperature surfaces using Equation 8.1, and the frequency of ground frosts was calculated.

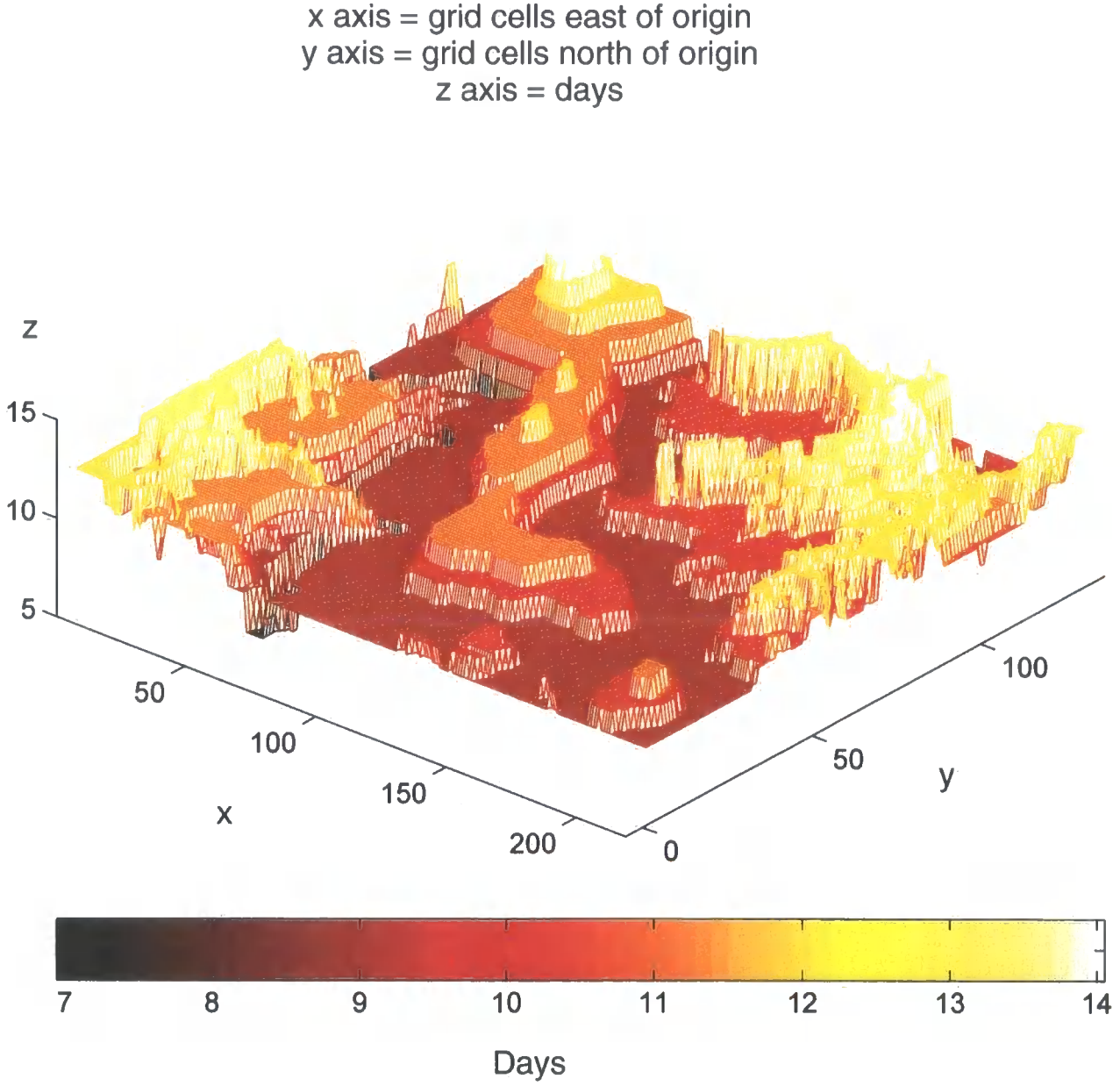

Figure 8.8. Modelled frequency of air frost
April 1999

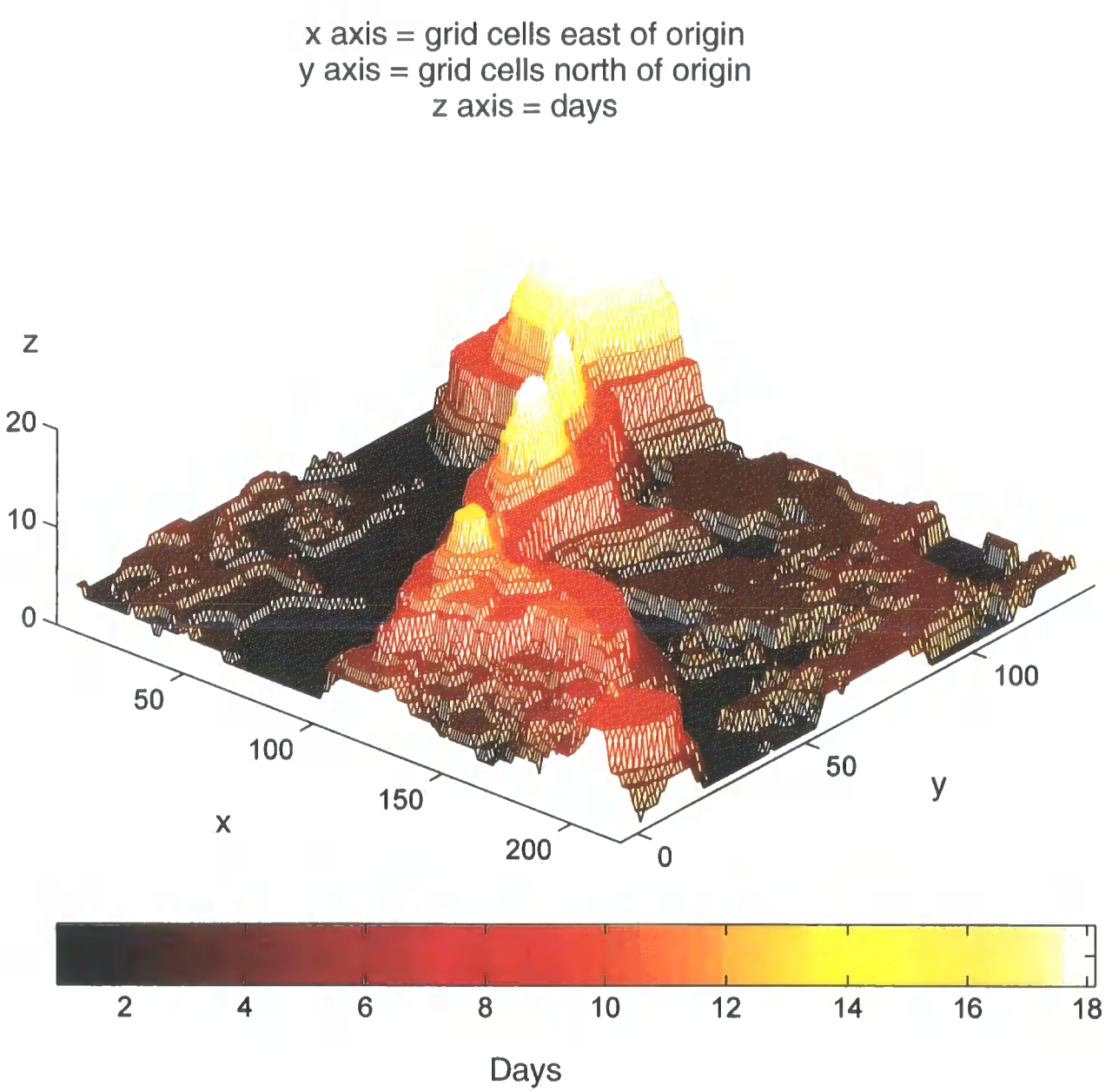

Figure 8.9. Modelled frequency of air frost
May 1999

The distribution of modelled ground frost is shown in Figure 8.10. The modelled frequency ranges from 19 days at the foot of the scarp slope to 27 days on the highest summits. The frequency on the eastern slopes is uniform at 23 days.

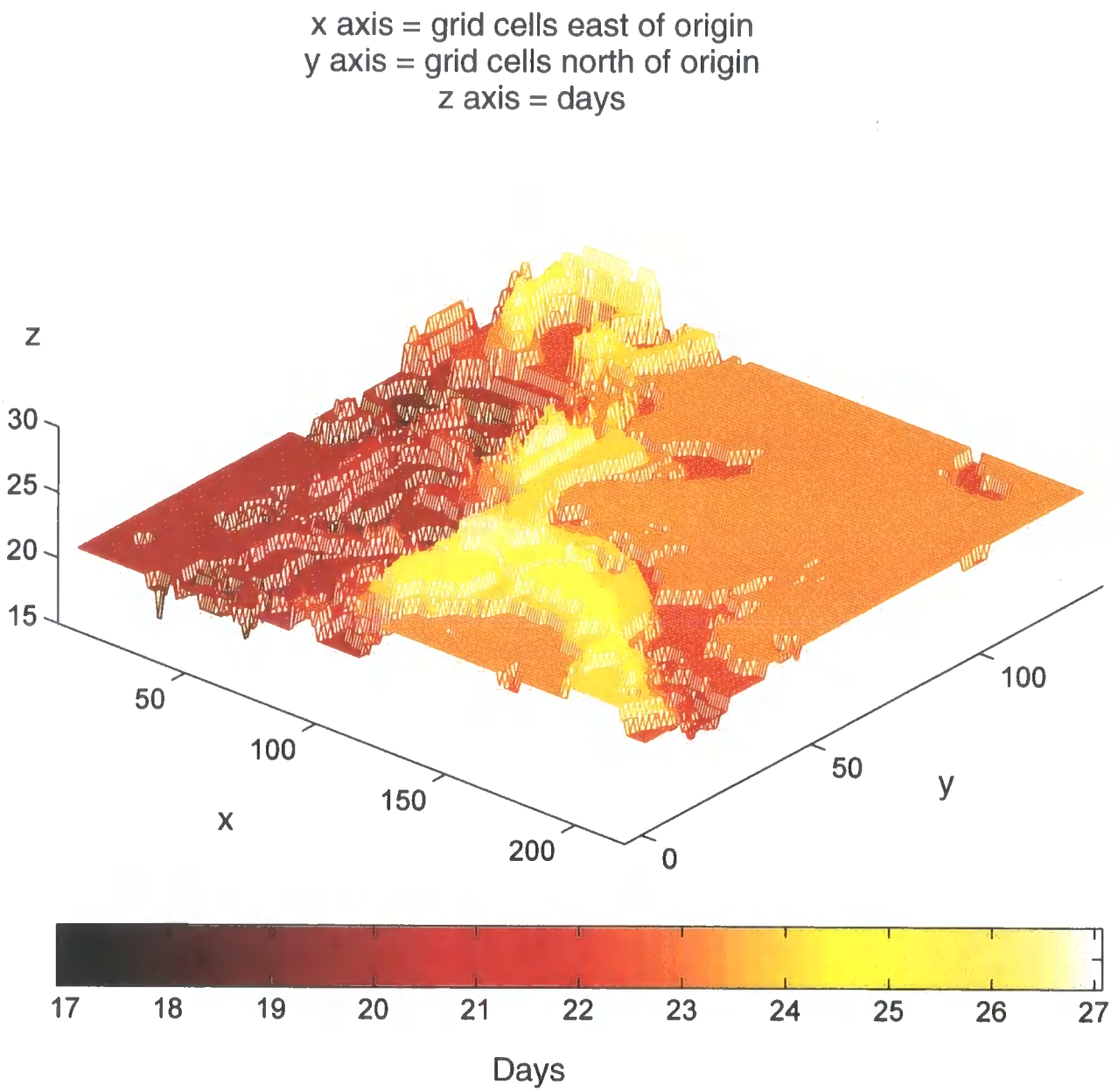

Figure 8.10. Modelled frequency of ground frost
April 1998

8.4. Moisture balance

Consecutive daily surfaces of *PE* (obtained by the methods described in Chapter 7) may be summed to derive composite totals for longer periods. Two example surfaces (Figures 8.11 and 8.12) were generated from the daily data for the months of July and August 1999 respectively.

During both July and August 1999, total *PE* is inversely proportional to elevation, with total monthly *PE* decreasing with elevation at a rate of -8.9×10^{-2} mm m^{-1} during July and at a rate of -4.5×10^{-2} mm m^{-1} during August. Below 300 m elevation in the Eden valley at the foot of the scarp slope monthly totals reach 110 mm during July and 85 mm during August, while above 850 m totals do not exceed 50 mm in either month.

The precipitation data do not show any systematic relationship with topography, and therefore daily precipitation totals were estimated by taking the mean of the catch measured at the Moor House station and at the Great Dun Fell summit station. In July 1999 the monthly total was 73.8 mm at Moor House, and 77.5 mm at Great Dun Fell summit, giving an estimated spatial mean value of 75.7 mm. In August 1999 the monthly total was 116.8 mm at Moor House and 116.5 mm at the summit, giving a spatial mean value of 116.7 mm. The *PE* surfaces can be subtracted from the spatial precipitation estimates to yield estimates of monthly moisture budget (Figures 8.13 and 8.14).

Moisture stress is higher at lower elevations due to the systematic relationship of *PE* with elevation. During July 1999 the modelled surface suggests that a moisture deficit exists below about 570 m, with *PE* exceeding precipitation. During August 1999 modelled precipitation exceeds *PE* throughout the study area. If precipitation does increase with elevation despite the lack of evidence in the data gathered by this study, the gradient of moisture stress with elevation may be even greater than these models suggest.

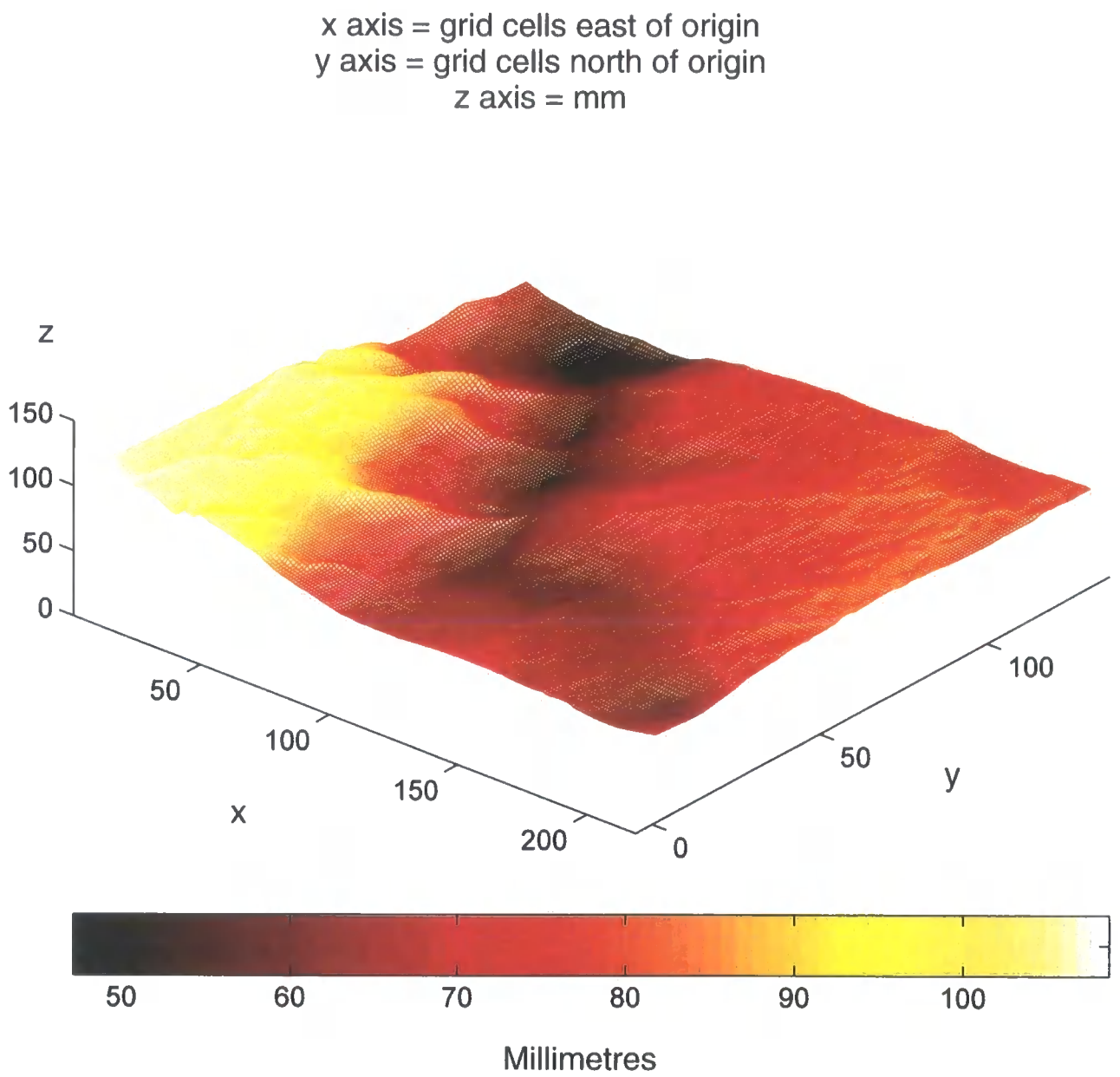

Figure 8.11. Modelled total potential evapotranspiration
July 1999

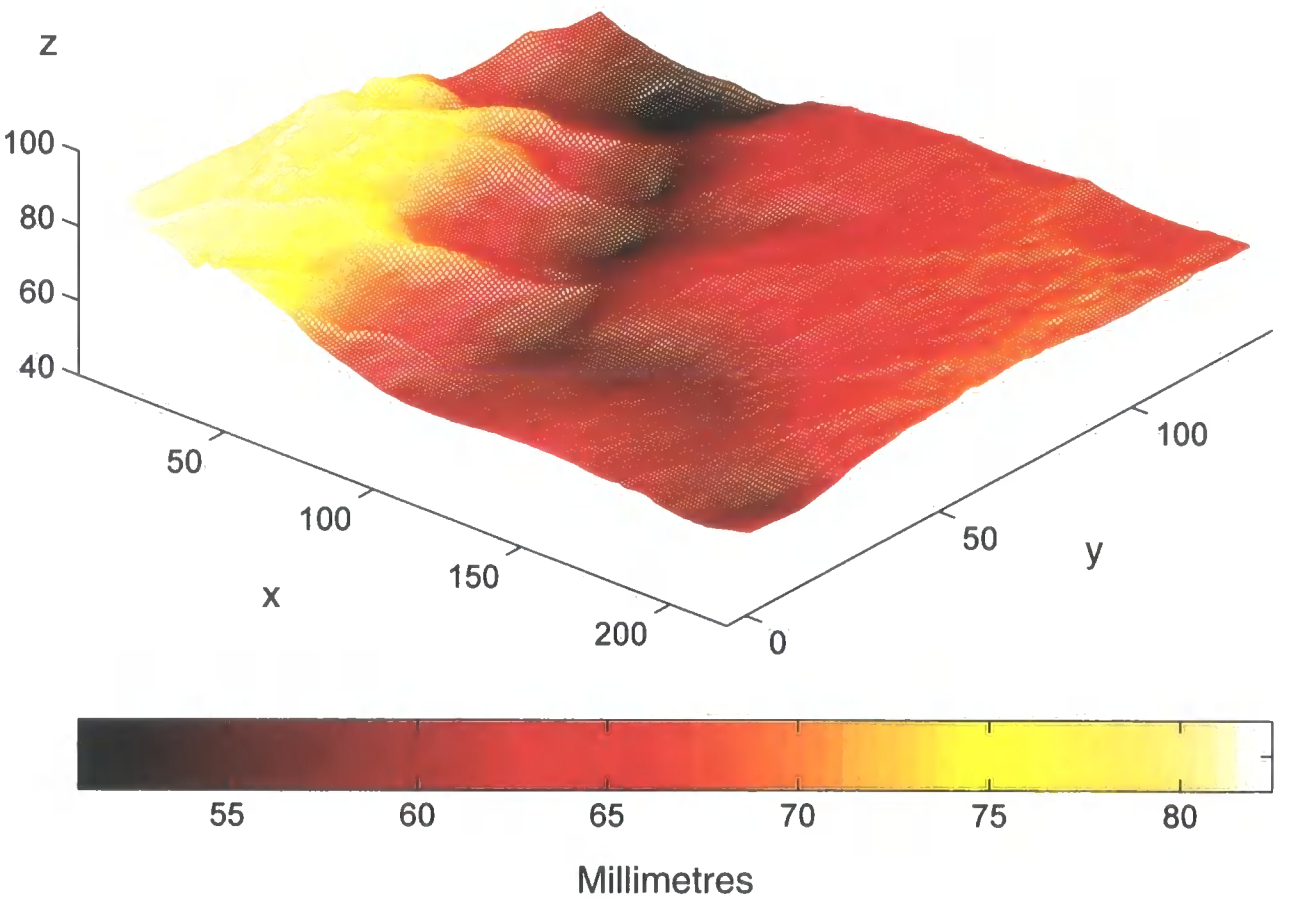

Figure 8.12. Modelled total potential evapotranspiration August 1999

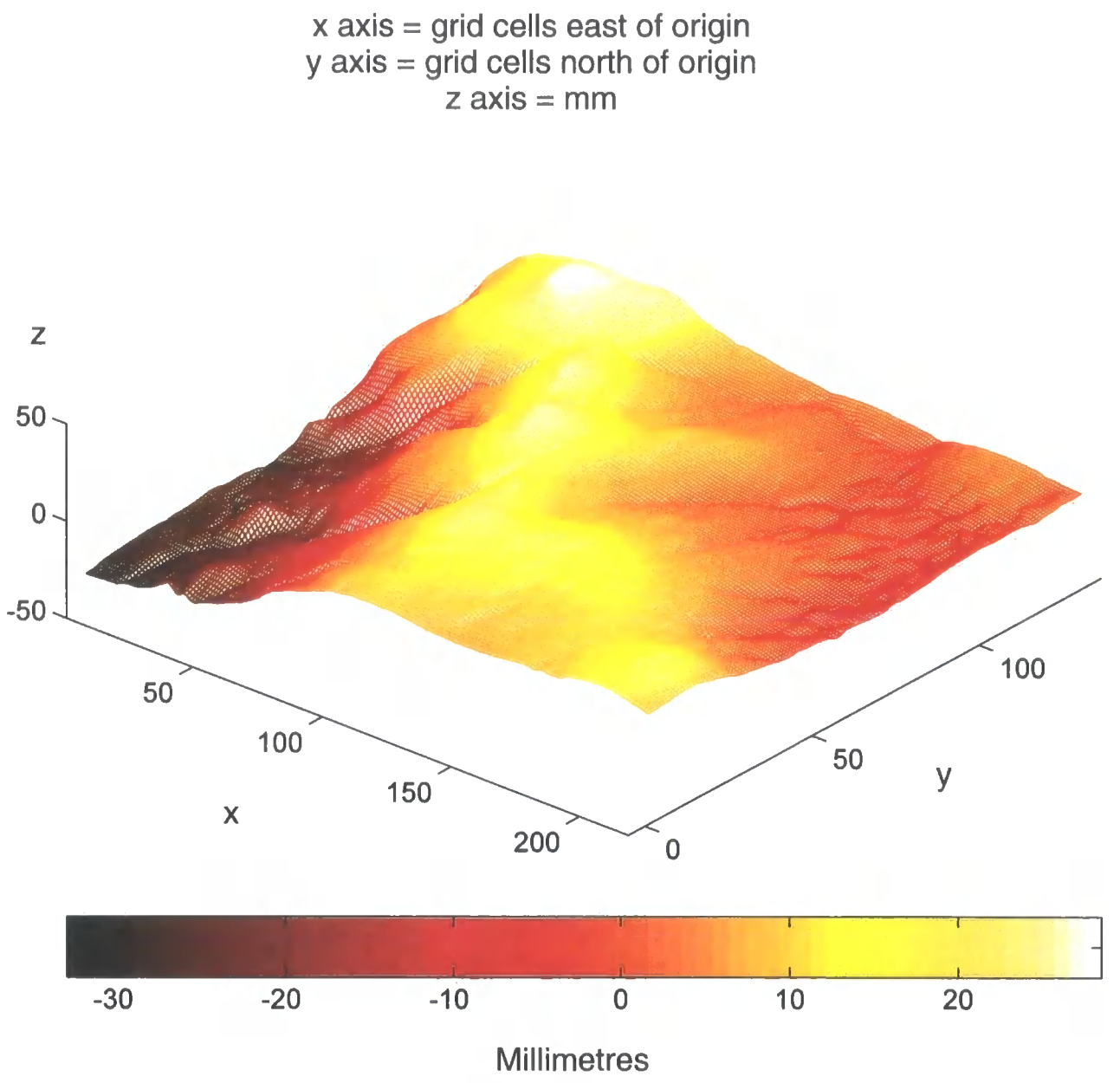

Figure 8.13. Modelled moisture budget (precipitation minus *PE*) July 1999

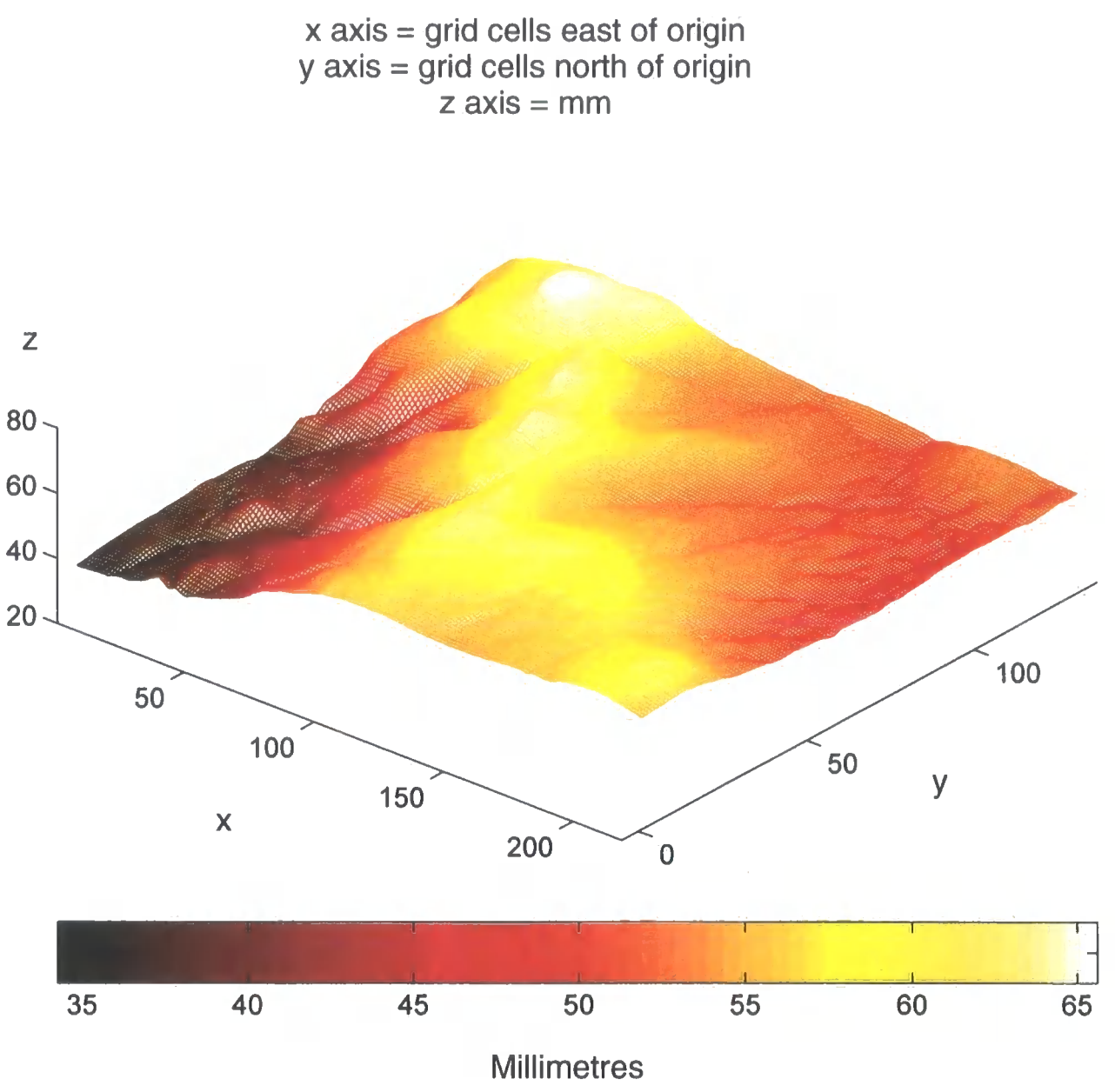

Figure 8.14. Modelled moisture budget (precipitation minus *PE*)
August 1999

8.5. Discussion

Fluctuations of temperature and lapse rate, including the development of temperature inversions, have a profound influence on the spatial distribution of temperature. Such fluctuations are short-lived and illustrate the need to use a daily time step for modelling the climate surfaces. Surfaces derived for longer time periods (e.g. a month or growing season) should be calculated from the original daily surfaces to ensure such high-frequency effects are retained in the data.

The frost surfaces generated for April and May 1998 and 1999 show that the frequency and spatial distribution of frost vary markedly over time, both between consecutive days and months, and inter-annually. The complexity of the relationship between frost and elevation in the study site has been noted previously, with the occasional tendency for temperature minima in the Eden valley to fall below minima on the summits (Manley, 1942). The methods presented here allow the quantification and spatial modelling of these phenomena.

There is a discrepancy between climatic variables which are conducive to spatial modelling (e.g. air temperature at screen height) and those which are of most relevance to ecological studies (e.g. temperature in the soil or at the ground surface). Air temperature recorded at screen height is relatively well correlated over larger distances than ground surface measurements, which are more affected by local conditions (Linacre, 1992). Climate in the soil or near the ground is likely to show micro-scale variations associated with differences in soil heat capacity, conductivity, emissivity and moisture content, as well as vegetation characteristics. For example, the frequency of ground frost greatly exceeds the frequency of air frost due to rapid radiation loss from the poorly drained surface and coarse vegetation (Manley, 1980). In addition to the weak spatial correlation of soil and ground surface climate, these variables are also relatively sparsely sampled (none of the roving AWS have soil or surface sensors). Ground surface temperature measurements are available from a single station, necessitating an empirical regression model to estimate spatial surfaces of grass minimum temperature. The surfaces of other temperature variables are estimated using the process-based daily lapse rate model and can be interpreted with a greater level of confidence than the surfaces of grass minimum temperature and ground frost surfaces.

For ecological applications there is a need to consider actual evapotranspiration, rather than *PE* which is calculated purely from atmospheric variables. The availability of soil moisture affects evaporation rates. The thin soils on the Pennine ridge will dry more quickly than the deeper peat soils at lower elevations, causing differences in the ecological response to water stress. The moisture budget estimates presented in this chapter are calculated by accumulating the deficit or surplus of *PE* relative to precipitation calculated at a daily time scale. The method does not account for important hydrological processes such as storage and transport of moisture within the soil, nor does it address the fact that prior climatic and hydrological events exert a lagged effect on soil moisture.

Chapter 9. General discussion and conclusion

Practical constraints prevented the experimental AWS networks from extending beyond the boundary of the Moor House NNR. Due to these geographical limitations, the models have not been tested outside the 72 km^2 modelling region. The methods cannot be used with confidence to extrapolate absolute daily estimates of climate beyond this region. Nevertheless, previous work suggests that correlation between station data may fall linearly with distance (Linacre, 1992), implying that these model surfaces could be used to estimate approximate climatic conditions in other areas of the northern Pennines. The physically-based lapse rate models for temperature and *PE* could be applied to other sites with similar climatic boundary conditions, although the effects of topography on the residuals from the linear lapse rate model would require re-quantification. The solar radiation model is more empirical, but should perform with similar accuracy at other sites if the model parameters (e.g. grid cell resolution, the area and latitude of the study site) are similar to those used here.

A daily time resolution was used throughout for modelling climate surfaces. This resolution was chosen to complement the landscape-scale spatial resolution. The resulting surfaces identify climatic patterns related to topographic complexity and day-to-day climatic fluctuations which are not captured by methods designed to operate at larger scales. However, any sampling strategy necessarily overlooks variability at scales smaller than the chosen temporal and spatial resolution (in this case 1 day and 50 m). Systematic climatic variation occurs at smaller scales (e.g. variation in lapse rate with time of day (Pielke and Mehring, 1977), or with local soil characteristics or micro-scale exposure) but analysis of these effects is beyond the scope of this research.

The optimum method for estimating daily climate within complex terrain depends on the size and topographic characteristics of the site. Other methods previously developed have been designed to spatialise data over a larger area, e.g. 400 000 km^2 (Thornton *et al.*, 1997). However, the grid cell resolution was an order of magnitude coarser than was used for the model described here, and the larger spatial coverage necessitates numerical smoothing of the surfaces (Thornton *et al.*, 1997). At smaller scales, models based on lapse rates tend to output data for a specific site rather than generating spatial climate

surfaces. Such models typically require an elevation difference in excess of 500 m between a base station and target site (Running *et al.*, 1987). The measured and modelled associations between climate, landscape and ecological processes are scale-dependent and an appropriate spatial resolution must be chosen to capture the processes of interest (Turner, Dodson and Marks, 1996). The models developed here thus meet an explicit need, having been designed specifically to account for climatic variability at a landscape-scale within the geographical parameters of the study site.

The use of 50 m grid cells may be approaching the finest feasible resolution for landscape-scale modelling of climate. The difficulty of attributing field measurements accurately to a particular grid cell increases with spatial resolution, although the removal of selective availability from the GPS system in May 2000 (Cruddace and Clarke, 2000) mitigates this problem. More importantly, variations in local surface energy budget characteristics are likely to become increasingly important at smaller scales, reducing the accuracy of landscape-scale methods. Different predictor variables (e.g. soil heat capacity, emissivity and moisture content, surface albedo and roughness) may be needed to explain the geographical controls on climate at the scale of interest (Lennon and Turner, 1995). If this work is to be extended to smaller scales, spatial analysis of climate will benefit from a reduced modelling area, using intensive sampling at experimental plots on selected slopes. As the focus shifts towards micro-scale processes it will also become necessary to sample boundary-layer climate variables at the ground surface or at the interface between vegetation and atmosphere.

Estimation of daily climate surfaces for the study site using partial thin plate splines is not feasible. This method would prove excessively costly in terms of computing resources and time, requiring a separate interpolation for each climate variable and each day. The accuracy of spline interpolations decreases markedly when the station data are sparse (Bates and Wahba, 1982), the number of AWS available within the study site is insufficient to support numerical interpolation (Hutchinson and Gessler, 1994). In contrast, the methods developed here require observed data from a minimal number of weather stations to estimate a reliable daily surface. Although networks of roving stations were used to calibrate and test the models, daily surfaces can now be estimated using data from only two

base stations within the study site. Data from these base stations are also used to provide information about larger-scale atmospheric circulation, for example summit wind direction is used to indicate regional-scale wind flow.

At the scale of the Moor House reserve, elevation exerts a fundamental control on temperature, an influence enhanced by the steep mean lapse rates characteristic of the maritime air masses which prevail in northern Britain (Barry, 1992). Whereas latitude and longitude are used effectively as statistical predictors of temperature or to interpolate temperature numerically at much larger geographical and temporal scales, elevation can be used as the primary predictor within the relatively small area of the study site, in conjunction with daily temperature data. The vertical dimension captures the fundamental variability of temperature arising from adiabatic energy exchange. Horizontal energy fluxes are also accounted for; the model quantifies temperature variance on axes defined by the *dist* and *drain* variables rather than latitude and longitude.

Many ecological applications estimate temperature at remote sites by extrapolating from data observed at a lower station, using a constant lapse rate calculated empirically from long-term mean data, e.g. -6.0×10^{-3} °C m^{-1} for the Austrian Alps (Gottfried, Pauli and Grabherr, 1999) or relating to idealised atmospheric conditions, e.g. the US Standard Atmosphere lapse rate of -6.5×10^{-3} °C m^{-1} (Burman and Pochop, 1994). In reality, lapse rates vary dramatically from day-to-day and this variability must be captured in any temperature data used for ecological analysis. The mean lapse rate at any site is unlikely to correspond with an ideal value, and even a slight discrepancy will cause a systematic and cumulative error in the calculated temperature. The approach described here represents a major improvement, incorporating the anomalous conditions occurring during short-term events which may have a profound ecological influence.

In the context of scenarios of climate change for the uplands, the down-scaling of climate data from GCM models requires information about lapse rate and atmospheric circulation as well as temperature for each grid cell. The relative frequency of weather systems and air masses is particularly important (Houghton *et al.*, 1996) as a change in the frequency of particular weather types can affect climate without any change in weather type

characteristics. Within Britain, recent warming has coincided with enhanced progressive westerly circulation during winter and spring (Briffa, Jones and Kelly, 1990). However, the polar maritime air masses associated with westerly air flow have steep lapse rates (Manley, 1980), so even under a scenario of sea-level warming, mean conditions in the uplands may thus remain stable (Garnett, Ineson and Adamson, 1997) or become cooler. The frequency of snowfall and duration of snow lying may even increase at high elevations (Mordaunt, 1999). Similarly, an amelioration of temperature sufficient to raise the tree line within the study site from 600 m to 800 m could result purely from an increase in the frequency of summer anticyclones (Manley, 1942). Explicit handling of temperature lapse rate by the model is necessary to capture the dependence of temperature on elevation, this is as important for the analysis of climate change impacts as it is at the daily time scale.

Topo-climatic complexity causes heterogeneous communities to develop within small areas due to variations in elevation, slope orientation and soil properties. High levels of genetic, species and ecosystem diversity are common in upland areas (Gross, 1999), as is endemism, for example *Gentiana verna* L. in Upper Teesdale (Huntley *et al.*, 1998). Upland ecosystems are vulnerable however, because they are adapted to marginal climatic conditions and are sensitive to climatic change (Bellamy *et al.*, 1969). For example, diversity has increased at some European upland sites due to invaders from lower elevations (Gottfried *et al.*, 1999). The developed models will allow monitoring of spatial climate changes throughout the Moor House reserve, in addition to the on-going monitoring at the ECN site. Numerous climate-dependent ecological phenomena are under investigation within the Moor House NNR, such as the distribution of insect larvae in relation to temperature and moisture availability (Briones *et al.*, 1997). Previously, these analyses have been limited to specific sites or transects; in future the climate surfaces developed here will allow spatial modelling throughout the study site.

The work provides methodologies for estimating surfaces of climatic data for small-scale ecological applications in complex terrain, at sites where dense station data are not available. The models are based on physical principles and the site-specific effects of topographic complexity are included using empirically-calculated relationships. The models result in high resolution daily climate surfaces that capture landscape-scale

influences. Discrete surfaces are calculated for each day, capturing the full range of day-to-day climate variability. The data requirements for these methods are minimal, and the modelling is computationally inexpensive.

Improvements to the climate modelling within the study site would result from the exposure of the pyranometers parallel to the slope at the AWS base stations at Moor House and Great Dun Fell summit. This arrangement provides a more ecologically meaningful measurement in complex terrain, and allows better estimation of the spatial models of daily solar radiation. The measurement of precipitation within the study site would benefit from the installation of the rain gauge at Great Dun Fell summit within a ground pit as suggested by ECN protocols (Sykes and Lane, 1997) in order to minimise the effects of turbulence at this extremely exposed site. This would standardise the sampling of precipitation at the two base stations. The installation of infra-red lamps (Perla and Martinelli, 1976) would prevent the loss of data which regularly occurs in winter when rime ice accumulates on the wind and radiation sensors, particularly on the Great Dun Fell summit AWS. Infra-red lamps may be economically viable if the value of an unbroken sequence of climate surfaces exceeds the costs of installation and operation. A barometer would be a useful addition to the AWS instrumentation, at one or both base stations. Atmospheric pressure is one of the easiest climatic variables to monitor unambiguously, and daily observations would allow improvements to the modelling of vapour pressure and *PE*.

References

Archer, D. and Stewart, D. (1995) The installation and use of a snow pillow to monitor snow water equivalent. *Journal of the Chartered Institution of Water and Environmental Management.* **9**, 221-230.

Barrow, E. and Hulme, M. (1997) Describing the surface climate of the British Isles. Pages 33-62 in Hulme, M. and Barrow, E. (eds.) *Climates of the British Isles, past, present and future*. Routledge, London.

Barrow, E.M., Hulme, M. and Jiang, T. (1993) *A 1961-90 baseline climatology and future climate change scenarios for Great Britain and Europe, part 1: A 1961-90 Great Britain baseline climatology*. Report accompanying the datasets prepared for the landscape dynamics and climate change TIGER IV consortium. Climatic Research Unit, Norwich.

Barry, R.G. (1992) *Mountain weather and climate*. Routledge, London.

Barton, J.S. (1984) Observing mountain weather using an automatic station. *Weather* **39**, 140-5.

Bates, D. and Wahba, G. (1982) Computational methods for generalised cross-validation with large data sets. Pages 283-296 in Baker, C. and Miller, G. (eds.) *Treatment of integral equations by numerical methods*. Academic Press, London.

Baylis, M., Meiswinkel, R. and Venter, G.J. (1999) A preliminary attempt to use climate data and satellite imagery to model the abundance and distribution of *Culicoides imicola* in southern Africa. *Journal of the South African Veterinary Association* **70**, 80-89.

Beard, G.R., Scott, W.A. and Adamson, J.K. (1999) The value of consistent methodology in long-term environmental monitoring. *Environmental Monitoring and Assessment* **54**, 239-258.

Becker, C.F. and Boyd, J.S. (1957) Solar radiation and availability on surfaces in the United States as affected by season, orientation, latitude, altitude and cloudiness. *Solar Energy* **1**, 13-21.

Bellamy, D.J., Bridgewater, P., Marshall, C. and Tickle, W.M. (1969) Status of the Teesdale rarities. *Nature* **222**, 238-243.

Bjorkman, O. (1981) The response of photosynthesis to temperature. Pages 273-301 in Grace, J., Ford, E.D. and Jarvis, P.G. (eds.) *Plants and their atmospheric environment*. Blackwell, London.

Blaszczynski, J.S. (1997) Landform characterization with geographic information systems. *Photogrammetric Engineering and Remote Sensing* **63**, 183-191.

Bloom, A.J. (1996) Principles of instrumentation for physiological ecology. Pages 1-13 in Pearcy, R.W., Ehleringer, J., Mooney, H.A. and Rundel, P.W. (eds.) *Plant physiological ecology*. Chapman and Hall, London.

Bolstad, P.V., Swift, L., Collins, F. and Regniere, J. (1998) Measured and predicted air temperatures at basin to regional scales in the southern Appalachian mountains. *Agricultural and Forest Meteorology* **91**, 161-176.

Bradley, R.S. and Jones, P.D. (1992) Climate since A.D. 1500: Introduction. Pages 1-16 in Bradley, R.S. and Jones, P.D. (eds.) *Climate since A.D. 1500*. Routledge, London.

Briere, J.F., Pracros, P., le Roux, A.Y. and Pierre, J.S. (1999) A novel rate model of temperature dependent development for arthropods. *Population Ecology* **28**, 22-29.

Briffa, K.R., Jones, P.D. and Kelly, P.M. (1990) Principal component analysis of the Lamb catalogue of daily weather types: part 2, seasonal frequencies and update to 1987. *International Journal of Climatology* **10**, 549-563.

Briones, M.J.I., Ineson, P. and Piearce, T.G. (1997) Effects of climate change on soil fauna: responses of enchytraeids, Diptera larvae and tardigrades in a transplant experiment. *Applied Soil Ecology* **6**, 117-134.

Brock, T.D. (1981) Calculating solar radiation for ecological studies. *Ecological Modelling* **14**, 1-19.

Buchan, A. (1893) The influence of high winds on the barometer at the Ben Nevis observatory. *Journal of the Scottish Meteorological Society* **9**, 132-137.

Burman, R. and Pochop, L.O. (1994) *Evaporation, evapotranspiration and climatic data*. Elsevier, Amsterdam.

Burt, T.P. (1994) Long term study of the natural environment: perceptive science or mindless monitoring? *Progress in Physical Geography* **18**, 475-496.

Burt, T.P., Adamson, J.K. and Lane, A.M.J. (1998) Long term rainfall and streamflow records for north central England: Putting the Environmental Change Network site at Moor House, Upper Teesdale, in context. *Hydrological Sciences Journal* **43**, 775-787.

Caporn, S.J.M., Risager, M. and Lee, J.A. (1994) Effect of nitrogen supply on frost hardiness in *Calluna vulgaris* (L) Hull. *New Phytologist* **128**, 461-468.

Chapman, H.M. and Bannister, P. (1994) Vegetative production and performance of *Calluna vulgaris* in New Zealand, with particular reference to Tongariro National Park. *New Zealand Journal of Ecology* **18**, 109-121.

Chapman, H.M. and Bannister, P. (1995) Flowering, shoot extension and reproductive performance of heather, *Calluna vulgaris* (L) Hull, in Tongariro National Park, New Zealand. *New Zealand Journal of Botany* **33**, 111-119.

Chuan, G.K. and Lockwood, J.G. (1974) An assessment of the topographic controls on the distribution of rainfall in the central Pennines. *Meteorological Magazine* **103**, 275-87.

Clapham, A.R., Tutin, T.G. and Moore, D.M. (1987) *Flora of the British Isles*. University Press, Cambridge.

Cooper, P.I. (1969) The absorption of solar radiation in solar stills. *Solar Energy* **12**, 333-336.

Craig, M.H., Snow, R.W. and le Sueur, D. (1999) A climate-based distribution model of malaria transmission in sub-Saharan Africa. *Parasitology Today* **15**, 105-111.

Cruddace, P. and Clarke, P. (2000) Spot on? Is GPS becoming more useful? *Summit* **19**, 34-35.

Davies, T., Kelly, P.M. and Osborn, T. (1997) Explaining the climate of the British Isles. Pages 11-32 in Hulme, M. and Barrow, E. (eds.) *Climates of the British Isles, present, past and future*. Routledge, London.

Dewey, K.F. (1977) Daily maximum and minimum temperature forecasts and the influences of snow cover. *Monthly Weather Review* **105**, 1594-1597.

Duffie, J.A. and Beckman, W.A. (1980) *Solar engineering of thermal processes.* Wiley, New York.

Eddy, A., Welch, D. and Rawes, M. (1969) The vegetation of the Moor House National Nature Reserve in the northern Pennines, England. *Vegetatio* **16**, 239-284.

Essery, R. and Pomeroy, J. (1999) A distributed model of blowing snow over complex terrain. *Hydrological Processes* **13**, 2423-2438.

Fitter, A.H., Self, G.K., Brown, T.K., Bogie, D.S., Graves, J.D., Benham, D. and Ineson, P. (1999) Root production and turnover in an upland grassland subjected to artificial soil warming respond to radiation flux and nutrients, not temperature. *Oecologia* **120**, 575-581.

Flocas, H.A., Helmis, C.G., Blikas, S.N., Asimakopolous, D.N., Bartzis, J.G. and Deligiorgi, D.G. (1998) Mean characteristics of the katabatic flow of a 1024 m high knife edge mountain. *Theoretical and Applied Climatology* **59**, 237-249.

Foot, J.P., Caporn, S.J.M., Lee, J.A. and Ashenden, T.W. (1996) The effect of long-term ozone fumigation on the growth, physiology and frost sensitivity of *Calluna vulgaris*. *New Phytologist* **133**, 503-511.

Ford, E.D. and Milne, R. (1981) Assessing plant response to the weather. Pages 333-362 in Grace, J., Ford, E.D. and Jarvis, P.G. (eds.) *Plants and their atmospheric environment.* Blackwell, London.

Fotheringham, A.S. and Rogerson, P.A. (1993) GIS and spatial analytical problems. *International Journal of Geographical Information Systems* **7**, 3-19.

Franks, S.W. and Beven, K.J. (1997) Estimation of evapotranspiration at the landscape scale: A fuzzy disaggregation approach. *Water Resources Research* **33**, 2929-2938.

Fritts, H.C. and Shao, X.M. (1992) Mapping climate using tree-rings from western North America. Pages 269-295 in Bradley, R.S. and Jones, P.D. (eds.) *Climate since A.D. 1500.* Routledge, London.

Fujita, T., Baralt, G. and Tsuchiya, J. (1968) Aerial measurement of radiation temperatures over Mt. Fuji and Tokyo areas and their application to the determination of ground and water surface temperatures. *Journal of Applied Meteorology* **7**, 801-816.

Furman, R.W. (1978) Wildfire zones on a mountain ridge. *Annals of the Association of American Geographers* **68**, 89-94.

Garnett, M.H., Ineson, P. and Adamson, J.K. (1997) A long-term upland temperature record: no evidence for recent warming. *Weather* **52**, 342-351.

Geiger, R., Aron, R.H. and Todhunter, P. (1995) *The climate near the ground.* Vieweg, Braunschweig.

Glaisher, J. (1848) On the corrections to be applied to meteorological observations. *Philosophical Transactions* **1**, 125-139.

Gloyne, R.W. (1971) A note on the average annual mean of daily earth temperature in the United Kingdom. *Meteorological Magazine* **100**, 1-6.

Goodale, C.L., Aber, J.D. and Ollinger, S.V. (1998) Mapping monthly precipitation, temperature and solar radiation for Ireland with polynomial regression and a digital elevation model. *Climate Research* **10**, 35-49.

Gottfried, M., Pauli, H., Reiter, K. and Grabherr, G. (1999) The Austrian research initiative: global change effects at the low temperature limits of plant life: a progress report. Pages 54-56 in Price, M. (ed.) *Global change in the mountains.* Parthenon, Carnforth.

Goudie, A.S. and Brunsden, D. (1994) *The environment of the British Isles, an atlas.* Clarendon Press, Oxford.

Goudriaan, J. (1986) A simple and fast numerical method for the computation of daily totals of crop photosynthesis. *Agricultural and Forest Meteorology* **38**, 249-254.

Grace, J. (1981) Some effects of wind on plants. Pages 31-56 in Grace, J., Ford, E.D. and Jarvis, P.G. (eds.) *Plants and their atmospheric environment.* Blackwell, London.

Grace, J. (1996) Measurement of wind speed near vegetation. Pages 57-73 in Pearcy, R.W., Ehleringer, J., Mooney, H.A. and Rundel, P.W. (eds.) *Plant physiological ecology.* Chapman and Hall, London.

Green, F.H.W. and Harding, R.J. (1979) The effects of altitude on soil temperature. *Meteorological Magazine* **108**, 81-91.

Green, F.H.W., Harding, R.J. and Oliver, H.R. (1984) The relationship of soil temperature to vegetation height. *International Journal of Climatology* **4**, 229-240.

Gross, T. (1999) Biodiversity and sustainable development in mountain regions. Pages 4-6 in Price, M. (ed.) *Global change in the mountains*. Parthenon, Carnforth.

Gueymard, C. (1987) An isotropic solar irradiance model for tilted surfaces and its comparison with selected engineering algorithms. *Solar Energy* **38**, 367-386.

Gullan, P.J. and Cranston, P.S. (1996) *The insects, an outline of entomology*. Chapman and Hall, London.

Guo, X. and Palutikof, J.P. (1990) A study of two mass-consistent models: problems and possible solutions. *Boundary Layer Meteorology* **53**, 303-32.

Gustavsson, T., Karlsson, M., Bogren, J. and Lindqvist, S. (1998) Development of temperature patterns during clear nights. *Journal of Applied Meteorology* **37**, 559-571.

Harding, R.J. (1978) The variation of the altitudinal gradient of temperature within the British Isles. *Geografisker Annaler* **60**, 43-9.

Harding, R.J. (1979a) Altitudinal gradients in temperature in the northern Pennines. *Weather* **34**, 190-201.

Harding, R.J. (1979b) Radiation in the British uplands. *Journal of Applied Ecology* **16**, 161-70.

Hargy, V.T. (1997) Objectively mapping accumulated temperature for Ireland. *International Journal of Climatology* **17**, 909-927.

Harrison, S.J. and Kelly, I. (1996) A field-based index of topographic shelter and its application to topoclimatic variation. *Applied Geography* **16**, 53-63.

Hewer, F.E. (1998) Non-linear numerical model predictions of flow over an isolated hill of moderate slope. *Boundary Layer Meteorology* **87**, 381-408.

Holdridge, L.R. (1947) Determination of world plant formations from simple climatic data. *Science* **105**, 367-368.

Houghton, J.T. (1977) *The physics of atmospheres*. University Press, Cambridge.

Houghton, J.T., Meira Filho, L.G., Callander, B.A., Harris, N., Kattenberg, A. and Maskell, K. (1996) *Climate change 1995: the science of climate change*. University Press, Cambridge.

Hubbard, C.E. (1954) *Grasses: a guide to their structure, identification, uses and distribution in the British Isles*. Penguin, London.

Hulme, M. (1996) *Climate change and southern Africa: an exploration of some potential impacts in the SADC region*. Report commissioned by WWF International. Climatic Research Unit, Norwich.

Hulme, M., Conway, D., Jones, P.D., Jiang, T., Barrow, E.M. and Turney, C. (1995) Construction of a 1961-1990 European climatology for climate-change modeling and impact application. *International Journal of Climatology* **15**, 1333-1363.

Hulme, M., Conway, D., Joyce, A. and Mulenga, H. (1996) A 1961-90 climatology for Africa south of the equator and a comparison of potential evapotranspiration estimates. *South African Journal of Science* **92**, 334-343.

Hunt, L.A., Kuchar, L. and Swanton, C.J. (1998) Estimation of solar radiation for use in crop modelling. *Agricultural and Forest Meteorology* **91**, 293-300.

Huntley, B., Baxter, R., Lewthwaite, K., Willis, S.G. and Adamson, J.K. (1998) Vegetation responses to local climatic changes induced by a water storage reservoir. *Global Ecology and Biogeography Letters* **7**, 241-257.

Hutchinson, M.F. (1987) Methods for generation of weather sequences. Pages 149-157 in Bunting, A.H. (ed.) *Agricultural environments: characterisation, classification and mapping*. CAB, Wallingford.

Hutchinson, M.F. and Gessler, P.E. (1994) Splines - more than just a smooth interpolator. *Geoderma* **62**, 45-67.

Iversen, J. (1944) *Viscum, Hedera* and *Ilex* as climate indicators. *Geologiska Föreningens i Stockholm Förhandlingar* **66**, 463-483.

Jenkinson, A.F. and Collison, F.P. (1977) *An initial climatology of gales over the North Sea*. Synoptic Climatology Branch Memorandum 62. Meteorological Office, Bracknell.

Jones, P.D., Conway, D. and Briffa, K. (1997) Precipitation variability and drought. Pages 197-219 in Hulme, M. and Barrow, E. (eds.) *Climates of the British Isles, present, past and future*. Routledge, London.

Jones, R.J.A. and Thomasson, A.J. (1985) *An agroclimatic databank for England and Wales*. Soil Survey of England and Wales, Harpenden.

Joyce, A. (2000) Daily temperature anomalies at Durham, 1961-98. *Weather* **55**, 327-335.

Kneizys, F.X., Shettle, E.P., Abreu, L.W., Chetwynd, S.H., Anderson, G.P., Gallery, W.O., Selby, J.E.A. and Clough, S.A. (1988) User's guide to LOWTRAN-7. In *Air Force geophysics laboratory report AFGL-TR-88-0177*. Bedford, Massachusetts.

Kondratyev, K., Johannessen, O.M. and Melentyev, V.V. (1996) *High latitude climate and remote sensing*. Wiley, Chichester.

Lamb, H.H. (1972) *British Isles weather types and a register of the daily sequence of circulation patterns, 1861-1971*. Meteorological Office Geophysical Memoir 116. HMSO, London.

Lamb, H.H. (1977) *Climatic history and the future*. University Press, Princeton.

Laurini, R. and Thompson, D. (1992) *Fundamentals of spatial information systems*. Academic Press, London.

Leemans, R. and Cramer, W.P. (1991) *The IIASA database for mean monthly values of temperature, precipitation and cloudiness on a global terrestrial grid*. Working paper WP-90-41, IIASA, Laxenburg.

Legates, D.R. and Willmott, C.J. (1990) Mean seasonal and spatial variability in gauge-corrected global precipitation. *International Journal of Climatology* **10**, 111-128.

Lennon, J.J. and Turner, J.R.G. (1995) Predicting the spatial distribution of climate: temperature in Great Britain. *Journal of Animal Ecology* **64**, 370-392.

Leuning, R., Kelliher, F.M., de Pury, D.G.G. and Schulze, E.D. (1995) Leaf nitrogen, photosynthesis, conductance and transpiration: scaling from leaves to canopies. *Plant, Cell and Environment* **18**, 1183-1200.

Lin, L. (1989) A concordance correlation coefficient to evaluate reproducibility. *Biometrics* **45**, 255-268.

Linacre, E. (1981) Caracteristicas das varias escalas de clima. *Boletin da Sociedade de Meteorologia* **5**, 11-14.

Linacre, E. (1992) *Climate data and resources*. Routledge, London.

Lindkvist, L. and Chen, D. (1999) Air and soil frost indices in relation to plant mortality in elevated clear-felled terrain in central Sweden. *Climate Research* **12**, 65-75.

Lindkvist, L. and Lindkvist, S. (1997) Spatial and temporal variability of nocturnal summer frost in elevated complex terrain. *Agricultural and Forest Meteorology* **87**, 139-153.

Lindsay, S.W. and Martens, W.J.M. (1998) Malaria in the African highlands: past, present and future. *Bulletin of the World Health Organisation* **76**, 33-45.

Lindsay, S.W., Parson, L. and Thomas, C.J. (1998) Mapping the ranges and relative abundance of the two principal African malaria vectors, *Anopheles gambiae sensu stricto* and *Anopheles arabiensis*, using climate data. *Proceedings of the Royal Society* **265**, 847-854.

Loevinsohn, M.E. (1994) Climatic warming and increased malaria incidence in Rwanda. *The Lancet* **343**, 714-718.

Lowry, W.P. (1980) *Direct and diffuse solar radiation: variations with atmospheric turbidity and altitude.* Urbana-Champaign Institute for Environmental Studies. Research Report number 6, University of Illinois.

Mackey, B.G., McKenney, D.W., Yang, Y., McMahon, J.P. and Hutchinson, M.F. (1996) Site regions revisited: a climatic analysis of Hill's site regions for the province of Ontario using a parametric method. *Canadian Journal of Forest Research* **26**, 333-354.

Manley, G. (1936) The climate of the northern Pennines: the coldest part of England. *Quarterly Journal of the Royal Meteorological Society* **62**, 103-115.

Manley, G. (1942) Meteorological observations on Dun Fell, a mountain station in northern England. *Quarterly Journal of the Royal Meteorological Society* **68**, 151-165.

Manley, G. (1943) Further climatological averages for the northern Pennines, with a note on topographical effects. *Quarterly Journal of the Royal Meteorological Society* **69**, 251-262.

Manley, G. (1945) The effective rate of altitudinal change in temperate Atlantic climates. *Geographical Review* **35**, 408-17.

Manley, G. (1952) *Climate and the British scene.* Collins, London.

Manley, G. (1980) The northern Pennines revisited: Moor House, 1932-78. *The Meteorological Magazine* **109**, 281-292.

McKenzie, B.A. and Hill, G.D. (1989) Environmental control of lentil *(Lens culinaris)* crop development. *Journal of Agricultural Science* **113**, 67-72.

Meteorological Office (1975) *Maps of mean and extreme temperature over the UK 1941-70.* HMSO, London.

Meteorological Office (1982) *Observers' handbook* (4th edition). HMSO, London.

Milford, G., Scott, T., Jones, R., Siddons, P. and Huyghe, C. (1995) The use of simple physiological models of plant development to predict where autumn-sown determinate white lupins (*L. albus* L.) might be grown. In *2nd European Conference on Grain Legumes.* Copenhagen.

Millar, A. (1964) Notes on the climate near the upper forest limit in the northern Pennines. *Quarterly Journal of Forestry* **63**, 239-246.

Monteith, J.L. and Unsworth, M.H. (1990) *Principles of environmental physics.* Arnold, London.

Moore, I.D., Grayson, R.B. and Ladson, A.R. (1991) Digital terrain modelling - a review of hydrological, geomorphological and biological applications. *Hydrological Processes* **5**, 3-30.

Mordaunt, K. (1999) Association between weather conditions, snow-lie and snowbed vegetation in the Scottish Highlands. Pages 62-63 in Price, M. (ed.) *Global change in the mountains*. Parthenon, Carnforth.

Mossman, R.C. (1893) Thunderstorms at Ben Nevis observatory. *Journal of the Scottish Meteorological Society* **9**, 33-38.

Muirhead-Thomson, R.C. (1951) *Mosquito behaviour in relation to malaria transmission and control in the tropics*. Edward Arnold, London.

Murray, F.W. (1967) On the computation of saturation vapour pressure. *Journal of Applied Meteorology* **6**, 203-204.

Naess, A., Clausen, P.H. and Sandvik, R. (2000) Gust factors for locations downstream of steep mountain ridges. *Journal of Wind Engineering and Industrial Aerodynamics* **87**, 131-146.

New, M., Hulme, M. and Jones, P. (1999) Representing twentieth-century space-time variability. Part 1: development of a 1961-90 mean monthly terrestrial climatology. *Journal of Climate* **12**, 829-856.

North, P.R.J. (1994) Estimation of annual solar insolation for mountainous terrain. Pages 63-76 in Hill, M. O. (ed.) *Effects of rapid climatic change on plant biodiversity in boreal and montane ecosystems*. Second annual project report, ITE project TO7069u5. Institute of Terrestrial Ecology, Monks Wood.

Oke, T.R. (1978) *Boundary layer climates*. Methuen. London.

Oliver, H.R. (1992) Studies of surface energy balance of sloping terrain. *International Journal of Climatology* **12**, 55-68.

Oliver, J. (1962) The thermal regime of upland peat soils in a maritime temperate climate. *Geografisker Annaler* **44**, 293-302.

Oliver, J.E. (1981) *Climatology: selected applications*. Edward Arnold, London.

Olmo, F.J., Vida, J., Foyo, I., Castro-Diez, Y. and Alados-Arboledas, L. (1999) Prediction of global irradiance on inclined surfaces from horizontal global irradiance. *Energy* **24**, 689-704.

Omond, R.T. (1896) Comparison of observations at the low-level observatory and at the public school, Fort William. *Journal of the Scottish Meteorological Society* **10**, 49-55.

Omond, R.T. (1900) Change of temperature with height during anticyclones on Ben Nevis and at some continental stations. *Journal of the Scottish Meteorological Society* **11**, 65-71.

Ortega, M.D., Holbrook, F.R. and Lloyd, J.E. (1999) Seasonal distribution and relationship to temperature and precipitation of the most abundant species of *Culicoides* in five provinces of Andalucia, Spain. *Journal of the American Mosquito Control Association* **15**, 391-399.

Palacios, D. and Sanchez Colomer, M.G. (1997) The distribution of high mountain vegetation in relation to snow cover: Penalara, Spain. *Catena* **30**, 1-40.

Palomino, I. and Martin, F. (1994) A simple method for spatial interpolation of the wind in complex terrain. *Journal of Applied Meteorology* **34**, 1678-1693.

Paton, J. (1983) *Ben Nevis observatory*. Royal Meteorological Society, London.

Patz, J.A. and Lindsay, S.W. (1999) New challenges, new tools: the impact of climate change on infectious diseases. *Current opinion in microbiology* **2**, 445-451.

Pearcy, R.W. (1996) Radiation and light measurements. Pages 97-116 in Pearcy, R.W., Ehleringer, J., Mooney, H.A. and Rundel, P.W. (eds.) *Plant physiological ecology*. Chapman and Hall, London.

Peixoto, J.P. and Oort, A.H. (1992) *Physics of climate*. American Institute of Physics, New York.

Penman, H.L. (1948) Natural evaporation from open water, bare soil and grass. *Proceedings of the Royal Society* **193**, 120-145.

Pepin, N., Benham, D. and Taylor, K. (1999) Modelling lapse rates in the maritime uplands of northern England: implications for climate change. *Arctic, Antarctic and Alpine Research* **31**, 151-164.

Perla, R.I. and Martinelli, M. (1976) *Avalanche Handbook*. US Department of Agriculture, Fort Collins.

Pfister, C. (1992) Monthly temperature and precipitation in central Europe 1525-1979: quantifying documentary evidence on weather and its effects. Pages 118-142 in Bradley, R.S. and Jones, P.D. (eds.) *Climate since A.D. 1500*. Routledge, London.

Pielke, R.A. and Mehring, P. (1977) Use of mesoscale climatology in mountainous terrain to improve the spatial representation of mean monthly temperatures. *Monthly Weather Review* **105**, 108-112.

Pigott, C. D. (1978) Climate and vegetation. Pages 102-121 in Clapham, A. R. (ed.) *Upper Teesdale, the area and its natural history*. Collins, London

Pisek, A., Larcher, W., Vegis, A. and Napp-Zinn, K. (1973) The normal temperature range. Pages 102-194 in Precht, H., Christophersen, J., Hensel, H. and Larcher, W. (eds.) *Temperature and life*. Springer-Verlag, New York.

Ploeg, A.T. (1999) Influence of temperature on multiplication and egg hatching of *Longidorus africanus*. *Journal of Nematology* **31**, 75-80.

Porter, J.R. (1993) AFRCWHEAT2: a model of the growth and development of wheat incorporating responses to water and nitrogen. *European Journal of Agronomy* **2**, 69-82.

Prentice, I.C., Cramer, W., Harrison, S.P., Leemans, R., Monserud, R.A. and Solomon, A.M. (1992) A global biome model based on plant physiology and dominance, soil properties and climate. *Journal of Biogeography* **19**, 117-134.

Priestley, C.H.B. and Taylor, R.J. (1972) On the assessment of surface heat flux and evaporation using large scale parameters. *Monthly Weather Review* **100**, 81-92.

Rawes, M. (1983) Changes in two high altitude blanket bogs after the cessation of sheep grazing. *Journal of Ecology* **71**, 219-235.

Reitan, C.H. (1963) Surface dew point and water vapour aloft. *Journal of Applied Meteorology* **2**, 776-779.

Reynolds, G. (1965) A history of rain gauges. *Weather* **20**, 106-114.

Rogers, D.J. and Randolph, S.E. (2000) The global spread of malaria in a future, warmer world. *Science* **289**, 1763-1766.

Rorison, I.H. (1981) Plant growth in response to variations in temperature: field and laboratory studies. Pages 313-332 in Grace, J., Ford, E.D. and Jarvis, P.G. (eds.) *Plants and their atmospheric environment*. Blackwell, London.

Rundel, P.W. and Jarrell, W.M. (1996) Water in the environment. Pages 29-56 in Pearcy, R.W., Ehleringer, J., Mooney, H.A. and Rundel, P.W. (eds.) *Plant physiological ecology*. Chapman and Hall, London.

Running, S.W., Nemani, R.R. and Hungerford, R.D. (1987) Extrapolation of synoptic meteorological data in mountainous terrain and its use for simulating forest evapotranspiration and photosynthesis. *Canadian Journal of Forest Research* **17**, 472-483.

Salby, M.L. (1996) *Fundamentals of atmospheric physics*. Academic Press, London.

Salter, M.d.C.S. (1918) The relation of rainfall to configuration. *British Rainfall* **1918**, 40-56.

Saunders, S.C., Chen, J.Q., Drummer, T.D. and Crow, T.R. (1999) Modelling temperature gradients across edges over time in a managed landscape. *Forest Ecology and Management* **117**, 17-31.

Schaefer, J.A. and Messier, F. (1995) Scale dependent correlations of arctic vegetation and snow cover. *Arctic and Alpine Research* **27**, 38-43.

Scheifinger, H. and Kromp-Kolb, H. (2000) Modelling global radiation in complex terrain: comparing two statistical approaches. *Agricultural and Forest Meteorology* **100**, 127-136.

Schimel, D.S., Braswell, B.H., McKeown, R., Ojima, D.S., Parton, W.J. and Pulliam, W. (1996) Climate and nitrogen controls on the geography and timescales of terrestrial biogeochemical cycling. *Global Biogeochemical Cycles* **10**, 677-692.

Simpson, J.E. (1999) *Gravity currents in the environment and the laboratory.* University Press, Cambridge.

Smith, A.J.E. (1978) *The moss flora of Britain and Ireland.* University Press, Cambridge.

Smith, L.P. (1976) *The agricultural climate of England and Wales, areal averages 1941-70.* Ministry of Agriculture Fisheries and Food, London.

Squire, G.R. (1981) Thermal time and tea. Pages 363-368 in Grace, J., Ford, E.D. and Jarvis, P.G., (eds.) *Plants and their atmospheric environment.* Blackwell, London.

Steichen, T.J. (1998) Concordance correlation coefficient. *Stata Technical Bulletin* **43**, 35-39.

Stone, R.G. (1934) The history of mountain meteorology in the United States and the Mount Washington observatory. *Transactions of the American Geophysical Union* **15**, 124-33.

Strangeways, I.C. (1996a) Back to basics: the met. enclosure part 2a - rain gauges. *Weather* **51**, 274-279.

Strangeways, I.C. (1996b) Back to basics: the met. enclosure part 2b - rain gauges, their errors. *Weather* **51**, 298-303.

Sturman, A.P., McGowan, H.A. and Spronken-Smith, R.A. (1999) Meso-scale and local climates in New Zealand. *Progress in Physical Geography* **23**, 611-635.

Supit, I. and van Kappel, R.R. (1998) A simple method to estimate global radiation. *Solar Energy* **63**, 147-160.

Sykes, J.M. and Lane, A.J.M. (1997) *The United Kingdom Environmental Change Network: protocols for standard measurements at terrestrial sites*: Centre for Ecology and Hydrology, NERC.

Tabony, R.C. (1985) Relations between minimum temperature and topography in Great Britain. *Journal of Climatology* **5**, 503-520.

Taylor, J.A. (1976) Upland climates. Pages 264-287 in Chandler, T.J. and Gregory, S. (eds.) *The climate of the British Isles.* Longman, London.

Taylor, W.G. (1996) Statistical relationships between topography and precipitation in a mountainous area. *Northwest Science* **70**, 164-178.

Thiessen, A.H. (1911) Precipitation averages for large areas. *Monthly Weather Review* **39**, 1082-1084.

Thom, A.S. and Oliver, H.R. (1977) On Penman's equation for estimating regional evaporation. *Quarterly Journal of the Royal Meteorological Society* **103**, 345-357.

Thornthwaite, C.W. (1948) An approach toward a rational classification of climate. *Geographical Review* **38**, 55-94.

Thornton, P.E., Hasenaur, H. and White, M.A. (2000) Simultaneous estimation of daily solar radiation and humidity from observed temperature and precipitation: an application over complex terrain in Austria. *Agricultural and Forest Meteorology* **104**, 255-271.

Thornton, P.E., Running, S.W. and White, M.A. (1997) Generating surfaces of daily meteorological variables over large regions of complex terrain. *Journal of Hydrology* **190**, 214-251.

Tromp, S.W. (1980) *Biometeorology*. Heyden International Topics in Science. Heyden, London.

Turner, D.P., Dodson, R. and Marks, D. (1996) Comparison of alternative spatial resolutions in the application of a spatially distributed biogeochemical model over complex terrain. *Ecological Modelling* **90**, 53-67.

UNIRAS (1985) *GEOINT manual. Geopak interpolation version 5.4.* Inter-University committee on computing. University of Manchester.

Unwin, D.M. (1980) *Microclimate measurement for ecologists*. Biological techniques series. Academic Press, London.

VEMAP members (1995) Vegetation and ecosystem modelling and analysis project. *Global Biogeochemical Cycles* **9**, 407-437.

Virtanen, T., Neuvonen, S. and Nikula, A. (1998) Modelling topoclimatic patterns of egg mortality of *Epirrita autumnata* (Lepidoptera: Geometridae) with a geographical information system: predictions for current climate and warmer climate scenarios. *Journal of Applied Ecology* **35**, 302-310.

Wahba, G. (1990) *Spline models for observational data*. CBMS-NSF regional conference series in applied mathematics. SIAM, Philadelphia.

Wahba, G. and Wendelberger, J. (1980) Some new mathematical models for variational objective analysis using splines and cross validation. *Monthly Weather Review* **108**, 1122-1143.

Walton, D.W.H. (1982) Instruments for measuring biological microclimates for terrestrial habitats in polar and high alpine regions: a review. *Arctic and Alpine Research* **14**, 275-286.

Whiteman, C.D., Bian, X.D. and Sutherland, J.L. (1999) Wintertime surface wind patterns in the Colorado River valley. *Journal of Applied Meteorology* **38**, 1118-1130.

Wilby, R.L. (1997) Non-stationarity in daily precipitation series: implications for GCM downscaling using atmospheric circulation indices. *International Journal of Climatology* **17**, 439-454.

Wilks, D.S. (1999) Simultaneous stochastic simulation of daily precipitation, temperature and solar radiation at multiple sites in complex terrain. *Agricultural and Forest Meteorology* **96**, 85-101.

Winter, F. (1958) Das Spätfrostproblem im Rahmen der Neuordnung des südwestdeutschen Obstbaus. *Gartenbauwissensch* **23**, 342-362.

Wobrock, W., Flossmann, A.L., Colvile, R.N. and Inglis, D.W.F. (1997) Modelling of air flow and cloud fields over the northern Pennines. *Atmospheric Environment* **31**, 2421-2439.

Young, C.B., Nelson, B.R., Bradley, A.A., Smith, J.A., Peterslidard, C.D., Kruger, A. and Baeck, M.L. (1999) An evaluation of NEXRAD precipitation estimates in complex terrain. *Journal of Geophysical Research - Atmospheres* **104**, 19691-19703.

Zheng, X. and Basher, R. (1995) Thin-plate smoothing spline modelling of spatial climate data and its application to mapping south Pacific rainfalls. *Monthly Weather Review* **123**, 3086-3102.

Appendix 1. List of symbols and abbreviations

Symbol	Description	Units
α	Albedo	none
Δ	Slope of the curve of saturation vapour pressure against temperature	hPa $^{o}C^{-1}$
ε	Surface emissivity	none
γ	Psychrometric coefficient	h Pa $^{o}C^{-1}$
η	Daily fraction of maximum daylight duration	none
Θ	Angle between incident beam and a plane normal to the surface	degrees
ρ	Pearson correlation coefficient	none
ρ_c	Concordance correlation coefficient	none
σ	Stefan-Boltzmann constant	W m^{-2} K^{-4}
A	Latitude	degrees
a	Daily climate anomaly from Moor House	various
aspect	Slope aspect	degrees
az	Solar azimuth	degrees
B	Bowen ratio	none
b	Aerodynamic coefficient	none
c	Aerodynamic coefficient	none
d	Solar declination	degrees
diff	Daily mean minus daily minimum temperature	^{o}C
dir	Daily mean wind direction at Great Dun Fell	degrees
dist	Distance relative to the Pennine ridge	m
dra	Diurnal range of temperature	^{o}C
drain	Topographic drainage potential	m
DTM	Elevation surface	m
Ea	Aerodynamic term in Penman equation	none
ele	Elevation above sea level	m
e_s	Saturation vapour pressure	hPa
gd	Gaussian fraction of daylight duration	none
gra	Daily grass minimum temperature	^{o}C
H	Solar hour angle	degrees
H_s	Solar hour angle at sunset	degrees
$K\uparrow$	Reflected short wave radiation	W m^{-2}
$K\downarrow$	Incident short wave radiation	W m^{-2}
$K\downarrow_i$	Incident short wave radiation perpendicular to solar beam	W m^{-2}
$L\uparrow$	Emitted long wave radiation	W m^{-2}
$L\downarrow$	Incident long wave radiation	W m^{-2}
light	Daylight duration	hours
lr	Daily lapse rate	^{o}C m^{-1}
MAE	Mean absolute error	various
MH	Daily observed climate value at Moor House	various

Nm	Time elapsed since vernal equinox	days
PE	Potential evapotranspiration	mm day^{-1}
Q_a	Extra-terrestrial radiation	W m^{-2}
Q_e	Latent heat flux	W m^{-2}
Q_h	Sensible heat flux	W m^{-2}
Q_n	Net radiation	W m^{-2}
ratio	Ratio of observed solar radiation to cell value in *SOLAR4* surface	none
residual	Daily station climate observation minus daily modelled value	various
rh	Relative humidity	%
ridge	Ridge topography index	grid cells
RMSE	Root mean square error	various
S	Daily observed climate value at weather station	various
sa	Solar altitude	degrees
sd	Standard deviation of anomalies for GPS fixes	m
se	Earth-sun distance correction	none
shelter	Topographic shelter	m
slope	Slope gradient	degrees
solar	Daily solar radiation at Moor House	W m^{-2}
SOLAR1	Daily illumination surface	none
$[SOLAR1]_{MAX}$	Maximum cell value in *SOLAR1* surface	none
SOLAR2	Preliminary daily modelled solar radiation surface	W m^{-2}
$[SOLAR2]_{MH}$	Moor House cell value in *SOLAR2* surface	W m^{-2}
SOLAR3	Modelled daily solar radiation surface	W m^{-2}
SOLAR4	Modelled daily solar radiation surface smoothed for cloudiness	W m^{-2}
T	Temperature	K
TEMP	Daily modelled temperature surface	°C
tmn	Daily minimum air temperature	°C
tmp	Daily mean air temperature	°C
tmx	Daily maximum air temperature	°C
turb	Index of atmospheric turbidity	none
vap	Daily mean vapour pressure	hPa
vpd	Daily mean vapour pressure deficit	hPa
wet	Daily mean wet-bulb temperature	°C
wind	Daily mean wind speed	m s^{-1}
$x_{95\%}$	95% critical value for GPS fixes	m
$\bar{x}$	Mean value of anomalies for GPS fixes	m

Appendix 2 Modelling preliminary topographic surfaces

Using the GRID program in ARC/INFO:

1. Generate a grid of elevation relative to the Moor House station using the GRID command:

ELEV = *DTM* - 550

where 550 m is the elevation of the Moor House station.

2. Calculate a grid of distance relative to the Pennine ridge using the GRID command:

DIST = eucdistance (test (*DTM*, "value < 280.0")

3. Calculate a grid of topographic drainage potential using the GRID command:

DRAIN = *DTM* - (focalmin (*DTM*, rectangle, 10, 10))

Appendix 3 Modelling daily mean temperature surfaces

Using a spreadsheet or similar software:

1. Input hourly data from Moor House (*MH*) and Great Dun Fell (*GDF*) weather stations.

2. Extract daily mean values of hourly air temperature at both sites (tmp_{MH} and tmp_{GDF}). Add the empirical correction constant (+0.1 °C) to the daily mean temperature data for Great Dun Fell.

3. Extract daily mean values of wind direction at Great Dun Fell.

4 Calculate daily lapse rates of mean temperature, lr_{tmp} (°C m^{-1}):

$$lr_{tmp} = \frac{(tmp_{GDF} - tmp_{MH})}{295}$$

where 295 m is the elevation difference between the two stations.

Using the GRID program in ARC/INFO:

5. Generate a mean temperature surface for each day:

$$TEMP_{tmp} = lr_{tmp} \times ELEV + tmp_{MH}$$

6. Generate a surface of temperature corrections:

$$RESIDUALS_{tmp} = -1.534 \times (DIST \times 10^{-4}) + 1.09$$

7. If the daily mean wind direction at Great Dun Fell is between 90° and 180°;

Adjust the mean temperature surface by adding the modelled residuals:

$$TEMP2_{tmp} = TEMP_{tmp} + RESIDUALS_{tmp}$$

Appendix 4 Modelling daily minimum temperature surfaces

Using a spreadsheet or similar software:

1. Input hourly data from Moor House (*MH*) and Great Dun Fell (*GDF*) weather stations.

2. Extract daily minimum values of hourly air temperature at both sites (tmn_{MH} and tmn_{GDF}). Add the empirical correction constant (+0.1 °C) to the daily minimum temperature data for Great Dun Fell.

3. Calculate daily lapse rates of minimum temperature, lr_{tmn} (°C m^{-1}):

$$lr_{tmn} = \frac{(tmn_{GDF} - tmn_{MH})}{295}$$

where 295 m is the elevation difference between the two stations.

Using the GRID program in ARC/INFO:

4. Generate a minimum temperature surface for each day:

$$TEMP_{tmn} = lr_{tmn} \times ELEV + tmn_{MH}$$

5. Generate a surface of temperature corrections:

$$RESIDUALS_{tmn} = 0.0285(DRAIN) - 0.83$$

6. If the lapse rate of minimum temperature is greater than -2.03×10^{-3} °C m^{-1};

Adjust the daily minimum temperature surface by adding the modelled residuals:

$$TEMP2_{tmn} = TEMP_{tmn} + RESIDUALS_{tmn}$$

Appendix 5 Modelling daily maximum temperature surfaces

Using a spreadsheet or similar software:

1. Input hourly data from Moor House (*MH*) and Great Dun Fell (*GDF*) weather stations.

2. Extract daily maximum values of hourly air temperature at both sites (tmx_{MH} and tmx_{GDF}). Add the empirical correction constant (+0.1 °C) to the daily maximum temperature data for Great Dun Fell.

3. Calculate daily lapse rates of maximum temperature, lr_{tmx} (°C m^{-1}):

$$lr_{tmx} = \frac{(tmx_{GDF} - tmx_{MH})}{295}$$

where 295 m is the elevation difference between the two stations.

Using the GRID program in ARC/INFO:

4. Generate a maximum temperature surface for each day:

$$TEMP_{tmx} = lr_{tmx} \times ELEV + tmx_{MH}$$

Appendix 6 Modelling daily solar radiation surfaces

Using the FORTRAN program solar.f:

1. Calculate daily values for the top-of-the-atmosphere solar radiation (Q_a).

2. Calculate solar altitude (*sa*) and azimuth (*az*) at five Gaussian fractions of day length.

The program solar.f is given in appendix 7.

Using a spreadsheet or similar software:

3. Input hourly data from Moor House weather station

4. Extract daily mean values of hourly solar radiation ($solar_{MH}$).

Using the GRID program in ARC/INFO:

5. Generate five illumination surfaces for each day using Gaussian weights:

$ILLUM_1 = 0.11846 \times$ hillshade (DTM, az_1, sa_1)

$ILLUM_2 = 0.23931 \times$ hillshade (DTM, az_2, sa_2)

$ILLUM_3 = 0.28444 \times$ hillshade (DTM, az_3, sa_3)

$ILLUM_4 = 0.23931 \times$ hillshade (DTM, az_4, sa_4)

$ILLUM_5 = 0.11846 \times$ hillshade (DTM, az_5, sa_5)

6. Sum the five surfaces to give a daily illumination surface

$$SOLAR1 = \sum_{n=1}^{5} (ILLUM_n)$$

7. Find the maximum value in *SOLAR1*, $[SOLAR1]_{MAX}$, using the command *describe SOLAR1*.

8. Create a surface in W m^{-2} using the top of the atmosphere value Q_a:

$$SOLAR2 = \left(\frac{SOLAR1}{[SOLAR1]_{MAX}} \right) Q_a$$

9. Find the Moor House grid cell value of the *SOLAR2* surface, $[SOLAR2]_{MH}$:

cellvalue *SOLAR2* 375700 532800

10. Scale the *SOLAR2* surface using the observed Moor House value:

$$SOLAR3 = \left(\frac{solar_{mh}}{[SOLAR2]_{MH}} \right) SOLAR2$$

11. Smooth the modelled surface to the Moor House value to take account of cloudiness:

$$SOLAR4 = solar_{mh} - \left(\frac{solar_{mh} - SOLAR3}{Qa/solar_{mh}} \right)$$

12. Model the solar declination d:

$$d = 23.45 \sin\left(\frac{360}{365.25} \right) Nm$$

13. Model the hour angle at sunset H_s:

$$\cos H_s = -\tan A \tan d$$

where A = latitude of the site (54.68°)

14. Model daylight duration *light*:

$$light = \frac{H_s}{7.5}$$

15. Model the seasonal correction factor η:

$$\eta = \frac{light}{17.0}$$

16. Multiply the modelled solar surface by the correction factor η:

$$SOLAR5 = SOLAR4 \times \eta$$

Appendix 7 Program solar.f

```
C=================================================
C   Calculates hour angle of the sun, solar elevation and azimuth
C   at five times of day (Leuning, Kelliher et al 95) for gaussian
C   integration of daily average.
C   Also calculates extra-terrestrial radiation input at site.
C   gaussian distances: 0.04691,0.23075,0.5,0.76925,0.95309
C   gaussian weights: 0.11846,0.23931,0.28444,0.23931,0.11846
C   Andy Joyce 15 May 1998
C=================================================
    PROGRAM SOLAR
C
    INTEGER date,Nm,
    REAL Qa,az1,az2,az3,az4,az5,sa1,sa2,sa3,sa4,sa5,pi,
   & H1,H2,H3,H4,H5,se,Hs,A,Ar,d,day

    OPEN (5,FILE='astro',STATUS='UNKNOWN')
    OPEN (6,FILE='jday.365',STATUS='OLD')
C
    DO 100 N=1,365
C
    READ(6,402) date,Nm
C
401  format(i3,2f8.1,f6.1,f8.1,f6.1,f8.1,f6.1,f8.1,
   & f6.1,f8.1,f6.1)
402  format(i6,i5)
C
    pi=3.14159
    A=54.68       !latitude of Moor House, deg
C
    alb=pi/180.0*30.0*(month+0.0333*day+2.25)
    alb=0.29+0.06*sin(alb)     !albedo, Wright 1982
C
    Ar=A*pi/180.0            !latitude, radians
C
    d=(23.45*pi/180.0)*sin(2.0*pi/365.0*Nm)
                    !declination of sun, radians
C
    Hs=acos(-tan(Ar)*tan(d))   !hour angle of sun at sunset, radians
C
C   now calculate times corresponding to Leuning & Kelliher 1995
C   Hour angle coefficients below are calculated from gaussian
C   distances (if gd=0.0, hour angle=-Hs, sunrise
C        and if gd=0.5, hour angle=0.0, solar noon)
C   therefore hour angle coefficient = -1.0*(1.0-gd/0.5)
C
    H1=Hs*-0.90618 !hour angle at gaussian distance 1, radians
    H2=Hs*-0.5385  !hour angle at gaussian distance 2, radians
```

```
      H3=0.0        !hour angle at noon (gaussian distance 3), radians
      H4=Hs*0.5385  !hour angle at gaussian distance 4, radians
      H5=Hs*0.90618 !hour angle at gaussian distance 5, radians
C
      se=(2.0*pi*Nm/365.0)-(2.0*pi*198.0/365.0)
      se=(pi/180.0)+(pi*0.0344/180.0)*sin(se)
      se=180.0*se/pi            !eccentricity of earth's orbit
C
      Qa=(24.0/pi*1360.0)*se*(Hs*sin(Ar)*sin(d)+cos(Ar)*cos(d)*sin(Hs))
                        !total daily insolation W/m2 for one day
      Qa=Qa/24.0                !W/m2
C
      day=(Hs*180.0/pi)/7.5     !daylength,hours
C
      sa1=sin(d)*sin(Ar)+cos(d)*cos(Ar)*cos(H1)
      sa1=asin(sa1)
      sa5=sa1  !solar altitude 1 and 5, radians
C
      sa2=sin(d)*sin(Ar)+cos(d)*cos(Ar)*cos(H2)
      sa2=asin(sa2)
      sa4=sa2  !solar altitude 2 and 4, radians
C
      sa3=sin(d)*sin(Ar)+cos(d)*cos(Ar)*cos(H3)
      sa3=asin(sa3) !solar altitude 3 (noon), radians
C
      az1=(sin(d)-sin(Ar)*sin(sa1))/cos(Ar)*cos(sa1)
      az1=acos(az1)
C
      az2=(sin(d)-sin(Ar)*sin(sa2))/cos(Ar)*cos(sa2)
      az2=acos(az2)
C
      az3=-1.0*cos(d)*sin(H3)/cos(sa3)
      az3=asin(az3) !solar azimuth 3, radians
C
      az4=(sin(d)-sin(Ar)*sin(sa4))/cos(Ar)*cos(sa4)
      az4=acos(az4)
C
      az5=(sin(d)-sin(Ar)*sin(sa5))/cos(Ar)*cos(sa5)
      az5=acos(az5)
C
C     !now convert everything to degrees
C
      sa1=sa1*180.0/pi
      sa2=sa2*180.0/pi
      sa3=sa3*180.0/pi
      sa4=sa4*180.0/pi
      sa5=sa5*180.0/pi
      az1=az1*180.0/pi
      az2=az2*180.0/pi
```

```
      az3=az3*180.0/pi
      az4=az4*180.0/pi
      az5=az5*180.0/pi
C
       az3=180.0+az3
       az4=360.0-az4
       az5=360.0-az5
C
      WRITE(5,401) date,Qa,az1,sa1,az2,sa2,az3,sa3,az4,
     & sa4,az5,sa5
C
100    CONTINUE
C
       STOP
       END
```

Appendix 8 Modelling daily *PE* surfaces

Using a spreadsheet or similar software:

1. Input hourly data from Moor House (*MH*) and Great Dun Fell (*GDF*) weather stations.

2. Extract daily mean values of hourly air temperature (*tmp*), wet-bulb air temperature (*wet*), wind speed (*wind*) and net radiation (Q_n) at both sites. Extract daily maximum and minimum values of hourly air temperature (*tmx* and *tmn*) at both sites. Add the empirical correction constant (+0.1 °C) to the *tmp*, *tmx* and *tmn* data for Great Dun Fell.

3. Using the FORTRAN program penman.f, calculate daily values of *PE* for each site. The program penman.f follows in appendix 9.

4. Calculate daily gradients of *PE* on elevation, lr_{PE} (mm m^{-1}):

$$lr_{PE} = \frac{(PE_{GDF} - PE_{MH})}{295}$$

where 295 m is the elevation difference between the two stations.

Using the GRID program in ARC/INFO:

4. Generate a *PE* surface for each day:

$$PE = lr_{pet} \times ELEV + PE_{MH}$$

Appendix 9 Program penman.f

```
C=======================================================
C    Calculates daylength, net irradiance, vapour pressure
C    & Penman ET from daily climate data
C    For sites throughout UK
C    Andy Joyce 14 July 1998
C
C    check latitude & elevation!!!
C=======================================================
     PROGRAM PENMAN
C
     INTEGER day,Nm,log,year
     REAL wet,tmp,tmx,tmn,pen,td,A,Ar,z,se,
    & Tk,ea,es,Qn,alb,Qa,light,d,Hs,pi,psych,delta,
    & fe,fu,wnd,penman,act,u,wind,rh,eap,sat,bolz,
    & psy,del,qnet,thom1,thom2,cru
C
     OPEN (4,FILE='86.raw',STATUS='OLD')
C    OPEN (5,FILE='86.cru',STATUS='UNKNOWN')
     OPEN (6,FILE='86.vpd',STATUS='UNKNOWN')
C
     DO 100 N=1,139
C
     READ(4,400) log,year,day,Qn,wet,tmx,tmp,tmn,wind
C
400  format(i5,2i6,6f8.1)
401  format(3i5,3f7.1)
402  format(4i5,7f6.1,f5.2)
C
     pi=3.14159
     alb=0.18              !albedo estimate
     A=54.68               !latitude of site, deg
     z=755.0               !elevation of site, m
C
     Ar=A*pi/180.0         !latitude, radians
C
     if(day.LT.80) then
      Nm=day+285
     end if
C
     if(day.GT.79) then
      Nm=day-80
     end if
C
     d=(23.45*pi/180.0)*sin(2.0*pi/365.0*Nm)
                    !declination of sun, radians
C
     Hs=acos(-tan(Ar)*tan(d))   !hour angle of sun at sunset, radians
```

```
C
      se=(2.0*pi*Nm/365.0)-(2.0*pi*198.0/365.0)
      se=(pi/180.0)+(pi*0.0344/180.0)*sin(se)
      se=180.0*se/pi            !eccentricity of earth's orbit
C
      Qa=(24.0/pi*1360.0)*se*(Hs*sin(Ar)*sin(d)+cos(Ar)*cos(d)*sin(Hs))
                        !total daily insolation W/m2day
      Qa=Qa/24.0                !W/m2
C
      light=(Hs*180.0/pi)/7.5     !daylength,hours
C
      IF(wet.GE.tmp) then
      wet=tmp-0.001
      end if
C
      Tk=tmp+273.15                !mean temperature,Kelvin
      u=real(wind)
      u=u*0.514              !windspeed,m/s
C
      td=0.52*tmn+0.6*tmx-0.009*tmx**2-2.0
                  !dewpoint temperature,deg C
C
      sat=0.6108*EXP(17.27*tmp/(tmp+237.3))
C                           !sat. vap pressure,kPa Murray 1967
C
C     act=0.6108*EXP(17.27*td/(td+237.3))  !ambient vap,kPa
C
      es=sat*10.0                !saturation vapour pressure,hPa
      ea=es-0.8*(tmp-wet)          !ambient vapour pressure,hPa
C     ea=act*10.0                !ambient vapour pressure,hPa
      rh=ea/es                   !relative humidity
      act=ea/10.0
C
      IF(rh.GT.1.0) then
      rh=1.0
      end if
C
      pen=(0.015+(tmp*4E-4)+z*10**-6)
      pet=(380.0*(tmp+0.006*z)/(84.0-a)-40.0+4.0*u*(tmp-td))
      pen=pen*pet                !Penman evapotranspiration,mm/day
C                           !Linacre 1992
C     IF(pen.LT.0.0) then
C     pen=0.0
C     end if                     !corrects -ve penman values
C
      Qn=Qn/11.574               !net irradiance,MJ/m2/day
C
C ORIGINAL PENMAN 1963 ALGORITHM BELOW
C
```

```
      PSYCH=0.6108*EXP(17.27*wet/(wet+237.3))
      PSYCH=PSYCH-act
      PSYCH=PSYCH/(tmp-wet)
C
      IF(PSYCH.LE.0.0) then
      PSYCH=0.0001
      end if
C
      DELTA=(tmp+237.3)*(tmp+237.3)
      DELTA=2503/DELTA
      DELTA=DELTA*EXP(17.27*tmp/(tmp+237.3))     !kPa/deg C
C
      fe=(1.0-rh)*sat                    !kPa
C
      wnd=u*86.4                         !wind, km/day
      fu=1.0+0.0062*wnd
C
      PENMAN=psych/(delta+psych)*6.43*fu*fe
      PENMAN=PENMAN+(delta/(delta+psych)*Qn)     !MJ/m2/day
      PENMAN=PENMAN*11.574/14.1                  !mm/day
C
C     CRU algorithm for Penman ET below
C
      thom1=2.5 !or 1.0 for original
      thom2=2.4 !or 1.0 for original
      bolz=5.67
      psy=0.66
C
      hum=rh*100.0

      del=6.11*237.3*17.269*EXP(17.269*tmp/(237.3+tmp))
      del=del/((237.3+tmp)*(237.3+tmp))

      qnet=Qn*11.574/14.1        !net rad (mm/day)

      eap=0.26*(es-ea)*(1.0+wnd/160.0)
      cru=(del*qnet+thom1*psy*eap)/(del+thom2*psy)

C     write(5,401) log,year,day,pen,PENMAN,cru
      write(6,402) log,year,day,nint(z),cru,PENMAN,pen,
     & wind,ea,Qn,(es-ea),rh
C
100   CONTINUE
C
      STOP
      END
```

Appendix 10 Calculating frost frequency

Using the GRID program in ARC/INFO:

1. Generate daily binary surfaces of frost occurrence from minimum temperature surfaces:

$FROST$ = con ($TEMP_{tmn} < 0.0$, 1 , 0)

2. Sum the resulting consecutive *FROST* surfaces for the desired time period.

Appendix 11 Calculating temperature sums

Using the GRID program in ARC/INFO:

1. Generate daily surfaces of mean temperature above a threshold (e.g. 5.0°C):

$TSUM$ = con ($TEMP_{tmp} > 5.0$, ($TEMP_{tmp}$ - 5.0) , 0.0)

2. Sum the resulting consecutive $TSUM$ surfaces for the desired time period.